Investigation of
Two-Higgs-Doublet Models

by

Alexander Woodcock

ORCID: 0000-0002-8184-9713

A thesis submitted in total fulfillment for the
degree of Master of Philosophy

in the
Department of Physics
School of Physical Sciences
THE UNIVERSITY OF ADELAIDE

July 2023

Abstract

Much of our knowledge of particle physics has been incorporated into the Standard Model (SM), which is a gauge field theory that describes 17 fundamental, structureless particles. While the SM has been extremely successful, it leaves some striking deficiencies which we aim to address. The Two-Higgs-Doublet model (2HDM) is a simple extension of the SM with an additional Higgs doublet. Electroweak symmetry breaking in the 2HDM reveals a total of 5 massive scalar bosons including 2 CP-even scalars, a CP-odd scalar, and 2 degenerate charged scalars. We consider three types of 2HDMs; namely, the Type-I 2HDM, Type-II 2HDM and the Inert Doublet Model (IDM). The former two have additional flavour-changing charged currents which may help explain anomalies in flavour observables, while the latter includes a suitable dark matter (DM) candidate. Global fits are performed using the GAMBIT software at tree-level with results presented as frequentist profile likelihood ratio plots. The 2HDM was previously implemented in GAMBIT, but is further enhanced with new features, bug fixes, and performance improvements. Separate plots are presented for a variety of different theoretical and experimental constraints. The theoretical constraints we consider are S-matrix unitarity, perturbativity and vacuum stability, whereas the experimental constraints arise from measurements of the electroweak S, T, and U parameters; dark matter direct and indirect detection; flavour physics observables; and measurements of Higgs signal rates from collider experiments. Results are found to favour an SM-like scenario in general. The Type-II 2HDM provides the strongest lower bounds on the scalar masses due to flavour constraints, while the Type-I 2HDM has weaker limits which arise only from collider constraints. This is a result of a particular SM-like limit in Type-I model which weakens the flavour constraints. Results for the hidden-Higgs scenario, where the heavier CP-even scalar is considered to be SM-like, are presented separately. The main difference is that the scalar masses have a strict upper limit of 600 GeV set by the theoretical constraints. In the Type-II 2HDM, we find that this conflicts with the lower bound for charged scalar mass set by flavour constraints. Preliminary results using the 2-loop-level FlexibleSUSY spectrum generator are also presented with the main difference being a stricter limit on the couplings. The IDM is initially generated by the GUM software which writes the required code into GAMBIT to implement the new model. New features are also added to GUM and further additions are made in the IDM implementation in GAMBIT, including a tree-level spectrum generator, theoretical constraints and new bases. Results for the IDM scans are presented at tree-level. We apply the observed relic density as an upper bound, to allow the possibility of other dark matter candidates. We find lower bounds on the scalar masses arising from experimental constraints except when the DM-SM couplings are close to zero, or near the Higgs resonance.

Declaration of Authorship

I, Alex Woodcock, certify that this work contains no material which has been accepted for the award of any other degree or diploma in my name in any university or other tertiary institution and, to the best of my knowledge and belief, contains no material previously published or written by another person, except where due reference has been made in the text. In addition, I certify that no part of this work will, in the future, be used in a submission in my name for any other degree or diploma in any university or other tertiary institution without the prior approval of the University of Adelaide and where applicable, any partner institution responsible for the joint award of this degree. I give permission for the digital version of my thesis to be made available on the web, via the University's digital research repository, the Library Search and also through web search engines, unless permission has been granted by the University to restrict access for a period of time. I acknowledge the support I have received for my research through the provision of an Australian Government Research Training Program Scholarship.

Signed: _____

Date: _____31/07/2023_____

Acknowledgements

Contents

List of Figures

List of Tables

List of Acronyms

2HDM	Two Higgs Doublet Model
2HDMC	2HDM Calculator
BR	Branching Ratio
BSM	Beyond the Standard Model
C	Charge
CKM	Cabibbo Kobayashi Maskaw
CL	Confidence Level
CMB	Cosmic Microwave Background
CP	Charge Parity
CS	Cross Section
DD	Direct Detection
DE	Differential Evolution
DM	Dark Matter
EFT	Effective Field Theory
FCCC	Flavour Changing Charged Current
FCNC	Flavour Changing Neutral Current
GAMBIT	Global And Modular BSM Inference Tool
GCP	Generalized Charge Parity
GUM	GAMBIT Universal Model Machine
HF	Higgs Family
HHS	Hidden Higgs Scenario
HPC	High Performance Computer
IDM	Inert Doublet Model
KED	Kinetic Energy Density
LEP	Large Electron Positron collider
LFV	Lepton Flavour Violation

LHC   Large Hadron Collider

LO   Leading Order

MCMC   Markov Chain Monte Carlo

MLE   Maximum Likelihood Estimate

MS   Minimal Subtraction

MSSM   Minimal Supersymmetric Standard Model

NLO   Next-to-Leading Order

NP   Nuisance Parameter

PGD   Particle Data Group

PMNS   Pontecorvo Maki Nakagawa Sakata

QCD   Quantum ChromoDynamics

QED   Quantum ElectroDynamics

QFT   Quantum Field Theory

QFV   Quark Flavour Violation

RGE   Renormalization Group Equation

SM   Standard Model

STXS   Simplified Template Cross Section

SUSY   SUperSYmmetry

VEV   Vacuum Expectation Value

Chapter 1

Introduction

The main goal of particle physics is to identify the fundamental constituents of matter and to understand the rules that govern their behaviour [15, 16]. Remarkable progress has been made over the last century, from the discovery of the electron in 1897 by J. J. Thompson [17] to the discovery of the Higgs boson in 2012 by the ATLAS and CMS experiments [18]. Much of our knowledge has been incorporated into the Standard Model (SM), which is a gauge field theory that includes 17 fundamental, structureless particles and describes their interactions via three fundamental forces. These are known as the strong, weak, and electromagnetic forces. As shown in Figure 1.1, the matter particles can be categorised by:
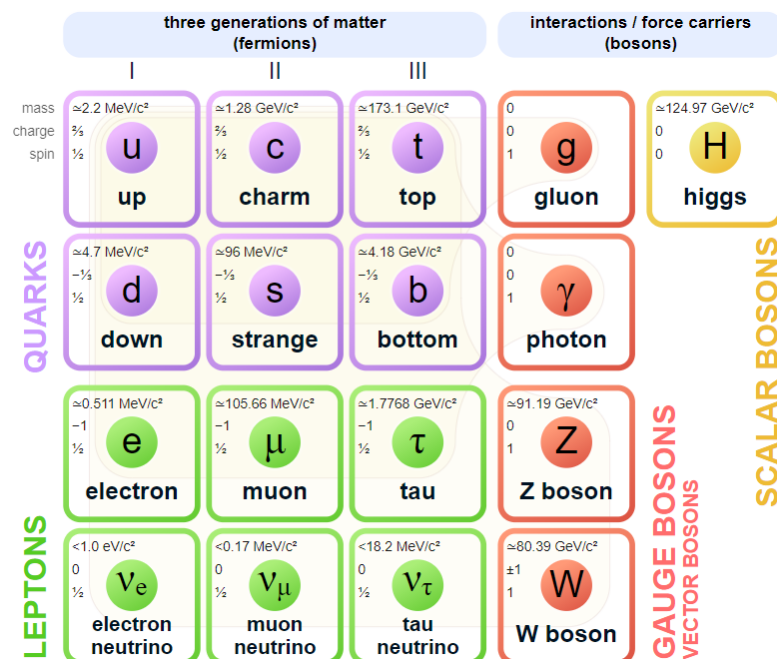
FIGURE 1.1: Elementary particles of the standard model [1].

- **Spin:** The SM can be divided into two spin categories. Fermions are particles which carry half-integer spin whereas bosons have integer spin.

- **Colour:** Fermions are further categorised as either *quarks*, which carry *colour charge*, or *leptons*, which do not. Colour charge enables quarks to interact via the strong force.

- **Generation:** Each row of fermions includes three generations of similar particles differing in only their mass (see columns labelled I, II, III). All stable matter is composed predominantly of first-generation particles.

Fermions are matter particles which obey the Pauli Exclusion Principle. This prevents them from reinforcing to create macroscopic fields. There are two types: quarks and leptons. Quarks are always found in bound states called hadrons, such as protons, neutrons and mesons. Bosons are force-carrier particles that mediate the electromagnetic, strong, and weak forces. The familiar electromagnetic force binds electrons to protons to form atoms. The weak force is responsible for radioactive decay of certain nuclei and the strong force is responsible for the formation of hadrons. Most bound states of these fundamental particles are short-lived, so our world is composed mainly of electrons, protons, and neutrons in the form of atoms. Particles are differentiated by their mass, spin and by a set of charges that they carry. In the SM, the types of charges that particles carry are determined by the representation of an internal symmetry group that each belongs to.

The SM is a remarkably successful theory. One of the greatest successes is the prediction of a scalar particle called the Higgs Boson, which was discovered after it had been theorised for over 50 years. Furthermore, the existence of the W and Z bosons, gluons, and the top, bottom and charm quarks were predicted before they were observed – including various properties of these particles. The SM also predicts the electric dipole moment of the electron to incredible accuracy, given by $a = 0.00115965218073(28)$ – which is accurate to one part in a billion. Despite its success, the SM still leaves some striking deficiencies, for example:

- **Gravity:** There is no description of gravity as it does not seem to be compatible with quantum field theory (QFT) – which the SM is built from. Instead, gravity is best explained by Einstein's theory of General Relativity – a classical theory.

- **Dark Matter:** Cosmological and astronomical evidence suggests that most of the universe's mass is in the form of cold, non-baryonic matter known as dark matter

[19]. Dark matter particles are believed to interact only via gravity and the weak force. However, the SM provides no dark matter candidate.[1]

- **Dark Energy:** Cosmological evidence suggests that 70% of the universe's energy is in the form of so-called dark energy with a constant vacuum density. The SM (and QFT in general) has no way of explaining this dark energy.[2]

- **Hierarchy Problem:** Corrections to the Higgs couplings, and thus particle masses, tend to push the Higgs mass much larger than the experimental value of 125 GeV. This means that the SM requires very unnatural fine-tuned cancellation of sub-amplitudes (where terms of order 10^{16} GeV cancel to leave 125 GeV).

- **Baryon Asymmetry**: The SM does not explain why the universe is composed predominantly of matter, with only a small amount of anti-matter. Charge-parity (CP) violation of the weak interaction may account for some of this, but more CP violation would be required to match the observed asymmetry.

- **Input Parameters:** The SM requires 19 numerical constants whose values are unrelated and arbitrary.

Recently, some experimental tensions have also started emerging. For example, Fermilab measurements of the W-boson mass [20] show a 7 standard deviation discrepancy with the SM prediction. The observed value of the muon anomalous magnetic moment was also measured at Fermilab with a value that differs by 4.2 standard deviations [21]. Furthermore, a variety of observables from flavour physics show some deviation although with a lower significance level compared to the aforementioned electroweak observables.

1.1   Extending the Standard Model

Despite its deficiencies, the SM has largely proven to be very accurate and useful. Hence, our aim is to extend it so that it is alleviated from these shortcomings, rather than abandon it. From a theoretical standpoint, it is not difficult to add new particles and interactions to the SM in ways that achieve this. For example, a new heavy weakly-interacting particle may provide a suitable dark matter candidate. The observed baryon asymmetry may be solved by adding additional sources of CP violation. The Hierarchy problem may be solved by Super-Symmetric (SUSY) Models [22], which add an additional boson partner for every SM fermion.

---

[1]Note that we are making two key assumptions here: (i) that DM is composed of particles, and (ii) that it is weakly interacting. It is much easier to detect DM under these assumptions, so this possibility should be ruled out first before considering alternatives.

[2]It is surely not the famous "zero-point energy" which is off by 120 orders of magnitude.

However, generally speaking, we lack the experimental evidence to determine which of these extensions is preferred. Instead, we can only place further constraints on these models. These limit the strength of new interactions and push the masses of new particles above that which can be produced and therefore detected at particle colliders. This is expected, since there are no positive discoveries of Beyond the Standard Model (BSM) particles or interactions.

It is important not to add unnecessary complexity to our models. We can always add new terms to some theory that are exceedingly close to zero without conflicting with any experimental evidence. But this would reduce the model's *predictive power*, making it less useful in practice. We therefore aim to find models that explain our observations in the simplest manner possible.

In this thesis, we study the Two-Higgs-Doublet Model (2HDM). This is a simple extension of the SM with additional scalar particles. In the low-energy universe that we live in today, the 2HDM provides 5 additional scalar bosons. There are a variety of methods to produce these. Particle collider experiments smash together beams of high energy protons or electrons resulting in the production of various other particles. Future upgrades, with increased beam energy and intensity, will allow heavier particles to be detected. It is useful to know whether the additional particles are within reach of future detectors, and therefore providing mass bounds is of vital importance. Flavour observables involve processes where particles change from one generation to another. The most commonly measured are rare decays of the B-meson which are suppressed in the SM. Additional scalar bosons contribute to the decay rate via quantum loops as virtual particles. Thus, flavour observables provide a powerful probe of new physics, even at low energy. The 2HDM also provides new loop corrections to electroweak observables, such as the *W*-boson mass and *STU* parameters. Finally, a special case of the 2HDM called the Inert Doublet Model (IDM) provides a dark matter candidate. A variety of experiments place constraints on dark matter observables which we consider for the IDM.

Note that the mathematical framework applied in this thesis is quantum field theory, as this is the language of both the standard model and the 2HDM. Quantum mechanics – of all varieties – consists of states, operators which act on states and a set of equations of motion (EOMs) for these states and operators. Any physical system is fully described by its state, which is denoted by $|\psi\rangle$. The equations of motion govern how the state and operators change over time. Observables such as angular momentum, linear momentum, spin, and electric charge are extracted via the action of operators on states.[3] This is

---

[3]Actually, the situation is a little more complicated in QFT (compared to Schrodinger Mechanics) as classical fields are postulated to obey the equations of motion and commutation relations, rather than states themselves. States are then created and destroyed via the action of these fields on the vacuum state: $\psi|0\rangle$.

denoted by $\langle \psi | \hat{O} | \psi \rangle$.

There are also alternatives to QFT which make use of completely different mathematics. These include, most notably, *string theory*, *super gravity* and *loop-quantum gravity*. Such theories promise to combine quantum mechanics and general relativity – QFT on the other hand does not seem to be amenable to this task. Given the extreme complexity of these theories and lack of experimental evidence, we still continue to develop QFT. Gravity is by far the weakest force, so the SM is still able to produce accurate results without it. It is believed that the SM is a low-energy Effective Field Theory (EFT) of some more complete theory. Any QFT can only be valid up to the Planck scale where gravity becomes important. The 2HDM may also be a low energy EFT of some more general QFT. Indeed, additional scalars are a common feature of BSM theories. Some of these, most notably the Minimal Supersymmetric Standard Model, include two Higgs doublets, and it is therefore possible that the 2HDM provides a valid theory at some intermediate energy scale.

1.2   Research Methodology

In general, physics aims to identify models with a number of free parameters to describe some aspect of our universe. We would like to constrain the parameter space as much as possible – until the theory is ruled out or until we identify a set of parameters that appear to agree with nature. The Higgs boson discovery provided the experimental value of the final unknown SM parameter. Hence, there is little freedom to vary this model. In contrast, the Type-I/Type-II 2HDMs that we consider include 6 additional free parameters, and the IDM includes 5 extra parameters.

In this thesis, we run scans of the parameter space of the Type-I, Type-II, and Inert 2HDMs using the open-source global fitting software: GAMBIT [12]. It is important to use *global fits* since new physics may be observed simultaneously in multiple sectors. By applying theoretical and experimental constraints, we construct profile likelihood ratios for each 2HDM parameter, including additional plots for each constraint. The theoretical constraints we apply are S-matrix unitarity, perturbativity and vacuum stability, whereas the experimental constraints include electroweak precision observables, dark matter observables, flavour physics observables and measurements of Higgs signal rates obtained at collider experiments.

1.3   Organisation of this Thesis

This thesis consists of three parts. In the first part, we provide a brief background on the standard model, 2HDM and IDM, followed by further background reading on the theoretical and experimental constraints, relevant statistics, and the computational software that we use.

In the second part, we present our results for the Type-I and Type-II 2HDMs. We begin with just the theoretical constraints and show their individual effects. Following this, we present results for each experimental constraint in isolation. Finally, we present the global fits where all constraints are activated simultaneously. Results are mostly presented at tree-level with a separate chapter to discuss preliminary results using the loop-level FlexibleSUSY spectrum generator. An additional chapter discusses the hidden-Higgs scenario for both models.

In the third part, we present our results for the IDM. We begin with the theoretical constraints, followed by the separate experimental constraints and finally the global fits for the IDM.

Finally, we state our conclusions and list any further work that could be done.

Part I

BACKGROUND READING

Chapter 2

Outline of the Standard Model

In this chapter, we outline the SM and the fundamental physics that it is built from.

2.1 Motivation

The SM has many attractive features. Firstly, it is a gauge field theory meaning that all interactions and vector fields originate from a single principle, thus greatly reducing the number of terms which must be inserted by hand. It accounts for the experimental fact that parity is not conserved in weak interactions. It successfully predicted the existence of a CP-even scalar, known as the Higgs boson, to explain the origin of mass. It gives a consistent way of encoding three of the four fundamental forces observed in nature. The following sections are based on Refs [23], [16] and [24].

2.2 Selecting a Lagrangian

All quantum field theories begin with a Lagrangian[1], which encodes the physics of the theory into a single equation. We begin by describing how such Lagrangians are constructed. We know from everyday experience that the laws of physics are invariant under spacetime translations, rotations, and boosts – which together are known as Poincaré transformations (or Lorentz transformations if not including the translations). If this were not the case, then no experiment we perform on Earth would be consistent since the velocity and position of our planet changes constantly as it revolves around the sun. Hence, we must ensure that our Lagrangian is invariant under the relativity

---

[1] Technically it is a "Lagrangian *density*", but we shorten this to just "Lagrangian" – as is commonplace in the literature.

principle of our universe[2] – which, as confirmed by the last 100 years of experimental results, is the special theory of relativity proposed by Einstein. In practice, our notation ensures that this is the case. Each term in our Lagrangian carries a set of (possibly zero) spacetime indices: e.g., $F_{\mu v}$ or A^μ. So long as all covariant indices are contracted with contravariant indices (and all spinors are multiplied by their adjoint), the resulting Lagrangian is a Lorentz (and Poincaré) scalar and obeys special relativity.

Lagrangians are composed from quantum fields. As an example, the Lagrangian for some scalar field, φ, can be written: $\mathcal{L} = \partial^\mu \varphi \partial_\mu \varphi - m \varphi^2$. A particle can be created via the action of this quantum field on the vacuum state: $|\varphi\rangle = \varphi |0\rangle$. We may define a particle as a set of states which mix amongst themselves under Poincaré transformations. Only the particle's spin[3] orientation, position and momentum change under the transformation. Particles also carry a set of charges, such as electric charge, weak isospin and colour charges, which are conserved in all interactions. Noether's theorem states that such conserved charges arise from additional symmetries in our Lagrangian, known as internal symmetries. For example, if we would like our theory to conserve electric charge, the Lagrangian must have a U(1) symmetry. An important prediction of QFT is that certain quantities like mass and coupling strengths depend on the energy scale of the particles that we are observing (they are said to "run" with energy). For example, the electromagnetic coupling strength becomes stronger at high energies while the strong force becomes weaker. Renormalisation group equations predict exactly how these quantities run with energy. In order to find such equations, our theory must be renormalisable. It can be shown that if a Lagrangian contains terms with a mass dimension greater than four, then it is not renormalisable. This means that, for example, we cannot include interaction vertices with 5 scalars or 4 fermions.

Another important requirement is that our particle states must belong to unitary representations of the Lorentz group. This is because the observables we compute and measure take the form: $\mathcal{M} \equiv \langle \psi_1 | \psi_2 \rangle$ and must themselves be Poincaré scalars. Under the transformation

$$\langle \psi_1 | \psi_2 \rangle \rightarrow \langle \psi_1 | \psi_2 \rangle\prime = \langle \psi_1 | P^\dagger P | \psi_2 \rangle, \tag{2.1}$$

we must have $P^\dagger P = 1$, which confirms that the particle states are unitary. There is also an even stronger requirement – that the S-matrix is unitary. This places a constraint on the dynamics of the theory. We shall discuss this more in Section 4.1.

---

[2]Any relativity principle seeks to answer the following question: 'consider two observers A and B whose location and velocity with respect to some origin may differ. If A takes some measurements of something then how would the values differ from those made by B?'

[3]The spin of a particle depends on the Poincaré representation that it belongs to. Particles with integer spin belong to tensor representations, while those with half-integer spin belong to spinor representations.

2.2.1   Gauge Invariance

According to the gauge principle, the interactions of our theory arise from the promotion of global symmetries in the Lagrangian to local ones. Gauge theories are important since, as shown by t'Hooft [25, 26], they are renormalisable. The process of making our Lagrangian locally symmetric (aka gauge invariant) under some Lie group is not entirely straight-forward. Thus, in this section we develop a technique to achieve this. We begin with a Lagrangian that exhibits a global symmetry under some compact Lie group. When we try to promote it to a local symmetry, we will find extra terms originating from the derivatives which break the symmetry. We need to eliminate these terms. To do this, we introduce a new vector field into the theory with a specific transformation rule. This generates new terms which cancel off any local symmetry violating terms, thus enabling the theory to be locally symmetric. We describe how this is done for specific groups in the sections below.

2.2.2   Local U(1) symmetry and Quantum Electrodynamics

Quantum electrodynamics describes interactions between the photon and charged particles (such as the electron). Electrons are spin-½ particles, so in QFT they are created by a Dirac field ψ. Photons are spin-1 particles and are created by a massless vector field A^μ. We shall begin with a free spin-½ Lagrangian given by

$$\mathcal{L}_0^{1/2} = i\bar{\psi}\gamma^\mu\partial_\mu\psi - m\bar{\psi}\psi, \tag{2.2}$$

and demonstrate that the correct photon interactions can be obtained via the gauge principle. We notice that the Lagrangian is invariant under a global U(1) transformation of the field given by

$$\psi \to \psi' = e^{iq\alpha}\psi, \quad \alpha \in \mathbb{R}. \tag{2.3}$$

According to the gauge principle, we should promote this global symmetry to a local one, $\alpha \to \alpha(x)$. As it stands, the above Lagrangian is not locally gauge invariant since

$$\psi^\dagger\partial_\mu\psi \to \left(\psi^\dagger\right)'(\partial_\mu\psi)' = \left(\psi e^{-iq\alpha}\right)\left(e^{iq\alpha}\left(iq\alpha + 1\right)\partial_\mu\psi\right) \neq \psi^\dagger\partial_\mu\psi. \tag{2.4}$$

The derivative in the above equation does not transform covariantly due to the extra $iq\alpha$ term. Now consider the introduction of a new vector field A_μ into the derivative

$$\partial_\mu \to D_\mu \equiv (\partial_\mu + iqA_\mu), \tag{2.5}$$

where the new field is given the transformation rule[4]

$$A_\mu \to A'_\mu = A_\mu - \partial_\mu \alpha. \tag{2.6}$$

Clearly the term in the derivative will cancel the $iq\alpha$ term above and restore the symmetry. Thus, the new derivative term, $D_\mu \psi$, transforms covariantly (meaning "with ψ"). It is called the "covariant derivative", and the above procedure where we take $\partial_\mu \to D_\mu$ is called minimal substitution.[5]

The coefficient q is the electromagnetic coupling coefficient. We had the freedom to add q because it will be cancelled in the transformation rule above. We should also add the Kinetic Energy Density (KED)[6] for A_μ which in this case is just the typical KED for a vector field. To summarise, the resulting Lagrangian,

$$\mathcal{L} = i\bar{\psi}\gamma^\mu \partial_\mu \psi - m\bar{\psi}\psi - \frac{1}{16\pi}F^{\mu v}F_{\mu v} - q\bar{\psi}\gamma^\mu \psi A_\mu, \tag{2.7}$$

$$\text{where} \quad F^{\mu v} \equiv \partial^\mu A^v - \partial^v A^\mu, \tag{2.8}$$

obeys the local U(1) symmetry. We see the appearance of an interaction between the fermion (electron) and photon. This is precisely the interaction of QED; here it was a result of the gauge principle. It turns out that it is possible to derive all classical electrodynamics from this Lagrangian. Note that we cannot add a mass term for A_μ as this would break the gauge symmetry.

2.2.3 Non-Abelian Gauge theory

Now that we have successfully obtained the interactions in QED via the gauge principle, we wonder whether the weak and strong interactions may be obtained in the same manner.

---

[4]Notice that the required transformation rule for A_μ looks just like a gauge transformation in classical electrodynamics.

[5]There is also another way of understanding this. First recall that the derivative can be defined by: $dx^\mu \partial \psi(x) = \psi(x + dx) - \psi(x)$. But since we are considering a local symmetry, where all spacetime coordinates may be rotated independently, it is meaningless to compare the field at different spacetime points as above. Hence, we need a way to parallel transport the $\psi(x)$ to the gauge at $x + dx$ so that we can compare them. The extra term in the derivative is what allows us to do this.

[6]Sometime known as the "kinetic terms".

Before doing so we will need to develop gauge theory for multiple fields. Consider the following Lagrangian which exhibits a global $SU(2)$ symmetry[7]

$$\mathcal{L} = \begin{bmatrix} \bar{\psi}_1 & , \bar{\psi}_2 \end{bmatrix} \gamma^\mu \partial_\mu \begin{bmatrix} \psi_1 \\ \psi_2 \end{bmatrix} - \begin{bmatrix} \bar{\psi}_1 & , \bar{\psi}_2 \end{bmatrix} m \begin{bmatrix} \psi_1 \\ \psi_2 \end{bmatrix}. \tag{2.9}$$

Notice that this is just the Lagrangian for two non-interacting Dirac fields. We can also write it as

$$\mathcal{L} = \left(i\bar{\psi}_1 \gamma^\mu \partial_\mu \psi_1 - m\bar{\psi}_1 \psi_1 \right) + \left(i\bar{\psi}_2 \gamma^\mu \partial_\mu \psi_2 - m\bar{\psi}_2 \psi_2 \right). \tag{2.10}$$

Note that the full symmetry group of this Lagrangian is actually $U(2)$. But the $U(1)$ part of this leads to the same results as the previous section, so we shall only consider the $SU(2)$ symmetry here. We can write the transformation as

$$\begin{bmatrix} \psi_1 \\ \psi_2 \end{bmatrix} \rightarrow \begin{bmatrix} \psi_1 \\ \psi_2 \end{bmatrix}' = \exp\left\{ (t^a \theta_a) \begin{bmatrix} \psi_1 \\ \psi_2 \end{bmatrix} \right\}, \tag{2.11}$$

where t^a are the generators of $SU(2)$. We usually give each independent symmetry a name – as an example we may call this YM symmetry. The above-column vector is called an $SU(2)_{YM}$-doublet and transforms via the fundamental representation of this group. Now we would like to promote this to a local symmetry. This is not as easy as the U(1) case. The trouble comes from the derivative, given by

$$\partial_\mu \psi \rightarrow \partial_\mu \psi + \frac{1}{2} \left[t^a \theta_a(x) \right] \partial_\mu \psi + \frac{i}{2} \left[t^a \partial_\mu \theta_a(x) \right] \psi + \mathcal{O}\left(\theta^2 \right). \tag{2.12}$$

The third term prevents $\partial_\mu \psi$ from being invariant. So, we introduce new gauge fields which will cancel this term when they transform. It can be shown that the substitution

$$\partial_\mu \rightarrow D_\mu = \partial_\mu - \frac{i}{2} g \, t^a W_{\mu,a}\left(x \right), \tag{2.13}$$

will enforce the local gauge symmetry. Here g is called the $SU(N)$ coupling constant. If this procedure is going to work, we need $D_\mu \psi$ to transform the same way that ψ does. The required transformation rule for the gauge fields is

---

[7]Note that the equations presented here extend directly to SU(N).

$$\tau^a W_{\mu a} \to \tau^a W_{\mu a} + \frac{1}{g}\tau^a \partial_\mu \alpha_a - \tau^a \left(\varepsilon_{abc}\alpha^b W_\mu^c \right). \tag{2.14}$$

We would also like to add the kinetic terms for each of the gauge bosons. The standard terms, $F^{\mu v}F_{\mu v} = (\partial^\mu A^v - \partial^v A^\mu)^2$ do not preserve the $SU(2)$ symmetry under the above transformation rule. Instead, the appropriate terms which preserve the symmetry are[8]

$$W^{\mu v,a}W_{\mu v,a}, \tag{2.15}$$

$$\text{where:}\quad W_{\mu v,a} \equiv \partial_\mu W_{v,a} - \partial_v W_{\mu,a} + f_{abc}W_b W_c. \tag{2.16}$$

Here f_{abc} are the structure constants of SU(2). This term takes the role of $F_{\mu v}$ from U(1) theory. But unlike the U(1) case, we now have interactions amongst the gauge bosons.

Substitution of the covariant derivative into the Lagrangian will provide the interactions between matter and gauge fields. The final Lagrangian which preserves the local SU(2) symmetry is

$$\mathcal{L} = \left(i\bar{\psi}\gamma^\mu D_\mu \psi - m\bar{\psi}\psi \right) + W_{\mu v,a}W^{\mu v,a}. \tag{2.17}$$

2.2.4 Products of gauge groups

It turns out that the SM gauge group is a direct product of unitary groups, so we must extend our gauge theory to this scenario. Suppose we have a Lagrangian that is invariant under the direct product

$$G = H \otimes K. \tag{2.18}$$

A matter field which belongs to some representation of this group will transform as

$$\varphi_{h,k} \to \varphi'_{h,k} = U_{hh'}V_{kk'}\varphi_{h'k'}, \tag{2.19}$$

where the matrices U and V are parameterised by w^a and x^a respectively, and belong to some representation of H and K. Note that the field, φ, has $\dim U \times \dim V$ components. The covariant derivative includes a separate term for each symmetry group, given by

---

[8]We can also write it as: $W_{\mu v,a} = D_\mu W_{v,a} - D_v W_{\mu,v}$, which may be considered more elegant since it takes the same form as the $U(1)$ case.

$$\mathcal{D}_\mu = \partial_\mu - \frac{i}{2} g_w w^a W_{\mu,a} - \frac{1}{2} g_x x^a X_{\mu,a}. \tag{2.20}$$

We can prove this simply by showing that $D_\mu \varphi$ transforms covariantly. The gauge fields $W_{\mu,a}$ and $X_{\mu,a}$ only transform under their corresponding groups H and K[9]. Hence, the full gauge KED just consists of separate KEDs for $W_{\mu,a}$ and $X_{\mu,a}$ (which take the same form as Equation 2.16) given by

$$\mathcal{T} = W_{\mu,a} W^{\mu,a} + X_{\mu,a} X^{\mu,a}. \tag{2.21}$$

2.3 Noether currents arising from Gauge symmetries

According to Noether's theorem, symmetries in a Lagrangian, such as the U(1) and SU(N) symmetries considered above, lead to conserved charges. As an example, the global $U(1)$ symmetry of the QED Lagrangian leads to conservation of electron number ($N \equiv$ (num. of electrons) $-$ (num. of positrons)), while a local U(1) symmetry would also lead a conservation of electric charge. There is a conserved Noether charge for each generator of each symmetry. Noether's theorem may be stated as follows – if a Lagrangian $\mathcal{L}(\varphi^r, \varphi^r{}_{,\mu})$ is symmetric with respect to the transformation $\varphi^r \to \varphi'^r(\alpha)$ then the following four-current is divergenceless

$$j^\mu \left(\varphi^r, \varphi^r{}_{,v} \right) \equiv \frac{\partial \mathcal{L}}{\partial \varphi^r{}_{,\mu}} \frac{\partial \varphi'^r}{\partial \alpha}, \quad \partial_\mu j^\mu = 0. \tag{2.22}$$

For the U(1) and SU(N) theories in the previous sections, the Noether current becomes

$$J_a^\mu \equiv \frac{1}{2} \overline{\psi} \gamma^\mu t_a \psi, \quad a = 1, .., N^2 - 1. \tag{2.23}$$

We can integrate away the spatial dimensions (assuming the current goes to zero at infinity) to obtain the corresponding conserved Noether charges, i.e.[10]

$$Q_a \equiv \int d^3x \left(\frac{1}{2} \psi^\dagger t_a \psi \right), \quad \partial_t Q_a = 0, \quad a = 1, .., N^2 - 1. \tag{2.24}$$

---

[9]i.e. they belong to the trivial representation of the respective groups.

[10]Note that non-diagonal generators will lead to charge operators that couple different fields together and therefore taking the expectation value leads to zero charge. Hence, only diagonal generators (i.e. the Cartan subalgebra elements) lead to non-trivial charge operators.

Note that while we have only considered charge and current *operators* so far, it follows that the expectation values of the corresponding charge observables are also conserved, that is

$$\partial_t \bar{Q}_a = 0, \quad \bar{Q}_a = \langle state | Q_a | state \rangle, \tag{2.25}$$

$$\partial_\mu \bar{J}_a^\mu = 0, \quad \bar{J}_a^\mu = \langle state | J_a^\mu | state \rangle. \tag{2.26}$$

This is what is meant when we say that Q_a or J_a^μ is conserved.

2.4 Standard Model Lagrangian

We now introduce the SM as a gauge field theory. In the early universe, from roughly 10^{-36} to 10^{-12} seconds after the Big Bang, all SM particles were massless and the Lagrangian was more symmetric than it is today. As the universe cooled down the symmetry was broken into a smaller symmetry group, and this leads to the appearance of mass. In this section we shall describe exactly how this symmetry breaking is carried out and derive the mass terms for the SM particles. This section is based on Refs [23] and [24] with some group theoretic aspects from Refs [27] and [28].

2.4.1 Particle content of the standard model

The SM is a gauge field theory whose Lagrangian is locally symmetric under an SU(3)$_C \otimes$ $SU(2)_L \otimes U(1)_Y$ group. The subscripts here refer to "Colour", "Left", and "Weak Hypercharge Y", and give a name to each symmetry component. Following the framework provided in the previous section, we must provide (a) the matter fields of the theory, (b) which representation of the above group that they belong to, and (c) which combinations of fields get transformed into each other. All interactions between matter fields and gauge fields follow from the gauge principle. We are unable to add mass terms as they spoil the symmetry. But later we show how such terms can arise as a result of spontaneous symmetry breaking. The matter particles are listed in Table 2.1 (Dirac fields) and Table 2.2 (scalar fields).

There are three generations of similar Dirac particles. They belong to the same representation of the SM group and have the same charges but are differentiated by their mass. We shall hereon refer to them as up-type quarks u_i, down-type quarks d_i, charged leptons e_i and neutrinos v_i. Charged leptons are complex Dirac fields. Up and down

Name	Particle	DOFs
up quark	u_1	12
charm quark	u_2	12
top quark	u_3	12
down quark	d_1	12
strange quark	d_2	12
bottom quark	d_3	12
electron	e_1	4
muon	e_2	4
tau	e_3	4
electron neutrino	v_1	4
muon neutrino	v_2	4
tau neutrino	v_3	4

TABLE 2.1: Dirac (spin-1/2) particles of the SM.

Name	Particle	DOFs
Higgs Doublet	$\Phi \equiv \begin{bmatrix} \varphi^+ \\ \varphi^0 \end{bmatrix} \equiv \begin{bmatrix} \varphi_1 + i\varphi_2 \\ \varphi_3 + i\varphi_4 \end{bmatrix}$	4

TABLE 2.2: Scalar (spin-0) particles of the SM.

type quarks are also complex Dirac fields but have an additional 3-times degeneracy known as colour, giving them 12 DOFs each. Neutrinos were originally believed to be massless, left-chiral Weyl fields. But neutrinos have been observed to "oscillate", meaning that there is a non-zero probability of measuring a different neutrino flavour than what we started with after propagating some distance L. This probability depends on the squared mass difference between the neutrinos and proves that at least 2 of 3 neutrinos are massive. Hence, we shall assume that neutrinos are massive Dirac particles like the other fermions.[11]

It is an experimental fact that parity is not conserved. This fact is implemented in the SM by its different treatment of left-chiral versus right-chiral components of fermion fields. Nature has decided that only left-chiral[12] field components participate in interactions at high energies. The chirality operator, γ_5, is defined by $\gamma_5 \equiv \gamma_0\gamma_1\gamma_2\gamma_3$. Its eigenstates,

---

[11]It is still possible that neutrinos are Majorana particles, rather than Dirac particles, meaning that they are their own antiparticle. In this case, experimental observations can be explained by the fact that anti-neutrinos would have the opposite chirality.

[12]Some background on chirality and Weyl fields: it turns out that for massless particles, the Dirac equation breaks apart into 2 sets of coupled equations in two unknowns (rather than 4 coupled equations in 4 unknowns). The solutions of each set are single-chirality eigenstates called Weyl fields. This is rather

denoted ψ_L, ψ_R, have eigenvalues $+1, -1$ and are said to have left-chirality and right-chirality respectively.[13] For any Dirac field, we can extract the left and right-chiral components using the projection operators

$$\psi_L \equiv P_L \psi \equiv \frac{1}{2} \left(1 - \gamma_5\right) \psi,$$
$$\psi_R \equiv P_R \psi \equiv \frac{1}{2} \left(1 + \gamma_5\right) \psi, \tag{2.27}$$

where these obey the usual properties of projection operators,

$$P_L + P_R = 1, \ P_L^2 = P_L, \ P_R^2 = P_R. \tag{2.28}$$

2.4.2 Standard model gauge fields

All fields belong to the fundamental representation of the $U(1)_Y$ part of the group. The amount by which they transform is called the weak hypercharge. The multiplets of fields that are transformed by the remaining gauge group are given in Table 2.3. We call those belonging to the SU(3) 3-dimensional, fundamental representation colour triplets, and those of the $\mathrm{SU}(2)_L$ 2-dimensional, fundamental representation weak isospin doublets.

Following Section 2.2.1, we introduce gauge fields so that our Lagrangian is locally symmetric. These fields appear when we apply the minimal substitution procedure $\partial_\mu \to D_\mu$; the required terms in each covariant derivative depend on which symmetry it transforms under (for clarity, they are listed in Table 2.5). We introduce 8 gauge fields $(G_1^\mu, \ldots, G_8^\mu)$ for SU(3), 3 gauge fields $(W_1^\mu, W_2^\mu, W_3^\mu)$ for SU(2) and a single gauge field for (B^μ) U(1). The notation for the gauge fields and multiplets is provided in Table 2.4. The gauge fields also require a KED term in the Lagrangian. We will make use of the notation

$$B^{\mu v} \equiv \partial^\mu B^v - \partial^v B^\mu, \tag{2.29}$$

$$W^{a,\mu v} \equiv \partial^\mu W^{av} - \partial^v W^{a\mu} + g_2 \varepsilon_{abc} W^{b\mu} W^{cv}, \ \ a, b, c \in \{1, 2\}, \tag{2.30}$$

$$G^{a,\mu v} \equiv \partial^\mu G^{av} - \partial^v G^{a\mu} + g_3 f_{abc} G^{b\mu} G^{cv}, \ \ a, b, c \in \{1, \ldots, 8\}. \tag{2.31}$$

---

simple in the Weyl representation (of the γ matrices) where Weyl fields can be represented by 2×1 column matrices.

[13]We are being careful not to confuse chirality with helicity here, where the latter describes states as being either left-handed or right-handed. Both are the same for massless particles (or in the limit $v \approx c$) but are different in general.

Field Multiplet	$SU(3)_C \otimes SU(2)_L$ representation
$\left[\begin{bmatrix} u_i \\ d_i \end{bmatrix}_r \quad \begin{bmatrix} u_i \\ d_i \end{bmatrix}_g \quad \begin{bmatrix} u_i \\ d_i \end{bmatrix}_b \right]_L$	$3 \otimes 2$
$\begin{bmatrix} u_{i,r}^* & u_{i,g}^* & u_{i,b}^* \end{bmatrix}_L$	$3^* \otimes 1$
$\begin{bmatrix} d_{i,r}^* & d_{i,g}^* & d_{i,b}^* \end{bmatrix}_L$	$3^* \otimes 1$
$\begin{bmatrix} v_{i,L} \\ e_{i,L} \end{bmatrix}$	$1 \otimes 2$
$e_{i,L}^*, \quad v_{i,L}^*$	$1 \otimes 1$
$\begin{bmatrix} \varphi^+ \\ \varphi^0 \end{bmatrix}$	$1 \otimes 2$

TABLE 2.3: SM matter field representations.

SU(N) Multiplet	Notation
Singlets	$e_{i,R}, \; v_{i,L}, \; v_{i,R}$
SU(2) Doublets	$Q_{i,L} \equiv \begin{bmatrix} u_{i,L} \\ d_{i,L} \end{bmatrix}, \; L_{i,L} \equiv \begin{bmatrix} v_{i,L} \\ e_{i,L} \end{bmatrix}, \; \Phi \equiv \begin{bmatrix} \varphi^+ \\ \varphi^0 \end{bmatrix}$
SU(2) Gauge Fields	$W^\mu \equiv \begin{bmatrix} W_1^\mu \\ W_2^\mu \\ W_3^\mu \end{bmatrix}$
SU(3) Triplets	$U_i \equiv \begin{bmatrix} u_{i,R} \\ u_{i,G} \\ u_{i,B} \end{bmatrix}, \quad D_i \equiv \begin{bmatrix} d_{i,R} \\ d_{i,G} \\ d_{i,B} \end{bmatrix}$
SU(3) Gauge Fields	$G^\mu \equiv \begin{bmatrix} G_1^\mu \\ \vdots \\ G_8^\mu \end{bmatrix}$

TABLE 2.4: Notation for each SU(N) multiplet. The gauge fields belong to the adjoint representation of their corresponding symmetry group.

$Q_{i,L}$	$D_\mu = \partial_\mu$	$+ \ iYg_1 B^\mu$	$+ \ \frac{ig_2}{2}W^{\mu a}\sigma^a$	$+ \ \frac{ig_3}{2}G^{\mu a}\lambda^a$
$L_{i,L}$	$D_\mu = \partial_\mu$	$+ \ iYg_1 B^\mu$	$+ \ \frac{ig_2}{2}W^{\mu a}\sigma^a$	
$u_{i,R}$	$D_\mu = \partial_\mu$	$+ \ iYg_1 B^\mu$		$+ \ \frac{ig_3}{2}G^{\mu a}\lambda^a$
$e_{i,R}$	$D_\mu = \partial_\mu$	$+ \ iYg_1 B^\mu$		
Φ	$D_\mu = \partial_\mu$	$+ \ iYg_1 B^\mu$	$+ \ \frac{ig_2}{2}W^{\mu a}\sigma^a$	

TABLE 2.5: Covariant derivatives for each multiplet.

Here, ε_{abc} are the structure constants of SU(2) and f_{abc} are the structure constants of SU(3).

According to Noether's theorem, symmetries give rise to conserved charges. To obtain the charge of a given particle, we may construct a Noether charge operator by integrating the Noether current from Equation 2.22, and take the expectation value for each particle state $Q = \langle state|\hat{Q}|state \rangle$. Doing so for the SM Lagrangian (see Equation 2.33 below), we would obtain the charges given in Table 2.6.[14,15] Here we have included electric charge, which by definition is the sum of the hypercharge and third weak isospin charge. However, the electric charge will only become relevant when the SM symmetry group is spontaneously broken, which is the case for the low energy universe that we live in today.

2.4.3   Putting it together

We are now ready to state the full SM Lagrangian. It may be divided into four sectors,

$$\mathcal{L}_{SM} \equiv \mathcal{L}_{\text{Fermion}} + \mathcal{L}_{\text{Gauge}} + \mathcal{L}_{\text{Scalar}} + \mathcal{L}_{\text{Yukawa}}, \tag{2.32}$$

where each sector is postulated to take the form

$$\mathcal{L}_{\text{Fermion}} \equiv i\Big(\bar{Q}_{i,L}\slashed{D}Q_{i,L} + \bar{L}_{i,L}\slashed{D}L_{i,L} + \bar{u}_{i,R}\slashed{D}u_{i,R} + \bar{d}_{i,R}\slashed{D}d_{i,R} + \bar{e}_{i,R}\slashed{D}e_{i,R} + \bar{v}_{i,R}\slashed{D}v_{i,R} \Big),$$

$$\mathcal{L}_{\text{Gauge}} \equiv -\frac{1}{4}B^{\mu v}B_{\mu v} - \frac{1}{4}W^{a,\mu v}W_{a,\mu v} - \frac{1}{4}G^{b,\mu v}G_{b,\mu v},$$

$$\mathcal{L}_{\text{Scalar}} \equiv (D^\mu \Phi)^\dagger (D_\mu \Phi) - \lambda \left(\Phi^\dagger \Phi - v^2/2 \right)^2 \text{ with } \lambda > 0, \ v > 0,$$

$$\mathcal{L}_{\text{Yukawa}} \equiv -Y_{ij}^D \bar{Q}_{i,L}\Phi d_{j,R} - Y_{ij}^U \bar{Q}_{i,L}\widetilde{\Phi}\, u_{j,R} - Y_{ij}^E \bar{L}_{i,L}\Phi e_{j,R} - Y_{ij}^N \bar{L}_{i,L}\widetilde{\Phi}\, v_{j,R} + H.c. \tag{2.33}$$

---

[14]Notice that RC neutrinos have no charges and hence experience no forces. This is why it wasn't clear if they even existed until neutrino oscillations were observed.

[15]The charges that we measure are actually $g_1 Y, g_2 I_3,$ and eQ.

Particle	Y	I	I_3	Q
$Q_{i,L}$	$\begin{bmatrix} +1/6 \\ +1/6 \end{bmatrix}$	$1/2$	$\begin{bmatrix} +1/2 \\ -1/2 \end{bmatrix}$	$\begin{bmatrix} +2/3 \\ -1/3 \end{bmatrix}$
$L_{i,L}$	$\begin{bmatrix} -1/2 \\ -1/2 \end{bmatrix}$	$1/2$	$\begin{bmatrix} +1/2 \\ -1/2 \end{bmatrix}$	$\begin{bmatrix} 0 \\ -1 \end{bmatrix}$
$u_{i,R}$	$+2/3$	0	0	$+2/3$
$d_{i,R}$	$-1/3$	0	0	$-1/3$
$v_{i,R}$	0	0	0	0
$e_{i,R}$	-1	0	0	-1
Φ	$\begin{bmatrix} +1/2 \\ +1/2 \end{bmatrix}$	$1/2$	$\begin{bmatrix} +1/2 \\ -1/2 \end{bmatrix}$	$\begin{bmatrix} +1 \\ 0 \end{bmatrix}$
$\widetilde{\Phi}$	$\begin{bmatrix} -1/2 \\ -1/2 \end{bmatrix}$	$1/2$	$\begin{bmatrix} +1/2 \\ -1/2 \end{bmatrix}$	$\begin{bmatrix} 0 \\ -1 \end{bmatrix}$

TABLE 2.6: Noether charges assigned to each SM multiplet. The electric charge is given by the Gell-Mann-Nishijima relation, $Q = Y + I_3$.

Here *H.c.* stands for the Hermitian conjugate of all former terms and is added to ensure that the Yukawa sector is Hermitian. In Section 3, which describes the 2HDM, we will see that its Lagrangian is only a small extension of this, hence why we have listed it in full detail here. In the 2HDM we include extra terms in the Yukawa and scalar sectors while everything else is kept the same.

In Equation 2.33 we have already applied minimal substitution, $\partial_\mu \to D_\mu$, so that the Lagrangian exhibits a local $\text{SU}(3)_C \otimes SU(2)_L \otimes U(1)_Y$ symmetry. Notice that we do not add any gauge-fermion or gauge-scalar interactions directly. Instead, all such interactions arise from the covariant derivative terms, which were a result of the gauge principle. We do, however, need to postulate the Higgs-fermion and Higgs-Higgs interactions. Also notice that no mass terms have been included. This is because mass terms would couple LC and RC Weyl components together and would thus spoil the symmetry (which gives special treatment to the LC Weyl fields). Furthermore, mass terms would require all multiplet components to have the same mass. For example, the electron and electron neutrino would have the same mass – which clearly does not match our observations.
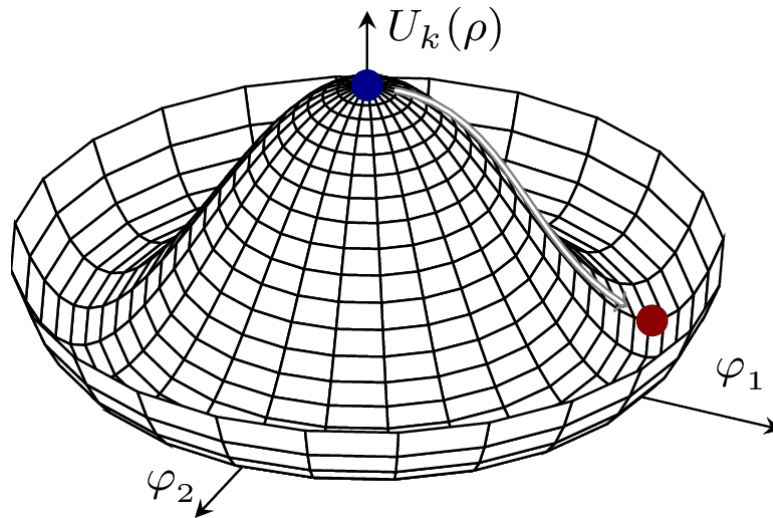
FIGURE 2.1: The Mexican hat potential in two field variables. The vertical axis represents the potential as a function of the number density of the fields.

2.5 Symmetry Breaking

While the SM Lagrangian does not yet appear to have mass terms, in this section we shall find that there are actually hidden mass terms arising from the scalar sector. Consider the scalar potential written as

$$\mathcal{V} = \mu^2 \Phi^\dagger \Phi + \lambda \left(\Phi^\dagger \Phi \right)^2. \tag{2.34}$$

Assuming that μ^2 is positive, the first term is just the mass term of the Higgs doublet. Now suppose what would happen if this term was negative. We cannot simply read off the mass term in this case. This is because the Feynman calculus is formulated as deviations from the vacuum state.[16] But the potential is not minimised for $\Phi = 0$, thus our fields represent perturbations about a false vacuum. So, we must shift the fields so that they are centred about the true vacuum, i.e. the minimum of the potential, before interpretation of the mass terms.

If we were to plot the above potential as a function of the fields, we would find that it takes a four-dimensional Mexican hat shape. To illustrate this we show a 2D Mexican hat potential in Figure 2.1, but note that we actually have 2 more field axes in the SM scenario. Also note that the axes here actually represent the average number densities of the corresponding fields (the fields themselves are operators and cannot be plotted).

---

[16]The vacuum state is by definition the lowest energy state. It is not necessarily a state with zero particles.

The key point is that the minimum of the potential occurs for a non-zero value of the fields, and hence the universe will tend to move towards a state where the vacuum expectation value of the Higgs field is non-zero. In other words, the universe is more stable in a state where a non-zero number density of scalar particles exists. There is a degenerate set of possible vacua along the valley of the Mexican hat and any of these can be selected as the true vacuum. We pick a vacuum such that the VEV of the Higgs doublet takes the form

$$\langle 0 \left| \Phi \right| 0 \rangle = \frac{1}{\sqrt{2}} \begin{bmatrix} 0 \\ v \end{bmatrix}. \tag{2.35}$$

The Higgs doublet can be written as a perturbation about the true vacuum as follows

$$\Phi = \frac{1}{\sqrt{2}} \begin{bmatrix} \eta_1 + i\eta_2 \\ (h + v) + i\eta_3 \end{bmatrix}, \tag{2.36}$$

where $\eta_1 \equiv \varphi_1, \;\; \eta_2 \equiv \varphi_2, (h + v) \equiv \varphi_3, \; \eta_4 \equiv \varphi_4$.

When we substitute this into the SM Lagrangian we find that the $SU(2) \otimes U(1)$ symmetry is broken. In particular, we find that three symmetry components are broken. Furthermore, if we were to plug Equation 2.36 back into the scalar potential, we would find mass terms for h while η_1, η_2, η_3 remain massless. This is a result of Goldstone's theorem, which states that for each global symmetry of $\mathcal{L}$ that is broken by the spectrum of physical states:

   I There exists a massless scalar (called a Nambu-Goldstone boson).

  II There is a degeneracy of possible true vacua.

 III The corresponding generator of the broken symmetry does not "annihilate the vacuum", meaning that $\delta\Phi = T_i\Phi \neq 0$.

Later we shall show that three mass terms for the gauge bosons will emerge. Hence, if we count the number of DOFs before and after the electroweak symmetry breaking, it appears that we have gained three additional DOFs.[17] However, some of our fields transform under the SM gauge group meaning that they cannot be observable quantities. Since the original Lagrangian is symmetric under the gauge symmetry, doing a gauge transformation could not possibly affect the phenomenology. Therefore, we are free to

---

[17]Note that massive vector fields have 1 more DOF than massless vector fields (3 rather than 2).

pick a gauge to simplify our theory. The simplest choice is to pick a gauge that eliminates the three additional DOFs, which in our case will be the three Goldstone bosons. This choice is called the unitary gauge. Our low-energy Higgs doublet then becomes

$$\Phi = \frac{1}{\sqrt{2}} \begin{bmatrix} 0 \\ h + v \end{bmatrix}. \tag{2.37}$$

The electroweak generators do not annihilate the vacuum since

$$
\begin{aligned}
\sigma^1 \Phi &= \begin{bmatrix} 0 & 1 \\ 1 & 0 \end{bmatrix} \begin{bmatrix} 0 \\ \frac{1}{\sqrt{2}} (v + h) \end{bmatrix} = \begin{bmatrix} \frac{1}{\sqrt{2}} (v + h) \\ 0 \end{bmatrix}, \\
\sigma^2 \Phi &= \begin{bmatrix} 0 & -i \\ i & 0 \end{bmatrix} \begin{bmatrix} 0 \\ \frac{1}{\sqrt{2}} (v + h) \end{bmatrix} = -i \begin{bmatrix} \frac{1}{\sqrt{2}} (v + h) \\ 0 \end{bmatrix}, \\
\sigma^3 \Phi &= \begin{bmatrix} 1 & 0 \\ 0 & -1 \end{bmatrix} \begin{bmatrix} 0 \\ \frac{1}{\sqrt{2}} (v + h) \end{bmatrix} = - \begin{bmatrix} 0 \\ \frac{1}{\sqrt{2}} (v + h) \end{bmatrix}, \\
I \Phi &= \begin{bmatrix} 1 & 0 \\ 0 & 1 \end{bmatrix} \begin{bmatrix} 0 \\ \frac{1}{\sqrt{2}} (v + h) \end{bmatrix} = \begin{bmatrix} 0 \\ \frac{1}{\sqrt{2}} (v + h) \end{bmatrix}.
\end{aligned} \tag{2.38}
$$

But notice that the following combination of generators does annihilate the vacuum

$$\frac{1}{2} \left(I + \sigma^3 \right) \Phi = \begin{bmatrix} 1 & 0 \\ 0 & 0 \end{bmatrix} \begin{bmatrix} 0 \\ \frac{1}{\sqrt{2}} (v + h) \end{bmatrix} = \begin{bmatrix} 0 \\ 0 \end{bmatrix}. \tag{2.39}$$

The corresponding symmetry group, denoted $U(1)_Q$,[18] is the only symmetry that is not spontaneously broken by the vacuum. In fact, this is just the familiar electromagnetic symmetry – its corresponding gauge boson is the photon.

This completes our discussion of electroweak symmetry breaking – the rest of the theory follows simply by plugging Equation 2.37 into the SM Lagrangian 2.33. In Table 2.7 we summarise the results of doing this, and in the sections below we carry out the algebra.

---

[18]Note that $U(1) \simeq \left\{ \exp iQ \begin{bmatrix} 1 & 0 \\ 0 & 0 \end{bmatrix} \right\}$.

Sector/Term	Significance
Scalar Potential	Higgs boson mass and self-coupling terms.
Scalar KED	Higgs boson KED, gauge boson mass terms, Weinberg angle, and Higgs-gauge couplings.
Yukawa Sector	Physical basis, quark/lepton mass terms, and couplings between the Higgs boson and physical quarks/leptons.
Fermion Sector	Quark/lepton KED and couplings between physical gauge bosons and quarks/leptons.
Gauge Sector	Gauge boson KED and couplings amongst the gauge bosons.

TABLE 2.7: What happens as a result of spontaneous symmetry breaking in the SM.

m_g, m_γ	0
m_W	$\frac{1}{2}vg_1$
m_Z	$\frac{1}{2}v\sqrt{g_1^2 + g_2^2}$
m_h	$\sqrt{2\lambda v^2}$
m_f	$\frac{Y_f v}{\sqrt{2}}$

TABLE 2.8: All masses of the Standard Model.

2.5.1 Symmetry breaking in the scalar potential

The scalar potential is just the SM scalar sector from Equation 2.33 but without the derivative terms, and is given by

$$\mathcal{V}_{\text{Scalar}} = \lambda\left(\Phi^\dagger\Phi - v^2/2\right)^2, \quad \text{where } \lambda > 0, \ v > 0. \tag{2.40}$$

Upon substitution of the low-energy Higgs doublet (Equation 2.37), we arrive at

$$\mathcal{V}_{\text{Scalar}} = \lambda v^2 h^2 - \lambda v h^3 - \frac{\lambda}{4}h^4 + \text{constant}, \tag{2.41}$$

where we see a three-Higgs and four-Higgs interaction along with a mass term for the Higgs boson. For future reference, we list all masses and couplings in Table 2.8 and Table 2.9 respectively. We will derive all expressions in these tables shortly.

Higgs-Higgs	$g[\text{hhh}]$	$-\dfrac{3im_h^2}{v}$
	$g[\text{hhhh}]$	$-\dfrac{3im_h}{v^2}$
Higgs-Gauge	$g[\text{h}\gamma_\mu\gamma_v], g[\text{h}g_\mu g_v],$ $g[\text{hh}\gamma_\mu\gamma_v], g[\text{hh}g_\mu g_v]$	0
	$g[\text{h}V_\mu V_v]$	$2i\dfrac{m_V^2}{v}g_{\mu v}$
	$g[\text{hh}V_\mu V_v]$	$2i\dfrac{m_V^2}{v^2}g_{\mu v}$
Higgs-Fermion	$g[\text{h}\bar{f}f]$	$-i\dfrac{m_f}{v}$
Gauge-Gauge	$g[g_1^{\mu a}g_2^{vb}g_3^{\lambda g}]$	$-g_s f^{abl}\left(g^{\mu v}(q_1^\lambda - q_2^\lambda) + g^{v\lambda}(q_2^\mu - q_3^\mu) + g^{\lambda\mu}(q_3^v - q_1^v)\right)$
	$g[g^{\mu a}g^{vb}g^{\lambda g}g^{\rho d}]$	$-ig_s^2\left(f^{abh}f^{gdh}(g^{\mu\lambda}g^{v\rho} - g^{\mu\rho}g^{v\lambda}) + f^{adh}f^{bgh}(g^{\mu v}g^{\lambda\rho} - g^{\mu\lambda}g^{v\rho})\right.$ $\left.+ f^{abh}f^{gdh}(g^{\mu\rho}g^{v\lambda} - g^{\mu v}g^{\lambda\rho})\right)$
	$g[Z_3^\mu W_1^{v+}W_2^{\lambda-}]$	$ig_W\cos(\theta_W)\left(g^{v\lambda}(q_1^\mu - q_2^\mu) + g^{\lambda\mu}(q_1^v - q_2^v) + g^{\mu v}(q_1^\lambda - q_2^\lambda)\right)$
	$g[Z^\sigma Z^\lambda W^{\mu+}W^{v-}]$	$ig_W^2\cos^2(\theta_W)\left(2g^{\mu v}g^{\lambda\sigma} - g^{\mu\lambda}g^{v\sigma} - g^{\mu\sigma}g^{v\lambda}\right)$
	$g[W^{v-}W^{\mu+}W^{\sigma-}W^{\lambda+}]$	$ig_W^2\left(2g^{\mu v}g^{v\sigma} - g^{\mu v}g^{\lambda\sigma} - g^{\mu\sigma}g^{v\lambda}\right)$
	$g[A_3^\mu W_1^{v+}W_2^{\lambda-}]$	$ig_e\left(g^{v\lambda}(q_1^\mu - q_2^\mu) + g^{\lambda\mu}(q_1^v - q_2^v) + g^{\mu v}(q_1^\lambda - q_2^\lambda)\right)$
	$g[A^\lambda A^\sigma W^{v-}W^{\mu+}]$	$-ig_e^2\left(2g^{\mu v}g^{\lambda\sigma} - g^{\mu\lambda}g^{v\sigma} - g^{\mu\sigma}g^{v\lambda}\right)$
	$g[A^\lambda Z^\sigma W^{v-}W^{\mu+}]$	$ig_e g_w\cos(\theta_W)\left(2g^{\mu v}g^{\lambda\sigma} - g^{\mu\lambda}g^{v\sigma} - g^{\mu\sigma}g^{v\lambda}\right)$
Gauge-Fermion	$g[\bar{f}fA^\mu]$	$ig_e\gamma^\mu$
	$g[\bar{q}qg^\mu]$	$-\dfrac{ig_s}{2}\lambda^\alpha\gamma^\mu$
	$g[\bar{v}_l l W^{\mu-}]$	$-\dfrac{ig_w}{2\sqrt{2}}\gamma^\mu(1-\gamma^5)V_{ij}^{PMNS}$
	$g[\bar{u}_j d_i W^{\mu-}]$	$-\dfrac{ig_w}{2\sqrt{2}}\gamma^\mu(1-\gamma^5)V_{ij}^{CKM}$
	$g[\bar{f}fZ^\mu]$	$-\dfrac{ig_z}{2}\gamma^\mu(I_3^f - 2Q^f - I_3^f\gamma^5)$
Fermion-Fermion	$g[only\ fermions]$	0

TABLE 2.9: All couplings of the Standard Model.

2.5.2 Symmetry breaking in the scalar KED

Now consider the derivative terms in the scalar potential, given by

$$\mathcal{T}_{\text{Scalar}} = \left(D^\mu \Phi\right)^\dagger \left(D_\mu \Phi\right). \tag{2.42}$$

The relevant covariant derivative from Table 2.5 can be expanded in matrix form as

$$D_\mu = \partial_\mu + \frac{1}{2}ig_1 B_\mu + \frac{1}{2}ig_2 W^a_\mu \sigma^a$$

$$= \partial_\mu + \frac{ig_1}{2}\begin{bmatrix} B^\mu & 0 \\ 0 & B^\mu \end{bmatrix} + \frac{ig_2}{2}\begin{bmatrix} W^3_\mu & W^1_\mu - iW^2_\mu \\ W^1_\mu + iW^2_\mu & -W^3_\mu \end{bmatrix}. \tag{2.43}$$

Plugging this into the scalar KED gives the following result

$$\left(D_\mu \Phi\right)^\dagger \left(D^\mu \Phi\right) = \left(\partial_\mu h\right)^\dagger \left(\partial^\mu h\right) - \frac{(v+h)^2}{4}\begin{bmatrix} W^{\mu 1} & W^{\mu 2} & W^{\mu 3} & B^\mu \end{bmatrix} M^2_{\text{Gauge}} \begin{bmatrix} W^{\mu 1} \\ W^{\mu 2} \\ W^{\mu 3} \\ B^\mu \end{bmatrix}, \tag{2.44}$$

where the mass matrix is given by

$$M^2_{\text{Gauge}} \equiv \begin{bmatrix} g_2^2 & & & \\ & g_2^2 & & \\ & & g_2^2 & -g_1 g_2 \\ & & -g_1 g_2 & g_1^2 \end{bmatrix}. \tag{2.45}$$

We see the appearance of mass terms but some of them couple different fields together. It is more convenient to work in a basis of gauge fields where the mass matrix is diagonal so that the gauge fields are independent. The lower 2x2 matrix can be diagonalised by a rotation matrix. The corresponding rotation angle, called the *Weinberg angle*, is given by

$$\cos\left(\theta_w\right) \equiv \frac{g_2}{\sqrt{g_1^2 + g_2^2}}, \tag{2.46}$$

and the mass matrix in the rotated basis takes the form

$$M^2_{\text{Gauge}} \equiv \begin{bmatrix} g_2^2 & & & \\ & g_2^2 & & \\ & & g_2^2 + g_1^2 & \\ & & & 0 \end{bmatrix}.$$ (2.47)

The physical gauge fields are written as

$$\begin{bmatrix} A_\mu \\ Z_\mu \end{bmatrix} = R\left(\theta_W\right) \begin{bmatrix} B_\mu \\ W_{3\mu} \end{bmatrix}.$$ (2.48)

In the diagonal mass matrix, we find that the mass of A_μ is zero. In fact, this is just the familiar photon field. Note that while $W_{1\mu}$ and $W_{2\mu}$ are mass eigenstates, they are not electric charge eigenstates. Since electric charge is the only type of weak charge that is conserved in the low-energy universe, it is convenient to rotate these into charge eigenstates. These are given by

$$W^\pm_\mu = \frac{1}{\sqrt{2}}\left(W_{1\mu} \mp iW_{2\mu}\right).$$ (2.49)

Notice that Equation 2.44 also includes interactions between the Higgs and weak gauge bosons.

2.5.3 Symmetry breaking in the Yukawa sector

The Yukawa sector (Equation 2.33) included all the couplings between the fermion fields and the Higgs doublet. In the low energy universe, we expect to instead find interactions between the Higgs boson, h, along with mass terms for the fermions. Plugging the Higgs doublet into Equation 2.33 yields

$$\mathcal{L}_{\text{Yukawa}} \equiv \frac{1}{\sqrt{2}}\left(v + h\right)\left(Y^D_{ij}\bar{d}_{i,L}d_{j,R} + Y^U_{ij}\bar{u}_{i,L}u_{j,R} + Y^E_{ij}\bar{e}_{i,L}e_{j,R} + Y^N_{ij}\bar{v}_{i,L}\,v_{j,R} + H.c.\right).$$ (2.50)

Clearly, the terms proportional to v will be bilinear in two fermion fields. However, these terms may couple different fermions together. To find the mass terms we must switch to a basis of fermions which diagonalises the Yukawa matrices so that all bilinear terms

couple the same field.[19] In general, any non-singular matrix can be diagonalised by two unitary matrices, i.e.,

$$M = UYK^\dagger, \quad \text{where } M \text{ is diagonal, and } U, K \text{ are both unitary.} \qquad (2.51)$$

Also note that M is positive definite, thus all mass terms have the appropriate sign. In our case we have four Yukawa matrices, Y^f, which are diagonalised by U^f and K^f, where $f = D, U, E, N$. We use a different notation for such a basis where the Yukawa matrices are diagonal given by[20]

$$\mathcal{L}_{\text{Yukawa}} \equiv \frac{1}{\sqrt{2}} (v + h) \left(M^D_{lm} \bar{d}_{l,L} d_{m,R} + M^U_{lm} \bar{u}_{l,L} u_{m,R} + M^E_{lm} \bar{e}_{l,L} e_{m,R} + M^N_{lm} \bar{v}_{l,L} \, v_{m,R} + H.c. \right),$$
$$(2.52)$$

where the fermions before and after the transformation are related via

$$f^L_l = U^f_{li} f^L_i, \quad f^R_l = K^f_{li} f^R_i, \quad f = d, u, e, v. \qquad (2.53)$$

We call this the physical basis, or alternatively the mass basis. The original basis we started with is called the flavour basis. Note that we have denoted physical basis fermions using the subscripts l, m, whereas we used i, j to denote the generic basis fermions. We can consider Y^f and M^f to be the Yukawa matrices in the flavour and physical bases respectively.

2.5.4 Symmetry breaking in the fermion sector

Originally, before minimal substitution, the fermion sector only included the KED for each fermion. We must now substitute in the covariant derivative from Table 2.5. We should also write the gauge bosons as charge eigenstates in their mass basis. Carrying out the algebra yields

$$\mathcal{L}_{\text{Fermion}} = -i \bar{f}_i \slashed{\partial} f_i - Q_f \bar{f}_i \slashed{A} f_i + Q_f \tan \theta_W \bar{f}_i \slashed{Z} f_i - \frac{g_2}{\cos \theta_W} I^3_f \bar{f}^L_i \slashed{Z} f^L_i$$

---

[19]In general we are free to re-define fields or rotate them into each other so long as the symmetries of our theory are preserved.

[20]Mass terms for Dirac particles can be written: $m\bar{\psi}\psi = m\bar{\psi} (P_R + P_L) \psi = m\bar{\psi}_L \psi_R + m\bar{\psi}_R \psi_L$. Both terms on the RHS are present due to the *H.c* in the Yukawa Lagrangian.

$$- \frac{g_2}{\sqrt{2}} \bar{v}_i^L W\!\!\!\!/^+ e_i^L - \frac{g_2}{\sqrt{2}} \bar{e}_i^L W\!\!\!\!/^- v_i^L - \frac{g_2}{\sqrt{2}} \bar{u}_i^L W\!\!\!\!/^+ d_i^L - \frac{g_2}{\sqrt{2}} \bar{d}_i^L W\!\!\!\!/^- u_i^L, \tag{2.54}$$

where a sum over $f = d, u, e, v$ is implied. Note that we have kept the fermions in the flavour basis. To write these in the physical basis, we will have to first expand the fermions into Weyl components. For the A_μ and Z_μ bosons, we have terms like

$$\bar{f}_i A_\mu \gamma^\mu f_i = \bar{f}_{i,R} A_\mu \gamma^\mu f_{i,R} + \bar{f}_{i,L} A_\mu \gamma^\mu f_{i,L}. \tag{2.55}$$

The terms for the $W^\pm$ boson are similar except that they couple different fields together

$$\bar{v}_i^L W_\mu^+ \gamma^\mu e_i^L = \bar{v}_i^L W_\mu^+ \gamma^\mu e_i^L + \bar{v}_i^L W_\mu^+ \gamma^\mu e_i^L. \tag{2.56}$$

So, when writing our fermions in the physical basis, we need just to insert a $U^\dagger U$ or $K^\dagger K$ term for the A_μ and Z_μ bosons, and a $U^{f_1\dagger} U^{f_2}$ term for the $W^\pm$ bosons. The former case is just the identity matrix, and we therefore conclude that the interactions with A_μ and Z_μ bosons look the same in both bases. However, we cannot assume that $U^{f_1} = U^{f_2}$, thus the $W^\pm$ terms include an additional mixing matrix when written in the physical basis. Writing this out in full yields

$$- \frac{g}{\sqrt{2}} \left(\bar{v}_l^L W\!\!\!\!/^+ U^V U^{E\dagger} e_l^L + \bar{e}_l^L W\!\!\!\!/^- U^E U^{V\dagger} v_l^L + \bar{u}_l^L W\!\!\!\!/^+ U^U U^{D\dagger} d_l^L + \bar{d}_l^L W\!\!\!\!/^- U^D U^{U\dagger} u_l^L \right), \tag{2.57}$$

where we notice that the matrices appear in pairs. These mixing matrices are denoted

$$V_{\text{PMNS}} \equiv U^E U^{V\dagger}, \quad V_{\text{CKM}} \equiv U^D U^{U\dagger}. \tag{2.58}$$

The first is called the Pontecorvo-Maki-Nakagawa-Sakata (PMNS) matrix and the second is called the Cabibbo-Kobayashi-Maskawa (CKM) matrix. The CKM and PMNS matrices are unitary and therefore have 9 DOFs each. However, 5 of them can be eliminated with the appropriate choice of basis. The remaining 4 can be parameterised as 3 rotation angles and one complex phase. This complex phase provides the only source of CP-violation in the SM.

When dealing with neutrino oscillations, it is more common to pick a basis where V_{PMNS} appears in the mass terms rather than the $W^\pm$ interactions. Therefore, we usually assume an alternative basis for leptons defined as

$$v_\alpha^L \equiv V_{\alpha l}^{\text{PMNS}} v_l^L, \quad v_\alpha^R \equiv \delta_{\alpha l} v_l^R, \quad e_\alpha^{L,R} \equiv \delta_{\alpha l} e_l^{L,R}, \quad M_{\alpha\alpha}^N \equiv \delta_{\alpha l} M_{ll}^N. \tag{2.59}$$

In this basis, the $W^\pm$ interactions take the simple form

$$-\frac{g}{\sqrt{2}} \left(\bar{v}_\alpha^L W\!\!\!/^+ e_\alpha^L + \bar{e}_\alpha^L W\!\!\!/^- v_\alpha^L \right), \tag{2.60}$$

while the mass terms are more complicated. These are given by

$$-\frac{v}{\sqrt{2}} \bar{v}_\alpha^R M_{\alpha\alpha} V_{\alpha\beta}^{\text{PMNS}\dagger} v_\beta^L - \frac{v}{\sqrt{2}} \bar{v}_\alpha^L V_{\alpha\beta}^{\text{PMNS}} M_{\beta\beta} v_\beta^R. \tag{2.61}$$

Finally, notice that the $W^\pm$ boson provides the only Flavour-Changing Charged Current (FCCC) in the SM and that there are no Flavour-Changing Neutral Currents (FCNCs).[21] This feature is strongly supported by experimental evidence [29, 30] and is therefore something we should preserve when extending to the 2HDM.

2.5.5 Symmetry breaking in the gauge sector

Since the Higgs doublet does not appear in the gauge sector, there are no masses or new interactions that arise from this sector. However, it would be more convenient to write the weak bosons as mass (and charge) eigenstates. We will not carry out the algebra here as it is rather lengthy but doing so will yield a variety of 3 and 4 gauge boson vertices. There are also terms which couple different gauge bosons, for example W^+W^-ZZ and $AAZZ$. Of course, charge must be conserved at all vertices so we cannot have terms like W^+ZZZ. All interactions can be found in Table 2.9.

---

[21]At least, there are no FCNCs at tree-level. We could however combine two FCCCs to create an effective FCNC at 1-loop level.

Chapter 3

Two-Higgs-Doublet Models

While the SM has the simplest possible scalar sector that allows for spontaneous symmetry breaking, there is no reason why it must be this way. Given that multiple fermion generations have already been observed, it would not be strange if we were to discover multiple Higgs generations. Veltman's ρ parameter provides an important restriction on which Higgs fields can be added to our theory [31, 32]. This parameter, defined by

$$\rho \equiv \left(\frac{m_W}{\cos \theta_W m_Z} \right), \tag{3.1}$$

relates the ratio of the weak boson masses to the Weinberg angle. In the SM it has a value of exactly 1 at tree level, and experimentally is it known to be very close to 1. In general, for a gauge theory with n scalar $SU(2)_L \otimes U(1)_Y$ multiplets with weak isospins, I_i, weak hypercharges, Y_i, and vacuum expectation values of the neutral components, v_i, the parameter is given by (at tree level)

$$\rho = \frac{\sum_{i=1}^{n} \left(I_i \left(I_i + 1 \right) - Y_i^2 \right) v_i}{\sum_i^n 2 Y_i^2 v_i}. \tag{3.2}$$

To obtain $\rho = 1$, we can either: (i) fine-tune the parameters of the potential to get the right VEVs, or (ii) only allow representations that lead to $\rho = 1$. Taking the later approach, one finds that both $SU(2)$ singlets (with $Y = 0$) and doublets (with $Y = \pm 1$) give $\rho = 1$, while other allowed representations are much more complicated. Hence, the simplest approach is the addition of a scalar singlet into the SM Lagrangian. The resulting theory is known as the Scalar Singlet model and may provide a DM candidate – but it is not studied in this thesis. The next step is to try adding another Higgs doublet.[1]

---

[1]Expanding the Higgs representation to $3 \otimes 2$ is no good as we introduce Higgs-gluon interactions.

3.1 Motivation

There are many good reasons to study the 2HDM. We list some key motivations below:

- **Electroweak observables:** Some observables from the electroweak sector show a potential discrepancy with the SM, including the W-boson mass and muon-anomalous magnetic moment. These may be accommodated in the 2HDM via new scalar loop corrections.

- **Flavour Observables:** Some flavour observables differ from the SM predictions. These may be accommodated by the 2HDM via new FCCCs involving the charged scalars $H^{\pm}$.

- **Dark Matter:** A special case of the 2HDM, known as the Inert Doublet Model (IDM), includes a DM candidate.

- **Baryon asymmetry:** The SM is unable to account for the dominance of matter over antimatter in our universe. Extra sources of CP-violation in the 2HDM may offer an explanation.

- **Low-energy limit:** The 2HDM may provide a low-energy EFT of more exotic models such as supersymmetric models and axion models, which require at least two Higgs doublets.

3.2 Overview

Carrying out electroweak symmetry breaking in the 2HDM reveals 5 massive scalar bosons (h, H, A, H^+, H^-) and 3 Goldstone bosons (G^0, G^+, G^-). Of the massive bosons there are two CP-even scalars (with one of them being the 125 GeV Higgs boson detected by collider experiments), two degenerate charged scalars, and one CP-odd scalar. Like the SM, all Goldstone bosons can be rotated into longitudinal modes of the W^+, W^-, and Z bosons enabling them to acquire mass. The most general 2HDM allows CP-violation (both explicit and spontaneous) and flavour changing neutral currents (FCNCs). These features are usually considered undesirable as they are tightly limited by experiment. In this work, we consider CP-conserving $\mathbb{Z}_2$-symmetric 2HDMs. In the scalar sector, all parameters are set real to eliminate the explicit CP-violation. When applied to the Yukawa sector, the $\mathbb{Z}_2$ symmetry eliminates all FCNCs, and we also apply this to scalar sector to prevent FCNCs from emerging at 1-loop level. In general, we expect parameter scans to favour SM-like behaviour, since the SM has so far been in remarkable agreement with experiment. In the regular Higgs scenario the lightest CP-even scalar

Name	Particle		DOFs
Higgs Doublet 1	$\Phi_1 \equiv \begin{bmatrix} \varphi_1^+ \\ \varphi_1^0 \end{bmatrix}$	$\equiv \begin{bmatrix} \varphi_1 + i\varphi_2 \\ \varphi_3 + i\varphi_3 \end{bmatrix}$	4
Higgs Doublet 2	$\Phi_2 \equiv \begin{bmatrix} \varphi_2^+ \\ \varphi_2^0 \end{bmatrix}$	$\equiv \begin{bmatrix} \varphi_5 + i\varphi_6 \\ \varphi_7 + i\varphi_8 \end{bmatrix}$	4

TABLE 3.1: Scalar (spin-0) fields of the 2HDM.

corresponds the SM Higgs boson, by which we mean that it has a mass of 125 GeV. The alternative scenario, called the Hidden Higgs scenario, has roles of the light and heavy CP-even scalars reversed. An important limit, known as the alignment limit, occurs when the 125 GeV CP-even scalar has the same coupling strengths as the SM Higgs boson, while the other CP-even scalar is completely decoupled from all fermions and gauge bosons at tree-level. SM-like behaviour may also occur when the additional scalars are so heavy that insufficient energy is available to produce them. This is known as the decoupling limit.

3.3   2HDM Lagrangian

Like the SM, the 2HDM is a gauge field theory whose Lagrangian exhibits a local $SU(3)_C \otimes SU(2)_L \otimes U(1)_Y$ symmetry [31]. It includes all particles of the SM (all belonging to the same representations of the gauge group) plus an additional Higgs doublet with the same charges as the first. The notation for the 2HDM scalar fields is provided in Table 3.1. The electric charge of each component is found using the charge operator, which is given by

$$Q = \begin{bmatrix} 1 & 0 \\ 0 & 0 \end{bmatrix}. \tag{3.3}$$

Applying this to the Higgs doublets reveals that φ_1^+ and φ_2^+ are positively charged – hence justifying our choice of notation. Furthermore, applying the CP-operator (i.e. complex conjugation) to the Higgs doublets will reveal that φ_3, φ_7 are CP-even, while φ_4, φ_8 are CP-odd.

The 2HDM Lagrangian looks very similar to the SM Lagrangian, and in shorthand notation is

$$\mathcal{L}_{\text{2HDM}} \equiv \mathcal{L}_{\text{Fermion}} + \mathcal{L}_{\text{Gauge}} + \mathcal{L}_{\text{Scalar}} + \mathcal{L}_{\text{Yukawa}}. \tag{3.4}$$

The fermion and gauge sectors have the same form as for the SM, while the Higgs and Yukawa sectors need to be modified to account for the additional doublet. A Lagrangian of any gauge field theory must satisfy Hermiticity, Lorentz invariance, gauge symmetry and renormalisability. Hence, writing down the most general scalar sector, we would obtain

$$\mathcal{L}_{\text{Scalar}} = \sum_{i=1}^{2} \left(D^{\mu} \Phi_i \right)^{\dagger} \left(D_{\mu} \Phi_i \right) - \mathcal{V}_{\text{2HDM}}, \tag{3.5}$$

where the scalar potential is

$$\mathcal{V}_{\text{2HDM}} = \mu_{ij} \Phi_i^{\dagger} \Phi_j + \frac{1}{2} \Lambda_{ijkl} \Phi_i^{\dagger} \Phi_j \Phi_k^{\dagger} \Phi_l, \quad i,j,k,l \in \{1,2\}. \tag{3.6}$$

Here we have simply listed all possible Higgs terms up to mass dimension 4 using index notation (where a sum is implied over i, j, k, l). In a similar manner, we construct the general Yukawa sector as

$$
\begin{aligned}
-\mathcal{L}_{\text{Yukawa}} = {} & \bar{Q}_{i,L} \left(Y_{1,ji}^{u} \widetilde{\Phi}_1 + Y_{2,ji}^{u} \widetilde{\Phi}_2 \right) u_{j,R} + \bar{Q}_{i,L} \left(Y_{1,ji}^{d} \Phi_1 + Y_{2,ji}^{d} \Phi_2 \right) d_{j,R} \\
& + \bar{L}_{i,L} \left(Y_{1,ji}^{e} \Phi_1 + Y_{2,ji}^{e} \Phi_2 \right) e_{j,R} + \bar{L}_{i,L} \left(Y_{1,ji}^{\nu} \widetilde{\Phi}_1 + Y_{2,ji}^{\nu} \widetilde{\Phi}_2 \right) v_{j,R} \\
& + H.c. \tag{3.7}
\end{aligned}
$$

We are reusing the notation from Equation 2.4 for the fermion doublets. Quantum mechanics requires the scalar potential to be Hermitian, leading to

$$\mu_{ij} = \mu_{ji}^{*}, \quad \Lambda_{ijkl} \equiv \Lambda_{klij} = \Lambda_{jilk}^{*}. \tag{3.8}$$

Removing this redundancy leads to

$$
\begin{aligned}
\mathcal{V}_{\text{2HDM}} = {} & m_{11}^2 \Phi_1^{\dagger} \Phi_1 + m_{22}^2 \Phi_2^{\dagger} \Phi_2 - (m_{12}^2 \Phi_1^{\dagger} \Phi_2 + \text{H.c.}) \\
& + \frac{1}{2} \lambda_1 (\Phi_1^{\dagger} \Phi_1)^2 + \frac{1}{2} \lambda_2 (\Phi_2^{\dagger} \Phi_2)^2 + \lambda_3 (\Phi_1^{\dagger} \Phi_1)(\Phi_2^{\dagger} \Phi_2)
\end{aligned}
$$

$$+ \lambda_4(\Phi_1^\dagger \Phi_2)(\Phi_2^\dagger \Phi_1) + \left[\frac{1}{2}\lambda_5(\Phi_1^\dagger \Phi_2)^2 \right.$$

$$\left. + \lambda_6(\Phi_1^\dagger \Phi_1)(\Phi_1^\dagger \Phi_2) + \lambda_7(\Phi_2^\dagger \Phi_2)(\Phi_1^\dagger \Phi_2) + \text{H.c}\right], \quad (3.9)$$

which is the most commonly used notation for the scalar potential in physics literature. The parameters are related via

$$m_{11}^2 \equiv \mu_{11}, \;\; m_{12}^2 \equiv -\mu_{12}, \;\; m_{22}^2 \equiv \mu_{22}, \;\; \lambda_1 \equiv \Lambda_{1111}, \;\; \lambda_2 \equiv \Lambda_{2222},$$

$$\lambda_3 \equiv \Lambda_{1221}, \;\; \lambda_4 \equiv \Lambda_{1122}, \;\; \lambda_5 \equiv \Lambda_{1212}, \;\; \lambda_6 \equiv \Lambda_{1112}, \;\; \lambda_7 \equiv \Lambda_{1222}, \quad (3.10)$$

and

$$m_{11}^2, m_{22}^2, \lambda_1, \lambda_2, \lambda_3, \lambda_4 \in \mathbb{R}, \;\; m_{12}^2, \lambda_5, \lambda_6, \lambda_7 \in \mathbb{C}. \quad (3.11)$$

The complex terms in the Lagrangian result in CP-violation.[2] Such CP-violation would cause the 3 neutral scalar states (h, H, and A) to mix together. The resulting states would not be eigenstates of CP. It is already confirmed that the experimentally measured scalar is not CP-odd, although there is still a possibility that it may be a mixed CP-state. We shall leave this possibility to a future study as it makes the analysis much more complicated. Hence, we eliminate this CP violation by taking all parameters to be real [33]. The resulting theory is known as the General CP-conserving (GCP) 2HDM.

3.4 Reparametrisation invariance and basis transformations

In general, a theory has reparametrisation invariance if two different sets of parameters lead to the same observables [31, 34]. Recall that our scalar potential was a function of both parameters and fields. The physical observables are a function of the parameters only, $\mathcal{O}(\mu, \Lambda)$, and not the fields themselves. This means that we are free to redefine the fields how we like. Furthermore, since both Higgs doublets carry the same charges we may consider them as components of a "hyperspinor", (Φ_1, Φ_2). Transformations of this hyperspinor leaves the symmetries of the theory invariant. Now consider some arbitrary transformation of the doublets

$$\Phi_i \to \Phi_i' = M_{ij}\Phi_j. \quad (3.12)$$

---

[2]This is called explicit CP violation. This is in contrast to spontaneous CP-violation which is caused by the VEV.

Sometimes it is possible to find a simultaneous transformation of the parameters which leave the potential invariant, i.e.

$$\mu'_{ab}\Phi'_a\Phi'_b \equiv t_{abcd}\mu_{cd}M_{ae}\Phi_e M_{bf}\Phi_f = \mu_{ab}\Phi_a\Phi_b. \tag{3.13}$$

In this case, the physics encoded by both sets of parameters must be the same. This would also imply that the transformation, M, is invertible and therefore belongs to some group G. The doublets, Φ_i, transform under $M \in G$, and the parameters, μ_{ab}, are put into the appropriate tensor representation of G to preserve $\mu_{ab}\Phi_a\Phi_b$. What we have stated in Equation 3.12 can also be considered a basis transformation where Φ_i are the basis vectors and μ'_{ab} are the coefficients in the transformed basis, Φ'_i. Sometimes the coefficients may be invariant under the transformation, i.e. $\mu_{ab} = \mu'_{ab}$. In this case the transformation is also a symmetry. Other times, we must put the coefficients into a non-trivial representation so that Equation 3.13 is satisfied.

We often use basis transformations to eliminate parameters from our theory. This allows us to identify how many DOFs are really present. For example, consider the selection of a basis where one of the parameters is zero, e.g. $\mu_{11} = 0$. Then we would find that the observables can be determined with fewer parameters than we originally thought. Notice that this is not possible if the transformation is also a symmetry.[3] Hence, we conclude that each generator which induces a non-trivial transformation of the parameters may be used to eliminate a parameter from the theory.

As an example, we can show that 3 parameters can be eliminated from the most general 2HDM potential – bringing the count down from 14 to 11. The 3 eliminated parameters correspond to the 3 generators of $SU(2)$. While we can consider a more general $U(2)$ basis transformation, the $U(1)$ part is already a symmetry and therefore cannot be used to eliminate a parameter.[4] In the $\mathbb{Z}_2$-symmetric 2HDMs that we consider, (which will be discussed shortly) a basis transformation may be used to render λ_5 real.

As a simple example of a basis transformation, consider a unitarity transformation of the doublets given by

$$\Phi'_a = U_{ab}\Phi_b, \quad \text{where } U \in U(2). \tag{3.14}$$

which induces the following transformation [35] on the parameters in Equation 3.5

---

[3]Since the parameters do not transform if it is also a symmetry.

[4]Note that when one imposes additional symmetries on the 2HDM Lagrangian, the number of parameters which may be eliminated through basis transformations may be less than three.

$$\mu'_{ab} = U_{ac}\mu_{cd}U^*_{bc},$$
$$\lambda'_{abcd} = U_{ae}U_{cg}\lambda_{efgh}U^*_{bf}U^*_{dh}, \tag{3.15}$$

All observables must of course be in singlet representations of this group. Note that the scalar KED is symmetric under this unitary transformation. This is important for this example since the KED does not have any parameters. In Appendix D we show how it is possible to generalise to the full $GL(2, C)$ group.

3.5 The generalised CP transformation

The standard CP-transformation for a theory with a single scalar field reads

$$CP : \Phi(t, x) \to \Phi^*(t, -x). \tag{3.16}$$

Note that parity is always conserved in a scalar theory: $\Phi(t, x) = \Phi(t, -x)$, thus we can suppress the spatial coordinates. The natural extension to two scalar fields would be

$$\Phi_i(t, x) \to \Phi_i^*(t, -x). \tag{3.17}$$

Now consider how this CP-transformation appears after a basis transformation is applied. It becomes

$$\Phi'_i = U_{ij}\Phi_j^*. \tag{3.18}$$

We can also do the basis transformation first, and then apply a CP transformation to the transformed basis. The result is

$$\Phi'_i = (U_{ij}\Phi_j)^* = U^*_{ij}\Phi_j^*. \tag{3.19}$$

However, these CP transformations now appear different. It is not possible to apply another basis transformation, $X_{ij} \in U(2)$, such that $X_{il}U^*_{lk}X^\dagger_{kj} = U_{ij}$. But a basis transformation could not possibly affect the phenomenology. Hence, we conclude that our definition of the CP transformation must be too restrictive. We can construct a

more general CP transformation (known as the generalised CP transformation [36]) by also incorporating a $U(2)$ transformation, i.e.

$$\text{GCP transformation: } \Phi_i \to U_{ij}\Phi_j^*. \tag{3.20}$$

3.6 Symmetries of the 2HDM

We may wonder what types of physics are possible in the 2HDM. By this we mean: "what are all the ways we can restrict the parameters to give a unique set of interactions / conservation laws?"[5] According to Noether's theorem, such conservation laws are induced by symmetries in the Lagrangian, so this question amounts to asking: "what are all the symmetries that the 2HDM Lagrangian may possess?"[6]

When imposing a symmetry, we must be careful not to modify the KED as it may leave the theory non-renormalisable. The most general symmetry group of the scalar KED is given by $HF \otimes GCP$, where HF is called the Higgs family symmetry and GCP is the generalised CP symmetry. These are defined by

$$
\begin{aligned}
HF : \quad & \Phi_i = U_{ij}\Phi_j, \quad \text{where U is unitary,} \\
GCP : \quad & \Phi_i = U_{ij}\Phi_j^*, \text{ where U is unitary.}
\end{aligned}
\tag{3.21}
$$

So, we just need to find all the subgroups of $HF \otimes GCP$. However, identifying *all* subgroups is quite inefficient as many are related by basis transformations and hence lead to the same phenomenology (they are said to belong to the same conjugacy class). In [37] it is proven that there are only 6 unique symmetry classes. They are listed in Table 3.2 and the restrictions on the parameters are given in Table 3.3 [38]. Example transformations for each symmetry are

$$
U(2) : \quad
\begin{bmatrix}
e^{-i\xi}\cos\theta & e^{-i\psi}\sin\theta \\
-e^{i\psi}\sin\theta & e^{i\xi}\cos\theta
\end{bmatrix},
$$

---

[5]Note that the symmetries and charges are not enough to determine the phenomenology of the theory – we must also know the specific parameter values. The symmetries only determine which interactions are allowed/forbidden, and whether particles acquire mass.

[6]We impose the symmetries by restricting the parameters to take specific values. Notice that this is quite different to basis transformations, where we put the parameters in some representation in order to keep the potential invariant. Only in the latter case do the parameters vary under the transformation.

Class	Symmetry	Type	Parameters	DOFs
G2HDM	N/A	N/A	14	11
Class I	U(2)	HF	3	3
Class II	CP3	GCP	4	4
Class III	CP2	GCP	8	5
Class IV	U(1)	HF	6	6
Class V	Z2	HF	8	7
Class VI	CP1	GCP	10	8

TABLE 3.2: The six symmetry classes of the 2HDM potential. The parameters column refers to the number of parameters that remain after imposing the relevant symmetry in the generic basis, while the DOFs refers to the minimum number of parameters in any basis.

Class	m^2_{11}	m^2_{22}	m^2_{12}	λ_1	λ_2	λ_3	λ_4	λ_5	λ_6	λ_7
Class I		m^2_{11}	0		λ_1		$\lambda_1 - \lambda_3$	0	0	0
Class II		m^2_{11}	0		λ_1			$\lambda_1 - \lambda_3 - \lambda_4$	0	0
Class III		m^2_{11}	0		λ_1					$-\lambda_6$
Class IV			0					0	0	0
Class V			0						0	0
Class VI			real					real	real	real

TABLE 3.3: Restrictions on the generic basis parameters for the six symmetry classes.

$$
U(1): \quad \begin{bmatrix} e^{-i\xi} & 0 \\ 0 & e^{i\xi} \end{bmatrix} = U(2)\,(\theta = 0)\,,
$$

$$
\mathbb{Z}_2: \quad \begin{bmatrix} 1 & 0 \\ 0 & -1 \end{bmatrix}\,,
$$

$$
CP3: \quad \begin{bmatrix} \cos\theta & \sin\theta \\ -\sin\theta & \cos\theta \end{bmatrix}\,,
$$

$$
CP2: \quad \begin{bmatrix} 0 & 1 \\ -1 & 0 \end{bmatrix} = CP3\,(\theta = -\pi/2)\,,
$$

$$
CP1: \quad \begin{bmatrix} 1 & 0 \\ 0 & 1 \end{bmatrix} = CP3\,(\theta = 0)\,, \tag{3.22}
$$

where ξ, ψ, θ are arbitrary real numbers.

The six models resulting from the imposition of each of those symmetries have different physical implications: different spectra of scalars, different interactions with gauge bosons, and, in some cases, predictions of massless axions or potential dark matter candidates. The least restrictive of these is the CP1 class with 8 free parameters. This is just the usual CP-transformation and is enforced by setting all parameters real. For our scans we use the $\mathbb{Z}_2$ symmetry class which has 7 free parameters. This results in $\lambda_6 = \lambda_7 = 0$ while all other couplings are real. In general, the large number of parameters of the general 2HDM reduces the theory's predictive power so any symmetries that we can impose are welcome.

3.7 Vacuum structure and Symmetry Breaking

Like the SM, all mass terms in the 2HDM are a result of spontaneous symmetry breaking, where the Higgs doublets acquire a VEV (in the low-energy universe), which breaks the gauge symmetry [31, 39]. In the SM, originally the VEV took the form

$$\langle 0 \left| \Phi \right| 0 \rangle = \begin{bmatrix} v_1 + iv_2 \\ v_3 + iv_4 \end{bmatrix}. \tag{3.23}$$

But importantly, we were able to pick an $SU(2) \times U(1)$ gauge transformation, M, to eliminate v_1, v_2, v_3 and thus leaving us with

$$\langle 0 \left| M\Phi \right| 0 \rangle = \begin{bmatrix} 0 \\ v \end{bmatrix}. \tag{3.24}$$

This means that the charge and CP violating components can be eliminated, and therefore these symmetries are not broken in the low-energy universe.[7] When we have two Higgs doublets, we are still able to exploit our gauge freedom to eliminate 3 components from the VEVs, but this still leaves 5 components – some of which may break charge or CP symmetry. All possible minimum solutions in the 2HDM were investigated in Ref [40]. It was shown that three types of minima are possible: (i) the charge-breaking minimum, (ii) CP-breaking minimum and (iii) the normal minimum. These are given in Equations 3.25, 3.26 and 3.27 respectively.[8]

---

[7]If we were to pick a different gauge we would still have electric charge conservation, but the electric charge operator would have to be defined differently.

[8]Finding the minimum of the potential requires us to solve $\partial V / \partial v_i = 0$, leading to $[\mu_{ij} + 2\Lambda_{ijkl} v_k^* v_l] v_j = 0$. Unfortunately, this equation cannot be solved explicitly.

$$\langle 0 \,|\Phi_1|\, 0 \rangle = \frac{1}{\sqrt{2}} \begin{bmatrix} \alpha \\ v_1 \end{bmatrix}, \quad \langle 0 \,|\Phi_2|\, 0 \rangle = \frac{1}{\sqrt{2}} \begin{bmatrix} 0 \\ v_2 \end{bmatrix} \quad \text{(Charge-breaking minimum)} \qquad (3.25)$$

$$\langle 0 \,|\Phi_1|\, 0 \rangle = \frac{1}{\sqrt{2}} \begin{bmatrix} 0 \\ v_1 \end{bmatrix}, \quad \langle 0 \,|\Phi_2|\, 0 \rangle = \frac{1}{\sqrt{2}} \begin{bmatrix} 0 \\ v_2 e^{i\theta} \end{bmatrix} \quad \text{(CP-breaking minimum)} \qquad (3.26)$$

$$\langle 0 \,|\Phi_1|\, 0 \rangle = \frac{1}{\sqrt{2}} \begin{bmatrix} 0 \\ v_1 \end{bmatrix}, \quad \langle 0 \,|\Phi_2|\, 0 \rangle = \frac{1}{\sqrt{2}} \begin{bmatrix} 0 \\ v_2 \end{bmatrix} \quad \text{(normal minimum)} \qquad (3.27)$$

The normal minimum is a special case of the CP-breaking minimum, which does not break CP or electric charge symmetry. Notice that we do not have a minimum that is simultaneously electric charge-breaking and CP-breaking.

Note that a charge-breaking VEV would result in a massive photon, while a CP-breaking VEV would effectively eliminate the near CP-symmetry that we observe in nature (particles would be able to switch between different CP-eigenstates as they propagate). Clearly these are not the minimum solutions of our universe, so from now on we assume a normal VEV.[9] Prior to interpretation of any mass terms, we must re-express our fields as fluctuations about the normal vacuum. We do this by writing the doublets as

$$\Phi_i = \begin{bmatrix} \varphi_i^+ \\ \frac{1}{\sqrt{2}} \left(v_i + h_i + i z_i \right) \end{bmatrix}. \qquad (3.28)$$

Rather than using v_1, v_2 as parameters it is more convenient to use $\tan\beta \equiv v_1/v_2$, $v \equiv \sqrt{v_1^2 + v_2^2}$. This will become apparent in Section 3.7.1 where we show that $v^2 = v_{SM}^2$. Since the VEVs correspond to the minimum of the potential, they must satisfy

$$\frac{\partial \mathcal{V}}{\partial \varphi_i} \bigg|_{\Phi_a = \langle 0|\Phi_a|0 \rangle} = 0, \quad i = 1, \dots, 8 \text{ and } a = 1, 2. \qquad (3.29)$$

Evaluating this gives 2 independent conditions for a normal minimum and 3 for a charge- or CP-breaking minimum. For the normal minimum these conditions are

---

[9]We should probably be more careful here since it may be possible to render the CP-breaking VEV real via a basis transformation. We shall derive more general conditions in Appendix G.

Sector/Term	Significance
Scalar Potential	Scalar mass matrices; the mass basis with 5 scalar bosons and 3 Goldstone bosons; couplings amongst the scalars.
Scalar KED	Scalar KED terms; gauge boson mass terms; scalar-gauge couplings.
Yukawa Sector	Physical basis and mass terms for quarks/leptons; couplings between the scalar bosons and physical quarks/leptons.
Fermion Sector	(identical to SM)
Gauge Sector	(identical to SM)

TABLE 3.4: What happens as a result of spontaneous symmetry breaking in the 2HDM.

$$m_{11}^2 v_1 - m_{12}^2 v_2 + \frac{\lambda_1}{2} v_1^3 + \frac{\lambda_{345}}{2} v_1 v_2^2 + \frac{1}{2} \left(3\lambda_6 v_1^2 v_2 + \lambda_7 v_2^3 \right) = 0,$$
$$m_{22}^2 v_1 - m_{12}^2 v_1 + \frac{\lambda_2}{2} v_2^3 + \frac{\lambda_{345}}{2} v_2 v_1^2 + \frac{1}{2} \left(\lambda_6 v_1^3 + 3\lambda_7 v_2 v_1^2 \right) = 0, \qquad (3.30)$$

where $\lambda_{345} \equiv \lambda_3 + \lambda_4 + \lambda_5$. These can be used to trade the m_{11}^2 and m_{22}^2 parameters for v_1, v_2, thus eliminating two parameters from our theory.

This completes our discussion of symmetry breaking in the 2HDM. The rest of the theory follows by substituting Equation 3.28 back into the 2HDM Lagrangian (Equation 3.4). The results of doing this are summarised in Table 3.4 and the following subsections carry out the algebra.

3.7.1 Symmetry breaking in the scalar potential

In the SM case, when we inserted the Higgs doublet into the scalar potential, we obtained mass terms for the Higgs boson as well as Higgs-Higgs interactions. We shall find that something similar happens for the 2HDM except that we now have mass terms for 5 scalar bosons and various interactions between these [14, 39]. Extracting the mass terms for the scalars and writing them in matrix form yields

$$\mathcal{V}_{\text{mass}} = - \begin{bmatrix} \varphi_1^- & \varphi_2^- \end{bmatrix} M_\varphi^2 \begin{bmatrix} \varphi_1^+ \\ \varphi_2^+ \end{bmatrix} - \begin{bmatrix} z_1 & z_2 \end{bmatrix} M_\eta^2 \begin{bmatrix} z_1 \\ z_2 \end{bmatrix} - \begin{bmatrix} h_1 & h_2 \end{bmatrix} M_\rho^2 \begin{bmatrix} h_1 \\ h_2 \end{bmatrix}, \qquad (3.31)$$

where the mass matrices are given by

$$M_\varphi^2 \equiv \left(m_{12}^2 - \left(v^2/2\right)(\lambda_4 + \lambda_5 + \lambda_6 \cot\beta + \lambda_7 \tan\beta)\sin\beta\cos\beta\right)\begin{bmatrix} \tan\beta & -1 \\ -1 & \cot\beta \end{bmatrix},$$

$$M_z^2 \equiv \left(m_{12}^2 - \left(v^2/2\right)(2\lambda_5 + \lambda_6 \cot\beta + \lambda_7 \tan\beta)\sin\beta\cos\beta\right)\begin{bmatrix} \tan\beta & -1 \\ -1 & \cot\beta \end{bmatrix},$$

$$M_h^2 \equiv M_z^2 + B^2,$$

$$B^2 \equiv v^2 \begin{bmatrix} \lambda_1 \cos^2\beta + \lambda_5 \sin^2\beta + 2\lambda_6 \sin\beta\cos\beta & (\lambda_3 + \lambda_4)\sin\beta\cos\beta + \lambda_6 \cos^2\beta + \lambda_7 \sin^2\beta \\ (\lambda_3 + \lambda_4)\sin\beta\cos\beta + \lambda_6 \cos^2\beta + \lambda_7 \sin^2\beta & \lambda_2 \sin^2\beta + \lambda_5 \cos^2\beta + 2\lambda_7 \sin\beta\cos\beta \end{bmatrix}.$$

$$(3.32)$$

We would like to move to a basis in which these matrices are diagonal, so that the fields are not coupled together. The parameter β works out to be the rotation angle, which diagonalises both M_φ^2 and M_z^2 simultaneously. We define the parameter α as the rotation angle that diagonalises M_h^2. It is related to the other parameters via

$$\sin(2\alpha) = \frac{2M_{h,12}^2}{\sqrt{\left(M_{h,11}^2 - M_{h,22}^2\right)^2 + 4\left(M_{h,12}^2\right)^2}},$$

$$\cos(2\alpha) = \frac{M_{h,11}^2 - M_{h,22}^2}{\sqrt{\left(M_{h,11}^2 - M_{h,22}^2\right)^2 + 4\left(M_{h,12}^2\right)^2}}. \tag{3.33}$$

The transformed basis (with diagonal mass matrices) is called the physical basis, while the basis we started with is called the generic basis. The two bases are related by

$$\begin{bmatrix} G^- \\ H^- \end{bmatrix} \equiv R(\beta)\begin{bmatrix} \varphi_1^- \\ \varphi_2^- \end{bmatrix}, \quad \begin{bmatrix} G^+ \\ H^+ \end{bmatrix} \equiv R(\beta)\begin{bmatrix} \varphi_1^+ \\ \varphi_2^+ \end{bmatrix}, \quad \begin{bmatrix} G^0 \\ A^0 \end{bmatrix} \equiv R(\beta)\begin{bmatrix} z_1 \\ z_2 \end{bmatrix}, \quad \begin{bmatrix} H^0 \\ h^0 \end{bmatrix} \equiv R(\alpha)\begin{bmatrix} h_1 \\ h_2 \end{bmatrix},$$

$$(3.34)$$

where $R(\omega)$ denotes a rotation matrix through angle ω. Here $H^\pm$ are charged scalar bosons, $G^\pm$ are charged Goldstone bosons, G^0 is a neutral CP-odd Goldstone boson, A^0 is a neutral CP-odd scalar boson and H, h are neutral CP-even scalar bosons. The mass of the physical states can be read off the diagonalised mass matrices. We summarise the results below

$$m_A^2 = \bar{m}^2 - \frac{v^2}{2} \left(2\lambda_5 + \lambda_6 \cot\beta + \lambda_7 \tan\beta \right),$$

$$m_{H^+}^2 = m_A^2 + \frac{v^2}{2} \left(\lambda_5 - \lambda_4 \right),$$

$$m_h^2 = m_A^2 \cos^2(\beta - \alpha) + v^2 (\lambda_1 \cos^2\beta \sin^2\alpha + \lambda_2 \sin^2\beta \cos^2\alpha - 2\lambda_{345} \cos\alpha \cos\beta \sin\alpha \sin\beta$$
$$+ \lambda_5 \cos^2(\beta - \alpha) - 2\lambda_6 \cos\beta \sin\alpha \cos(\beta + \alpha) + 2\lambda_7 \sin\beta \cos\alpha \cos(\beta + \alpha)),$$

$$m_H^2 = m_A^2 \sin^2(\beta - \alpha) + v^2 (\lambda_1 \cos^2\beta \cos^2\alpha + \lambda_2 \sin^2\beta \sin^2\alpha + 2\lambda_{345} \cos\alpha \cos\beta \sin\alpha \sin\beta$$
$$+ \lambda_5 \sin^2(\beta - \alpha) + 2\lambda_6 \cos\beta \cos\alpha \sin(\beta + \alpha) + 2\lambda_7 \sin\beta \sin\alpha \sin(\beta + \alpha)),$$

$$m_{G^\pm}^2 = m_{G^0}^2 = 0. \tag{3.35}$$

Here we made use of $\lambda_{345} \equiv \lambda_3 + \lambda_4 + \lambda_5$. Notice that the mass of the two CP-even scalars is different. By convention, we choose H to be the heavier one and h to be the lighter one. To accommodate collider data, we usually cannot have an additional scalar that is lighter than 125 GeV. So, we usually take $h = h_{125}$ which also corresponds to h_{SM}, while H remains as a heavier unobserved CP-even scalar. The alternative scenario with $H = h_{125}$ is known as the *hidden-Higgs scenario*. For completeness we will run parameter scans of both scenarios. We can also write our Higgs doublets in terms of the physical states

$$\Phi_1 = \frac{1}{\sqrt{2}} \begin{bmatrix} \sqrt{2} \left(G^+ \cos\beta - H^+ \sin\beta \right) \\ v\cos\beta + (-h\sin\alpha + H\cos\alpha) + i \left(G^0 \cos\beta - A^0 \sin\beta \right) \end{bmatrix},$$

$$\Phi_2 = \frac{1}{\sqrt{2}} \begin{bmatrix} \sqrt{2} \left(G^+ \sin\beta + H^+ \cos\beta \right) \\ v\sin\beta + (h\cos\alpha + H\sin\alpha) + i \left(G^0 \sin\beta - A^0 \cos\beta \right) \end{bmatrix}. \tag{3.36}$$

So far, we have neglected the rest of the scalar potential, which consists of the interactions amongst the scalars. Writing this term out in full would take the form

$$\mathcal{V}_{\text{interactions}} = C_{ijk}\varphi_i\varphi_j\varphi_k + C_{ijkl}\varphi_i\varphi_j\varphi_k\varphi_l \quad (\text{sum over } i,j,k,l \text{ implied}), \tag{3.37}$$

where: $\varphi_i = \{H^+, H^-, G^+, G^-, A, G^0, h, H\}$, and C_{ijk}, C_{ijkl} are the coefficients of the 3-scalar and 4-scalar couplings respectively. All couplings which violate CP or electric charge conservation are zero. It is possible to write the couplings as a function of the scalar masses (rather than the generic couplings λ_i), which gives somewhat simpler

expressions. We shall not carry out the full algebra here, but the results are listed in Refs [14, 41, 42].

3.7.2 Symmetry breaking in the scalar KED

Similar to the SM, the gauge-scalar interactions, and the gauge mass terms originate from the scalar KED. As usual, the Goldstone bosons can be eliminated with the appropriate choice of gauge (called the unitary gauge). In this gauge, the DOFs appear as longitudinal modes for the weak bosons. The scalar KED is

$$\mathcal{T}_{\text{Scalar}} \equiv (D^\mu \Phi_1)^\dagger (D_\mu \Phi_1) + (D^\mu \Phi_2)^\dagger (D_\mu \Phi_2). \tag{3.38}$$

Multiplying the covariant derivative with the Higgs doublets yields

$$D_\mu \Phi_i = \begin{bmatrix} \partial_\mu \varphi_i^+ + ((ig_2/\cos\theta_W)(1/2 - \sin^2\theta_W) Z_\mu + ieA_\mu) \varphi_i^+ + \left(ig/\sqrt{2}\right) W_\mu^+ \varphi_i^0 \\ \partial_\mu \varphi_i^0 + (ig_2/2\cos\theta_W) Z_\mu \varphi_i^0 + \left(ig/\sqrt{2}\right) W_\mu^- \varphi_i^+ \end{bmatrix}. \tag{3.39}$$

Next, we plug this into Equation 3.38 to get the interactions and gauge boson mass terms. We should also write the scalars in their mass basis using Equation 3.36. Expanding this out for just the mass terms yields

$$\mathcal{T}_{\text{Scalar}} = \frac{1}{2} (\partial_\mu \varphi_i)(\partial^\mu \varphi_i) + \frac{1}{4} g_2^2 \left(v_1^2 + v_2^2\right) W_\mu^+ W^{-\mu} + \frac{1}{4} \left(g_1^2 + g_2^2\right) \left(v_1^2 + v_2^2\right) Z_\mu Z^\mu$$
$$+ \mathcal{T}_{\text{interactions}}, \tag{3.40}$$

where $\varphi_i = \{h, H, A, H^\pm\}$. Note that we have prematurely rotated the W_i^μ and B^μ into the mass-eigenstates that were found for the SM. However, in the above equation there is no mixing amongst these fields and no mass term for A_μ and therefore the mass-eigenstates in the 2HDM are derived using the same rotation of the gauge mass matrix (c.f. Equation 2.46). We can read off the masses as

$$m_W^2 = \frac{g_2^2}{4} \left(v_1^2 + v_2^2\right) = \frac{g^2 v^2}{4},$$
$$m_Z^2 = \frac{g_1^2 + g_2^2}{4} \left(v_1^2 + v_2^2\right) = \frac{g_1^2 + g_2^2}{4} v^2. \tag{3.41}$$

$h^0 VV$	$\sin(\beta - \alpha)$
$H^0 VV$	$\cos(\beta - \alpha)$
$A^0 VV$	0

TABLE 3.5: Reduced gauge-scalar couplings, where $VV = W^+ W^-, ZZ$.

Looking back at the SM masses for these gauge bosons (see Equation 2.44), we can identify $v^2 = v_{SM}^2$, which justifies our choice of notation. So far, we have neglected the remainder of the scalar KED – which consists of gauge-scalar interactions. These terms take the generic form

$$\mathcal{T}_{\text{interactions}} = \mathcal{T}_{VVH} + \mathcal{T}_{VVHH} + \mathcal{T}_{VHH}, \tag{3.42}$$

$$H = \left\{ h, H, A, H^+, H^-, G^0, G^+, G^- \right\}, \quad V = \left\{ W^+, W^-, Z \right\}. \tag{3.43}$$

As usual, any term that violates charge or CP symmetries in the above expressions must vanish. We shall not do the full substitution here as the results are quite lengthy. All vertices are provided in Ref [14] using the physical basis. Alternatively, Ref [41] provides the vertices for the G2HDM using a basis-independent formalism (see also Ref [39]). The $\varphi_i W^+ W^-$ and $\varphi_i ZZ$ interactions are of high phenomenological importance, so we list the reduced couplings (g_{2HDM}/g_{SM}) for these in Table 3.5.

3.7.3 Higgs bases (Interlude)

Before continuing our investigation of symmetry breaking within the 2HDM, we first need to introduce Higgs bases; these make it easier to obtain the physical states and masses, and to identify scenarios with SM-like scalar structure. So far, we have been working with Higgs doublets in the generic ($\mathbb{Z}_2$ eigenstate) basis. A Higgs basis is by definition any basis in which the VEV appears only in the first doublet. It is related to the generic basis via [43]

$$H_1 \equiv \begin{bmatrix} H_1^+ \\ H_1^0 \end{bmatrix} \equiv (\Phi_1 \cos\beta + \Phi_2 \sin\beta),$$

$$H_2 \equiv \begin{bmatrix} H_2^+ \\ H_2^0 \end{bmatrix} \equiv e^{-i\chi_0} (-\Phi_1 \sin\beta + \Phi_2 \cos\beta), \tag{3.44}$$

which is unique up to an overall rephasing of H_2. Note that we have assumed that the relative complex phase of the VEVs is zero, i.e., the normal vacuum from Equation 3.27. [10] In the Higgs basis, the scalar potential takes the same form as the generic basis, except with new coefficients. The potential is given by

$$
\begin{aligned}
\mathcal{V} = {}& M_{11}^2 H_1^\dagger H_1 + M_{22}^2 H_2^\dagger H_2 - \left(M_{12}^2 H_1^\dagger H_2 + H.c. \right) \\
& + \frac{1}{2}\Lambda_1 \left(H_1^\dagger H_1 \right)^2 + \frac{1}{2}\Lambda_2 \left(H_2^\dagger H_2 \right)^2 + \Lambda_3 \left(H_1^\dagger H_1 \right)\left(H_2^\dagger H_2 \right) + \Lambda_4 \left(H_1^\dagger H_2 \right)\left(H_2^\dagger H_1 \right) \\
& + \left(\frac{1}{2}\Lambda_5 \left(H_1^\dagger H_2 \right)^2 + \left(\Lambda_6 \left(H_1^\dagger H_1 \right) + \Lambda_7 \left(H_2^\dagger H_2 \right) \right) H_1^\dagger H_2 + H.c. \right).
\end{aligned}
\tag{3.45}
$$

The parameters are related to the generic basis by

$$
\begin{aligned}
\Lambda_1 ={}& \lambda_1 \cos^4\beta + \lambda_2 \sin^4\beta + \frac{1}{2}\lambda_{345}\sin^2(2\beta) + 2\sin(2\beta)\left[\cos^2\beta\lambda_6 + \sin^2\beta\lambda_7\right], \\
\Lambda_2 ={}& \lambda_1 \sin^4\beta + \lambda_2 \cos^4\beta + \frac{1}{2}\lambda_{345}\sin^2(2\beta) - 2\sin(2\beta)\left[\sin^2\beta\lambda_6 + \cos^2\beta\lambda_7\right], \\
\Lambda_3 ={}& \frac{1}{4}\sin^2(2\beta)(\lambda_1 + \lambda_2 - 2\lambda_{345}) + \lambda_3 - \sin(2\beta)\cos(2\beta)(\lambda_6 - \lambda_7), \\
\Lambda_4 ={}& \frac{1}{4}\sin^2(2\beta)(\lambda_1 + \lambda_2 - 2\lambda_{345}) + \lambda_4 - \sin(2\beta)\cos(2\beta)(\lambda_6 - \lambda_7), \\
\Lambda_5 e^{-i\chi_0} ={}& \frac{1}{4}\sin^2(2\beta)(\lambda_1 + \lambda_2 - 2\lambda_{345}) + \lambda_5 - \sin(2\beta)\cos(2\beta)(\lambda_6 - \lambda_7), \\
\Lambda_6 e^{-i\chi_0} ={}& -\frac{1}{2}\sin(2\beta)\left(\lambda_1\cos^2\beta - \lambda_2\sin^2\beta - \lambda_{345}\cos(2\beta)\right) + \cos\beta\cos(3\beta)\lambda_6 + \sin\beta\sin(3\beta)\lambda_7 \\
\Lambda_7 e^{-i\chi_0} ={}& -\frac{1}{2}\sin(2\beta)\left(\lambda_1\sin^2\beta - \lambda_2\cos^2\beta + \lambda_{345}\cos(2\beta)\right) + \cos\beta\cos(3\beta)\lambda_7 + \sin\beta\sin(3\beta)\lambda_6
\end{aligned}
\tag{3.46}
$$

Under a rephasing of the second doublet, $H_2 \to e^{i\chi}H_2$, the parameters transform via

$$
\left[M_{12}^2, \Lambda_6, \Lambda_7 \right] \to e^{i\chi}\left[M_{12}^2, \Lambda_6, \Lambda_7 \right], \quad \Lambda_5 \to e^{-2i\chi}\Lambda_5.
\tag{3.47}
$$

For a CP-conserving potential, it can be shown that a basis exists that renders all parameters real and therefore we can restrict χ to be a multiple of π,

$$
\chi = n\pi, \quad n = 0, 1, 2, \dots
\tag{3.48}
$$

---

[10]In Ref [43] the Higgs basis is provided for the more general CP-violating VEV. In this case the Higgs basis parameters include complex terms arising from the relative phase difference ξ which we have set to zero.

This means that for an explicitly CP-conserving potential, there is only one unique transformation of the Higgs basis parameters that leads to the same phenomenology. The minimisation conditions from Equation 3.30 become

$$M_{11}^2 = -\frac{1}{2}\Lambda_1 v^2, \quad M_{12}^2 = \frac{1}{2}\Lambda_6 v^2. \tag{3.49}$$

The Higgs doublet components are rotated onto their mass eigenstates,

$$H_1 = \frac{1}{\sqrt{2}} \begin{bmatrix} \sqrt{2}G^+ \\ v + h_1' + iG^0 \end{bmatrix}, \quad e^{i\chi_0}H_2 = \frac{1}{\sqrt{2}} \begin{bmatrix} \sqrt{2}H^+ \\ h_2' + iA^0 \end{bmatrix}, \tag{3.50}$$

except for the CP-even scalars which remain mixed through an angle of $\beta - \alpha$,

$$\begin{bmatrix} H \\ h \end{bmatrix} = \begin{bmatrix} \cos(\beta - \alpha) & -\sin(\beta - \alpha) \\ \sin(\beta - \alpha) & \cos(\beta - \alpha) \end{bmatrix} \begin{bmatrix} h_1' \\ h_2' \end{bmatrix}. \tag{3.51}$$

This is why it is usually easier to work with doublets in the Higgs basis. In the alignment limit where $\cos(\beta - \alpha) = 0$, we find that $h_1' = h^0$, $h_2' = H^0$, and H_1 takes the same form as the SM Higgs doublet with h^0 corresponding to the SM Higgs boson. The Hidden-Higgs scenario is similar except that we instead have H^0 appearing in H_1. Hence, the heavier CP-even boson corresponds to the SM-Higgs boson.

3.7.4 Symmetry breaking in the Yukawa sector

The Yukawa sector is easier to analyse in the Higgs basis.[11] In the Higgs basis, we can write a simple set of interactions between the fermions and physical scalar states. Transforming the Yukawa sector from Equation 3.7 into the Higgs basis yields

$$\begin{aligned} -\mathcal{L}_{\text{Yukawa}} = & \bar{Q}_{i,L} \left(k_{ij}^u \widetilde{H}_1 + \xi_{ij}^u \widetilde{H}_2 \right) u_{j,R} + \bar{Q}_{i,L} \left(k_{ij}^d H_1 + \xi_{ij}^d H_2 \right) d_{j,R} \\ & + \bar{L}_{i,L} \left(k_{ij}^v \widetilde{H}_1 + \xi_{ij}^v \widetilde{H}_2 \right) v_{j,R} + \bar{L}_{i,L} \left(k_{ij}^e H_1 + \xi_{ij}^e H_2 \right) e_{j,R} \\ & + H.c., \end{aligned} \tag{3.52}$$

where the Higgs basis Yukawa matrices are related to those in the generic basis via

---

[11]See Ref [41] for a discussion of the most general Yukawa sector in a basis independent formalism.

$$k^f = Y^f \cos\beta + Y_2^f \sin\beta, \quad \xi^f = -Y_1^f \sin\beta + Y_2^f \cos\beta, \quad f = u, d, e, v. \tag{3.53}$$

We will assume that the unitary gauge has been applied. Hence, the Higgs doublets in the Higgs basis can be written

$$H_1 = \frac{1}{\sqrt{2}} \begin{bmatrix} 0 \\ \sin(\beta - \alpha)h + \cos(\beta - \alpha)H \end{bmatrix},$$

$$H_2 = \frac{1}{\sqrt{2}} \begin{bmatrix} \sqrt{2}H^+ \\ \cos(\beta - \alpha)h + \sin(\beta - \alpha)H + iA \end{bmatrix}. \tag{3.54}$$

In the SM, the generic and physical bases for fermions were related by the U^f and K^f matrices (cf. Equation 2.53). In the 2HDM, k^f takes the role of the SM Yukawa matrix, since it is multiplied by H_1 – which provides all the mass terms via v. Hence, using the same notation from Equation 2.51, the transformation to the physical basis looks like

$$\bar{Q}_{i,L} k_{ij}^d H_1 d_{j,R} = \begin{bmatrix} \left(\bar{u}_k U_{kn}^{U\dagger}\right) U_{ni}^U U_{il}^{D\dagger} \\ \left(\bar{d}_i U_{il}^{D\dagger}\right) \end{bmatrix}^T H_1 \left(U_{li}^D k_{ij}^d K_{jm}^{\dagger D}\right) \left(K_{mj}^D d_{j,R}\right)$$

$$\equiv \bar{Q}_{l,L} H_1 M_{lm}^D d_{m,R}, \tag{3.55}$$

where we also get a similar term for k^u, k^v, and k^e by transforming the other terms in Equation 3.52. Note that the M^f matrix is just given by

$$M^f = \frac{\sqrt{2}}{v} \operatorname{diag}\left(m_{f_1}, m_{f_2}, m_{f_3}\right), \quad f = u, d, e, v. \tag{3.56}$$

Also note that the l, m indices in Equation 3.55 are used to denote physical basis fermions[12], while i, j are used for the generic basis. Notice that we have used U_{li}^D (rather than U_{li}^U) in the definition of M^D as this matches the SM case. But in doing so, we have created a mess in the upper component of $\bar{Q}$. In fact, the upper components of $\bar{Q}$ (and $\bar{L}$) include an extra CKM (and PMNS) matrix defined in Equation 2.58 and restated below

$$V_{\text{PMNS}} \equiv U^E U^{V\dagger}, \quad V_{\text{CKM}} \equiv U^D U^{U\dagger}. \tag{3.57}$$

---

[12]Not to be confused with the scalar physical basis that was mentioned previously.

	Type-I	Type-II	Type-X	Type-Y
Up-type quarks	Φ_2	Φ_2	Φ_2	Φ_2
Down-type quarks	Φ_2	Φ_1	Φ_2	Φ_1
Charged leptons	Φ_2	Φ_1	Φ_1	Φ_2

TABLE 3.6: Fermion couplings for each doublet as a result of the $\mathbb{Z}_2$-representation assignments. Note that we do not consider Higgs couplings with neutrinos.

In the SM, the upper component of the Higgs doublet was zero, so we always pick out the lower component from $\bar{Q}_l$. This is also true here since the upper component of H_1 is zero. But when we consider H_2 below, we will find that interactions with H^+ include a CKM or PMNS matrix.

In general, the basis used to diagonalise k_{ij}^f will not simultaneously diagonalise ξ_{ij}^f. Therefore, we still have non-diagonal entries in ξ_{ij}^f which lead to FCNCs at tree-level. These are tightly limited by experiment, and not present in the SM at all. There are a few approaches that we can take to deal with these:

   I Assume that the 2HDM parameters are close to the decoupling limit, where the light CP-even scalar remains at the electroweak scale while the additional scalars appear at a much larger scale.

  II Assume that the Yukawa matrices in the generic basis are proportional, i.e., $Y_1^f = cY_2^f$, so that they are both diagonalised simultaneously. Hence, in the fermion mass basis there will be no FCNCs. The resulting 2HDM is called the *aligned 2HDM*. This could be a result of some symmetry or unknown flavour dynamics associated with a UV completion of the model [44].

 III Apply a theorem due to Glashow, Weinberg, and Paschos, which states that in a model with multiple Higgs doublets, tree-level FCNCs will be absent if all fermions of the same electric charge couple to no more than one Higgs doublet [45, 46].

In this work, we shall choose option III. This is achieved via the introduction of a $\mathbb{Z}_2$-symmetry where Φ_1 belongs to the odd representation while Φ_2 belongs to the even representation. We are free to choose whether up-quarks, down-quarks, and charged leptons belong to even/odd representations. The different choices lead to 4 different types of $\mathbb{Z}_2$-symmetric 2HDMs. In Table 3.6, we list which doublets each fermion couples to as a result of the $\mathbb{Z}_2$ assignments.

Since there are no FCNCs in the $\mathbb{Z}_2$-symmetric 2HDMs, ξ^f must be proportional to k^f. The constant of proportionality is denoted κ_f, resulting in

	Type-I	**Type-II**	**Type-X**	**Type-Y**
Γ_h^u		$\dfrac{\cos\alpha}{\sin\beta}$		
Γ_H^u		$\dfrac{\sin\alpha}{\sin\beta}$		
Γ_A^u		$\cot\beta$		
Γ_h^d	$\dfrac{\cos\alpha}{\sin\beta}$	$-\dfrac{\sin\alpha}{\cos\beta}$	$\dfrac{\cos\alpha}{\sin\beta}$	$-\dfrac{\sin\alpha}{\cos\beta}$
Γ_H^d	$\dfrac{\sin\alpha}{\sin\beta}$	$\dfrac{\cos\alpha}{\cos\beta}$	$\dfrac{\sin\alpha}{\sin\beta}$	$\dfrac{\cos\alpha}{\cos\beta}$
Γ_A^d	$-\cot\beta$	$\tan\beta$	$-\cot\beta$	$\tan\beta$
Γ_h^e	$\dfrac{\cos\alpha}{\sin\beta}$	$-\dfrac{\sin\alpha}{\cos\beta}$	$-\dfrac{\sin\alpha}{\cos\beta}$	$\dfrac{\cos\alpha}{\sin\beta}$
Γ_H^e	$\dfrac{\sin\alpha}{\sin\beta}$	$\dfrac{\cos\alpha}{\cos\beta}$	$\dfrac{\cos\alpha}{\cos\beta}$	$\dfrac{\sin\alpha}{\sin\beta}$
Γ_A^e	$-\cot\beta$	$\tan\beta$	$\tan\beta$	$-\cot\beta$

TABLE 3.7: Reduced fermion-scalar couplings for $\mathbb{Z}_2$-symmetric 2HDMs.

$$\xi^f = \kappa_f k^f. \tag{3.58}$$

Note that κ_f depends on the model type.[13] We can substitute Equations 3.58, 3.56 and 3.54 into the Yukawa Lagrangian to find the scalar couplings for each 2HDM. After carrying out the algebra, the result is

$$
\begin{aligned}
-\mathcal{L}_{\text{Yukawa}} =& \sum_{f=u,d,e,v} \frac{m_f}{v}\left(v\bar{f}f + \Gamma_h^f \bar{f}fh + \Gamma_H^f \bar{f}fH - i\Gamma_A^f \bar{f}\gamma_5 fA \right) \\
&+ \frac{\sqrt{2}}{v}\left(\bar{u}_l V_{lm}^{\text{CKM}}\left(\Gamma_A^d m_{d_m} P_R + \Gamma_A^u m_{u_m} P_L \right) d_m H^+ + H.c. \right) \\
&+ \frac{\sqrt{2}}{v}\left(\bar{v}_l V_{lm}^{\text{PMNS}}\left(\Gamma_A^E m_{e_l} P_R + \Gamma_A^N m_{v_l} P_L \right) e_l H^+ + H.c. \right),
\end{aligned}
\tag{3.59}
$$

where: $\Gamma_h^f = \sin(\beta-\alpha) + \kappa_f\cos(\beta-\alpha)$, $\Gamma_H^f = \cos(\beta-\alpha) - \kappa_f\sin(\beta-\alpha)$, $\Gamma_A^f = \kappa_f$.

In the SM, the Higgs couplings are given by m_f/v. In the above equation we notice that the various Γ factors are just reduced couplings, defined by the ratio: $g_{\varphi ii}^{\text{2HDM}}/g_{hii}^{\text{SM}}$. We list all reduced couplings in Table 3.7.

In the Type-I 2HDM, all h-fermion couplings take the same form, which we can write as

$$\kappa_h = \frac{\cos\alpha}{\sin\beta} = \sqrt{1 - \cos^2(\beta-\alpha)} + \frac{\cos(\beta-\alpha)}{\tan\beta}. \tag{3.60}$$

---

[13]It can be found by setting the appropriate Yukawa matrix in Equation 3.53 to zero, and eliminating the remaining unknown Yukawa matrix.

We see that in the alignment limit, where $\cos(\beta - \alpha) = 0$, the couplings of h are exactly SM-like and the couplings of H vanish. In the opposite case with $\cos(\beta - \alpha) = \pm 1$ we find that H is SM-like and couplings of h vanish.

Finally, we mention that the $\mathbb{Z}_2$-symmetry imposed on the Yukawa sector should also be extended to the scalar sector, otherwise the $\mathbb{Z}_2$-violating terms would result in large FCNCs at 1-loop level. This results in $\lambda_1 = \lambda_2 = 0$ for the generic basis and two extra conditions for the Higgs basis given at the end of Appendix E.6.

3.8 Conventions and basis independence

When selecting a set of parameter ranges, one problem that we face is that the parameter space is redundant, meaning that there are multiple ways of picking parameters that lead to the same phenomenology. This is because there is some basis transformation that relates such combinations of parameters. We would like to establish a set of conventions so that the parameters are well defined (they are upgraded to observables). We shall do this by artificially restricting the values that each redundant parameter may take. First, consider the Higgs basis where there is only one basis transformation in which we rephase the second doublet [47]. The Higgs basis parameters then transform via

$$\left[M_{12}^2, \Lambda_6, \Lambda_7\right] \to e^{i\chi}\left[M_{12}^2, \Lambda_6, \Lambda_7\right] \ , \quad \Lambda_5 \to e^{-2i\chi}\Lambda_5,$$
$$\text{under} \quad H_2 \to e^{i\chi}H_2. \tag{3.61}$$

However, we are only interested in CP-conserving 2HDMs, thus we restrict all parameters to be real. In this case, the only possible basis transformation is

$$\left[M_{12}^2, \Lambda_6, \Lambda_7\right] \to -\left[M_{12}^2, \Lambda_6, \Lambda_7\right] \qquad \text{under} \quad H_2 \to -H_2. \tag{3.62}$$

Note that M_{12}^2 and Λ_6 are not independent parameters as they are related via the minimisation conditions (c.f. Equation 3.49). So, in fact we only have one way to change parameters while keeping observables fixed. This can be done by flipping the sign of both Λ_6 and Λ_7 simultaneously.

The CP-even scalar fields, H and h, are only defined up to an overall sign. This is because the sign of each can be flipped via a sign change of $\sin(\beta - \alpha)$, $\cos(\beta - \alpha)$ or H_2. For example

$$\cos(\beta - \alpha) \to -\cos(\beta - \alpha),\ \sin(\beta - \alpha) \to -\sin(\beta - \alpha),\ H_2 \to +H_2 \implies H \to -H,\ h \to -h$$
$$\cos(\beta - \alpha) \to +\cos(\beta - \alpha),\ \sin(\beta - \alpha) \to -\sin(\beta - \alpha),\ H_2 \to -H_2 \implies H \to +H,\ h \to -h$$
$$\cos(\beta - \alpha) \to -\cos(\beta - \alpha),\ \sin(\beta - \alpha) \to +\sin(\beta - \alpha),\ H_2 \to -H_2 \implies H \to -H,\ h \to +h$$
$$(3.63)$$

This implies that $\beta - \alpha$ is only well defined modulo π. We are free to pick any interval of length π. In our convention we assume that

$$0 \le \beta - \alpha < \pi, \tag{3.64}$$

leading to

$$-1 \le \cos(\beta - \alpha) \le +1, \quad 0 \le \sin(\beta - \alpha) \le 1. \tag{3.65}$$

We can also see that the product $\sin(\beta - \alpha)\cos(\beta - \alpha)$ is a pseudo-invariant under $H_2 \to -H_2$.

In the process of diagonalizing the CP-even mass matrix in the Higgs basis, we can derive relationships between $\beta - \alpha$ and the parameters given by

$$\Lambda_1 v^2 = m_h^2 \sin^2(\beta - \alpha) + m_H^2 \cos^2(\beta - \alpha), \tag{3.66}$$
$$\Lambda_6 v^2 = \left(m_h^2 - m_H^2\right) \sin(\beta - \alpha)\cos(\beta - \alpha), \tag{3.67}$$
$$m_A^2 + \Lambda_5 v^2 = m_H^2 \sin^2(\beta - \alpha) + m_h^2 \cos^2(\beta - \alpha). \tag{3.68}$$

Since we choose h to be the lightest CP-even scalar, Equation 3.67 leads to the requirement that:

$$\Lambda_6 \sin(\beta - \alpha)\cos(\beta - \alpha) \le 0. \tag{3.69}$$

Furthermore, it can be shown that $\tan\beta$ changes sign under $H_2 \to -H_2$. We shall pick a convention where $\tan\beta$ is positive, which fixes the sign of H_2. Using the above equation,

Λ_6 is fixed by our conventions (and also Λ_7 since $\Lambda_6\Lambda_7$ is an invariant). We can then derive the expressions

$$\cos(\beta - \alpha) = -sgn(\Lambda_6)\sqrt{\frac{\Lambda_1 v^2 - m_h^2}{m_H^2 - m_h^2}},$$

$$\sin(\beta - \alpha) = \sqrt{\frac{m_H^2 - \Lambda_1 v^2}{m_H^2 - m_h^2}}. \tag{3.70}$$

3.9 Inert models

Before closing this chapter, we briefly comment on how the Inert Doublet Model (IDM) differs from the 2HDM [48–50]. The IDM is a 2HDM with an exact $\mathbb{Z}_2$-symmetry, which implies that the lightest $\mathbb{Z}_2$-odd particle is stable and therefore a potential DM candidate.[14] Previously, we kept m_{12}^2 as a soft $\mathbb{Z}_2$-violating parameter but now we must set it to zero. Of course, the hard $\mathbb{Z}_2$-violating parameters, λ_6 and λ_7, are also fixed to zero. These are the only changes made to the scalar potential from Equation 3.9.

We desire a set of physical states that respect the $\mathbb{Z}_2$-symmetry; this requires either $v_1 = 0$ or $v_2 = 0$. The choice is arbitrary but to be consistent with literature we choose $v_2 = 0$. This results in $v_1 = v$ and $\tan\beta = 0$. With this convention, the first doublet becomes SM-like while the second is known as the inert doublet. The doublets can be written in terms of the physical states quite simply as

$$\Phi_1 = \frac{1}{\sqrt{2}}\begin{bmatrix} \sqrt{2}G^+ \\ v_1 + h + iG^0 \end{bmatrix}, \quad \Phi_2 = \frac{1}{\sqrt{2}}\begin{bmatrix} \sqrt{2}H^+ \\ H + iA \end{bmatrix}. \tag{3.71}$$

We now only have 1 vacuum minimisation condition given by

$$m_{11}^2 + \frac{\lambda_1}{2}v_1^2 = 0. \tag{3.72}$$

We also desire the $\mathbb{Z}_2$-symmetry to be preserved in the Yukawa sector. We discussed this previously for the 2HDM which lead to the 4 2HDM types in Table 3.6. However, if we were to select a generation of fermions to couple to the inert doublet then this generation would remain massless. Hence, we choose all fermions to couple with the SM-like doublet. This corresponds to a Type-I 2HDM but the convention differs from Table 3.6 (where

---

[14]This symmetry is sometimes called the D-symmetry, but we will keep calling it the $\mathbb{Z}_2$-symmetry since there are no other $\mathbb{Z}_2$ symmetries that we consider in the IDM.

all fermions coupled to the second doublet). Instead, we have a convention where all fermions couple to only the first doublet.[15]

Switching between the doublet conventions, i.e. $\Phi_1 \leftrightarrow \Phi_2$, results in the parameter transformations

$$
\begin{aligned}
m_{11}^2 &\to m_{22}^2, \quad m_{22}^2 \to m_{11}^2, \quad m_{12}^2 \to \left(m_{12}^2\right)^*, \\
\lambda_1 &\to \lambda_2, \quad \lambda_2 \to \lambda_1, \quad \lambda_5 \to \lambda_5^*, \quad \lambda_6 \to \lambda_6^*, \quad \lambda_7 \to \lambda_7^*, \\
Y_{d1} &\to Y_{d2}^*, \quad Y_{d2} \to Y_{d1}^*, \quad Y_{u1} \to Y_{u2}^*, \quad Y_{u2} \to Y_{u1}^*, \quad Y_{e1} \to Y_{e2}^*, \quad Y_{e2} \to Y_{e1}^*, \\
v_1 &\to v_2, \quad v_2 \to v_1, \quad \tan\beta \to 1/\tan\beta, \quad \alpha \to \alpha - \pi/2.
\end{aligned}
\tag{3.73}
$$

Here we have listed the most general transformation in the 2HDM – which also applies for the IDM.

We can obtain the masses by substituting Equation 3.71 into the scalar potential, resulting in

$$
\begin{aligned}
m_h^2 &= v^2 \lambda_1, \\
m_H^2 &= \frac{1}{2} v^2 \bar{\lambda}_{345} + m_{22}^2, \\
m_A^2 &= \frac{1}{2} v^2 \lambda_{345} + m_{22}^2, \\
m_{H^+}^2 &= \frac{1}{2} v^2 \lambda_3 + m_{22}^2,
\end{aligned}
\tag{3.74}
$$

where $\lambda_{345} \equiv \lambda_3 + \lambda_4 + |\lambda_5|$ and $\bar{\lambda}_{345} \equiv \lambda_3 + \lambda_4 - |\lambda_5|$. Here we have used the vacuum minimisation condition (Equation 3.72) to eliminate m_{11}^2. Notice that λ_2 is not related to the masses at all, while λ_1 and m_h are decoupled from the other masses and are only related to each other.

In doing this substitution, we also justify our assumption that the physical states appear in the doublets, as in Equation 3.71. Note that the conventions for the scalars differ in the IDM. In the 2HDM we had two CP-even scalars that were mixed together via $\cos(\alpha - \beta)$, and a CP-odd scalar A. There is nothing to differentiate the CP-even scalars apart from their mass, so we picked a convention where $m_h < m_H$. This is different in the IDM since h is $\mathbb{Z}_2$-even while H and A are both $\mathbb{Z}_2$-odd. Therefore, we do not have

---

[15]It should be clarified – we are not saying that the choice of whether fermions couple to Φ_1 or Φ_2 is equivalent. Only that that we are free to choose which is the inert doublet and which is the SM-like doublet. In either case fermions couple to the SM-like doublet.

$m_h < m_H$ in general. In fact, h just corresponds to the SM Higgs – by which we mean that it has identical couplings to all SM particles. The λ_1 parameter just corresponds to the SM Higgs coupling, λ. Furthermore, while H and A are relatively CP-odd, their actual CP-state is arbitrary since there are no A-fermion or H-fermion interactions that could determine it. We can consider the IDM to have two separate CP symmetries.

We can also derive equations to calculate the couplings from the masses. These are given by

$$
\begin{aligned}
\lambda_1 &= m_h^2/v^2, \\
\lambda_3 &= 2\left(m_{H^+}^2 - m_{22}^2\right)/v^2, \\
\lambda_4 &= \left(m_H^2 + m_A^2 - 2m_{H^+}^2\right)/v^2, \\
\lambda_5 &= -\left|m_H^2 - m_A^2\right|/v^2.
\end{aligned}
\tag{3.75}
$$

We can also find the scalar-scalar and scalar-gauge couplings by substituting Equation 3.71 into the scalar potential and scalar KED respectively. These couplings are much simpler for the IDM, compared to the 2HDM, and we therefore list all of them in Table 3.8. Here we notice that all h-DM couplings depend on either λ_3, λ_{345}, or $\bar{\lambda}_{345}$, and all DM-DM interactions depend on only λ_2. We do not list the scalar-fermion couplings since they are just the same Higgs-fermion couplings in the SM.

Since the IDM has an exact $\mathbb{Z}_2$ symmetry, the lightest $\mathbb{Z}_2$-odd particle must be stable. This may be either H, A or H^+. Since we would like this to be a DM candidate, we must reject points where H^+ is the lightest of the three. Such a charged DM candidate interacts with photons and therefore would not be dark! We may take either H or A as the DM candidate, however the choice is arbitrary since the two particles switch roles roles under $\lambda_5 \to -\lambda_5$. To avoid this redundancy, we take H to be the DM candidate and fix $\lambda_5 < 0$. This results in $m_H < m_A$ and $m_H < m_{H^+}$. This is the reason why we used the absolute value of λ_5 in the previous equations.

In the IDM we have 5 free parameters, which we may choose to be $\lambda_2, \ldots, \lambda_5$ and m_{22}^2. The λ_1 and m_{11}^2 parameters are constant since these are related to SM-like Higgs mass which was measured to be 125 GeV, while v corresponds to v_{SM} with an experimental value of 246 GeV.

	$C\left[hhh\right]$	$6i\lambda_1 v$
	$C\left[hhhh\right]$	$6i\lambda_1$
	$C\left[hHH\right]$	$i\lambda_{345} v$
	$C\left[hhHH\right]$	$i\lambda_{345}$
	$C\left[hAA\right]$	$i\bar{\lambda}_{345} v$
	$C\left[hhAA\right]$	$i\bar{\lambda}_{345}$
	$C\left[hH^+H^-\right]$	$i\lambda_3 v$
	$C\left[hhH^+H^-\right]$	$i\lambda_3$
Scalar-Scalar	$C\left[HHHH\right]$	$6i\lambda_2$
	$C\left[AAAA\right]$	$6i\lambda_2$
	$C\left[H^+H^-H^+H^-\right]$	$4i\lambda_2$
	$C\left[HHAA\right]$	$2i\lambda_2$
	$C\left[HHH^+H^-\right]$	$2i\lambda_2$
	$C\left[AAH^+H^-\right]$	$2i\lambda_2$
	$C\left[hZ_\mu Z_v\right]$	$-igm_W\eta_{\mu v}$
	$C\left[hW_\mu^+W_v^-\right]$	$-igm_W\eta_{\mu v}$
	$C\left[hhZ_\mu Z_v\right]$	$\frac{ig^2}{2}\eta_{\mu v}$
	$C\left[hhW_\mu^+W_v^-\right]$	$\frac{ig^2}{2}\eta_{\mu v}$
	$C\left[HHZ_\mu Z_v\right]$	$\frac{ig^2}{2}\eta_{\mu v}$
	$C\left[HHW_\mu^+W_v^-\right]$	$\frac{ig^2}{2}\eta_{\mu v}$
	$C\left[AAZ_\mu Z_v\right]$	$\frac{ig^2}{2}\eta_{\mu v}$
Scalar-Gauge	$C\left[AAW_\mu^+W_v^-\right]$	$\frac{ig^2}{2}\eta_{\mu v}$
	$C\left[H^+H^-Z_\mu Z_v\right]$	$2ie^2\cot\left(2\theta_W\right)\eta_{\mu v}$
	$C\left[H^+H^-W_\mu^+W_v^-\right]$	$\frac{ig^2}{2}\eta_{\mu v}$
	$C\left[H^+H^-A_\mu A_v\right]$	$2ie^2\eta_{\mu v}$
	$C\left[H^+H^-A_\mu Z_v\right]$	$-2ie^2\cot^2\left(2\theta_W\right)\eta_{\mu v}$
	$C\left[H^\pm AW_\mu^\mp A_v\right]$	$\pm\frac{1}{2}g^2\sin\left(\theta_W\right)\eta_{\mu v}$

TABLE 3.8: Scalar-scalar and scalar-gauge couplings in the IDM. We do not list the Goldstone or ghost couplings here but they can be found in Ref [14].

Chapter 4

Constraints

We outline the theoretical and experimental constraints on the THDMs below. Theoretical constraints determine whether a given set of parameters leads to a valid theory, whereas experimental constraints determine how favourable the parameters are based on experimental evidence.

4.1 Theoretical Constraints

4.1.1 Vacuum Stability

The lowest-energy state in a QFT is known as the vacuum state and corresponds to the minimum of the potential. The potential of our theory must have a global minimum so that a stable vacuum exists. In this section we derive the conditions required for a stable vacuum.

Weak versus strong stability conditions

Given a 2HDM potential with some parameter values, vacuum stability requires that it is bounded from below in all regions of field space. Since our 2HDM potential is a polynomial function of the fields Φ_i, vacuum stability can be guaranteed simply by requiring that the potential is positive as the fields go to infinity for all directions in field space. This is easier to analyse if we use a radial parameterisation of our potential [51], given by

$$|\Phi_1| = r\cos\gamma, \quad |\Phi_2| = r\sin\gamma, \quad \frac{\Phi_2^\dagger \Phi_1}{|\Phi_1|\,|\Phi_2|} = \rho e^{i\theta}, \tag{4.1}$$

where we use the following ranges for our radial parameters

$$r \geq 0, \quad \gamma \in [0, \pi/2], \quad \rho \in [0, 1], \quad \theta \in [0, 2\pi). \tag{4.2}$$

In this notation, the potential takes the form

$$\mathcal{V} = r^2 \mathcal{V}_2 + r^4 \mathcal{V}_4, \tag{4.3}$$

where

$$\mathcal{V}_2\left(m_{ij}^2\right) = m_{11}^2 r^2 \cos^2 \gamma + m_{22}^2 r^2 \sin^2 \gamma - 2m_{12}^2 r^2 \cos \gamma \sin \gamma \rho \cos \theta \tag{4.4}$$

$$\mathcal{V}_4\left(\lambda_i\right) = \frac{1}{2}\lambda_1 \cos^4 \gamma + \frac{1}{2}\lambda_2 \sin^4 \gamma + \lambda_3 \cos^2 \gamma \sin^2 \gamma + \lambda_4 \rho^2 \cos^2 \gamma \sin^2 \gamma$$
$$+ \lambda_5 \rho^2 \cos(2\theta) \cos^2 \gamma \sin^2 \gamma + 2\lambda_6 \rho \cos \theta \cos^3 \gamma \sin \gamma + 2\lambda_7 \rho \cos \theta \cos \gamma \sin^3 \gamma. \tag{4.5}$$

Assuming that $\mathcal{V}_4\left(\gamma, \rho, \theta\right) \neq 0$, the quartic term will dominate as $r \to \infty$, and the vacuum will be stable if $\mathcal{V}_4 > 0$. This is known as the strong stability requirement [37]. If $\mathcal{V}_4 = 0$ for some direction in field space, we still have a stable vacuum so long as $\mathcal{V}_2 > 0$. We can write these conditions as

$$\min_{\{\gamma,\rho,\theta\}} \mathcal{V}_4\left(\lambda_i\right) > 0 \ or \ \min_{\{\gamma,\rho,\theta\}} \mathcal{V}_4\left(\lambda_i\right) \geq 0, \ \min_{\{\gamma,\rho,\theta\}} \mathcal{V}_2\left(m_{ij}^2\right) > 0. \tag{4.6}$$

In what follows, we shall only check the strong stability requirement. This means that we are being overly restrictive.

Stability conditions using the radial parameterisation

While the full stability condition requires checking the minimum with respect to all directions of field space, we can derive some very simple conditions by checking specific field directions [51]. For example

$$\mathcal{V}_4\left(\gamma = 0\right) = \frac{1}{2}\lambda_1 > 0, \tag{4.7}$$

$$\mathcal{V}_4\left(\gamma = \pi/2\right) = \frac{1}{2}\lambda_2 > 0, \tag{4.8}$$

$$\mathcal{V}_4\left(\rho = 0\right) = \frac{1}{2}\lambda_1 \cos^4 \gamma + \frac{1}{2}\lambda_2 \sin^4 \gamma + \lambda_3 \cos^2 \gamma \sin^2 \gamma > 0, \tag{4.9}$$

$$\mathcal{V}_4\left(\rho=1, \theta=\pi/2\right) = \frac{1}{2}\lambda_1\cos^4\gamma + \frac{1}{2}\lambda_2\sin^4\gamma + (\lambda_3+\lambda_4-\lambda_5)\cos^2\gamma\sin^2\gamma > 0. \quad (4.10)$$

The third and fourth conditions are both minimised for $\tan^2\gamma = \sqrt{\lambda_1/\lambda_2}$ and thus the conditions on our parameters are

$$\lambda_3 > -2\sqrt{\lambda_1\lambda_2}\,, \quad \lambda_3+\lambda_4-\lambda_5 > -2\sqrt{\lambda_1\lambda_2}. \quad (4.11)$$

So far we have not assumed a specific 2HDM potential. Now consider a potential where $\lambda_6, \lambda_7 = 0$. In this case the quartic terms become

$$\mathcal{V}_4\left(\lambda_i\right) = \frac{1}{2}\lambda_1\cos^4\gamma + \frac{1}{2}\lambda_2\sin^4\gamma + \lambda_3\cos^2\gamma\sin^2\gamma$$
$$+ \lambda_4\rho^2\cos^2\gamma\sin^2\gamma + \lambda_5\rho^2\cos(2\theta)\cos^2\gamma\sin^2\gamma, \quad (4.12)$$

which can be written as

$$\mathcal{V}_4 = \lambda_1\cos^4\gamma + \lambda_2\sin^4\gamma + \Lambda\cos^2\gamma\sin^2\gamma > 0, \quad \Lambda \equiv \left(\lambda_3 + \lambda_4\rho^2 + \lambda_5\rho^2\cos(2\theta)\right). \quad (4.13)$$

Recognising that this takes the same form as Equation 4.9, this leads to the condition

$$\Lambda > -2\sqrt{\lambda_1\lambda_2}, \quad (4.14)$$

and therefore we have

$$\lambda_3 + \lambda_4 - |\lambda_5| > -2\sqrt{\lambda_1\lambda_2}. \quad (4.15)$$

While these are necessary conditions for vacuum stability, we still have not proven whether they are sufficient since we did not consider all directions in field space. It turns out that these conditions (Equations 4.7, 4.8, 4.11, and 4.15) are sufficient for the $\mathbb{Z}_2$-symmetric model. We prove this using a different approach in Appendix F. For the general 2HDM, we still need three more sets of conditions arising from the boundaries $\cos\theta = \pm 1$, $\rho = 1$. Unfortunately, these do not have a simple form [52].

4.1.2   Vacuum meta-stability

We also require the VEV to correspond to the global minimum, rather than a local minimum. If a deeper vacuum exists then we have the possibility of quantum tunnelling

to the true vacuum, leading to a phase transition. The conditions for multiple normal minima are[1]

$$m_{11}^2 + k^2 m_{22}^2 < 0, \quad x^{2/3} + y^{2/3} \leq 1, \tag{4.16}$$

where

$$k = (\lambda_1/\lambda_2)^{1/4},$$

$$x = \frac{4k\, m_{12}^2}{m_{11}^2 + k^2\, m_{22}^2} \frac{\sqrt{\lambda_1 \lambda_2}}{\lambda_{345} - \sqrt{\lambda_1 \lambda_2}}, \tag{4.17}$$

$$y = \frac{m_{11}^2 - k^2\, m_{22}^2}{m_{11}^2 + k^2\, m_{22}^2} \frac{\sqrt{\lambda_1 \lambda_2} + \lambda_{345}}{\sqrt{\lambda_1 \lambda_2} + \lambda_{345}}. \tag{4.18}$$

Then if more than one minimum exists, the inequality

$$D = m_{12}^2 \left(m_{11}^2 - k^2 m_{22}^2\right)(\tan\beta - k) < 0, \tag{4.19}$$

can be used to determine if our VEV corresponds to the deepest minimum. In other words, if $D < 0$, our vacuum is meta-stable.

4.1.2.1 Vacuum stability in the IDM

The vacuum stability constraints given above are not applicable to the IDM. The problem stems from the fact that there is only a single vacuum minimisation condition (c.f. Equation 3.72). Re-deriving these expressions for the IDM yields

$$m_{22}^2 < \begin{cases} R\, m_{11}^2 \sqrt{\lambda_1/\lambda_2}, & \text{if } |R| < 1, \\ m_{11}^2 \sqrt{\lambda_1/\lambda_2}, & \text{if } R > 1, \end{cases}$$

where

$$R \equiv \lambda_{345}/\sqrt{\lambda_1 \lambda_2}. \tag{4.20}$$

The absence of a charge-breaking vacuum is guaranteed by

$$\lambda_4 - |\lambda_2| < 0. \tag{4.21}$$

---

[1] we only have the possibility of tunnelling between normal minima.

This is a sufficient but not necessary condition for the vacuum to be neutral. A neutral vacuum can also be achieved for positive $\lambda_4 - |\lambda_2|$. However, in this case the lightest DM candidate will be the charged scalar, which we do not consider in this thesis anyway.

4.1.3 Perturbativity of the couplings

When calculating observables we rely on perturbation theory, which assumes that the matrix elements can be written as a series that gets progressively smaller at larger orders of the couplings λ_i, and thus allows us to consider only the leading terms.

If $|\lambda/4\pi| \geq 1$ then the series does not converge (it is known as strongly coupled), and the perturbation theory is not valid. Even for values less than 1, the series may still not converge, or we may not have enough terms for our approximation to be valid. When multiple couplings are present, the cut-off is lower, but a suitable value is not obvious, so we use a conservative value of 1. This leads to a limit on the 2HDM generic couplings given by

$$|\lambda_i(m_Z)| < 4\pi, \quad i = 1, \ldots, 7. \tag{4.22}$$

This is enforced in the generic basis by the parameter ranges (at least for the input scale which we set to m_Z). We may improve this constraint further by considering all 4-scalar couplings. This leads to the constraint

$$\left| C_{\varphi_i \varphi_j \varphi_k \varphi_l} \right| < 4\pi, \quad \varphi_i = h^0, H^0, A^0, H^+, H^-. \tag{4.23}$$

Extending this constraint to the Yukawa sector leads to the requirement that all Yukawa couplings are less than $\sqrt{4\pi}$.

4.1.4 Perturbativity of the scalar masses

When we renormalise the 2HDM spectrum, we have the running scalar masses calculated at $Q_{\text{in}} = m_Z$ as well as the pole masses. To ensure that the corrections to the masses remain perturbative, we place an upper limit. The pole mass for some scalar ϕ is given by

$$m_\phi = \overline{m}_\phi(m_Z) + \Sigma(m_\phi), \tag{4.24}$$

where $\overline{m}_\phi(m_Z)$ is the running mass and $\Sigma(m_\phi)$ contains the corrections. We choose a cut-off such that the corrections are less than half the running mass, i.e.

$$\Sigma(m_\phi) < \frac{1}{2}\overline{m}_\phi(m_Z). \tag{4.25}$$

4.1.5 S-Matrix Unitarity

Given some initial state $|i\rangle$ we determine the final state $|f\rangle$ using the scattering operator $|f\rangle = S|i\rangle$, and we obtain the scattering matrix elements via $S_{fi} = \langle f|S|i\rangle$. We require probability current to be conserved, and therefore that S_{fi} is unitary. If unitarity is violated, then the theory is non-perturbative, and some high-energy new physics must appear to restore the unitarity. We assume that the 2HDM is weakly coupled and therefore unitarity should be satisfied at all orders.[2] To derive the unitarity conditions [52–55], we first separate the scattering operator as: $S = I + iT$ and write the amplitude T as a sum of partial waves, i.e.

$$T_{fi}(s,t,u) = \sum_{l=0}^{\infty} 16\pi(2l+1)a_l(s)P_l(\cos\theta). \tag{4.26}$$

Here s,t,u are the Mandelstam variables[3], $P_l(x)$ is the l-th Legendre polynomial and a_l are called the partial wave amplitudes.[4] We shall only consider 2-particle to 2-particle scattering processes. Now, the differential cross-section for a two-body elastic scattering process is given by

$$\frac{d\sigma}{d\Omega} = \frac{1}{64\pi^2 s}|T|^2. \tag{4.27}$$

Using the orthogonality relation for the Legendre polynomials, we can solve for the cross-section. The result is

$$\sigma = \frac{16\pi}{s}\sum_{l=0}^{\infty}(2l+1)|a_l|^2. \tag{4.28}$$

The optical theorem, given by

---

[2]In a strongly-coupled theory the S-matrix contributions may be arbitrarily large, but cancel in the full sum.

[3]Given by $s = (p_1 + p_2)^2$, $t = (p_1 - p_3)^2$, $u = (p_1 - p_4)^2$.

[4]a_0 is called the S-wave amplitude.

$$\sigma = \frac{16\pi}{s} \sum_{l=0}^{\infty} (2l+1) \operatorname{Im}(a_l), \tag{4.29}$$

relates the cross section to the forward scattering amplitude. Combining this with the previous expression for the scattering cross-section, we get

$$|a_l|^2 = \operatorname{Im}(a_l), \ \forall l,$$
$$\operatorname{Re}(a_l)^2 + \operatorname{Im}(a_l)^2 = \operatorname{Im}(a_l), \quad \forall l. \tag{4.30}$$

This is nothing but the equation of a circle with radius $\frac{1}{2}$ and centre $(0, 1/2)$. We see that at leading order (where $\operatorname{Im}(a_l) = 0$)

$$|\operatorname{Re}(a_l)| < \frac{1}{2}. \tag{4.31}$$

Starting from our original equation and using orthogonality of the partial waves, we can solve for $a_l(s)$, leaving us with

$$a_l(s) = \frac{1}{32\pi} \int_{-1}^{1} d(\cos\theta) P_l(\cos\theta) \mathcal{M}(s,t,u). \tag{4.32}$$

We shall only consider the tree-level $J = 0$ s-wave amplitude in the high-energy limit. We can show that the s-wave amplitude takes the form

$$a_0(s) = \frac{1}{16\pi} \left[Q + T_h^{12} T_h^{34} \frac{1}{s - M_h^2} - \frac{1}{s} \left(c_t T_h^{13} T_h^{24} + c_u T_h^{14} T_h^{23} \right) ln\left(1 + \frac{2}{m_h^2}\right) \right]. \tag{4.33}$$

The first term in the brackets is the contribution of the quartic coupling to the amplitude, the second is the contribution of the s-channel diagram and the third term is the contribution from the t and u channels. In very high energy collisions, it can be shown that the dominant contribution is the one which is mediated by the quartic coupling, Q. Those contributions mediated by trilinear couplings are suppressed on dimensional grounds. Hence, the unitarity constraint reduces to the following constraint on the quartic coupling

$$|Q(S_1 S_2 S_3 S_4)| \leq 8\pi. \tag{4.34}$$

We can construct a scattering matrix with a variety of processes and consider the unitarity requirement for each of these. We shall consider all four-scalar couplings in the 2HDM. Deriving the four-scalar couplings in the mass basis in terms of λ_i, α, β is very-complicated. As shown by [56] making a clever choice of basis makes the process much simpler[5], enabling us to derive analytic expressions for the constraints on λ_i. The S-matrix eigenvalues take the form

$$
\begin{aligned}
\Lambda_{21\pm}^{\text{even}} &= \frac{1}{2}\left(\lambda_1 + \lambda_2 \pm \sqrt{(\lambda_1 - \lambda_2)^2 + 4\left|\lambda_5\right|^2}\right), \\
\Lambda_{21}^{\text{odd}} &= \frac{1}{16\pi}\lambda_3 + \lambda_4, \\
\Lambda_{20}^{\text{odd}} &= \lambda_3 - \lambda_4, \\
\Lambda_{01\pm}^{\text{even}} &= \frac{1}{2}\left(\lambda_1 + \lambda_2 \pm \sqrt{(\lambda_1 - \lambda_2)^2 + 4\lambda_4^2}\right), \\
\Lambda_{01\pm}^{\text{odd}} &= \lambda_3 \pm \left|\lambda_5\right|, \\
\Lambda_{00\pm}^{\text{even}} &= \frac{1}{2}\left(3\left(\lambda_1 + \lambda_2\right) \pm \sqrt{9\left(\lambda_1 - \lambda_2\right)^2 + 4\left(2\lambda_3 + \lambda_4\right)^2}\right), \\
\Lambda_{00\pm}^{\text{odd}} &= \lambda_3 + 2\lambda_4 \pm 3\left|\lambda_5\right|,
\end{aligned}
\tag{4.35}
$$

where we have used the notation from Ref [57] (which also applies for complex λ_5). The unitarity constraint is implemented simply by requiring that each eigenvalue is less than 8π.[6]

In our code we consider eigenvalues at next-to-leading-order (NLO) where the unitarity constraint is $|a_0 - i/2| \leq 1/2$. These were taken from [58]. We also include the wave-function corrections, and gauge coupling & Yukawa corrections from [59–61]. The NLO unitarity constraint is much stronger than LO.

4.2   Collider Constraints

Particle collider experiments use electromagnetic fields to propel charged particles to high energies, where they are then smashed into a stationary target or a beam in the

---

[5]To see how, first observe that that the Lagrangian is invariant under the symmetries: $\mathbb{Z}_2 : \Phi_2 \to -\Phi_2$, $CP : \Phi \to \Phi^\dagger$, $Y_\pi : \Phi_i \to e^{i\pi/2}\Phi_i$, and $G : \Phi_i \to e^{i\pi\sigma_2/2}\Phi_i^\dagger$. Rather than constructing two particle states out of $h, H, A, H^\pm, G^\pm, G^0$, an easier approach is to construct a basis of eigenstates of the aforementioned symmetries, since the S-matrix would be block diagonal in this case (with 9 blocks) [56].

[6]Note that this LO unitarity constraint is not necessary when using the perturbativity constraint, since the scalar couplings are also limited by the perturbativity constraint. But in that case, they were limited to 4π – making perturbativity more restrictive.

opposite direction. If enough energy is available, the particles may produce exotic heavy particles which are then detected via their decay signatures [2, 62].

In recent years, the main goal of these experiments has been to search for the SM Higgs boson. The Large Electron-Positron Collider (LEP) was the largest lepton collider ever built. It was dismantled in 2001 to make space for the LHC. Although it did not discover the Higgs boson, it did place a lower bound on the Higgs mass of 114 GeV. The Tevatron experiment, which was active up until 2011, also excluded various mass regions. The Large Hadron Collider (LHC), which primarily collides proton beams, is the largest particle collider ever built. The Higgs boson was first detected in 2012 by the ATLAS and CMS detectors at the LHC. The mass was determined to be 125 GeV, and limits have been placed on its couplings. So far, no significant deviation from the SM predictions has been observed. However, there still remains a possibility that it is part of an extended scalar sector of some BSM theory.

4.2.1   Higgs production and decay at particle colliders

Higgs searches at particle colliders detect processes like $X \to h \to Y$ where X are a set of particles that interact to produce a Higgs boson and Y are the decay products. Only the decay products are seen by the detector itself. At hadron colliders, the main production channels are: gluon-gluon fusion (ggF), vector boson fusion (VBF), associated production with a vector boson (VH) and associated production with top quarks (tth). Examples of leading-order diagrams are given in Figure 4.1.[7]

Important decay products include: $\gamma\gamma$, WW, ZZ, $Z\gamma$, gg, $\tau\tau$, cc, $\mu\mu$, and bb. Note that the decays to $\gamma\gamma$ and $Z\gamma$ occur at 1-loop level (see Figure 4.2) and are therefore suppressed. But they are still important due to the low backgrounds in the γ channels.

The fermion-scalar and gauge-scalar couplings determine the values of the cross-sections and decay rates for the above processes. The reduced couplings for all 2HDM types were given in Tables 3.7 and 3.5. In Equation 3.60, we showed that these couplings depend on two parameters at tree-level: $\tan\beta$ and $\cos(\beta - \alpha)$. The parameters m_{12}^2 and m_{H+} also enter due to loop effects. Since the SM is in excellent agreement with the experimental data, we expect reduced couplings involving h to be close to 1 while those involving H to be close to zero.

The couplings are also directly related to the mass of the particle involved, so heavier particles have stronger couplings to the Higgs boson. For example, the *htt* coupling is

---

[7]In hadron colliders, partons (quarks and gluons) are involved in the initial state, since these are found inside protons. We need information about the position and momentum distribution of such partons within their parent hadron, which are obtained from parton distribution functions.

(A) Gluon-gluon fusion: $gg \rightarrow h$

(B) Associated production with top quarks: $qq \rightarrow tth$

(C) Vector boson fusion: $qq \rightarrow qq^*h$

(D) Associated production with a gauge boson: $gg \rightarrow hZ$

(E) Associated production with a gauge boson: $qq \rightarrow hV$

(F) Associated production with a single top quark: $qq \rightarrow tbh$

(G) Associated production with top quarks: $gg \rightarrow tth$

(H) Associated production with a top and W: $gb \rightarrow tWh$
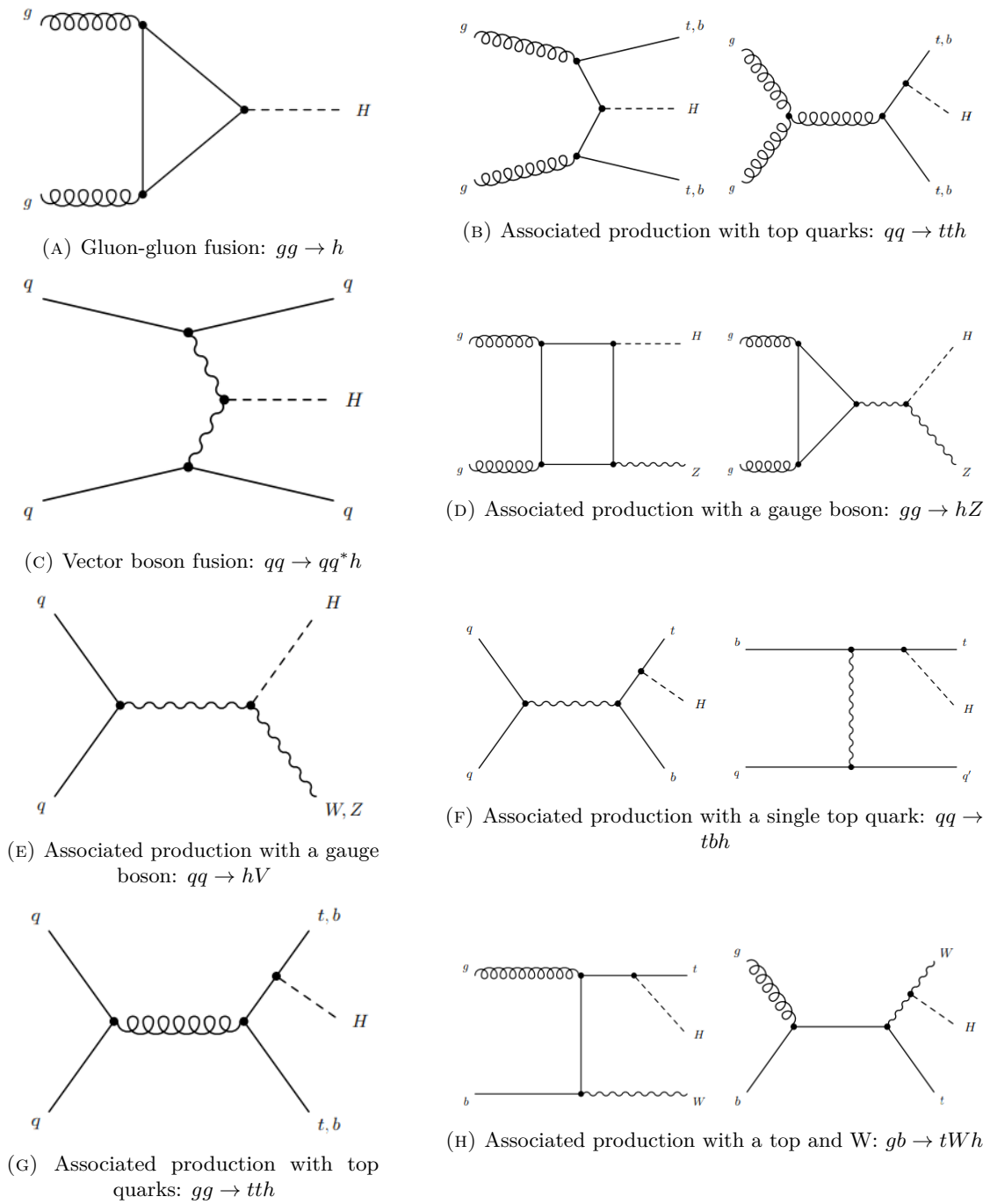
FIGURE 4.1: Leading order diagrams for the Higgs production channels [2].
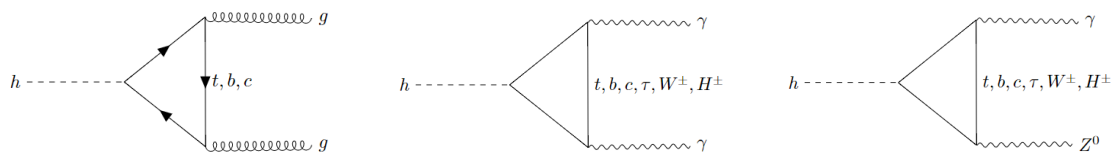
FIGURE 4.2: Leading order diagrams for the Higgs loop decay channels.
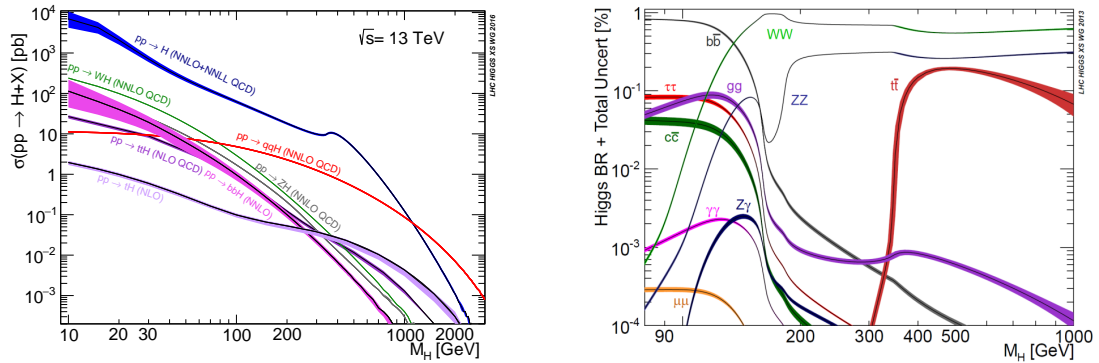
FIGURE 4.3: Production cross-sections at 13 TeV (left) and branching ratios (right) of an SM-like Higgs boson for different channels as a function of its mass [3].

far more important than *huu*. Of course, it is also important that the particular channel provides a clean signal free from background processes.

Figure 4.3 shows the cross-sections and BFs of an SM-like Higgs as a function of its mass. These can be applied to *h* and *H* in the 2HDM, although we must re-scale these by the appropriate reduced Yukawa couplings.

When dealing with collider observables, we often make the assumption that the production and decay modes are independent (called the narrow width approximation) and thus the rate of a given channel can be factorised as

$$\mu_{XY} \equiv \frac{\sigma\left[X \to h\right]^{\text{exp.}} \text{BR}\left[\text{h} \to \text{Y}\right]^{\text{exp.}}}{\sigma\left[X \to h\right]^{\text{SM}} \text{BR}\left[\text{h} \to \text{Y}\right]^{\text{SM}}}, \tag{4.36}$$

where 'exp.' indicates an experimental value. The denominator implies that this is normalised to the SM rate. This quantity, known as the signal strength, characterises the collider yields for some process. Since the SM is a good fit to current experimental data, the signal strengths are close to 1. Collider experiments often report results in the form of Higgs signal strength measurements (and correlations) for a variety of processes.[8]

More recently, an alternative measurement called the Simplified Template Cross Section (STXS) became available during run 2 of the LHC. The STXS concept was developed in order to simultaneously maximise the experimental sensitivity and minimise the theoretical uncertainty of the measurements. They are defined in mutually exclusive regions of phase space, called bins. The binning provides isolation (which channel) of possible BSM effects. We shall make use of both signal strengths and STXS measurements in our global fits.

---

[8]We cannot measure the cross-section and branching fraction separately without additional assumptions, hence why we must fit the full signal strength.

4.2.2 **HiggsBounds** and **HiggsSignals**

We use the HiggsBounds v5.8.0 [63] package to provide 95% exclusion bounds on a variety of BSM scalar processes using data from LEP, Tevatron and the LHC. HiggsBounds first determines the analysis with the tightest exclusion limit for each parameter point for the model under investigation. Then the parameter point is tested against the observed bound of this analysis, and only this analysis. The test is passed if none of the scalar bosons in the BSM theory are excluded. HiggsBounds will then report whether the parameter point is excluded and which analysis was applied.

We use the HiggsSignals v2.5.0 [64] package to compare model predictions of the observed 125 GeV Higgs to experiment. This uses three contributions to the total $\ln \mathcal{L}$ which are based on: *i*) combined LHC run 1 results, *ii*) latest results from the $\sqrt{s} = 13\,\text{TeV}$ analyses, and *iii*) results presented in the form of Simplified Template Cross Sections (STXS). HiggsSignals also takes into account the signal efficiencies and correlations of theoretical and experimental uncertainties. It fits both the signal rate observables and the mass measurements.

Both HiggsBounds and HiggsSignals have already been interfaced in GAMBIT and are part of the ColliderBit module (which we discuss later). They both use a set of model-independent inputs. This consists of the number of neutral scalars, and for each scalar, the mass, total decay rate, branching ratios into a selection of final states and cross sections. The cross sections are provided in the form of effective couplings (HiggsSignals will calculate the cross sections by a re-scaling of corresponding SM quantities).

4.3 Electroweak constraints

Constraints on the electroweak sector include measurements of the anomalous magnetic moment of the muon [65], W-boson mass [66], and electric dipole moment of charged leptons. But in this work, we focus on corrections to the gauge boson propagators.

M. Peskin and T. Takeuchi developed three parameters, called S, T and U, to characterise the corrections to the gauge boson propagators [67] (known as oblique corrections). They are constructed such that they are equal to zero in the SM in order to highlight the influence of new physics. Their current experimental values are close to zero, hence the SM is not challenged. They are defined as

$$S \equiv \frac{4e^2}{\alpha} \frac{d}{dq^2} \left[\Pi_{33}\left(q^2\right) - \Pi_{3Q}\left(q^2\right) \right] |_{q^2=0},$$

$$T \equiv \frac{e^2}{\alpha \; m_W^2 \sin^2 \theta_W} \left[\Pi_{11} \left(0 \right) - \Pi_{33} \left(0 \right) \right],$$

$$U \equiv \frac{4e^2}{\alpha} \frac{d}{dq^2} \left[\Pi_{11} \left(q^2 \right) - \Pi_{33} \left(q^2 \right) \right] |_{q^2=0}, \tag{4.37}$$

where $\Pi_{xy} \left(q^2 \right)$ represents the self-energies of the electroweak gauge bosons Z and Y with 4-momentum q^μ. The subscript i represents the W_i field and the subscript Q represents the B field. In defining these oblique parameters, a subtraction of the SM contributions is made. Their general impact is as follows:

- The S parameter is sensitive to the presence of new heavy fermions and provides a good constraint of composite Higgs models

- The T parameter measures the violation of the custodial symmetry, which is a residual symmetry of the Higgs sector, and is sensitive to additional scalars.

- The U parameter is only sensitive to changes in the $W^\pm$ boson decay width and hence is generally less constraining than the two other oblique parameters.

They are applicable only when the following criteria are met:

i. the electroweak gauge group is the same as the SM i.e., $SU(2)_L \otimes U(1)_Y$,

ii. any new particles must have suppressed light fermion couplings in comparison to gauge boson couplings,

iii. the scale of new particles is much greater than the electroweak scale.

The additional scalars in the 2HDMs couple to the gauge bosons. Hence, there are additional loop contributions to the W/Z boson self-energies that are not present in the SM. The oblique parameters are unaffected by the Yukawa couplings at 1-loop order and therefore are model independent.

Formulae for the oblique parameters can be found in Appendix C of [68]. We do not state them here as they are rather complicated. But the main observation is that the 2HDM contributions vanish when the mass splittings, $m_H - m_A$, $m_H - m_{H^+}$, or $m_A - m_{H^+}$, are zero. We demonstrate this for the simple case of the T parameter in the IDM [69], which is given by

$$T = \frac{1}{32\pi^2 \alpha v^2} \left[f_c \left(M_{H^+}^2, M_A^2 \right) + f_c \left(M_{H^+}^2, M_H^2 \right) - f_c \left(M_A^2, M_H^2 \right) \right], \tag{4.38}$$

$$f_c(x, y) \equiv \begin{cases} \frac{x+y}{2} - \frac{xy}{x-y} \log\left(\frac{x}{y}\right), & x \neq y, \\ 0, & x = y. \end{cases}$$

Now we expand f_c at $x = y$ and insert two squared masses, resulting in

$$f_c(x, y) \simeq \frac{(x-y)^2}{6y} - \frac{(x-y)^3}{12y^2} + \frac{(x-y)^4}{20y^3} - \dots$$

$$f_c\left(m_A^2, m_B^2\right) \approx \frac{(m_A - m_B)^2 (m_A + m_B)^2}{6m_B^2} \approx \frac{2}{3}(m_A - m_B)^2. \tag{4.39}$$

We find that mass splittings of the form $(m_A - m_B)^2$ control the T parameter. Since the experimental value is greater than zero (it is $T = 0.1 \pm 0.07$) we end up with two solutions for each $m_A - m_B$. The expressions for the S and U parameters are more complicated but in all cases the mass splittings are important.

We compute the STU parameters using the 2HDMC program and fit them to the observed values from the global electroweak fit, assuming $m_h^{\mathrm{ref}} = 125$ GeV and $m_t^{\mathrm{ref}} = 172.5$ GeV [70] (see also [71]). These are given by

$$\begin{aligned} S &= 0.04 \pm 0.11 \,, \\ T &= 0.09 \pm 0.14 \,, \\ U &= -0.02 \pm 0.11 \,, \end{aligned} \tag{4.40}$$

with the following correlation matrix

$$\Sigma = \begin{pmatrix} 1.0 & 0.92 & -0.68 \\ 0.92 & 1.0 & -0.87 \\ -0.68 & -0.87 & 1.0 \end{pmatrix}. \tag{4.41}$$

If we would like to consider new physics at the electroweak scale, we need to include an additional 3 parameters: V, W, and X. Slightly above the electroweak scale we can use the relations

$$\begin{aligned} S' &= S + 4s_W^2 c_W^2 V + 4(c_W^2 - s_W^2)X \,, \\ T' &= T + V \,, \\ U' &= U - 4s_W^2 c_W^2 V + 8s_W^2 X \,. \end{aligned} \tag{4.42}$$

As we increase the energy of our NP scale, V, W, $X \to 0$ and we recover the original set of three oblique parameters S, T and U. Equation 4.42 is implemented in GAMBIT, since 2HDMC provides all 6 parameters.

4.4 Flavour constraints

Each SM fermion carries a flavour quantum number that is preserved in strong and electromagnetic interactions but violated in weak interactions. For example, the charged leptons have an electron number, muon number and tau number. There are also similar numbers for neutrinos. The electron number for some state is given by the number of electrons minus the number of positrons. To be clear, the total lepton and quark numbers are always conserved, but the numbers for separate particles are violated in weak interactions.

Flavour physics studies flavour changing processes [72], where one flavour quantum number is converted to another. In particular, it focuses on processes with a change of generation. The CKM and PMNS matrices control how much flavour violation is allowed in the SM. The off-diagonal elements determine the couplings between different generations.

Because the CKM matrix is close to the identity, flavour changing interactions in the quark sector are rare. Therefore, they are highly sensitive to new flavour changing interactions in BSM theories. In the SM, the Wff interaction is a flavour-changing-charged-current (FCCC). There are no flavour changing neutral currents (FCNCs) at tree-level. We can of course combine two FCCCs to create an FCNC. However, these FCNCs are loop suppressed.

In some types of 2HDMs, Higgs-mediated FCNCs may be permitted at tree level [73]. Since such interactions are tightly constrained by experiment and we chose to eliminate them for this work (c.f. Section 3.7.4). The 2HDM also allows H^+ mediated FCCCs, as shown in Equation 3.59. We see that these interactions include the CKM matrix making them appear similar to the SM. But there are also three major differences: *i*) there are both left-chiral and right-chiral currents, *ii*) there is a dependence on the fermion mass and *iii*) there is a $\tan\beta$ or $\cot\beta$ factor that depends on the 2HDM type. Even when below the energy scale of the H^+, these charged scalars may appear off-shell in loop diagrams. Due to the sensitive nature of such flavour changing currents, these contributions may still be detected. Perhaps ironically, flavour physics often provides better sensitivity to high-mass particles than from direct collider searches.

4.4.1   Effective field theory

Flavour processes are calculated using an Effective Field Theory (EFT) framework. Before continuing we provide a brief explanation of EFT [74].

We are often interested in processes below a given energy scale, M. For example, flavour processes typically involve initial states with energy $M < M_W$. Insufficient energy is available to produce heavy states, such as H^+. Yet these states may still appear 'off-shell' as virtual particles which contribute to flavour processes. Therefore, we cannot simply ignore all states with masses above our energy scale M. However, we can make a great simplification to our theory by encoding the effects of these heavy states into a set of vertices. The operators that describe these vertices involve just the initial and final state while the heavy state only influences the coefficient. We say that the heavy state has been integrated out. It works since we are unable to resolve the heavy states directly. There are two steps needed to build an EFT:

1. **Power counting**: when calculating an interaction, we find that it expands out in terms of $(1/M)^n$, where M is the energy of the state that we are integrating out. When keeping only the non-negligible terms, we must decide how large to allow n. This is called power counting. We can add additional terms to build a more accurate EFT.

2. **Matching**: we end up with an effective Lagrangian that contains all relevant operators but with unknown coefficients (called Wilson coefficients). We then need to match this it to the original Lagrangian at the energy scale $\mu = M$.

For example, in the effective Lagrangian below we have chosen a cutoff scale $M = m_W$.

$$\mathcal{L}_{eff} = \mathcal{L}_{\text{QED}\times\text{QCD}}^{m < m_W} + \sum_i C_i(\mu)\,\mathcal{O}_i(\mu) \tag{4.43}$$

Here $\mathcal{O}_i$ are the operators and C_i are the corresponding Wilson coefficients. The first term encodes all physics below the scale m_W and the second encodes physics at or above the scale m_W. The result of eliminating heavy particles is inevitably a non-renormalisable theory, in which the effects of the heavy particles appear in operators with a dimension higher than four.

Another familiar example is Fermi's theory [75], which is a low-energy EFT for the weak interaction. The Wilson coefficient, called Fermi's coupling constant, is a function of the W mass. The effective vertex is shown in Figure 4.4, or mathematically takes the form
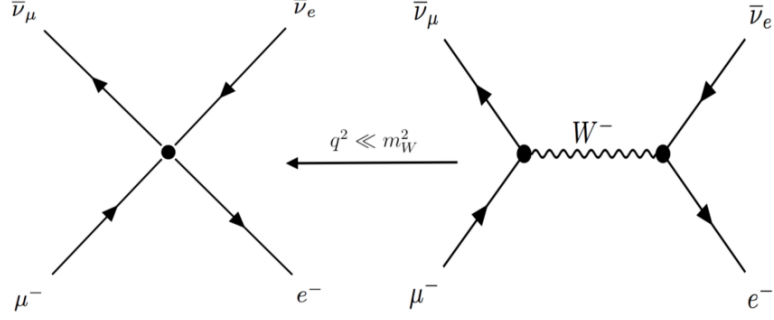
FIGURE 4.4: Fermi's theory of the weak force [4].

$$\mathcal{O}_F = \frac{G_F}{\sqrt{2}} \left(\bar{p}n\bar{e}v + \bar{n}p\bar{v}e \right). \tag{4.44}$$

In our flavour fits, operators that we consider have the generic form

$$\mathcal{O}_i = \left(\bar{\psi}_A P_R X \psi_B \right) \left(\bar{\psi}_C \widetilde{X} \psi_D \right). \tag{4.45}$$

where P_R, P_L are the right-chiral, left-chiral projection operators, $\psi_A, \psi_B, \psi_C, \psi_D$ are 4 (possibly identical) fermions, and X is some product of the matrices: I, γ_μ, $\sigma^{\mu v}$, and T^a. We use the set of operators listed below [76], which are mostly focused on rare B decays. The flavour observables are calculated purely from the Wilson coefficients [77], which in turn depend on the theory under investigation.

$$\mathcal{O}_1 \equiv \left(\bar{s}\gamma_\mu T^a P_L c \right) \left(\bar{c}\gamma^\mu T^a P_L b \right),$$
$$\mathcal{O}_2 \equiv \left(\bar{s}\gamma_\mu P_L c \right) \left(\bar{c}\gamma^\mu P_L b \right),$$
$$\mathcal{O}_3 \equiv \left(\bar{s}\gamma_\mu P_L b \right) \sum_q \left(\bar{q}\gamma^\mu q \right),$$
$$\mathcal{O}_4 \equiv \left(\bar{s}\gamma_\mu T^a P_L b \right) \sum_q \left(\bar{q}\gamma^\mu T^a q \right),$$
$$\mathcal{O}_5 \equiv \left(\bar{s}\gamma_{\mu_1}\gamma_{\mu_2}\gamma_{\mu_3} P_L b \right) \sum_q \left(\bar{q}\gamma_{\mu_1}\gamma_{\mu_2}\gamma_{\mu_3} q \right),$$
$$\mathcal{O}_6 \equiv \left(\bar{s}\gamma_{\mu_1}\gamma_{\mu_2}\gamma_{\mu_3} T^a P_L b \right) \sum_q \left(\bar{q}\gamma_{\mu_1}\gamma_{\mu_2}\gamma_{\mu_3} T^a q \right),$$
$$\mathcal{O}_7 \equiv \frac{e}{(4\pi)^2} m_b \left(\bar{s}\sigma^{\mu v} P_R b \right) F_{\mu v},$$
$$\mathcal{O}_8 \equiv \frac{g}{(4\pi)^2} m_b \left(\bar{s}\sigma^{\mu v} T^a P_R b \right) G^a_{\mu v},$$
$$\mathcal{O}_9 \equiv \frac{e}{(4\pi)^2} \left(\bar{s}\gamma^\mu P_L b \right) \left(\bar{l}\gamma_\mu l \right),$$
$$\mathcal{O}_{10} \equiv \frac{e}{(4\pi)^2} \left(\bar{s}\gamma^\mu P_L b \right) \left(\bar{l}\gamma_\mu\gamma_5 l \right). \tag{4.46}$$

	$\bar{u}_1$	$\bar{d}_1$	$\bar{u}_2$	$\bar{d}_2$	$\bar{u}_3$	$\bar{d}_3$
u_1	π^0	π^+	$\bar{D}^0$	K^+	T^0	B^+
d_1	π^-	π^0	D^-	K^0	T^-	B^0
u_2	D^0	D^+	η_c	D_s^+	$\bar{D}_c^0$	B_c^+
d_2	K^-	$\bar{K}^0$	D_s^-	η	T_s^-	B_s^0
u_3	T^0	T^+	T_c^0	T_s^+	η_t	T_b^+
d_3	B^-	$\bar{B}^0$	B_c^-	$\bar{B}_s^0$	T_b^-	η_b

TABLE 4.1: Table of Mesons in the SM. Note that some of these mesons are mixed together, in particular: $\pi^0 = \frac{1}{\sqrt{2}}\left(\bar{u}_1 u_1 - \bar{d}_1 d_1\right)$, and $\eta = \frac{1}{\sqrt{6}}\left(\bar{u}_1 u_1 + \bar{d}_1 d_1 - 2\bar{u}_2 u_2\right)$.

Here $f = u, d, s, c, b$, m_b is the b mass, T^a are the $SU(3)_C$ generators, and $F^{\mu v}, G_{\mu v}^a$ are the photon / gluon field-strength tensors. We also have a similar set of primed operators with $P_L \leftrightarrow P_R$. The effective Hamiltonian may be written

$$\mathcal{H}_{\text{eff}} = -\frac{4G_F}{\sqrt{2}}V_{tb}V_{ts}^* \sum_{i=1}^{10}\left(C_i\left(\mu\right)\mathcal{O}_i\left(\mu\right) - C_i'\left(\mu\right)\mathcal{O}_i'\left(\mu\right)\right), \tag{4.47}$$

where G_F is Fermi's constant, V_{tb}, V_{ts} are two CKM matrix elements, μ is the energy scale at which the calculation is being performed, $\mathcal{O}_i$ are local operators providing low-energy descriptions of high-energy physics, and C_i are the Wilson coefficients for each operator. Cross-sections for transitions from initial states i to final states f are proportional to squared matrix elements $|\langle f|H_{eff}|i\rangle|^2$.

4.4.2 Flavour Observables

In this work, we consider two types of flavour processes: meson decays and meson mixing. Mesons are a bound state consisting of one quark and one antiquark. The symbols for each meson are provided in Table 4.1. Flavour observables may be categorised as either quark flavour violating (QFV) or lepton flavour violating (LFV) depending on which flavour quantum numbers are violated. Most observables we consider are of the former type.

The strongest flavour constraints tend to involve B-mesons, which include a bottom quark and some other quark, with the most common type being the $b \to s$ transition.[9] Over the past decade, major experimental progress has been made using B factories such as BaBar and Belle, and the Tevatron. Some measurements of flavour observables have

---

[9]The top quark decays very rapidly and has never been observed in a bound state. Hence, mesons with top quarks are all hypothetical.
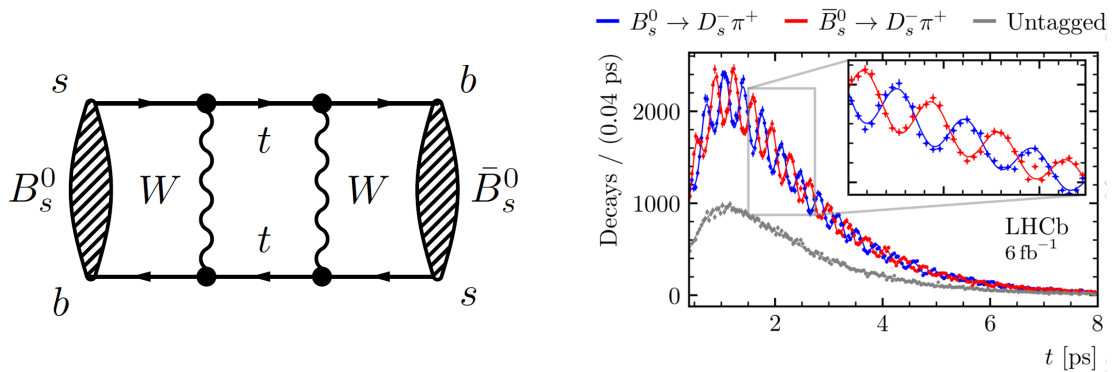
FIGURE 4.5: Meson mixing example [5].

shown tensions with their predicted values in the SM. It is still unclear if these might be accommodated by larger-than-expected QCD effects, statistical fluctuations, or some combination thereof.

We consider some observables that test 'lepton universality', which is the property that the couplings of leptons to all types of gauge boson are flavour-independent. To test lepton universality, we take the ratio of two decay rates which are identical except with a different lepton, for example

$$Br\left[B \to K^*\mu^+\mu^-\right]/Br\left[B \to K^*e^+e^-\right]. \tag{4.48}$$

The branching ratios here are of course different since there is a mass dependence in the phase space factor. But once this is accounted for, both should be the same. In the 2HDM, the H^+ff couplings include a mass-dependence, which breaks lepton flavour universality.

Meson mixing

Neutral mesons have the ability to oscillate between their matter and antimatter versions via box-diagrams before they decay. We show an example with B-mesons in Figure 4.5 for the process

$$\left(B \leftrightarrow \bar{B}\right) \to D^-\pi^+. \tag{4.49}$$

Up and down quantum numbers are not conserved, so this interaction can only be mediated by $W^\pm$ bosons in the SM. In some meson mixing processes the matter/antimatter versions have different masses or decay rates. For example, B mesons decay slightly faster than $\bar{B}$.
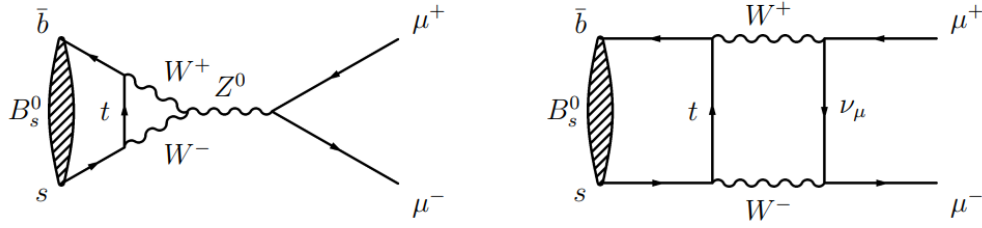
FIGURE 4.6: Leading order diagrams for the $B_s^0 \to \mu^+\mu^-$ process [6].

Meson decays

Meson decays can be categorised according to the type of current; either FCNC or FCCC, and according to their decay products; either fully leptonic (e.g. $D^\pm \to \mu^\pm v_\mu$), semi-leptonic (e.g. $\to K\mu^+\mu^-$), or radiative (e.g. $B \to K^*\gamma$). All flavour observables used in our global fits will be listed later in Table 9.1. As an example, we show two leading order diagrams for the $B_s^0 \to \mu^+\mu^-$ process in Figure 4.6.

Some decays, such as $BR[B \to K^*\mu^+\mu^-]$, exhibit large theoretical uncertainties of the Wilson coefficients. There are a couple of approaches we take to translate these into more useful observables. Firstly, following Ref [78], we may translate this decay into 12 angular functions $I_i^{(a)}$ and 12 CP-conjugate angular functions $\bar{I}_i^{(a)}$. Here i and a together count the twelve functions. We then construct the set of observables given below from these angular functions,

$$S_i^{(a)} = \left(\frac{d\left(\Gamma + \bar{\Gamma}\right)}{dq^2}\right)^{-1} \left(I_i^{(a)} + \bar{I}_i^{(a)}\right),$$
$$A_i^{(a)} = \left(\frac{d\left(\Gamma + \bar{\Gamma}\right)}{dq^2}\right)^{-1} \left(I_i^{(a)} - \bar{I}_i^{(a)}\right). \tag{4.50}$$

Note that these variables also depend on the energy at which they are evaluated. Another observable, the K^* forward-backward asymmetry, can also be written in terms of the above observables as

$$A_{FB} = \frac{3}{8}\left(S_6^S + S_6^C\right). \tag{4.51}$$

We also consider the K^* isospin asymmetry (and its zero crossing) which is written in terms of the widths as

$$A_I = \frac{\Gamma\left(B^0 \to K^{*0}\mu^+\mu^-\right) - \Gamma\left(B^\pm > K^{*+}\mu^+\mu^-\right)}{\Gamma\left(B^0 \to K^{*0}\mu^+\mu^-\right) + \Gamma\left(B^\pm > K^{*+}\mu^+\mu^-\right)}. \tag{4.52}$$

Another approach for dealing with the large Wilson coefficient uncertainties is to take a ratio with other semi-leptonic processes. This is because the uncertainties mostly cancel. As an example

$$\begin{aligned}
R_D &= \frac{BR\left(B \to D\tau\bar{\nu}_\tau\right)}{BR\left(B \to Dl\bar{\nu}_l\right)}, \\
R_D^* &= \frac{BR\left(B \to D^*\tau\bar{\nu}_\tau\right)}{BR\left(B \to D^*l\bar{\nu}_l\right)}, \quad l = e, \mu.
\end{aligned} \tag{4.53}$$

In our global fits, we will using all of the observable types described above.

SuperIso and HEPLike

The GAMBIT module responsible for calculation of flavour observables is called FlavBit [76]. It makes use of the SuperIso [79] and HEPLike [80] packages as backends. SuperIso calculates the predicted values for the flavour observables while HEPLike translates these into likelihoods by comparing with experimental data. The full set of Wilson coefficients is calculated within GAMBIT [77] and provided as input into SuperIso. Although SuperIso does include native 2HDM support, this feature was not used in our global fits.

4.5   Dark matter constraints

It is an astonishing fact that a majority of the mass-energy content of the universe is not part of the SM. About 71% of the universe's energy content is in the form of dark energy, which we do not study in this thesis. Dark matter is the second most abundant form of matter, at around 24%. This leaves only 5% for ordinary SM matter, making DM 5 times more abundant [19].

The microscopic nature of DM is unknown, except for the fact that it does not interact with photons. Initially it was believed that the missing mass in astrophysical observations was made up of baryonic matter in the form of dark objects like brown dwarfs, primordial black holes, and neutron stars. But these have since been ruled out as the main constituent of dark matter. We briefly outline the key astrophysical and cosmological evidence to support the existence of dark matter:
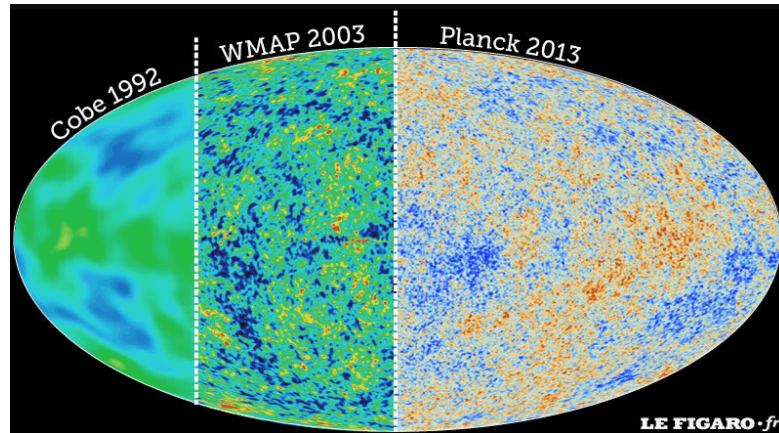
FIGURE 4.7: Measurements of CMB anisotropies by Cobe, WMAP and Planck [7].

- **Gravitational Lensing:** Einstein's theory of general relativity implies that massive objects distort spacetime, causing light to appear to bend around them. Observations have been made of bright distant objects (such as blazars) whose light passes through a lensing galaxy cluster. By studying the distorted image of the distant source, we can infer the amount of mass within the cluster. What we find is that the mass is much larger than what is inferred from the cluster's luminosity.

- **Cosmic Microwave Background:** CMB radiation is observed as a near homogeneous blackbody spectrum with a temperature of 2.726K. But there are tiny fluctuations in the radiance called anisotropies (shown in Figure 4.7). It turns out that the spectrum can only be well described if one allows a cosmological constant in Einstein's field equations as well as cold dark matter. This results in the ΛCDM (cold dark matter) model.

- **Galaxy rotation curves:** It turns out that the stars in the Milky Way are moving too quickly compared to predictions based on the mass of visible matter (estimated by the luminosity) and the galaxy should fly apart. Extra mass in the form of DM is required to hold the galaxy together.

- **Galaxy Clusters:** Observations of galaxy clusters, such as the Coma cluster, show that the individual galaxies in the cluster are moving too quickly based on the observed amount of ordinary matter estimated using the luminosity.

Now we briefly outline how we believe the DM originated [81] – assuming thermal production. The early universe was a hot plasma in which all particles were in thermal equilibrium. As the universe expanded and cooled, the first hydrogen atoms were formed 300,000 years after the Big Bang in an event called recombination. The universe became transparent, liberating the photons which we observe today as the cosmic microwave

background (CMB) radiation. Due to the expansion of the universe, the photons appear redshifted.

Assuming that DM does interact with ordinary matter via the weak force, DM may also be in thermal equilibrium in the early universe. As the universe expanded and cooled, there were not enough interactions to maintain thermal equilibrium. The time at which the thermal equilibrium was lost is called freezeout. After freezeout, the comoving number density of DM-particles remains roughly constant. In other words, the number density of DM decreases only due to the expansion of the universe.

The density of a specific particle species remaining at the time of freezeout is known as the relic density, denoted ρ_{DM}. We often convert this to the density parameter defined by: $\Omega_{DM} \equiv \rho_{DM}/\rho_{crit}$, where ρ_{crit} is the critical energy density at which the geometry of the universe is flat (which we believe to be the case).

The exact moment or temperature of freeze-out is calculated by equating the reaction rate to the Hubble rate. The evolution of its number density dn/dt is governed by the Boltzmann equation. If DM instead remains in thermal equilibrium, then the abundance decreases exponentially. The main variable that determines the relic density is $\langle \sigma v_{rel} \rangle$, where σ is the DM annihilation cross-section and v_{rel} is the relative velocity. A larger annihilation cross section means that we can maintain thermal equilibrium for longer (at lower DM densities). The abundance will continue to fall exponentially until thermal equilibrium is lost. Hence, a higher cross section leads to a lower relic density. This is illustrated in Figure 4.8.

There are 3 types of detection methods: indirect, direct and collider. These are illustrated in Figure 4.9 [82]. Indirect detection experiments look for the products of DM-DM annihilation, direct detection experiments look for energy deposited on regular matter in SM-DM interactions and collider experiments aim to produce DM using high-energy SM-SM interactions, which is detected as missing momentum.

4.5.1 Dark matter collider constraints

Since DM is assumed to consist of stable, neutral particles, it would appear as missing energy at collider experiments [83]. Searches are based on detection of the visible counterpart such as jets and/or charged leptons. It is unknown whether sufficient energy is available to produce DM at current or future colliders. The most commonly used DM searches at the LHC are:
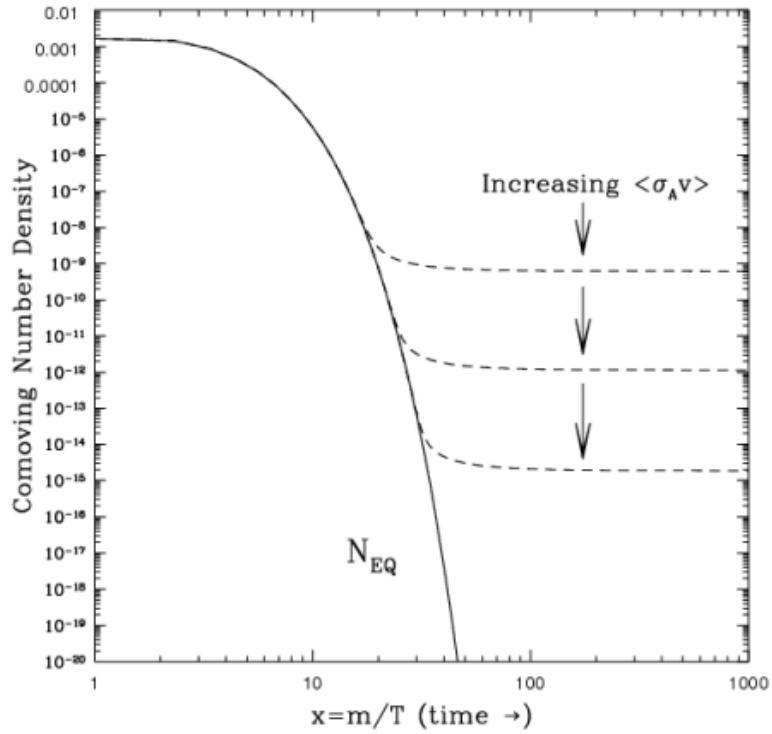
FIGURE 4.8: Thermal freezeout of Dark Matter [8].
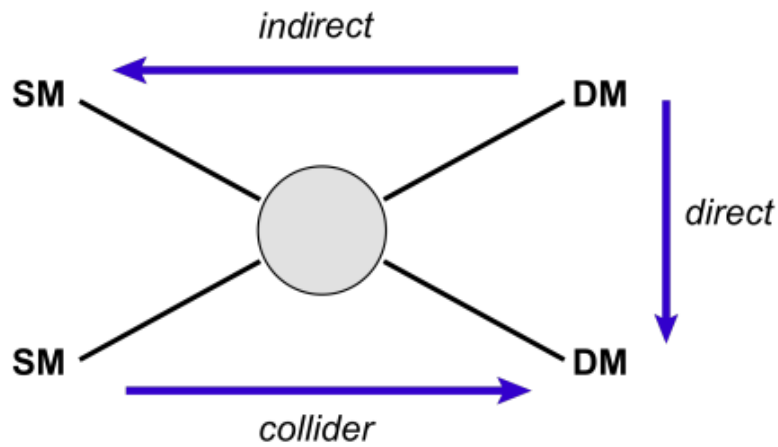
FIGURE 4.9: Methods for dark matter detection [9].

- **Mono-jet searches:** If a pair of DM particles can be produced from pp collisions, it should also produce one or more QCD jets from initial state radiation. So, we may search for jet events with a high missing transverse momentum.

- **Mono-V searches:** DM may also be produced together with a vector boson which is radiated by a quark in the initial state. While the corresponding production cross-section is significantly smaller than for the QCD radiation, the process is much cleaner and can be searched for with higher sensitivity.
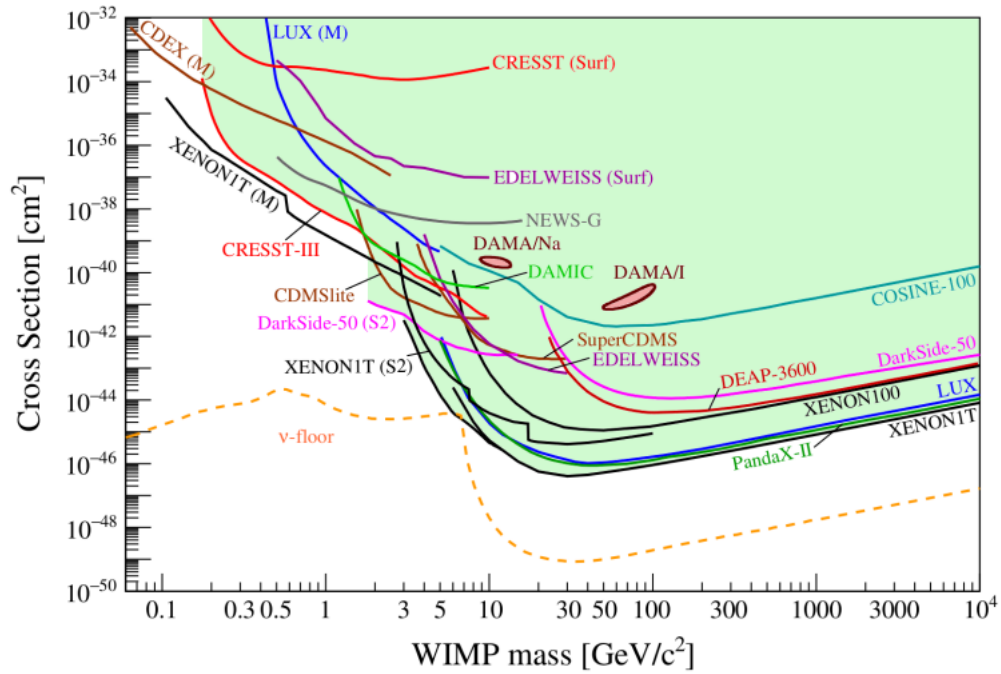
FIGURE 4.10: Lower bounds on the spin-independent DM-nucleon cross section as a function of DM mass for a variety of direct detection experiments. The yellow line is the neutrino floor. [10].

- **Invisible Higgs decays:** If the DM mass is less than half the SM Higgs boson mass, it may be possible to produce pairs of DM particles in Higgs decays.

4.5.2 Dark matter direct detection

Since DM is believed to be everywhere in the universe, it should be travelling through any detection apparatus on Earth at all times. It may occasionally bump into the nucleus of a detector atom and deposit some energy via weak currents [11]. The detection rate depends on the local DM abundance. Limits are placed on either the spin-independent or spin-dependent DM-nucleon cross-section, depending on which type of current the detector is sensitive to. Figure 4.10 displays the limits for a variety of detectors.

It is believed that DM energies are in the range of 1-100 keV. In contrast, natural radioactive elements emit MeV-scale energies. Hence, direct detection experiments must be thoroughly shielded from radioactive elements. Experiments must be placed deep underground to shield them from cosmic rays. There are a few ways to detect DM interacting with ordinary matter depending on how it deposits its energy:

- **Inelastic scattering**: the nucleus of an atom is excited into a higher energy state which then decays via photon emission.
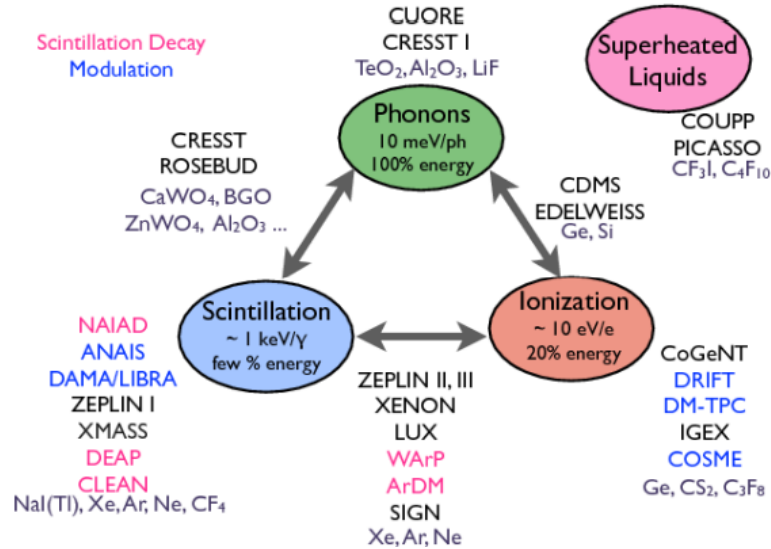
FIGURE 4.11: The various type of direct detection experiments [11].

- **Phonons**: the event appears as a vibration in the crystal lattice of the detector which can be measured using a thermometer.

- **Ionisation**: an electron gains enough energy to escape the pull of the nucleus. A small electric field pushes the electron to a detector.

- **Scintillation**: an electron absorbs enough energy to climb to a higher energy state. After a short time, the electron loses this energy and emits a photon which can be collected by photomultipliers and converted into an electric signal.

Noble gas detectors, such as XENON1T, PandaX and LUX, use a large volume of noble gas as the detection medium and observe both scintillation and ionisation simultaneously for each event. Other detectors, such as CRESST, EDELWEISS and EURECA, detect phonons released by the dark matter interacting with low temperature crystals. Figure 4.11 summarises the different types of direct detection experiments.

4.5.3 Dark matter indirect detection

DM annihilations throughout the universe produce SM particles (such as gamma rays, photons and neutrinos) which can be detected on Earth [84].

- Gamma Rays: DM annihilations may produce pions which then decay into gamma rays. Alternatively they may produce electrons and positrons which then produce additional gamma rays, X-rays and radio waves via Bremsstralung, inverse Compton and synchrotron emission. The Fermi-LAT telescope has been searching for gamma

rays from the galactic centre and dwarf galaxies that orbit the Milky Way. An excess has been found in the galactic centre which may be explained by DM. Alternatively it may also by due to pulsars. Gamma ray methods require knowledge of the DM distribution and velocity, which is not very well known. This leads to extra nuisance parameters that we need scan over.

- Neutrinos: Massive celestial bodies, like the Sun and the Earth, moving through the dark halo can gravitationally trap DM particles in their cores. In equilibrium, the annihilation rate would equal half the capture rate. Neutrinos from WIMP annihilations can escape and be searched for by neutrino telescopes. Detection typically involves a large volume of water or ice. The neutrinos interact with water molecules in the detector to create charged leptons. Muons are particularly important here as they leave a clean signal of Cherenkov radiation. This can be used to determine where the neutrino originated.

- CMB: Measurements of the CMB anisotropies provide an estimate of the DM relic abundance [85] (along with estimates of the abundance of ordinary matter, and dark energy). Currently Planck provides by far the most precise measurement which is: $\Omega_{\text{DM}}^{\text{Planck}} h^2 = 0.1184 \pm 0.0012$ [86]. In our study we enforce the DM relic density measurements as an upper limit, rather than a prediction. This is because the IDM may be embedded in a more complete model of the universe and thus there could be other DM candidates that provide the remaining relic density.

Chapter 5

Parameter inference and scanning

In previous chapters we described a variety of 2HDMs, and the theoretical and experimental constraints that we apply to them. Now we would like to know how these shape the 2HDM parameter space. Two key questions that we may want to answer are: (i) "given a set of models, which of these best fits the data?", and (ii) "for a given model, which regions of its parameter space best fit the data?". In this work we shall focus on the second question. We now outline the statistics [87, 88] and tools [12, 89] needed to answer this.

5.1 Parameter inference

Our BSM theories include a set of unknown parameters; for example, the Type-I/Type-II 2HDMs have 6 parameters (or 7 if we allow the SM-like Higgs mass to be varied) and the IDM has 5 parameters. We would like to estimate the best values of those parameters and determine the uncertainty of these estimates.

Suppose we have N physics observables and M measurements of each. The physics observables are denoted $\boldsymbol{x} \equiv \{x_1, \ldots, x_N\}$ and could include things like the branching ratio for $B \to K^* \mu^+ \mu^-$ or the Higgs signal strength for a vector-boson fusion production mode that decays into two photons. If we need to discuss individual measurements of these observables, then we add a second index: x_{ij}. In this notation the mean, variance and covariance take the form[1]

---

[1]What we list here are actually estimators known as the sample mean, sample variance and sample covariance. However, the distinction won't be important.

$$\mu_{x_i} = \frac{1}{N} \sum_{k=1}^{N} x_{ik},$$

$$\sigma_{x_i}^2 = \frac{1}{(N-1)} \sum_{k=1}^{N} (x_{ik} - \mu_{x_i})^2,$$

$$\Sigma_{x_i x_j} = \frac{1}{(N-1)} \sum_{k=1}^{N} (x_{ik} - \mu_{x_i}) \left(x_{jk} - \mu_{x_j} \right). \tag{5.1}$$

Now suppose that we have a model with P parameters, $\boldsymbol{\theta} \equiv \{\theta_1, \ldots, \theta_P\}$. We denote the (joint) probability density function (PDF) for our observables $p(\boldsymbol{x}|\boldsymbol{\theta})$. If the observables are independent then we can split this up as a product of PDFs of each individual observable, i.e.

$$p(\boldsymbol{x}|\boldsymbol{\theta}) = \prod_{i=1}^{n} p(x_i|\boldsymbol{\theta}). \tag{5.2}$$

In what follows, we need to consider the PDF as a function of the parameters rather than of the value of the measurements $\boldsymbol{x}$. In other words, we will switch the role of the dependent and independent variables. In this case we don't have a true PDF since

$$\int d\theta \; p(\theta) \neq 1 \text{ for fixed x}, \tag{5.3}$$

whereas a true PDF must be normalised to 1. To avoid confusion, we rename it as the 'likelihood' function and give it the symbol $\mathcal{L}$. Most of the time we do not actually know an analytical form of the likelihood. But we can calculate it for discrete values of the parameters. By taking enough samples throughout a given range for each parameter, we can construct an estimate of the likelihood as a function of the parameters.

Before we find the best combinations of parameters, we should first define exactly what we mean by this. There are two philosophically distinct ways of posing the question depending on our choice of statistical framework:

1. **Frequentist Statistical Framework:** How probable is it that we would have observed the data that we did if a model and a specific combination of its parameters were true?

2. **Bayesian Statistical Framework:** How probable is it that a model with a specific combination of its parameters is true, given the data that we observed?

Parameter	λ_1	λ_2	λ_3	λ_4	λ_5	m_{12}^2	$\tan\beta$
Min	0	0	-4π	-4π	-4π	-10^6	0
Max	4π	4π	4π	4π	4π	10^7	100

TABLE 5.1: Parameter ranges in the generic basis.

In this work, we will only be using a frequentist framework. Note that in a frequentist framework it is not valid to ask whether the model with a given set of parameters is true since we do not have any repeatable experiments to test this. We only have one universe, and in that universe the parameters have a particular value.

5.2 Parameter Ranges

We need to sample the likelihood function in order to reconstruct its mathematical form. We can only do this for a finite range of each parameter. Therefore, we need to first justify the parameter ranges that we select. Tables 5.1, 5.2 and 5.3 display the parameter ranges used for the generic, physical and a Hybrid basis respectively.[2] We justify these as follows; firstly, perturbativity requires that the absolute value of all couplings is less than 4π. This applies to both the generic basis and the Higgs basis couplings: $|\lambda_i| < 4\pi, |\Lambda_i| < 4\pi, \quad i = 1, \ldots, 7$. Vacuum stability leads to the requirement that $\lambda_1 > 0, \lambda_2 > 0, \Lambda_1 > 0,$ and $\Lambda_2 > 0$, thus giving a stricter lower bound for these parameters. Our conventions for α and β (see Section 3.8) lead to the parameter ranges: $\cos{(\beta - \alpha)} \in [-1, +1]$, $\sin{(\beta - \alpha)} \in [0, 1]$, and $\tan\beta \geq 0$. All physical masses are, of course, required to be positive. The upper limit of masses is arbitrary, although we select a value that is not too far beyond the reach of experimental constraints.

The limits are the upper bound of $\tan\beta$ and both the upper and lower bound of m_{12}^2. Both are more difficult to justify. Firstly, the upper limit of $\tan\beta$ is not well constrained but we shall see that values above 50 do not lead to any new/interesting phenomenology. The parameter m_{12}^2 contributes to the mass of all scalar bosons through the term $\bar{m} \equiv 2m_{12}^2/\sin{(2\beta)}$ – which suggests a rough scale of this parameter. But we cannot obtain a strict requirement, hence a larger than ideal parameter range is used.

The GAMBIT software, which we use to run our parameter scans, provides functionality to control the sampling density of each parameter throughout its range. We use a flat sampling density for $|m_{12}^2|$ less than $10,000$ GeV^2 since this tends to lead to appropriate masses for our scalars. Outside of this range, we set the sampling density to fall off logarithmically, which allows us to explore a larger region without degrading performance.

---

[2]These are the bases that we use in our parameter scans. We do not list the SM parameters here, but they are all fixed to their experimental values.

Parameter	m_h	m_H	m_A	m_{H+}	$\sin(\beta-\alpha)$	m_{12}^2	$\tan\beta$
Min	0	0	0	0	0	-10^6	0
Max	3000	3000	3000	3000	1	10^7	100

TABLE 5.2: Parameter ranges in the physical basis.

Parameter	m_h	m_H	Λ_4	Λ_5	Λ_7	$\cos(\beta-\alpha)$	$\tan\beta$
Min	0	0	-4π	-4π	-4π	-1	0
Max	3000	3000	4π	4π	4π	1	100

TABLE 5.3: Parameter ranges in a hybrid basis.

5.3 Frequentist inference

To infer the values of the parameters, we find an estimator, denoted $\widetilde{\boldsymbol{\theta}}$, of the true parameter values $\boldsymbol{\theta}_0$. We choose the estimator to be the $\boldsymbol{\theta}$-value which maximises the likelihood (called the maximum likelihood estimator (MLE)). The estimator is itself a random variable since it depends on the random data points. If we were to repeat our experiment, we would get a slightly different $\widetilde{\boldsymbol{\theta}}$ each time; i.e., there exists a PDF of the estimated parameters – which we denote $g\left(\widetilde{\boldsymbol{\theta}}|\boldsymbol{\theta}_0\right)$. The uncertainty of our estimated parameters is related to the spread of $\widetilde{\boldsymbol{\theta}}$ values. But as the number of data points increases, $\widetilde{\boldsymbol{\theta}}$ approaches $\boldsymbol{\theta}_0$. In this limit, it can also be shown that the PDF for $\widetilde{\boldsymbol{\theta}}$ approaches a normal distribution centred at $\boldsymbol{\theta}_0$.

To summarise the uncertainty of our estimators, we calculate confidence intervals for each parameter. A confidence interval is defined to be a interval which is expected to contain the true parameters $\boldsymbol{\theta}_0$ a fixed portion of the time. For a single parameter, θ, $[a, b]$ is a confidence interval at the confidence level CL if[3]

$$P\left(a \leq \theta_0 \leq b\right) = CL. \tag{5.4}$$

Here the bounds of this region are random variables that depend on the data, whereas the value we are trying to bound is fixed. Obtaining the exact confidence interval can be done using the Neyman construction and requires that we estimate the sampling distribution. This method is rather complicated. But if we can assume that the PDF for the parameters, $g\left(\widetilde{\theta}|\theta\right)$ is Gaussian distributed then, for a fixed confidence level CL, a and b can be found using the simplified formulae

---

[3]Note that this definition is not unique as we can always expand the lower bound while shrinking the upper bound such that the confidence level remains fixed. In practice, we use the central confidence interval, meaning that $P\left(a \leq \theta_0\right) = P\left(\theta_0 \geq b\right)$.

$$a = \widetilde{\theta} + \sigma_{\widetilde{\theta}} \Phi^{-1} \left(\frac{1 + CL}{2} \right),$$

$$b = \widetilde{\theta} - \sigma_{\widetilde{\theta}} \Phi^{-1} \left(\frac{1 + CL}{2} \right). \tag{5.5}$$

Here Φ^{-1} is the inverse of the cumulative distribution for $g\left(\widetilde{\theta}\big|\theta\right)$ (which we take to be a Gaussian distribution centred at $\widetilde{\theta}$ and with a standard deviation of $\sigma_{\widetilde{\theta}}$).

The above formula can easily be extended for multi-dimensional confidence regions of a vector of parameters. Now consider that we may want to plot a confidence interval/region in a lower dimensional space of parameters than the full set of parameters. Since we only have a finite number of samples to represent the likelihood, we need to divide up the parameter space into bins. We would then like to find an appropriate value to represent the likelihood for each bin. For frequentist statistics, this is just the maximum likelihood value throughout the entire set of points within each bin.[4] This process is called profiling.

5.4 Chi-squared test statistic

The χ^2 statistic summarises how well a set of observables fit the model predictions. Many physics packages report a χ^2 value rather than the likelihood, so we also describe it here and how it is related to the likelihood. Given a set of observables with mean $\mu_1, \ldots, \mu_N$, we define χ^2 as

$$\chi^2 = \sum_{i=1}^{N} \sum_{j=1}^{N} \left(\mu_i - \mu_i^{th} \right) \Sigma_{ij}^{-1} \left(\mu_j - \mu_j^{th} \right), \tag{5.6}$$

where $\mu_1^{th}, \ldots, \mu_N^{th}$ are the theoretical values derived using our model, and Σ^{-1} is the inverse of the covariance matrix. A χ^2 value of 0 represents a perfect fit and χ^2 increases away from 0 as the measurements deviate further from the expected values. Assuming that we have N independent observables that are all normally distributed, it can be shown that the χ^2 value is χ^2-distributed. This distribution takes the form

$$\chi^2(x; k) = \frac{\frac{1}{2} (x/2)^{(k/2)-1} e^{-x/2}}{\Gamma(k/2)}, \tag{5.7}$$

---

[4]This will usually be a large number since we only bin over a one or two dimensional space of parameters.

with the number of degrees of freedom, k, equal to $N - M$. For our parameter scans, we must convert the χ^2 value to a likelihood. It turns out that the χ^2 value is, to good approximation, proportional to the logarithm of the likelihood[5]

$$\ln \mathcal{L} = -\frac{1}{2}\chi^2. \tag{5.8}$$

It is easy to see why in the case of independent normally distributed observables since

$$\ln \mathcal{L} = \sum_{i=1}^{N} \ln \mathcal{N}\left(x_i : \mu_i, \sigma_i\right) \propto \sum_{i=1}^{N} -\frac{(x_i - \mu_i)^2}{2\sigma_i^2} = -\frac{\chi^2}{2}. \tag{5.9}$$

5.5 Scanner performance

Using the methods previously described we can sample a model's parameter space, calculate the likelihood for each sample and use this to determine the MLEs and a set of confidence regions. However, it turns out that parameter sampling itself is a major obstacle for two reasons: (i) the total parameter space is extremely vast in comparison to the size of the "good" regions where the likelihood is high, (ii) calculation of each point is computationally expensive. Hence, we need to develop techniques for efficient parameter sampling.

First, we investigate how we can more intelligently make a selection of points to sample. Perhaps the simplest approach is to define a uniformly spaced grid of points over the parameter ranges that we specify. We could also just randomly sample a set number of points within the specified parameter ranges. But neither of these approaches use the information from previously sampled points to help determine where the good regions of parameter space may lie. Alternatively, there are several sophisticated parameter sampling algorithms which make use of the likelihood from previously sampled points. Some examples include Markov Chain Monte Carlo (MCMC), Differential Evolution (DE), nested sampling, and ensemble Monte Carlo. The algorithm we choose depends on the statistical framework we are using. Estimation of the Bayesian posterior requires integration of the likelihood in various directions.[6] To maximise the accuracy of this integration we need the sampling density to be approximately proportional to the likelihood itself. This can be achieved using MCMC samplers. For frequentist statistics, we are more interested in "peak finder" samplers since our MLEs are just the peak of the likelihood function. We would also like an algorithm that can handle multimodal

---

[5]This is a result of Wilk's theorem.

[6]For frequentist statistics we instead must profile the likelihood in various directions.

likelihood functions and ensure sufficient sampling density around the peaks. For this task, DE is an appropriate sampling algorithm. The details of the algorithms are beyond the scope of this work. In the case of DE, it essentially works by iteratively improving upon a set of maxima based on an evolutionary process. Further details can be found in Ref [89].

After selection of an appropriate sampling algorithm, the next improvement is to use the logarithm of the likelihood rather than the likelihood itself. Assuming we have a set of independent measurements (see Equation 5.2) the total $\log \mathcal{L}$ is given by the sum

$$\log \mathcal{L}(\theta) = \sum_{i=1}^{n} \log \mathcal{L}(\theta_i). \tag{5.10}$$

There are two key reasons to do this (a) it aids sampling algorithms since the gradient of $\log \mathcal{L}$ is generally more consistent over the full parameter range and (b) since the likelihood is constructed by multiplying many typically very small components together, we find that the result would underflow if we did not do this.

Another problem we encounter is that theoretical constraints are a binary yes/no for a given point rather than a likelihood. Suppose that, for example, we have a parameter λ which must be less than λ_{max}. One way to translate this to a likelihood is using the hard-cutoff defined by

$$\mathcal{L}(\lambda) = \begin{cases} 1, & \text{if } \lambda < \lambda_{\mathrm{max}}, \\ \epsilon & \text{if } \lambda \geq \lambda_{\mathrm{max}}. \end{cases} \tag{5.11}$$

Here ϵ is chosen to be very small so that points are rejected by the sampler when the constraint is not met. However, this provides no information to help guide the scanner towards the valid region. To improve performance, we instead use the soft-cutoff given by

$$\mathcal{L}(\lambda) = \sqrt{\frac{2}{\pi\sigma^2}} \times \begin{cases} 1, & \text{if } \lambda < \lambda_{\mathrm{max}}, \\ \exp\left(-\frac{1}{2}\left(\frac{\lambda - \lambda_{\mathrm{max}}}{\sigma}\right)^2\right), & \text{if } \lambda \geq \lambda_{\mathrm{max}}. \end{cases} \tag{5.12}$$

This is known as a half-normal likelihood function. In this case we must remove the invalid points for $\lambda \geq \lambda_{\mathrm{max}}$ during the plotting stage, otherwise our theoretical constraints will appear to have smooth boundaries. Our sampling algorithms will give up on points when a likelihood component is too small.[7] Hence, we should choose σ large enough

---

[7]In practice, the scanner gives up when $\ln \mathcal{L}$ reaches a large negative number such as -10^7.
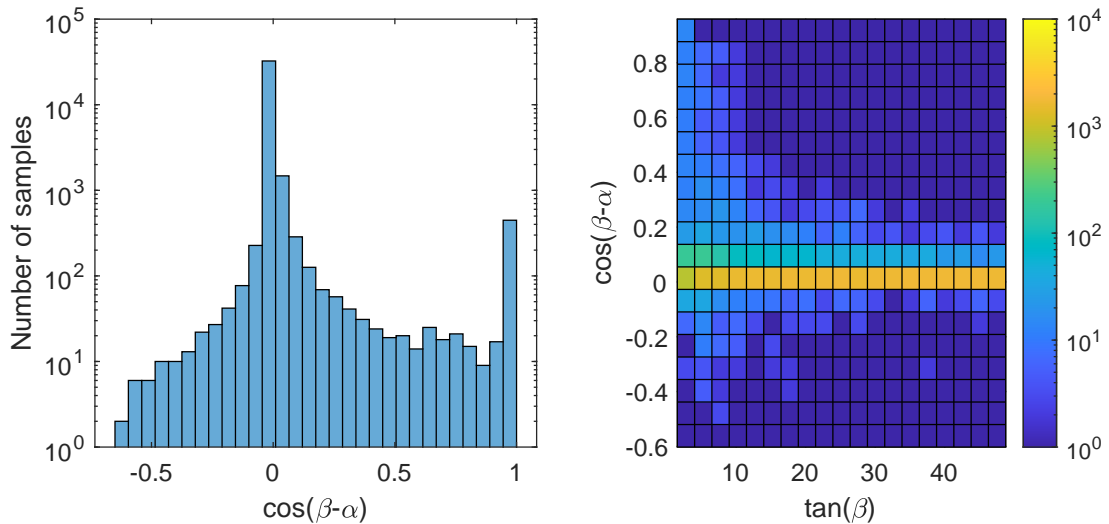
FIGURE 5.1: A histogram showing the number of samples along $\cos(\beta - \alpha)$ (left) and the number of samples in the $\cos(\beta - \alpha)$ vs. $\tan(\beta)$ plane (right). To produce these plots a $1,000,000$ point, random, tree-level scan was run using a Matlab script. This was done in the generic basis with the parameter ranges given in Section 5.2. Basic theoretical constraints were applied – these are, vacuum stability, leading-order unitarity, mass positivity and perturbativity of the generic couplings (leaving a total of $35,603$ valid points).

so that the scanner can still find sufficient valid points near the cutoff. We do not want σ to be too large, otherwise we will end up calculating the experimental likelihood components for many points that will be eliminated during the plotting stage. In general, the experimental constraints are more expensive to calculate, so we should avoid doing so where possible.

Sampling density is also a major problem for frequentist statistics as some regions of parameter space may be very difficult to reach (e.g. because they require severe fine-tuning of parameters).[8] Often using a different basis will allow easier exploration of these regions while other regions become more difficult. For example, it is easy to satisfy the theoretical constraints in the generic basis but difficult to explore the $\tan \beta$ vs. $\cos (\beta - \alpha)$ plane. The reverse situation is true for the physical basis. This is shown in Figure 5.1.

We explore this problem further in Section 7 where we define a hybrid basis that allows for better exploration of certain regions. We may also want to combine scan results using different bases or use targeted scans where we only sample a narrow region of parameter space that is difficult to explore, thus dedicating more points for this region.

---

[8]In Bayesian statistics this is less of an issue since we will be integrating over the parameter space which is small for these regions.

Chapter 6

Computational Software

In this section we describe the GAMBIT and GUM software. Extensions to both tools were made for this study to improve the existing implementation of the 2HDM and to provide support for the IDM (See Sections 7 and 13). Hence, we provide some details about how each tool works.

6.1   The **GAMBIT** software

The Global And Modular Beyond-the-Standard-Model Inference tool (GAMBIT) is an open-source software package for performing parameter scans of physics models [12, 90]. Since new physics may be observed from a number of experimental sources (including simultaneously from multiple sources) it is important that we use global fits, where all constraints are applied simultaneously. GAMBIT achieves this by providing a modular system, where new constraints and interfaces to external packages (known as backends) can be added effortlessly. A GAMBIT scan works as follows:

1. The user runs GAMBIT using the command, `./gambit -f yaml_files/my_yaml_file.yaml`, where `my_yaml_file` is an input file to control the GAMBIT scan. The file specifies which physics model to scan, the sampling algorithm to use, and which likelihood components and observables to calculate.

2. The GAMBIT core analyses the input file and enables the requested model. It then determines which module functions can provide the requested quantities, considering only those that are compatible with the given model. All dependencies of these module functions are considered. This may include other module functions or backend functions. GAMBIT constructs a directed acyclic graph of module functions to be called in a particular order.
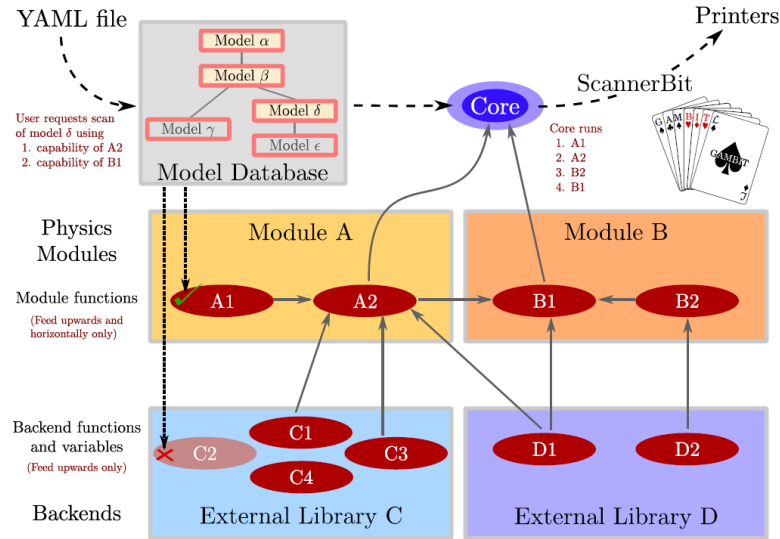
FIGURE 6.1: Schematic representation of a GAMBIT scan (image from [12]).

3. Control is then passed to a module within GAMBIT called ScannerBit. This employs the statistical sampling algorithm requested by the user. It calls the module functions in the appropriate order to collect samples of the model's parameter space. It is also capable of improving performance dynamically by changing the execution order whenever this is allowed.

4. The requested quantities are all outputted by the printer system which is configured by the .yaml file. For example, the user can request for GAMBIT to save the output in the HDF5 format. The output includes the set of likelihoods and observables for each sampled point.

The process is depicted in Figure 6.1. An example .yaml file for the 2HDM is provided in Appendix B. We now provide a summary of how the GAMBIT software itself works. After this, we outline further additions to GAMBIT generated by the GUM software.

6.1.1 Models

Models in GAMBIT are a set of named parameters and are used to represent the input parameters of physics models. These are intended to be sampled by some scanning algorithm. Their physical meaning is defined entirely by how they are used within module functions. Models can be declared as children of existing models, which implies that there exists a mapping from the child parameter space to some subspace of the parent space. Each child model comes with a function that defines the transformation required to take a parameter point in its space to a corresponding point in the parent parameter space. During a scan, the model's ancestry will be activated and all models will be

scanned simultaneously. Models can also be declared as friends of other models, which allows for links between family trees. A translation function must be provided to map the parameter space between the two models. Friend models can be used to explore the parameter space in different bases.[1] GAMBIT will automatically use the necessary translation functions, allowing use of module functions even if it has not been explicitly allowed for the model being scanned.

A model file is provided for each type of 2HDM, and also for each basis (including the physical, generic and hybrid bases). In practice, all parameters are converted to the generic basis before running the scan using a set of friend/parent translation functions.[2]

6.1.2 Backends

Backends are external tools that GAMBIT links to dynamically at runtime, in order to compute various physical observables and likelihoods. They consist of two parts: (1) the external packages, which provide the functionality and (2) the GAMBIT frontend functions for interfacing with these packages. The frontend functions are declared within GAMBIT, including the function signature and a capability. For the 2HDM, we use the 2HDMC [52], HiggsBounds [63], HiggsSignals [64], SuperIso [91], and HEPLike [80] backends. Furthermore, for the IDM we also use SPheno [92], micrOMEGAs [93], gamLike, DDCalc and DarkSUSY [94].

6.1.3 Modules

Modules, also known as 'bits', group together related pieces of code – each providing a set of module functions to the user. A module function calculates a [capability, type] pair. The capability is an identifier that specifies what the function calculates, and may be an observable, likelihood component, or some intermediate quantity. Module functions specify dependencies on models, backends and other capabilities. During a scan each module function is tested for compatibility with the active model; incompatible functions are disabled. Module functions are identified that can provide the requested quantities (specified in the input file), and other module functions are identified to fulfil their dependencies. Such dependencies are defined in terms of capabilities, not specific functions. This allows them to be modular, keeping the use of a module function's result

---

[1]Note that use of a different basis is equivalent to setting a multi-dimensional prior on our original basis.

[2]These use tree-level relations.

completely independent of its identity. The sections below outline the modules used in our GAMBIT scans.[3]

ScannerBit

ScannerBit [89] is responsible for sampling the model's parameter space. Parameter ranges are specified in the input file, where the user may also specify a "prior" for each parameter to control the sampling density throughout the parameter range. ScannerBit provides interfaces to external scanning and optimisation packages. Random and grid scanners are built-in, while external scanning algorithms include Markov Chain Monte Carlo (MCMC), differential evolution and nested sampling. Unlike the physics modules described below, ScannerBit does not consist of module functions.

SpecBit

The SpecBit [95] module has three different functions, which we describe below:

- **Spectrum Generation:** The main function of SpecBit is calculation of spectrum information. This includes the pole masses and running couplings/masses at some given energy scale. The full spectrum is stored in a `Spectrum` class and this gets passed around to various module functions to access it. The `Spectrum` class consists of three components: (i) `SMInputs`, (ii) `LE SubSpectrum`, and (iii) `HE SubSpectrum`.

  - `SMInputs` is a simple structure that stores SM input parameters as doubles. Some masses are given at their pole while others are given at a set energy scale in the $\overline{MS}$-scheme (according to the SLHA2 [96] conventions). These are used by external spectrum generators for matching RGEs at low energy.

  - The low-energy / high-energy `SubSpectra` are derived classes that wrap some external spectrum generator (or a simple tree-level generator inside GAMBIT). `SubSpectra` store a subset of the spectrum at a particular scale and support running the spectrum to a different scale.

  The low-energy `SubSpectrum` stores quark and lepton masses and their couplings with gauge bosons (i.e. just the QED $\otimes$ QCD EFT). We use the `softsusy::QedQcd` spectrum generator, which is part of the SOFTSUSY [97] package, to perform RGE running. `QedQcdWrapper` is the `SubSpectrum` class that wraps this. BSM parameters and masses are stored in the high-energy `SubSpectrum`. In practice this is the only

---

[3]There is also a NeutrinoBit module for neutrino observables and a CosmoBit module for cosmological observables but we do not use these in our scans.

`SubSpectrum` that we need to access throughout our code. We use a FlexibleSUSY [98] spectrum generator to run the 2HDM spectrum.[4] The `SubSpectrum` wrapper is called `THDMSpec<MI>` and is defined in `THDMSpec_head.hpp`. There is also a tree-level 2HDM `SubSpectrum` called `THDMSimpleSpec`. The tree-level calculations are first performed in `THDMSpec_basis.hpp` and are then fed to `THDMSimpleSpec`, which simply returns the values.

So far we have only described the standard GAMBIT `Spectrum` class but to enable compatibility with 2HDMC, a new class called `THDM_spectrum_container` was created that extends `Spectrum`. This class is filled in using the backend convenience function, `init_THDM_spectrum_container_CONV`. This copies the members of `Spectrum` and the `yukawa_type` into the `THDM_spectrum_container` and automatically overrides 2HDMC 's internal spectrum with the one calculated by GAMBIT. It also overrides 2HDMC 's SM parameters with those from `SMInputs`. Rather than using the standard `Spectrum` class, we will be mainly using `THDM_spectrum_container`.

- **HiggsCouplingTable:** SpecBit is also used to fill a table containing all effective reduced couplings between scalars and other particles[5] (scalars, fermions and gauge bosons). To do this we use the 2HDMC backend.[6] We also include the scalar decay rates in this structure, which are calculated by DecayBit.

- **Theoretical Constraints:** All theoretical constraints are included in the main SpecBit file. These are directly coded in GAMBIT based on the references provided in Section 4.1.

DecayBit

Particle decay calculations are handled by the DecayBit [95] module, after accepting the masses and couplings of particles from SpecBit. For each particle in the theory we fill a `DecayTable::Entry` class with the total decay width and all branching ratios. The full set of `DecayTable::Entry`s are then stored in a `DecayTable` class. We use 2HDMC to calculate the decays, but also added an interface to CalcHEP during development of the IDM. Both backends have been confirmed to give consistent results. We do not calculate the uncertainties on these decays as they are not yet used by our calculations.

---

[4]FlexibleSUSY requires the generic couplings $\lambda_1, \ldots, \lambda_7$, m_{12}^2 at the user-defined scale Q_{in}. It requires $\tan\beta$ at the scale of m_t. Inputs are in the $\overline{MS}$-scheme. FlexibleSUSY then calculates the gauge couplings as well as $v_1, v_2, m_{11}^2, m_{22}^2$ and the Yukawa couplings at the scale m_Z. Finally it calculates scalar masses in the $\overline{DR}$-scheme at the scale $Q_{in} = m_Z$ and also the pole masses.

[5]In reality, only the couplings between scalars and photons, $h_i\gamma\gamma$ and $h_iZ\gamma$, are effective couplings, and these are always approximated using decay rates.

[6]There is also an option to approximate all couplings using only the decay rates. To do this one applies the following formula: $C_{hAB} \approx \frac{\Gamma(h)}{\Gamma_{SM}(h)} \frac{BF(h \to AB)}{BF_{SM}(h \to AB)}$.

PrecisionBit

PrecisionBit [95] has multiple functions. Firstly, it provides constraints from the electroweak sector. BSM contributions to electroweak observables are often important since these are known with high experimental precision. In our scans we include constraints from measurements of the oblique parameters (STU), which are calculated using 2HDMC (although they can also be calculated by SPheno). Further work is still being done to add a W-boson mass constraint. The muon anomalous magnetic moment and electric dipole moments are also available for the 2HDM but are not yet used in our global fits. PrecisionBit also provides so-called SM nuisance likelihoods.[7] While we do allow the Higgs mass, m_h, to be varied, we shall use HiggsSignals to constrain this instead.

ColliderBit

Likelihoods for Higgs physics based on searches at the LHC, LEP and Tevatron colliders are available in ColliderBit via the HiggsSignals and HiggsBounds backends (c.f. Section 4.2). ColliderBit also provides Monte Carlo event simulations of signals at ATLAS and CMS for the specific model under investigation. We do not use this functionality, however, since it is computationally expensive, and since collider data has also been provided for generic Higgs searches which is more directly relevant for the 2HDM.

DarkBit

DM likelihoods are provided by the DarkBit [99] Module. A calculation of the DM relic abundance is provided by the micrOMEGAs backend along with predictions of the spin-independent and spin-dependent DM-nucleon cross-sections. Direct detection likelihoods are provided by DDCalc, and indirect detection likelihoods are provided by nulike (neutrinos) and gamLike (gamma rays). A constraint for the DM relic density is provided within GAMBIT and can be used as either a measurement or an upper bound based on the options in the `.yaml` input file. DarkBit stores properties of the DM candidate in a `ProcessCatalog` class, including its mass, spin, electric charge and various 2-to-2 cross-sections with other particles in the theory. The cross-sections are calculated using CalcHEP.

---

[7]These are likelihoods for various SM parameters. We might vary them within their experimentally allowed ranges when this has an impact on other important observables, but in doing so we also need a constraint for the SM-parameter.

6.2 The **GUM** software

Although adding a new model to GAMBIT is largely formulaic, it is still error prone and requires substantial knowledge of the GAMBIT software. Hence, the GAMBIT Universal Model Machine (GUM), was created for automatically generating the code required to implement a new model in GAMBIT based on Lagrangian-level inputs [100]. We will be using GUM to generate the IDM rather than the methods previously used for other 2HDMs. It works as follows:

1. The user calls GUM with the command: `./gum models/MyModel.gum`. The input file describes which Lagrangian level package to use (Feynrules or SARAH), the model to use within that package, the WIMP candidate if any, and the outputs to write into GAMBIT (SPheno / Pythia / CalcHEP / micrOMEGAs / Vevacious).

2. GUM then opens an interface to either Feynrules or SARAH via the Wolfram Symbolic Transfer Protocol (WSTP), and loads the model file that the user has requested.

3. GUM ensures that the outputs are valid based on the other options provided and calls a variety of sanity checks built-in to Feynrules and SARAH.

4. GUM extracts all particles, masses, parameters and relevant code outputs from the SARAH/Feynrules file and enumerates all code changes to be written into GAMBIT. It writes them into a '`.mug`' file which enables them to be removed later if the user wishes to do so.

5. Finally the code changes (in the form of patches) are written into GAMBIT allowing use of the new model and its constraints within GAMBIT. GUM also provides a sample `.yaml` input file.

6.2.1 Under the hood

The outputs that GUM generates depend on the options provided by a `.gum` input file. In our case (for the IDM), we will be using a SARAH model and will include the SPheno output with loop-decays, and also outputs for DarkBit, CalcHEP and micrOMEGAs (note that CalcHEP is required for micrOMEGAs). While GUM is written in python, we are able to communicate with SARAH via a C++ wrapper that uses the Wolfram Symbolic Transfer Protocol (WSTP) to communicate with Mathematica. After the SPheno spectrum generator is generated, a set of patches are applied for compatibility with GAMBIT. For example, any calculations that are not used by GAMBIT are commented

out for performance reasons, and any attempt to write files to disk must be removed. A new initialisation subroutine is added to ensure that SPheno starts out in the same state before each point is calculated. Further patches were added for this study to extract the Wilson coefficients from SPheno, as will be explained in Chapter 13. Further details about the specific amendments that GUM makes to GAMBIT are listed below:

- **Backends:** If SPheno output is requested, a new Backend called `model_name_SARAH-SPheno` is added. This includes code from the original SPheno, additional code generated by SARAH for the specific model, and a set of patches generated by GUM which are applied during the build stage. GUM also generates interfaces (frontends) to the backends so that they can be accessed within GAMBIT using its modular capability system. Some backends in GAMBIT work for generic BSMs, and only require amendments to the relevant GAMBIT module functions so that they provide the appropriate inputs for the new model. These include Vevacious, CalcHEP, micrOMEGAs, Pythia, HiggsBounds and HiggsSignals.

- **Models:** GUM creates a new model file in the GAMBIT `models` directory, which just includes a minimal set of input parameters to be varied for a scan. Code for any new particles is also added to the GAMBIT particle database, and code for the new model to the GAMBIT models database.

- **SpecBit:** New files are added in the GAMBIT `specbit` directory for the new model. The appropriate wrappers onto the GAMBIT `Spectrum` class are added. The capability `get_new_model_spectrum_SPheno` is added to get the spectrum via a backend requirement.[8]

- **DarkBit:** If the user specifies a WIMP candidate for a model then GUM will write a new source file for the model in DarkBit. If the user requests CalcHEP output, then a new module function, `TH_ProcessCatalog_new_model`, providing the Process Catalogue is written. All computations of indirect detection and relic density likelihoods in DarkBit make use of the Process Catalogue. If micrOMEGAs output is requested then GUM adds an entry to the module function `RD_oh2_Xf_MicrOmegas`, which enables the relic density calculator. GUM also provides an interface to the module function `DD_couplings_MicrOmegas` for use in DDCalc for computing likelihoods from direct detection experiments.

- **DecayBit:** Whenever decay information is requested, GUM amends `DecayBit.hpp`/`.cpp` files with decays of the new particles. There are actually two methods for getting the new decays: (i) CalcHEP generated decays can be obtained via the usual `all_decays`

---

[8]If requested, GUM will also write code to `SpecBit_VS.cpp` to check vacuum stability using Vevacious. However, this method is rather slow so we prefer to write our own model specific vacuum stability checks.

capability. CalcHEP calculates tree-level decays for each new BSM particle, plus new contributions to any existing particles. (ii) Alternatively, SPheno may be used to calculate all decays at leading order (but with some important higher order corrections) using the function `all_new_model_decays_from_SPheno`.[9] In either case the standard `DecayTable` class is returned containing a `DecayTable::Entry` to store the decay information for each particle.

- **ColliderBit:** New interfaces to HiggsBounds and HiggsSignals are added by GUM (using outputs from SARAH) for the study of Higgs physics at particle colliders. The interfaces are already mostly model independent – the main model-dependent step is filling out the `HiggsCouplingsTable` with all Higgs coupling/decay information for the specific model. GUM also supports adding interfaces to Pythia however these are not required for the 2HDM.

6.2.2 Further details about **SARAH** and **SPheno**

SARAH [101, 102] is a Mathematica package for analysing any renormalisable QFT model. It calculates all vertices, mass matrices, tadpole equations, one-loop corrections for tadpoles and self-energies, and two-loop RGEs. The Lagrangian-level theory is provided by a symbolic Mathematica input file. This includes (i) global symmetries, (ii) local symmetries, (iii) matter fields/superfields, (iv) the Lagrangian, (v) field rotations and (vi) descriptions of each particle in the theory (such as the output name, charge, and PDG code). SARAH also includes outputs for a variety of other physics tools. These include:

- Feynman rules in the UFO format for use by matrix element generators.[10]

- Outputs for Vevacious to check vacuum stability.

- Outputs for HiggsBounds/HiggsSignals for calculation of Higgs observables from collider experiments.

- Outputs for microMEGAs for calculation of DM observables.

- Generating code for calculation of Wilson coefficients and flavour observables.

- Generating a spectrum generator based on SPheno.

---

[9]We prefer the SPheno method here as it is more model specific.
[10]These UFO files encode information about the particles, the parameters and interaction vertices for a given model.

These outputs are then used by GUM to provide support from within GAMBIT. The SPheno output is worth elaborating on. SPheno was originally a tool for calculating SUSY spectra and decays, along with a limited set of flavour and electroweak observables [92]. The out-of-the-box SPheno code is largely modular and model independent, which enables SARAH to generate the remaining model-specific Fortran code compatible with the rest of SPheno. This means that a SPheno-based spectrum generator can be generated for any model that SARAH supports, including non-SUSY models. The SARAH-generated SPheno has the ability to calculate decay widths, cross-sections, anomalous magnetic moments of leptons, and a wide variety of observables from flavour physics. When adding the IDM to GAMBIT, we will use a SARAH-generated SPheno, rather than FlexibleSUSY (which was used for the other 2HDMs), as our spectrum generator.

6.2.3 **FlavorKit and custom operators**

While the SARAH-generated SPheno can be used for the study of flavour observables, all information about the underlying Wilson coefficients as well as the calculation of the flavour observables had been originally hard-coded into SARAH. This meant that it was not easy to extend it with new observables and operators. To solve this problem, SARAH was extended with a new tool called FlavorKit [13]. This includes a variety of new Wilson coefficients in a general symbolic form, and code snippets for calculating flavour observables (a total of 20 of them by default) – both of which can be translated into a complete Fortran code as part of the SPheno output. New operators can also be added using another Mathematica-based extension called PreSARAH. This uses FeynArts and FormCalc to derive the generic form factors at tree and 1-loop levels.[11] While Wilson Coefficients are model-dependent, it is possible to derive generic expressions for them – which SARAH then matches to the specific spectrum and interaction Lagrangian for any arbitrary model. The entire process is depicted in Figure 6.2.

The Wilson coefficients calculated by SPheno may then be used to cross check those calculated in GAMBIT. They may also be used to calculate flavour observables in the IDM, which are yet to be studied – though, the BSM contributions are expected to be small due to the lack of any new flavour-changing currents in the IDM (only loop effects contribute). Finally, the WCs are needed for the `DD_rel_WCs_flavscheme` capability which is used for the IceCube dark matter likelihoods.

---

[11]Note that it is limited to 4-fermion or 2-fermion plus 1 boson operators.
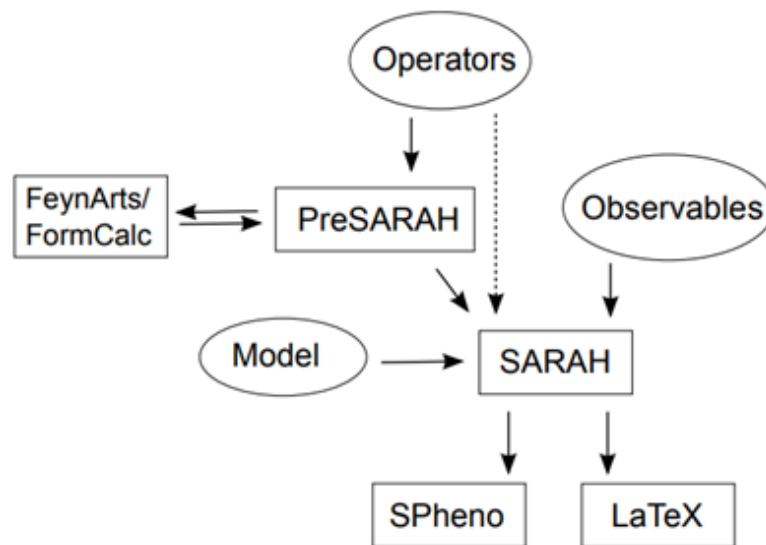
FIGURE 6.2: Schematic representation of FlavorKit. The user defines new operators. Then PreSARAH calculates the Wilson coefficients in a generic form using FeynArts and FormCalc and creates the necessary input files for SARAH. Later SARAH matches these to the specific model and converts the results into Fortran code. [13].

Part II

GLOBAL FITS OF THE 2HDM

Chapter 7

Contributions to the 2HDM in GAMBIT

7.1 Bases and sampling density

Sampling density is a major problem for frequentist statistics as some regions of parameter space may require severe fine-tuning of parameters. Many HPC hours are wasted trying to scan these hard-to-reach regions, or worse yet, the missing parameter regions may be mistaken as a feature. Often using a different basis will allow easier exploration of these regions while other regions become more difficult.[1]

In this section we introduce two new bases and show how they perform in comparison to the traditional `physical` and `generic` bases. Both bases were implemented in GAMBIT, but for the purposes of studying sampling density the tree-level 2HDM has been re-implemented in MATLAB.[2] This includes the basis transformations, and LO unitarity, simple perturbativity, and vacuum stability constraints.

The `generic` ($\mathbb{Z}_2$-eigenstate) basis is governed by 3 mass-squared parameters and 5 dimensionless parameters. We can trade two of the mass-squared parameters for v and $\tan\beta$. Since we know experimentally that $v = 246$ GeV we can eliminate one parameter. Hence, there are 7 real parameters to vary in parameter scans. The main problem with

---

[1]In Bayesian statistics, this is not a problem since these regions have a low volume of parameter space and therefore when we integrate over them, the contributions are small. A well-known problem with Bayesian statistics is that it sensitive to the choice of prior. There is no good way to select a prior for our parameters, hence usually a flat prior is assumed – regardless of the basis choice. Hence, Bayesian statistics is sensitive to the choice of basis. Frequentist statistics, on the other hand, does not have this flaw.

[2]The code is available here: https://github.com/Alex0125698/THDM_sampler. The reason for this is because the performance of MATLAB is around 3000 times better than GAMBIT (without the experimental constraints) since various inefficiencies are avoided.
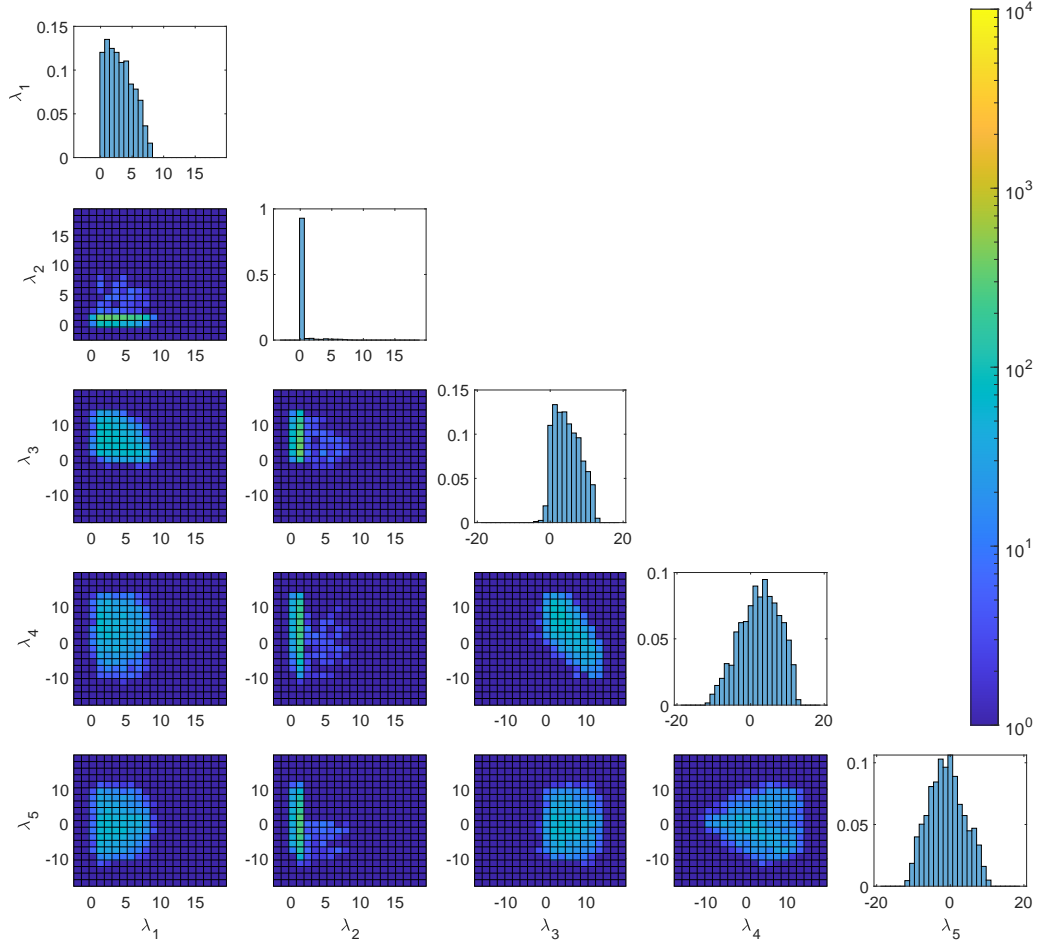
FIGURE 7.1: Sampling density of the generic couplings using the generic basis with all theoretical constraints applied.

this basis is that we do not specify the experimentally known Higgs mass (125 GeV), and therefore most points will be invalid. Also note that m_{12}^2 is not a good choice of parameter as there is no good argument to provide an upper and lower bound. In practice, we use a logarithmic prior to scan a large region for this parameter.[3]

Another common choice is the physical basis which includes $\tan\beta$, $\cos(\beta - \alpha)$, m_h, m_H, m_A, and m_{H^+} plus one additional parameter which is usually chosen to be m_{12}^2 or λ_5. Since we have included the Higgs mass in this basis, we only need to scan over 6 parameters. It may seem like this basis would therefore be easier to sample, but in fact the opposite it true. To see why, consider

$$\left(m_{H^+}^2 - m_A^2\right) = \frac{v^2}{2}\left(Z_5 - Z_4\right) = \frac{v^2}{2}\left(\lambda_5 - \lambda_4\right) \approx v^2\lambda,$$
$$\left(\bar{m}^2 - m_A^2\right) = v^2\lambda_5,$$

---

[3]Note that m_{12}^2 can usually be replaced with $\bar{m}$ – which is limited by perturbativity.
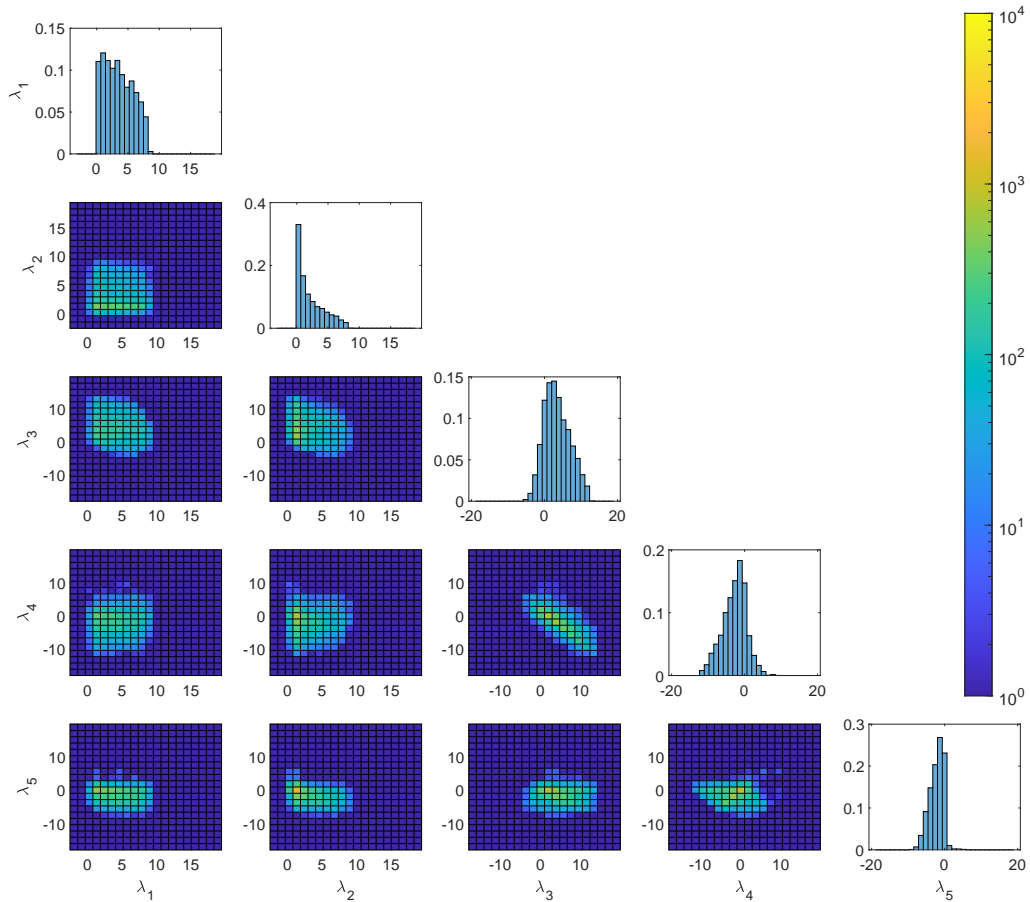
FIGURE 7.2: Sampling density of the generic couplings using the physical basis with all theoretical constraints applied.

$$\left(m_H^2 \sin^2\left(\beta - \alpha\right) - m_A^2 \right) = v^2 Z_5 - m_h^2 \cos^2\left(\beta - \alpha\right). \tag{7.1}$$

These can be derived using the Equations in Appendix E. We see that the perturbativity constraints (which require couplings to be of order $\mathcal{O}(4\pi)$) provide strong limits on the mass splittings. In Figure 8.3 of Chapter 8 we shall find that the unitarity constraint provides an even stronger limit. Therefore, for arbitrary values of the mass parameters, most points will not satisfy the theoretical constraints. This last relation would of course give a limit on $\left(m_H^2 - m_A^2\right)$ for the limit $\cos\left(\beta - \alpha\right) \to 0$. However, we can also derive another relation from Equation E.4 which looks like

$$\left(m_H^2 - m_A^2 \sin^2\left(\beta - \alpha\right) \right) = v^2 \left(2\lambda + \lambda_5 \sin^2\left(\beta - \alpha\right) \right). \tag{7.2}$$

Here we have picked the maximum scenario by assuming that the couplings are independent, and that each are of order $\lambda \approx \mathcal{O}(4\pi)$. When combined with Equation 7.1, we find
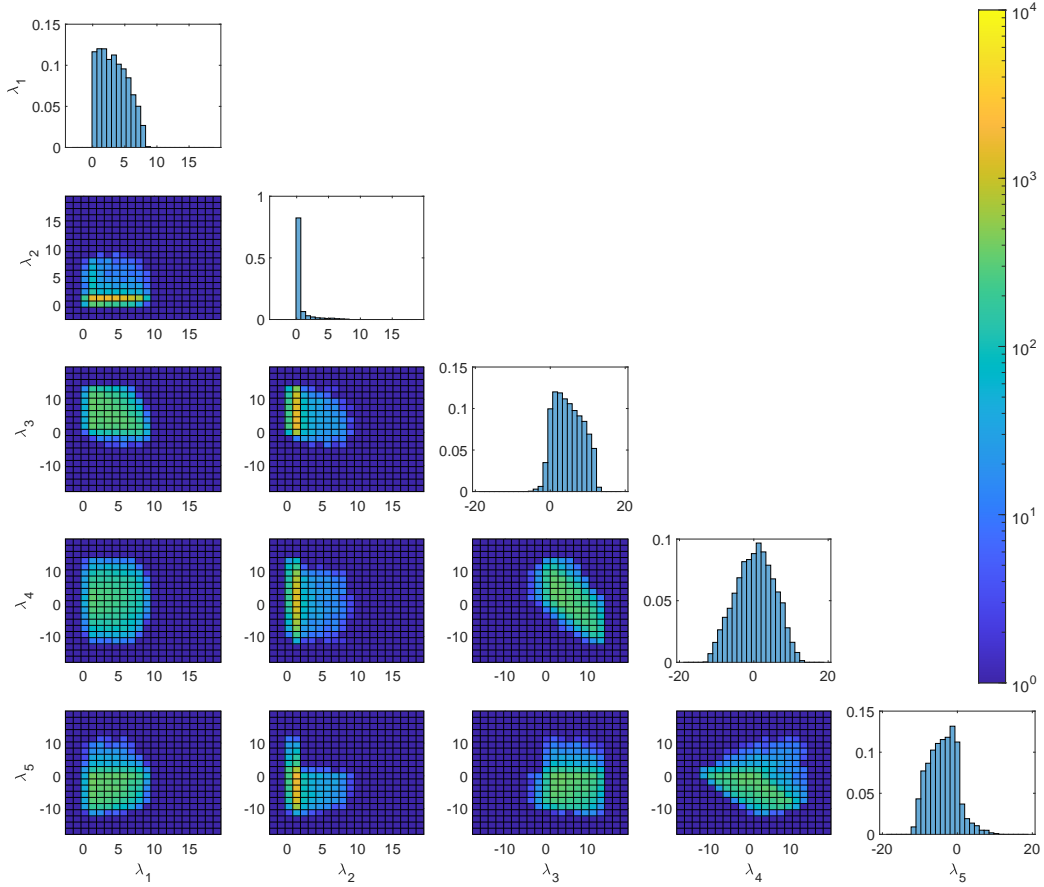
FIGURE 7.3: Sampling density of the generic couplings using the hybrid Higgs basis with all theoretical constraints applied.

$$\left(m_H^2 - m_A^2\right) = \frac{1}{1 + \sin^2\left(\beta - \alpha\right)} \left(v^2 \lambda \left(3 + \sin^2\left(\beta - \alpha\right)\right) - m_h^2 \cos^2\left(\beta - \alpha\right)\right). \quad (7.3)$$

Here the contribution from m_h^2 is no more than 125^2 GeV^2 and thus the squared mass splitting is strongly limited by perturbativity, even away from the alignment limit.

In a first attempt to improve scanner performance, a new `mass_diff` basis was created. This is similar to the `physical` basis except that we use m_A, $m_H^2 - m_A^2$, and $m_{H^+}^2 - m_A^2$ as parameters. Another basis called the `hybrid_Higgs` basis was also added which includes m_h, m_H, $\tan\beta$, $\cos\left(\beta - \alpha\right)$, and 3 Higgs couplings as input parameters (based on [47]). The parameter ranges for each basis were provided in Tables 5.1, 5.2, and 5.3. In Table 7.1 the failure rates are provided for each constraint/basis combination. The *Higgs mass* constraint checks that the value of m_h is within 5 GeV of the experimental value. If we were to ignore this requirement, the `generic` basis would out-perform the rest with the `hybrid_Higgs` being about 100 times worse. With the Higgs mass constraint included, the `hybrid_Higgs` performs the best in this test with the `generic`, `physical_diff`,

	hybrid_Higgs	generic	mass_diff	physical
Perturbativity	98.6 %	1.6 %	99.95 %	99.9975 %
Mass positivity	9.9 %	2.84 %	8.33 %	0 %
Vacuum stability	65.7 %	55.9 %	98.2 %	98.2 %
Vacuum meta-stability	36.2 %	0.23 %	14.9 %	10.5 %
LO unitarity	99.28 %	81.5 %	99.97 %	99.9984 %
Higgs mass 125 GeV	0 %	99.69 %	5.9 %	0 %
All theory	99.958 %	95.3 %	99.9977 %	99.99989 %
All theory + Higgs mass	99.958 %	99.979 %	99.9979 %	99.99989 %

TABLE 7.1: Failure rates for each theoretical constraint for each basis. The Higgs mass constraint here enforces the Higgs mass to be within 5 GeV of the experimental value.
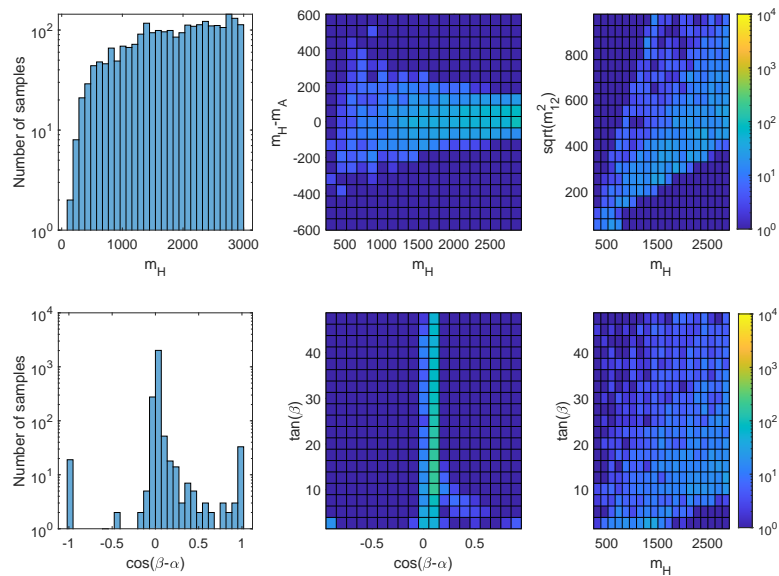
FIGURE 7.4: Theoretical constraints in the generic basis. Note that colours are the same as the above plots.

and physical bases, providing 1/2, 1/20, and 1/400 times the number of valid samples respectively. Note that while the mass_diff basis outperformed the physical basis, it was not particularly successful since the theoretical constraints were still violated too frequently.

Of course, these failure rates do not tell the whole story. We must also consider the sampling density in various planes on interest. Figures 7.1, 7.2, and 7.3 display the sampling density of the generic couplings. To produce these, we used 10^8 random samples of the parameters for each basis. We see that the hybrid_Higgs basis provides the best sampling of λ_2 whereas the generic basis struggles with $\lambda_2 > 2$.

Figures 7.4, 7.5, and 7.6 display a set of benchmark plots for each basis. We see that only hybrid_Higgs was able to adequately sample the $\cos(\beta - \alpha)$ vs $\tan\beta$ plane, while the
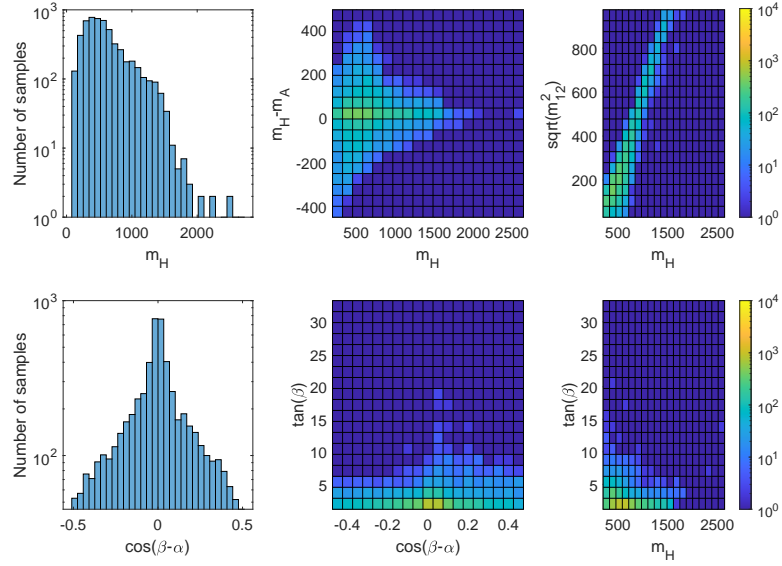
FIGURE 7.5: Theoretical constraints in the physical basis. Note that colours are the same as the above plots.
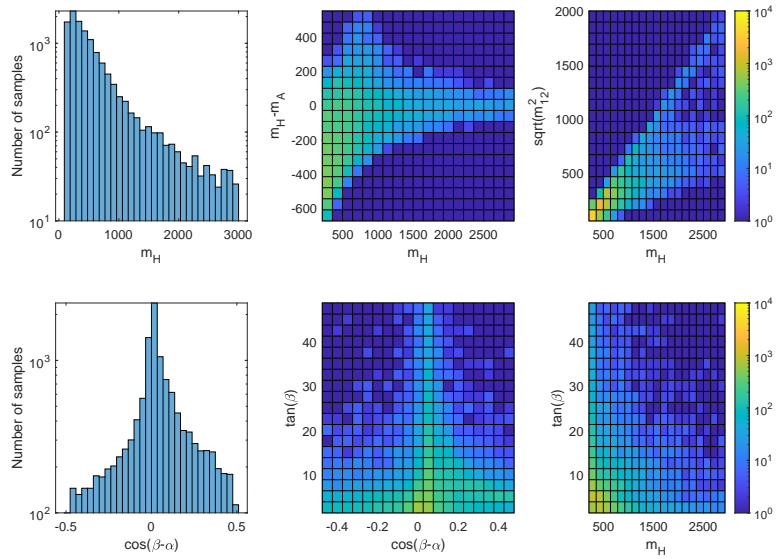
FIGURE 7.6: Theoretical constraints in the hybrid Higgs basis. Note that colours are the same as the above plots.

`generic` tends to stick to the alignment limit and `mass_diff` basis struggles with $\tan\beta > 10$ Overall, most planes are best explored using the `hybrid_Higgs` basis. One exception is for masses larger than 3000 GeV where the `generic` basis is now favoured. However, since we have m_H as a parameter in the `hybrid_Higgs` basis it is not difficult to just run targeted scans for these regions. Having both $\cos(\beta - \alpha)$ and $\tan\beta$ as input parameters is also a significant advantage for the `hybrid_Higgs` basis, since this allows us to run targeted scans in the plane of interest for collider experiments. Another important factor is that the Higgs mass constraint is provided by HiggsSignals, which runs quite slowly compared to the theoretical constraints. This is a huge advantage for any basis in which we can

fix the range for m_h since the points that violate theoretical constraints are ruled out quickly, whereas points with the wrong Higgs mass take much longer to be eliminated.

7.2 Changes to the 2HDM implementation in **GAMBIT**

Originally, the 2HDM implementation in GAMBIT was developed by a former Ph.D. student, Filip Rajec [103], based on the existing MSSM implementation. We have continued development of the 2HDM by adding new features, fixing bugs, and improving performance.

As discussed in Section 7.1, new bases were added to the existing 2HDM implementation to help achieve sufficient sampling density in all planes of interest. The `mass_diff` and `hybrid_Higgs` bases were mentioned previously. A third basis, named `hybrid_Higgs2`, was also added. This is the same as `hybrid_Higgs` except that we swap the m_H parameter for m_{H^+}. This latter basis was most frequently used in our scans as it assists in sampling the $\tan\beta$ versus m_{H^+} plane, which is important for flavour observables. These bases for were added for all 2HDM types. The full GAMBIT model name includes the 2HDM type, the basis name and a suffix to indicate if it uses a FlexibleSUSY spectrum generator. For example, `THDMI_hybrid_Higgs2atQ` is the Type-I 2HDM in the `hybrid_Higgs2` basis with FlexibleSUSY, while `THDMII_physical` is the Type-II 2HDM in the physical basis without FlexibleSUSY.

Some minor modifications to experimental likelihoods have been made. In particular, the user can now select which analyses to use for the HiggsSignals likelihood using the input option `HS_analysis`.[4] The STU electroweak constraint has been split into multiple capabilities so that user can select a capability to provide the predictions for the S, T, and U parameters. At the time of writing, the 2HDM predictions are provided by either 2HDMC or SPheno. These predictions can also now be printed. The `all_BFs` capability, which is used to print the BFs, now includes an option, `print_as_widths`, to print them as decay widths instead of BFs. Another option, `print_BF_error`, was added to print the uncertainties of the BFs or widths. Further options have also been added to exclude specific particles or processes.

A new capability, `higgs_scenario_LogLikelihood_THDM`, was added to eliminate points corresponding to either the hidden-Higgs or regular-Higgs scenarios, depending on the `exclude_Higgs_higgs` input option. If set to `True`, then this excludes the hidden Higgs scenario, otherwise it excludes the regular Higgs scenario. Note that in order to successfully scan the hidden-Higgs scenario, the user must use a basis which includes the m_H

---

[4]The allowed options are: -1 (all), 0 (LHC run 1), 1 (latest signal strengths), and 2 (latest STXS measurements).

parameter and set this close to the SM-like Higgs mass, otherwise very few points will be found. The regular Higgs scenario is generally easier to sample.

Some performance improvements were also necessary. An important speedup came from a new input option to check a basic set of theoretical constraints prior to spectrum generation (namely perturbativity and LO unitarity). This is possible since some theoretical constraints depend only on the couplings at the input scale.

Furthermore, a new option was added to the GAMBIT core that would allow the remaining point calculation to be skipped if the likelihood falls below a threshold. This threshold is module dependent and ideally set much lower for SpecBit compared to the experimental modules ColliderBit and FlavBit. The problem being addressed here is that some experimental constraints (especially the flavour likelihoods) take significantly longer to run than the spectrum generation, and typically have a much smaller impact on the total likelihood. Therefore, unless the likelihood from the theoretical constraints is above a certain threshold, it is better to guide the scanner with just the theoretical constraints alone. It may seem like skipping some likelihoods would lead to incorrect results, but the thresholds are set well below the global maximum likelihood and therefore these points are not visible on the plots anyway.[5] This change gave a 10 times performance boost when all flavour constraints were turned on.

Finally, we note that there were previously some inconsistencies with the 2HDM convention for $\beta - \alpha$. The code has now been updated to use the 2HDMC conventions: $\sin(\beta - \alpha) \in (-1, +1)$ and $\cos(\beta - \alpha) \in (0, +1)$. If required, the used can easily switch to a different convention during the plotting stage. The results presented in this thesis use an alternative convention where: $\cos(\beta - \alpha) \in (-1, +1)$ and $\sin(\beta - \alpha) \in (0, +1)$.

---

[5]One may also be concerned about the likelihood jumping near the thresholds. Typically the theoretical likelihoods are orders of magnitude lower than the experimental constraints (typically $\ln \mathcal{L} \approx -10^5$ versus $\ln \mathcal{L} \approx -10^1$ respectively) so these jumps are relatively small. Furthermore, the scanner we use is robust against these jumps since it does not use derivatives.

Chapter 8

Theoretical Constraints in the 2HDM

Finally, we begin our presentation of the results for the softly-broken $\mathbb{Z}_2$-symmetric 2HDMs. For brevity, only a small subset of all plots is presented in these chapters.

We begin with the theoretical constraints. Scans were done at tree-level, while results for a loop-level spectrum will be provided in Chapter 12. This is because more testing has been done at tree level and there are hints of some bugs with the FlexibleSUSY generated spectrum. We only present results for the Type-II 2HDM here since the theoretical constraints are independent of the 2HDM type. Scans are done in the `hybrid_Higgs`, `hybrid_Higgs2`, `generic`, `higgs`, and `physical` bases – each using a variety of parameter ranges. A total of 26 parameter range/basis combinations were merged into the final dataset. This ensures that all planes of interest are adequately sampled. We restricted the SM-like Higgs mass to the interval $(115, 135)$ GeV, which will be further constrained by HiggsSignals later. The Hidden-Higgs scenario was excluded for these scans and will be presented separately in Chapter 11.

Since theoretical constraints are a binary "yes/no" for each point (rather than a likelihood) we show availability plots. Later when we consider experimental constraints, we show 95% confidence regions. Theoretical constraints involve inequalities of some combination of generic (or Higgs) couplings. Therefore λ_i versus λ_j plots provide an ideal benchmark. Results are given in Figures 8.1 and 8.2.

The constraints are: (i) vacuum stability (including meta-stability), (ii) leading-order unitarity, (iii) perturbativity of all 4-scalar couplings and (iv) perturbativity of the Yukawa couplings. These were described in Section 4.1. Since Yukawa perturbativity provides no significant restriction of most planes, we do not include a separate contour
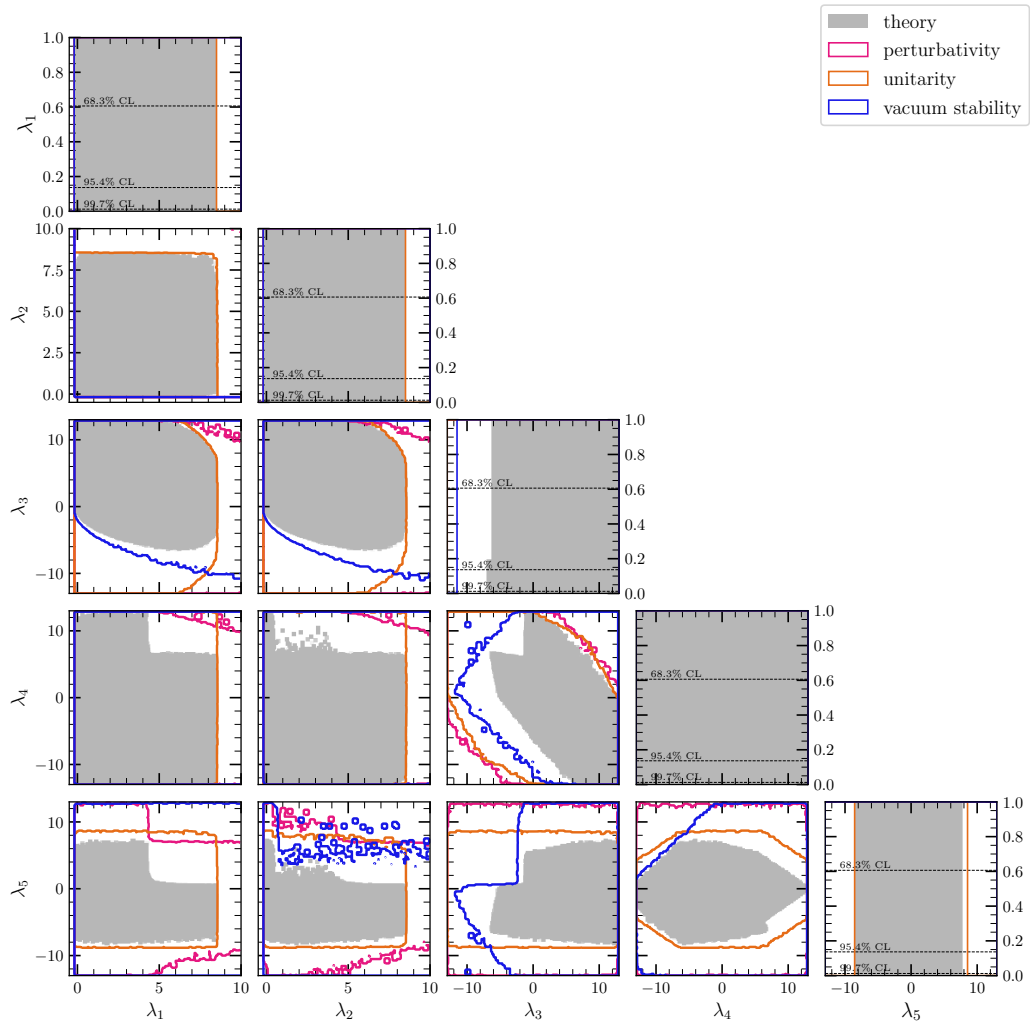
FIGURE 8.1: 1D and 2D availability plots of the theoretical constraints in planes of the generic couplings.

for this but do still include it in the combined theoretical constraint. Its main effect is to provide a lower bound on $\tan\beta$. For some theoretical constraints, the parameter ranges are unbounded in some directions. It is not practical to take parameters up to infinity and therefore we still include the generic perturbativity limits $\lambda_i < 4\pi$ in each theoretical constraint.

The generic couplings are not particularly intuitive since they are describing the interactions of the Higgs doublets in the high energy universe – before electroweak symmetry breaking. Therefore we provide a set of benchmark plots in Figure 8.3 which will also be used for the experimental constraints.[1] The reasons behind these parameter choices are as follows:

---

[1]After completing the results, a bug was identified that caused a region on the $\sqrt{M_{22}^2}$ verses m_{H^+} plot to become available and also caused some strange behaviour on $\sqrt{M_{22}^2}$ versus $\log(\tan\beta)$. No other plots were affected. These plots should look more like the loop-level results on Figure 12.2.
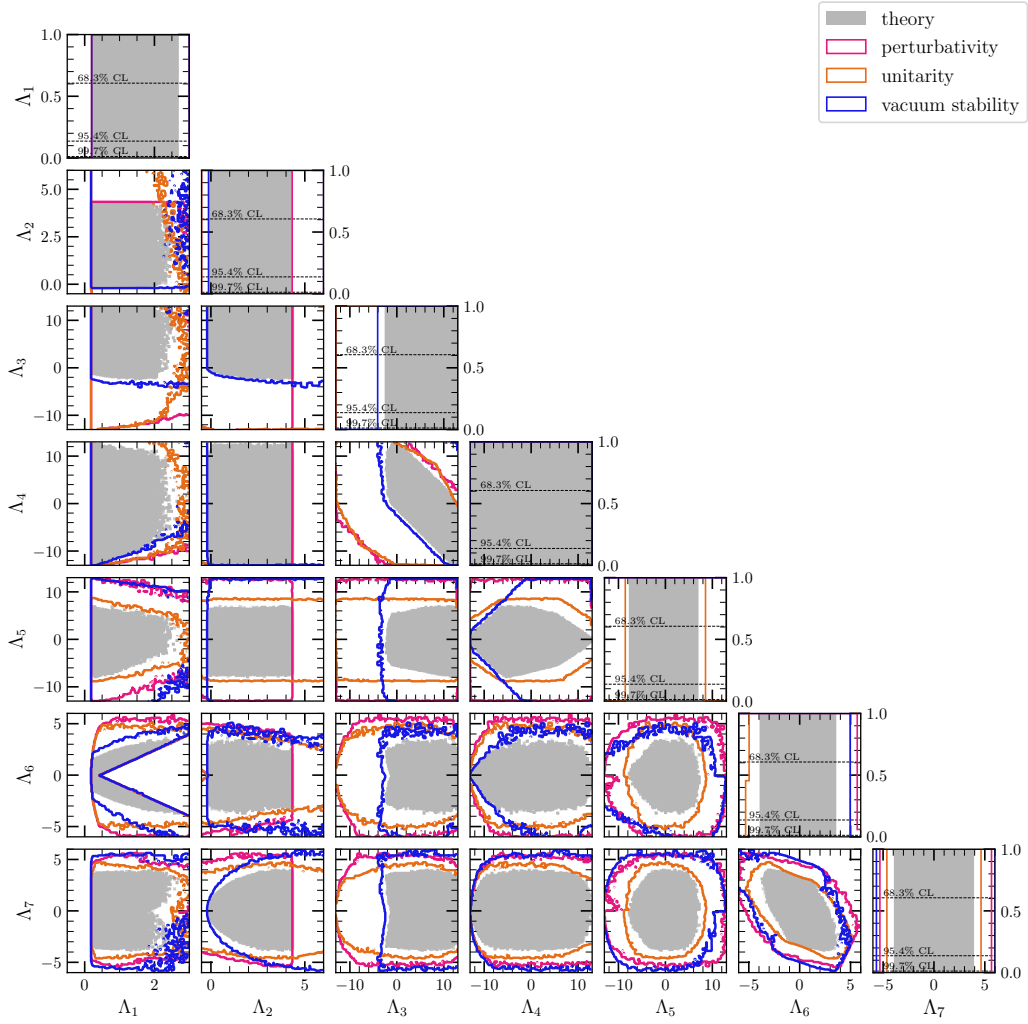
FIGURE 8.2: 1D and 2D availability plots of the theoretical constraints in planes of the Higgs couplings.

- H^+ is important for flavour observables since the charged scalar contributes to the FCCCs in a similar manner to W^+. The mass is important since it determines how "easily" we can produce a charged scalar – a smaller mass implies that the phase space is larger, hence the contribution to the Feynman amplitude is larger.

- $\tan\beta$ is also important for flavour observables since it determines the strength of the m_{H^+}-fermion interactions. It is also related to the neutral scalar-fermion interactions and thus is important for collider observables.

- $\cos(\beta - \alpha)$ is important since is determines the hVV and HVV coupling strengths used in collider observables and is also related to the neutral scalar-fermion couplings. When combined with $\tan\beta$, the latter couplings are fully determined.
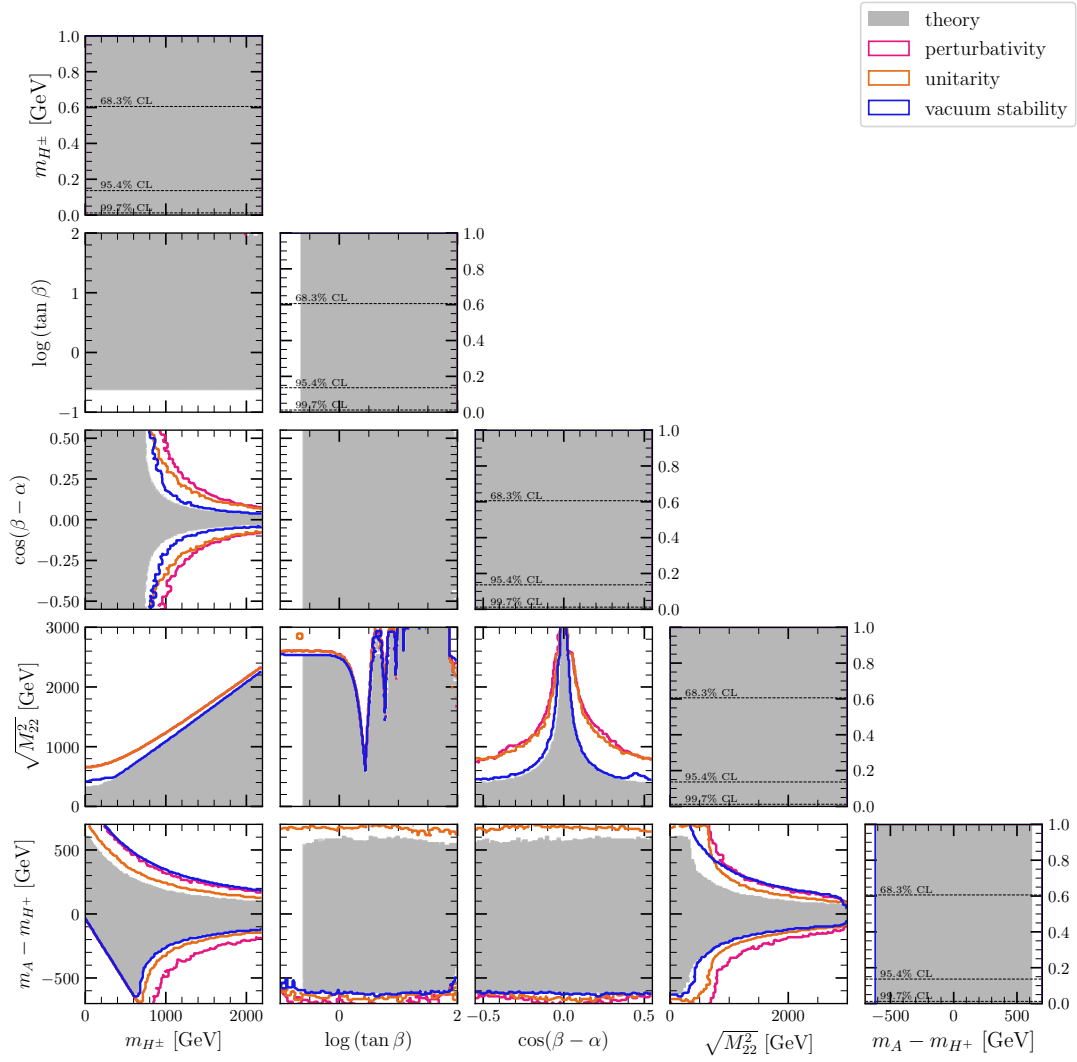
FIGURE 8.3: 1D and 2D availability plots of the theoretical constraints in planes of the benchmark parameters.

- $\sqrt{M_{22}^2}$ is a measure of the decoupling limit. When $M_{22}^2 \gg v^2$, the scalar masses m_{H^+}, m_A, and m_H are significantly larger than the SM-like Higgs mass, m_h.[2]

- $m_A - m_{H^+}$ is one of three mass splittings which are constrained by measurements the STU electroweak observables.

Notice that even without any experimental constraints imposed, $\cos(\beta - \alpha)$ is pushed towards 0 as M_{22}^2 is increased. This is because in the decoupling limit, we can show that $\cos(\beta - \alpha) \approx -v^2 \Lambda_6 / M_{22}^2$. Also notice that strong limits are already imposed on the mass splittings. The largest value of $m_{H^+} - m_A$ is roughly 1000 GeV, but this becomes

---

[2]The heavy scalar masses can be written $m_X^2 = M_{22}^2 + v^2 f(\Lambda_i)$ where $f(\Lambda_i)$ is some function of the Higgs basis couplings.

stricter at larger masses. This behaviour was anticipated from Equation 7.1, with the first given again below

$$\left(m_{H^+}^2 - m_A^2\right) = \frac{v^2}{2}\left(\lambda_5 - \lambda_4\right). \tag{8.1}$$

We can also write this as

$$(m_{H^+} - m_A) = \frac{v^2}{2}\frac{(\lambda_5 - \lambda_4)}{(m_{H^+} + m_A)}. \tag{8.2}$$

Now assuming the masses are large, we can take $(m_{H^+} + m_A) \approx 2\sqrt{M_{22}^2}$. Thus, the mass splittings have an approximate 1/mass fall-off in the high mass limit. The exact limit depends on the restriction on $\lambda_5 - \lambda_4$ which comes from the theoretical constraints. Finally, notice that the $\log(\tan\beta)$ versus m_{H^+} and $\log(\tan\beta)$ versus $\cos(\beta - \alpha)$ planes are completely open. Therefore, there are no theoretical limits on the scalar-fermion and scalar-boson couplings within our parameter ranges.

Chapter 9

Experimental Constraints in the 2HDM

In this chapter we highlight the individual effects of the experimental constraints. Note that in all cases theoretical constraints are also included. Results are presented as profile likelihoods ratios, as explained in Section 5. The 1D plots show the profile likelihood ratio, $\mathcal{L}/\mathcal{L}_{\max}$, on the vertical axis with three dotted horizontal lines representing the confidence levels 1σ (68.3%), 2σ (95.4%), and 3σ (99.7%) from top to bottom respectively. The 2D plots show either (i) a 95.4% CL contour or (ii) a colour scale with the profile likelihood ratio values shown on a colour bar. Note that 95.4% CL corresponds to $\mathcal{L}/\mathcal{L}_{\max} = 0.046$ for 2D plots.

Care must be taken when comparing with other results as most often a Bayesian framework is assumed where the other parameters are marginalised over rather than profiled out. The two approaches give different looking results, and their statistical interpretation also differs.

9.1 Electroweak constraints

The electroweak sector observables we consider are the oblique S, T, and U parameters which test loop corrections to the W and Z boson propagators, as explained in Section 4.3.[1]

---

[1]The code also includes a likelihood for the anomalous magnetic moment of the muon. However, this constraint tends to push the couplings outside of the perturbative limits and is hence not well explained by the $\mathbb{Z}_2$-symmetric 2HDMs (it can be explained by the general 2HDM). We don't consider constraints from precision measurements of m_W since predictions of this quantity do not yet exist in the GAMBIT framework.
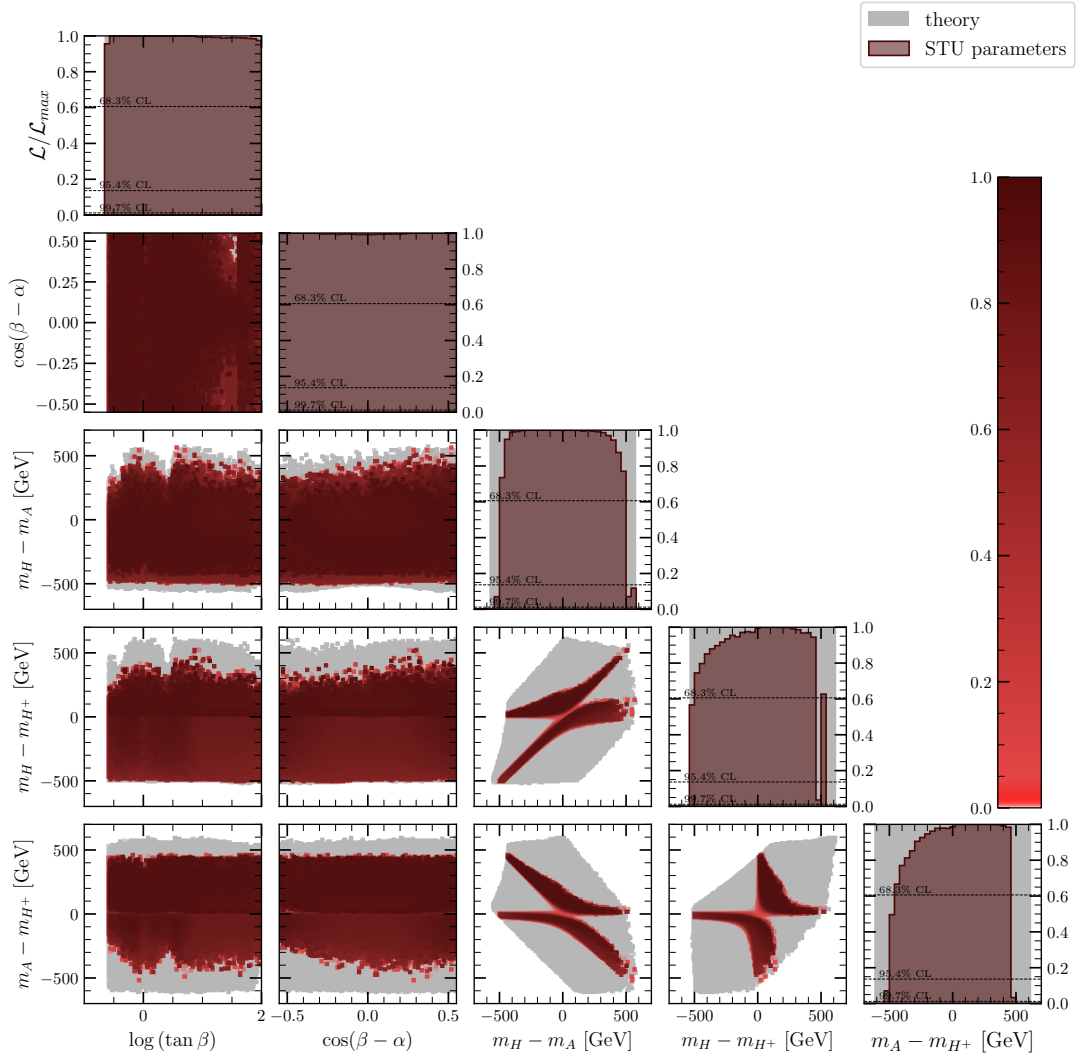
FIGURE 9.1: 1D and 2D profile likelihood ratio plots of the STU oblique constraints in planes of the angles and mass-splittings.

Just like the theoretical constraints, the electroweak observables are model independent. Hence, we only display results for the Type-II 2HDM. The expressions for the STU parameters in the 2HDM depend on the mass splittings: $m_H - m_A$, $m_{H^+} - m_A$ and $m_{H^+} - m_H$. Thus, the ideal benchmark plots for these constraints are mass splitting planes. We show these in Figure 9.1. In the simplified example from Equation 4.39, we found that there are actually two solutions for the mass splittings. Likewise, we see two regions that are separated by an invisible line in the mass splitting versus mass splitting planes. Notice that the two regions have approximately the same shape but are rotated 180° about the centre of the plots.

The two regions may also show up on other planes of interest. For example, they are barely visible on the generic coupling planes in Figure 9.2. We shall discuss this point further in the combined fits. When plotted against other parameters, the mass-splittings are not
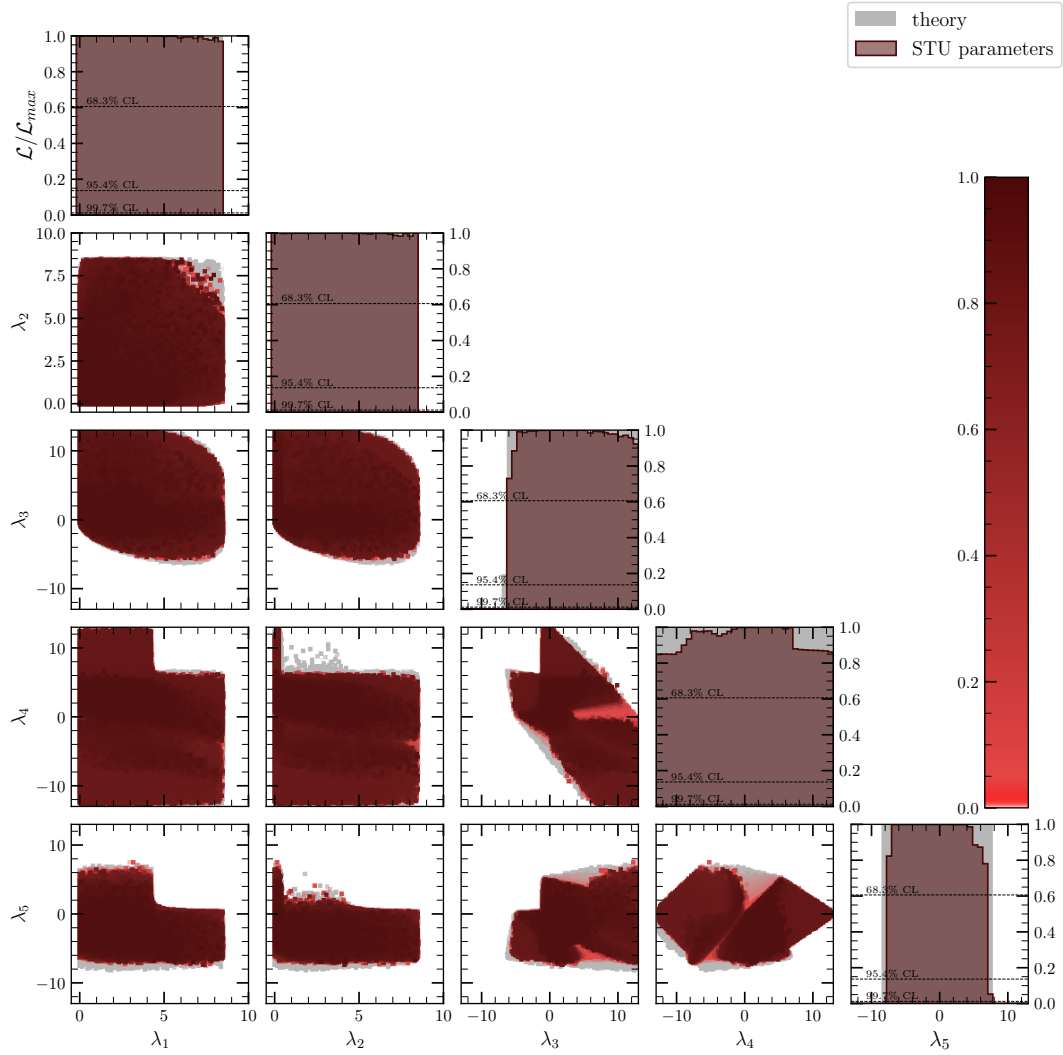
FIGURE 9.2: 1D and 2D profile likelihood ratio plots of the STU oblique constraints in planes of the generic couplings.

limited significantly below the theoretical limits. In fact, the theoretical constraints set a stronger limit for $\sqrt{M_{22}^2}$ above 1000 GeV (we shall see an example of this later in Figure 10.6).

Figure 9.3 shows the plots of the STU parameters, although these are done at low sampling density. The 2HDM can quite comfortably fit the experimental values from Equation 4.40.

9.2 Collider constraints

Collider constraints limit the Higgs signal rates measured at particle collider experiments. In particular, HiggsBounds provides upper bounds on the signal rates of additional
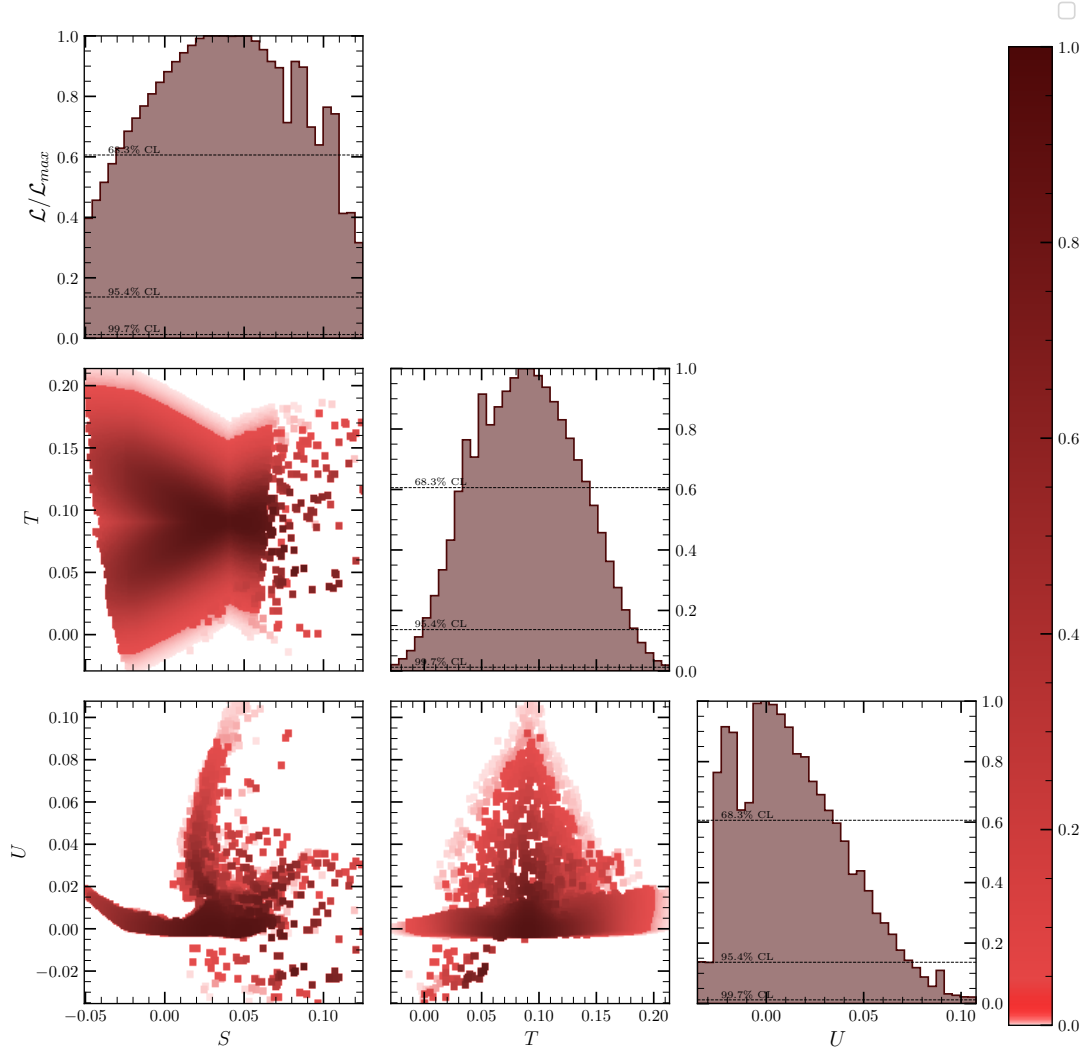
FIGURE 9.3: 1D and 2D profile likelihood ratio plots of the STU oblique constraints in planes of the S, T, and U parameters.

scalars while HiggsSignals fits the observed SM-like Higgs boson signal rates against experimental results. The results are shown in Figures 9.4 and 9.5 for Type-I and Type-II respectively. We show separate contours for the following likelihoods: (i) HiggsBounds, (ii) HiggsSignals (run1), (iii) HiggsSignals (SS), HiggsSignals (STXS), and (iv) combined collider likelihoods. Here SS and STXS are the LHC run 2 signal strengths and simplified template cross-sections respectively – both of which were explained in Section 4.2. To avoid double-counting, the combined collider likelihood only includes the STXS and not SS for the run 2 LHC data.

We see that $\cos{(\beta - \alpha)}$ is constrained to be close to 0. In this limit, known as the alignment limit, the Higgs-gauge couplings are SM-like for all 2HDM types (c.f. Table 3.5). The scalar-fermion couplings are model-dependent (c.f. Table 3.7), although in
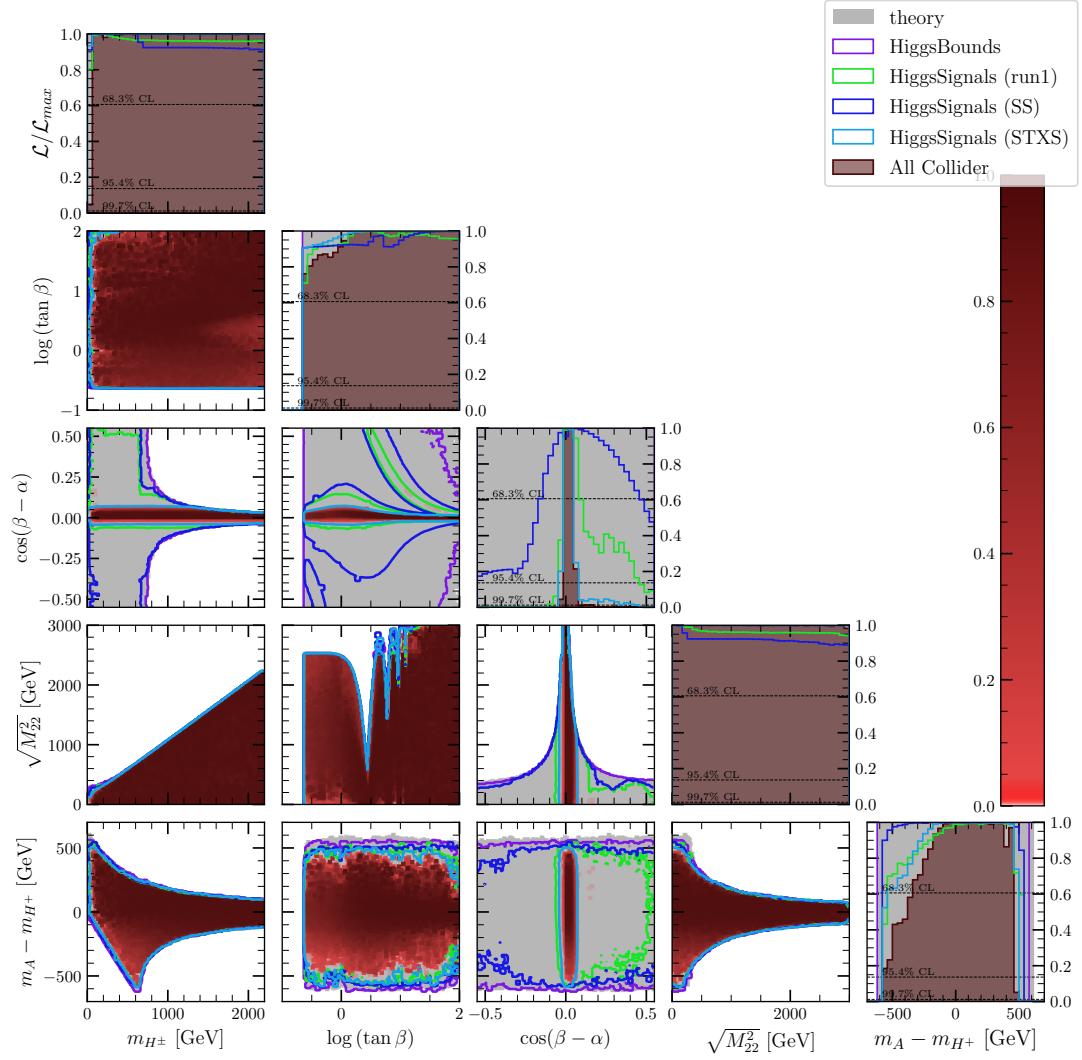
FIGURE 9.4: (Type-II) 1D and 2D profile likelihood ratio plots of the collider constraints in planes of the benchmark parameters.

either case only depend on the $\cos{(\beta - \alpha)}$ and $\tan{\beta}$ parameters.[2] We can write these couplings as

$$\Delta k_1 = \frac{\cos{\alpha}}{\sin{\beta}} - 1 = \sqrt{1 - \cos^2{(\beta - \alpha)}} + \frac{\cos{(\beta - \alpha)}}{\tan{\beta}} - 1$$
$$\approx -\frac{1}{2}\cos^2{(\beta - \alpha)} + \frac{\cos{(\beta - \alpha)}}{\tan{\beta}}, \tag{9.1}$$

$$\Delta k_2 = -\frac{\sin{\alpha}}{\cos{\beta}} - 1 = \sqrt{1 - \cos^2{(\beta - \alpha)}} - \cos{(\beta - \alpha)}\tan{\beta} - 1$$

---

[2]This is only true at tree level since we may also have loops containing heavy scalars. Such contributions are small, and we don't consider them in our scans.
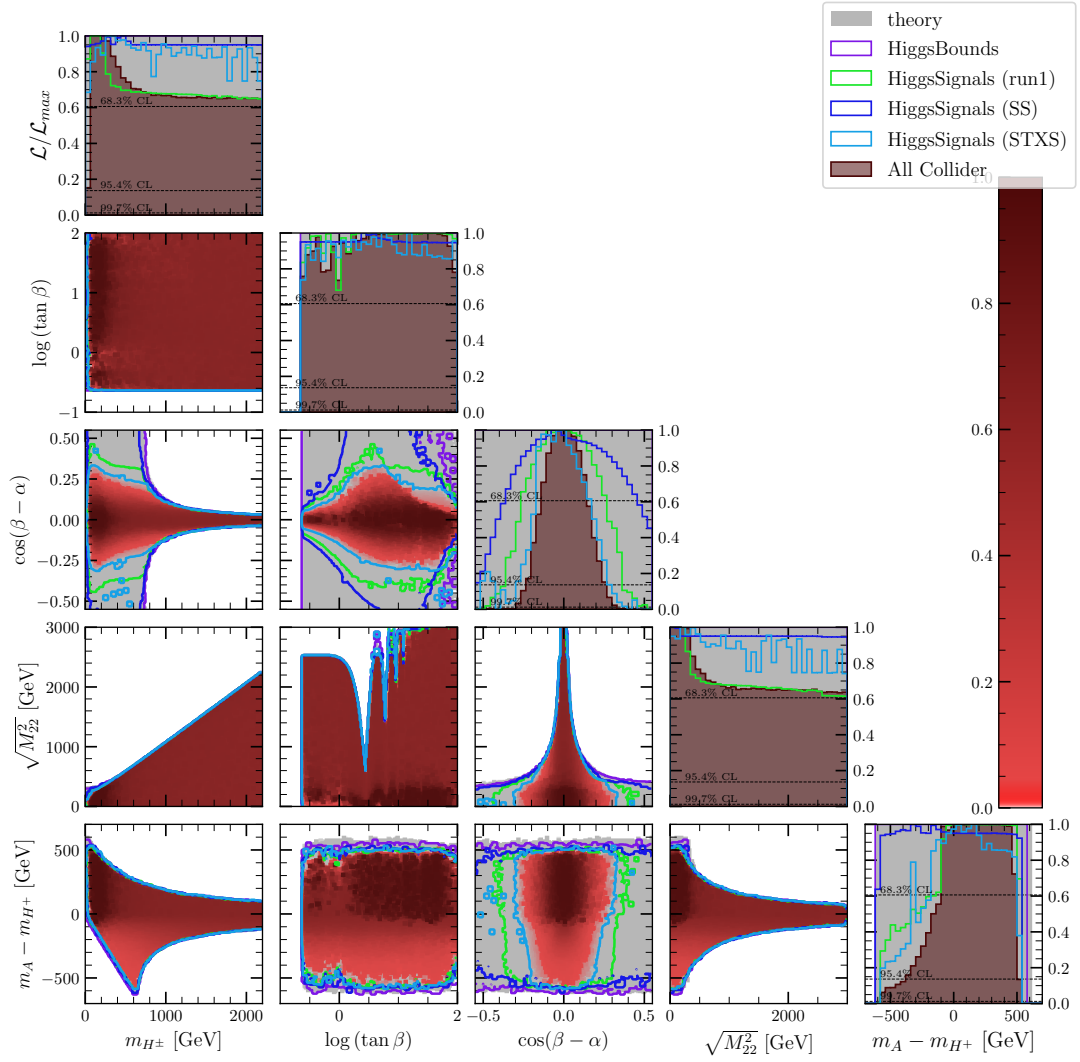
FIGURE 9.5: (Type-I) 1D and 2D profile likelihood ratio plots of the collider constraints in planes of the benchmark parameters.

$$\approx -\frac{1}{2}\cos^2\left(\beta - \alpha\right) - \cos\left(\beta - \alpha\right)\tan\beta. \tag{9.2}$$

Here, Δk_2 is the (deviation of the) reduced hd_id_i and he_ie_i coupling in the Type-II 2HDM, while all other reduced hff couplings are equal to Δk_1 (for both Type-I and Type-II). Since the SM is a good fit to collider data, both reduced couplings are close to 0. This may happen when $\cos\left(\beta - \alpha\right)$ is close to 0, or due to cancellation of the above terms. The latter case leads to the special arm regions on Figure 9.4 but these disappear in the combined fit. The arm above $\cos\left(\beta - \alpha\right) = 0$ corresponds to $\tan\beta = 2/\cos\left(\beta - \alpha\right)$ while the arm below corresponds to $\tan\beta = -\frac{1}{2}\cos\left(\beta - \alpha\right)$.

Notice that Δk_1 gets larger at low $\tan\beta$ while Δk_2 gets larger at high $\tan\beta$. Since the Type-I 2HDM only involves Δk_1, the parameter space remains open at large $\tan\beta$ where

the Type-I scalar-fermion couplings are SM-like. This is of course ignoring the effects of the effective $h\gamma\gamma$ and hgg couplings which eventually cause the parameter space to close at high $\tan\beta$. In the Type-II 2HDM, which depends on both Δk_1 and Δk_2, the parameter space is forced to the alignment limit at both high and low $\tan\beta$, and is slightly open somewhere in the middle. In the Type-II 2HDM there is no true SM-like limit for the scalar-fermion couplings.

The exclusion bounds from HiggsBounds are not visible here as they also depend on the masses of the heavy scalars. We need smaller masses of $m_H \lessapprox 600$ GeV before this constraint becomes visible. Note that the high $\tan\beta$ region away from the alignment limit is not constrained by HiggsBounds despite how the plot looks – this region is finely tuned and hence difficult to sample.

9.3 Flavour Constraints

In the $\mathbb{Z}_2$-symmetric 2HDMs, extra FCCCs are provided by the charged Higgs, H^+. This adds additional contributions to flavour observables at leading order. The flavour observables are calculated with SuperIso using the Wilson coefficients as inputs, as described in Section 4.4. The Wilson coefficients depend on the Yukawa couplings which, for $\mathbb{Z}_2$-symmetric 2HDMs, are fully determined by the $\tan\beta$ parameter (c.f. Equation 3.59), although there is a model-dependence (c.f. Γ_A^d in Table 3.6). We include a total of 18 flavour likelihood components listed in Table 9.1. The SL likelihood actually includes 11 observables: $Br\left[B \to D\tau\ v_\tau\right]/Br\left[B \to Dlv_l\right]$, $Br\left[B \to D^*\tau\ v_\tau\right]/Br\left[B \to D^*lv_l\right]$, $Br\left[B \to D\ e\ v_e\right]/Br\left[B \to D\mu v_\mu\right]$, $Br\left[B \to D\mu\ v_\mu\right]$, $Br\left[B \to D^*\mu\ v_\mu\right]$, $Br\left[B \to D\tau\ v_\tau\right]$, $Br\left[K^\pm \to \mu^\pm\ v_\mu\right]/Br\left[\pi^\pm \to \mu^\pm v_\mu\right]$, $Br\left[D_s^\pm \to \tau^\pm\ v_\tau\right]$, $Br\left[D_s^\pm \to \mu^\pm\ v_\mu\right]$, $Br\left[D^\pm \to \mu^\pm\ v_\mu\right]$, and $Br\left[D^\pm \to \tau^\pm\ v_\tau\right]$. The name is shorthand for 'semi-leptonic' although in reality only half of these observables are semi-leptonic while the remainder are fully leptonic. Notice that these all involve FCCCs, while all other observables in Table 9.1 involve FCNCs. In our plots we have renamed this combination to "$D, K, B \to D$ combo". We show individual flavour constraint plots for each model in Figures 9.6 and 9.7.

The RK and RK^* observables are given by the ratios

$$RK \equiv \frac{Br\left[B \to K\mu^+\mu^-\right]}{Br\left[B \to Ke^+e^-\right]}, \quad RK^* \equiv \frac{Br\left[B \to K^*\mu^+\mu^-\right]}{Br\left[B \to K^*e^+e^-\right]}. \tag{9.3}$$

Since most decay rate observations are close to the SM-predictions we expect to see SM-like behaviour. In all models, the $H^+\bar{u}_i P_L d_j$ coupling is proportional to $\cot\beta$ and we therefore expect to see a lower bound for $\tan\beta$ when this coupling becomes too large.
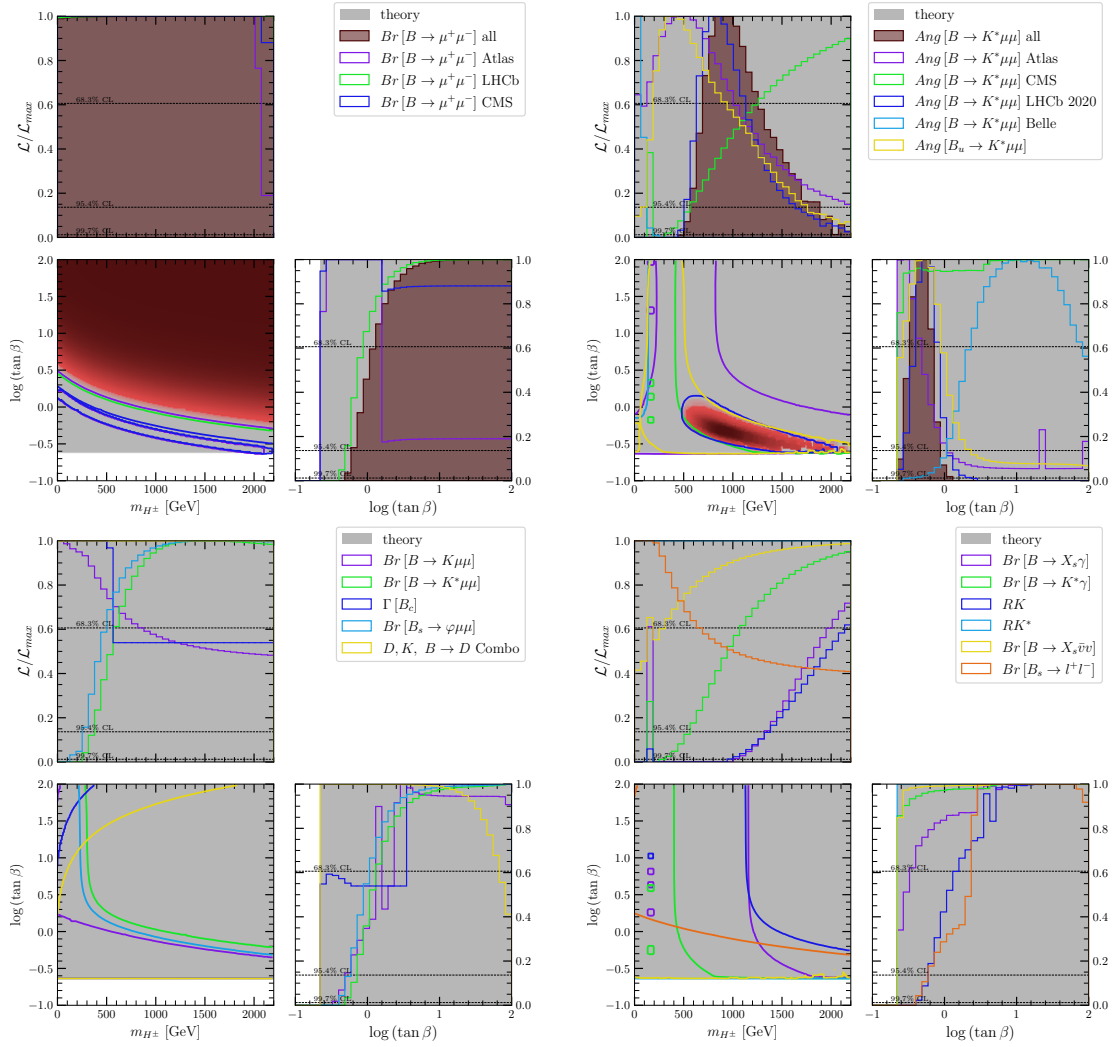
FIGURE 9.6: (Type II) 1D and 2D profile likelihood ratio plots of the individual flavour constraints against m_{H^+} and $\log(\tan\beta)$.

In the Type-I 2HDM, the $H^+\bar{u}_i P_R d_j$ coupling is also proportional to $\cot\beta$. This leads to an SM-like limit when $\tan\beta \to \infty$ – where both couplings vanish. In the Type-II 2HDM, this latter coupling is instead proportional to $\tan\beta$ and therefore both high and low $\tan\beta$ are expected to be excluded by flavour constraints.[3] In both models we have an SM-like limit for $m_{H^+} \to \infty$ where the heavy scalars are decoupled from the SM.

Some constraints may favour a different region to the SM scenario when the corresponding observables show an excess over the SM. This different region is required to fit the excess. We can see some examples in the above results. But the excess is small enough such that the combined flavour fits favour an SM-like scenario.

Besides $\tan\beta$, the mass of the charged Higgs strongly influences how large the 2HDM corrections to the decay rates are.

---

[3]Although the scenarios differ since $H^+\bar{u}P_L d$ includes a m_{u_i} factor while $H^+\bar{u}P_R d$ includes a m_{d_i} factor making the former more impactful.
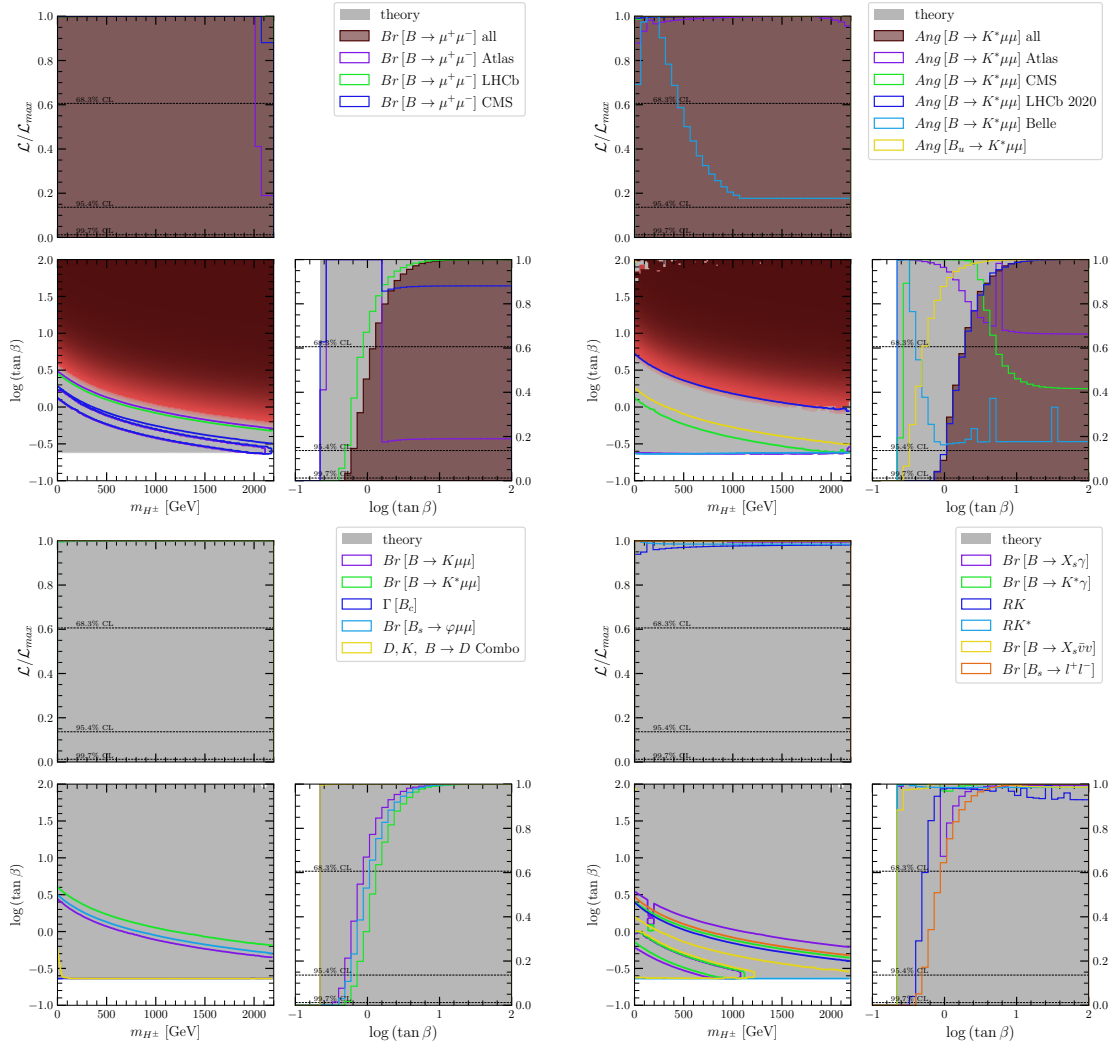
FIGURE 9.7: (Type I) 1D and 2D profile likelihood ratio plots of the individual flavour constraints against m_{H+} and $\log(\tan\beta)$.

The combined flavour fits are provided in Figures 9.8 and 9.9. In both models, a lower bound of $\tan\beta$ is set at around 1, and becomes larger at low m_{H+}. This is stronger than the Yukawa perturbativity limit.

Only the Type-II 2HDM sets a lower bound for m_{H+}. This is because in Type-I we still obtain SM-like behaviour for large $\tan\beta$.

The Type-II $B \to X_s\gamma$ observable provides an unusually high m_{H+} limit of around 1.1 TeV at the 95% confidence level. This is around 300 GeV higher than other works, such as [68]. The reason is still under investigation. It has been confirmed that the behaviour is coming from the SuperIso backend rather than GAMBIT.

The Type-II behaviour for the RK observable is unusual as it peaks far outside the plot. We do not scan such large $\tan\beta$ values but the results can be found in [68]. In their work, the RK observable was excluded from the combined fits as it seems to be

GAMBIT Name	Observable
B2Xsnunu	$Br\left[B \to X_s \bar{v}v\right]$
Bc_lifetime	$\Gamma\left[B\right]$
SL	$D, K,\ B \to D\ Combo$
b2sgamma	$Br\left[B \to X_s \gamma\right]$
B2Kstargamma	$Br\left[B \to K^* \gamma\right]$
Bs2phimumuBr	$Br\left[B_s \to \varphi \mu \mu\right]$
RK	RK
RKstar	RK^*
B2mumu (Atlas,LHCb,CMS)	$Br\left[B \to \mu^+ \mu^-\right]$
B2KstarmumuBr_LHCb	$Br\left[B \to K^* \mu \mu\right]$
B2KmumuBr_LHCb	$Br\left[B \to K \mu \mu\right]$
Bu2KstarmumuAng_LHCb_2020	$Ang\left[B_u \to K^* \mu \mu\right]$
B2KstarmumuAng (Atlas,CMS,LHCb_2020,Belle)	$Ang\left[B \to K^* \mu \mu\right]$

TABLE 9.1: flavour observables used in the 2HDM scans. Here 'Br' means branching ratio and 'Ang' means angular observables. Note that there are actually 3 likelihoods for $Br\left[B \to \mu^+ \mu^-\right]$ for the 3 experiments listed. Likewise there are 4 likelihoods for $Ang\left[B \to K^* \mu \mu\right]$.

incompatible with the other flavour constraints (although it was also mentioned that it did not significantly alter the combined fits). In our fits all flavour observables are included, and thus the lower bound for m_{H^+} may be slightly larger than other works.

For the combined flavour fits, the lower bound for m_{H^+} in the Type-II model was 1.1 TeV at the 95% confidence level. Although not shown here, it was found to be 200GeV lower when the RK observable is excluded.

Since the Type-II 2HDM gives a rather large lower bound for m_{H^+}, we can begin to see the effects on other planes. Firstly, most of the m_{H^+} versus $\cos\left(\beta - \alpha\right)$ plane is excluded. Since the theoretical constraints limit the value of $\cos\left(\beta - \alpha\right)$ at large masses, we also have a severe restriction of $\cos\left(\beta - \alpha\right)$ which is competitive with the collider constraints. The limits on the mass splittings can also be seen clearly in Figure 9.10. We shall have more to say about this for the global fits.
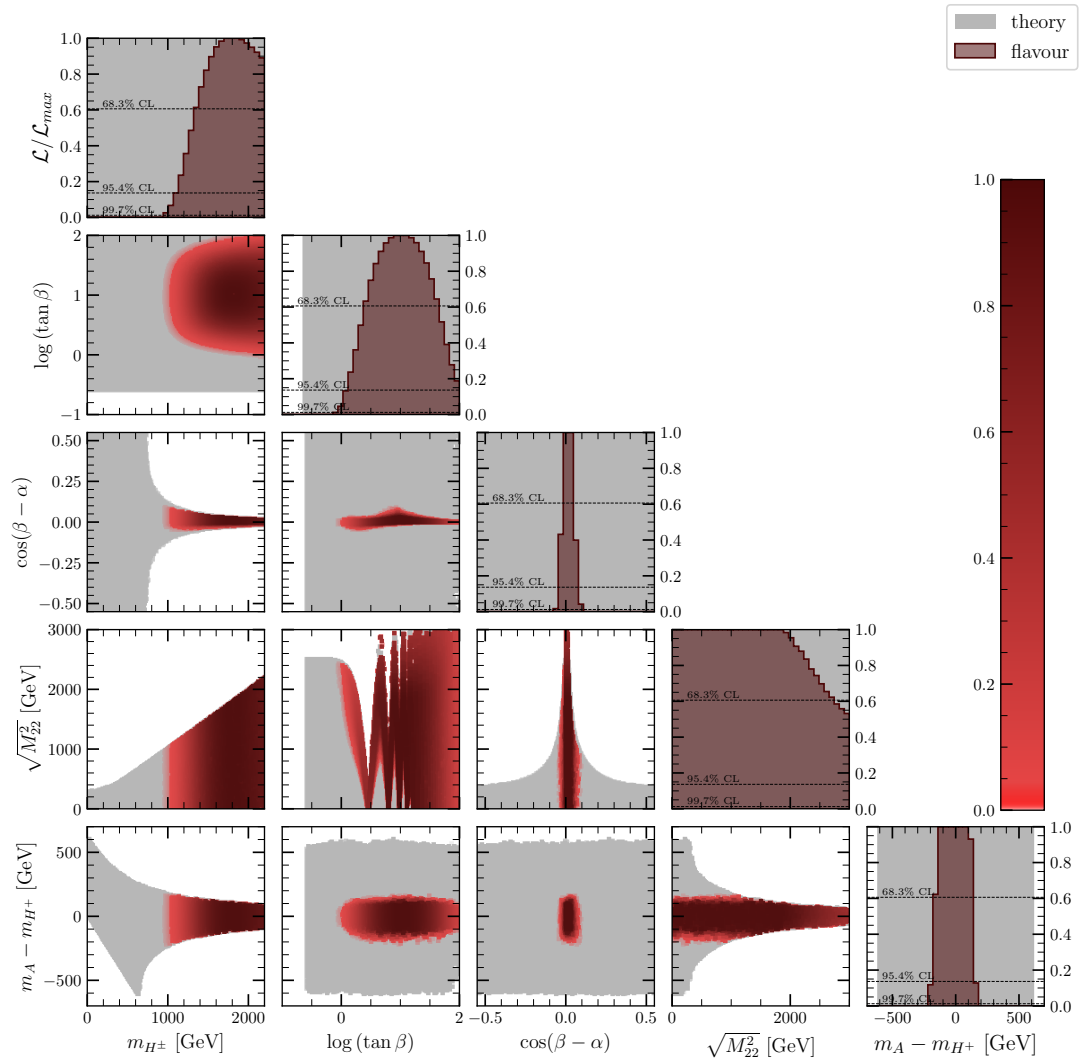
FIGURE 9.8: (Type-II) 1D and 2D profile likelihood ratio plots of the combined flavour constraints in planes of the benchmark parameters.
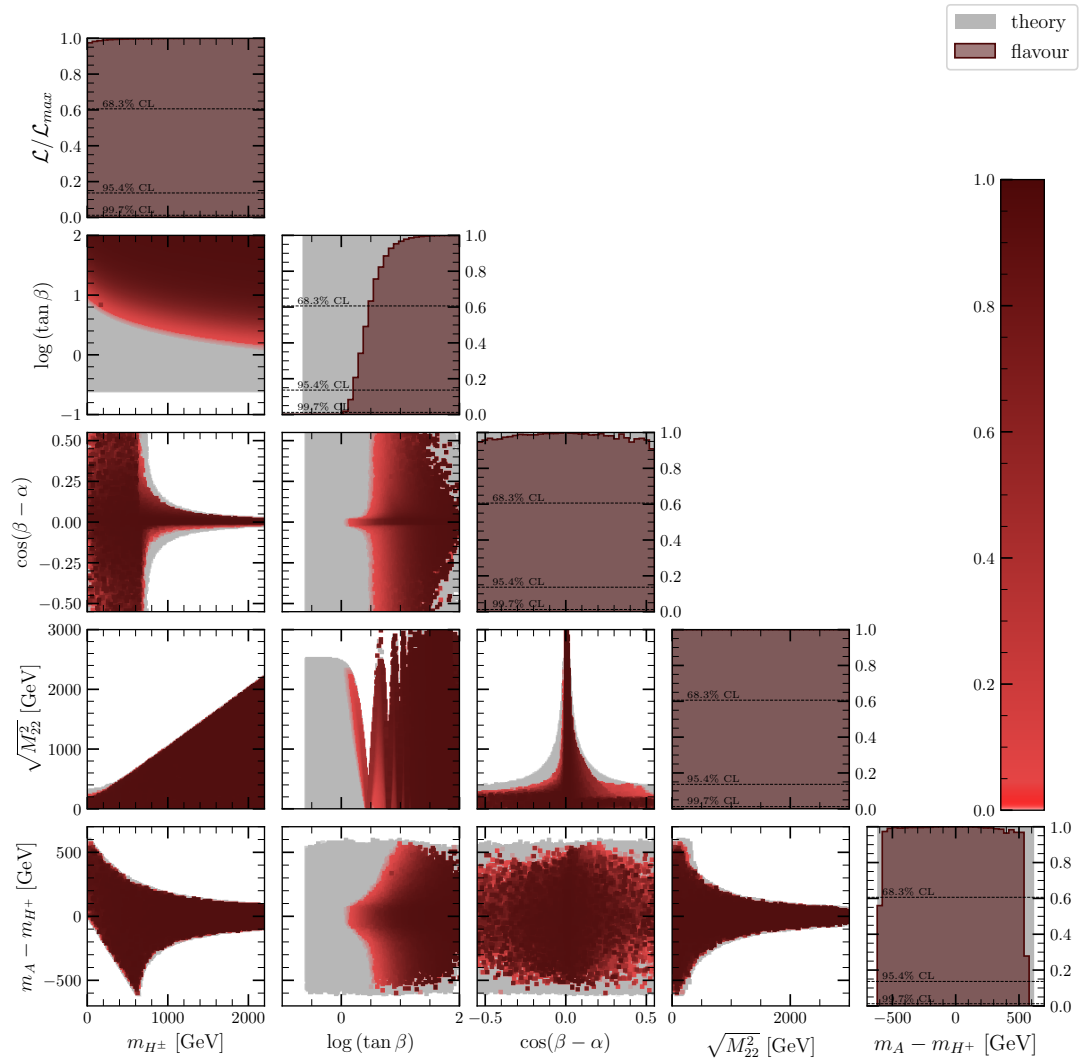
FIGURE 9.9: (Type-I) 1D and 2D profile likelihood ratio plots of the combined flavour constraints in planes of the benchmark parameters.
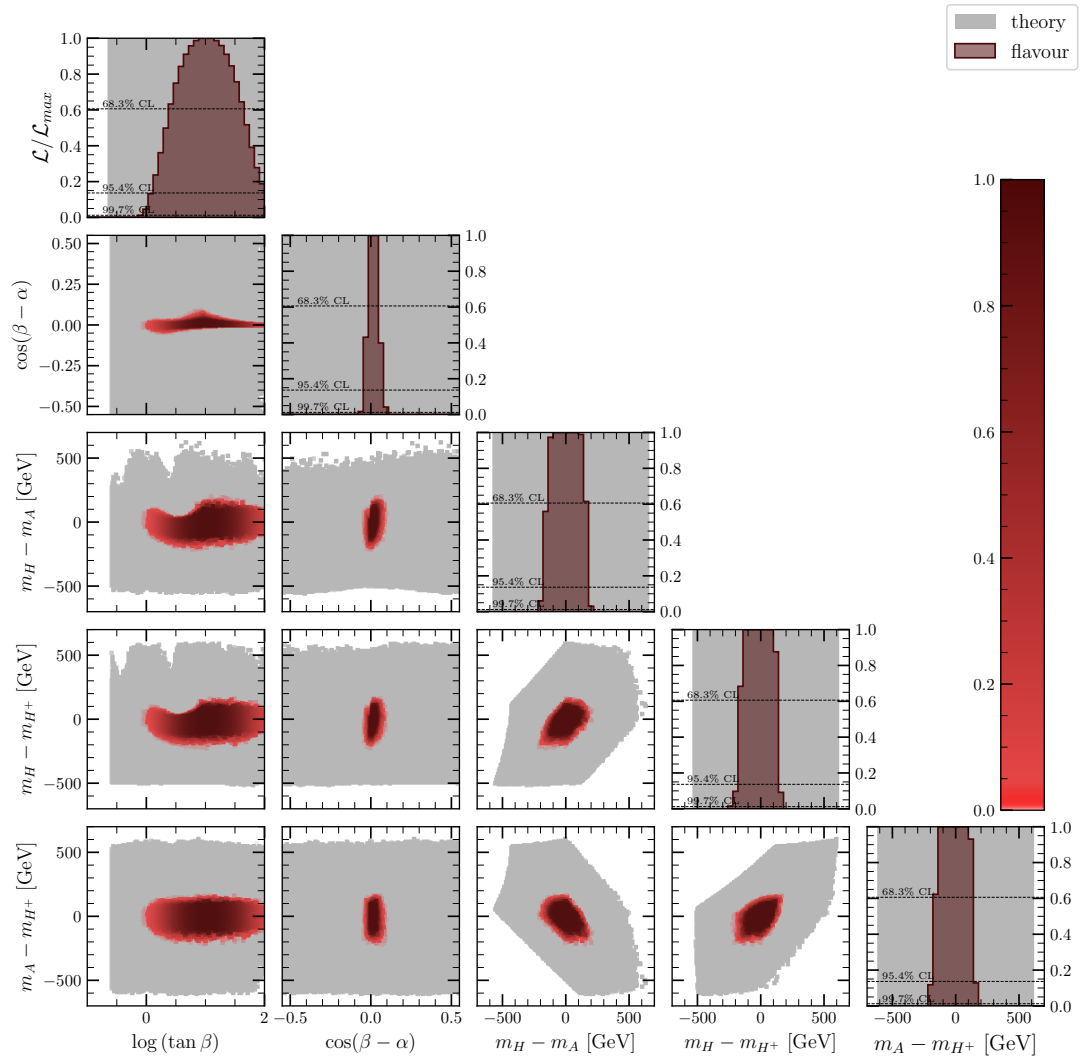
FIGURE 9.10: (Type-II) 1D and 2D profile likelihood ratio plots of the combined flavour constraints in planes of the angles and mass-splittings.

Chapter 10

Global fits of the 2HDM

In this chapter, we present results with all constraints turned on simultaneously in Figures 10.1 (Type-II) and 10.2 (Type-I). The best-fits points and a 95% confidence interval for all parameters are provided in Tables 10.1 and 10.2.

Starting with Type-II, in Figure 10.1 we see that the lower bound for m_{H^+} has remained at 1.1 TeV at the 95% confidence level, while the best fit is at 1.8 TeV. The limit is set by the flavour observables while the electroweak and collider observables have no impact. The lower limit of $\tan\beta$ is at around 1.7, and the peak is 15, which are again set by the flavour observables.

We see that both flavour and collider constraints have a large impact on the $\cos(\beta - \alpha)$ versus $\tan\beta$ plane, as anticipated in the previous section. We are left with a very narrow strip of available parameter space. The peak value of $\cos(\beta - \alpha)$ is set to 0.0027 with a 95% confidence interval of -0.0016 to 0.02. The large lower bound for m_{H^+} also limits the mass splittings (as a result of the theoretical constraints). In the $m_A - m_{H^+}$ planes we can just make out two regions above and below zero. These correspond to the two solutions for the electroweak constraints.

Now looking at Figure 10.2, we see that the mass-splittings are constrained to be close to zero, within a small circle. This is a result of the flavour and theoretical constraints. Hence, we have now localised the two regions that were set by the electroweak constraint to be within this small circle. These regions are now more easily distinguished on other planes of interest since they no longer cover such a large region and are less likely to overlap.

The results in Figure 10.3 are also interesting. So far, we did not discuss the important role of λ_2. It can be shown that in the limit $\tan\beta \to \infty$ we have $m_h = v^2\lambda_2$ and thus λ_2 corresponds to the SM Higgs coupling. Meanwhile, $m_H = m_{12}^2 \tan\beta$. These limits can be

Parameter	Best Fit	95% CI
λ_1	2.9	0.0024 to 7.4
λ_2	0.24	7.9e-05 to 0.44
λ_3	10.9	-1.05 to 12.5
λ_4	-9.46	-12.2 to 10.8
λ_5	0.82	-5.0 to 3.7
m_h	125.12	124.64 to 125.54
m_H	1800	1000 to 3000
m_A	1740	1100 to 2960
$m_{H^\pm}$	1830	1160 to 2970
$\tan_\beta$	15	1.7 to 77
α	-0.065	-0.51 to -0.012
Λ_1	0.2586	0.2564 to 0.2697
Λ_2	2.9	0.009 to 4.2
Λ_3	10.9	-1.06 to 12.7
Λ_4	-9.47	-12.2 to 10.8
Λ_5	0.82	-5.0 to 3.7
Λ_6	-0.14	-0.91 to 0.13
Λ_7	-0.04	-3.0 to 0.8
$\sin(\beta - \alpha)$	0.99999622	0.99980528 to 1.0
$\cos(\beta - \alpha)$	0.0027	-0.0016 to 0.02
$\sqrt{M_{22}^2}$	1400	7.4 to 2800
$m_H - m_A$	14	-110 to 51
$m_H - m_{H^+}$	-73	-150 to 65
$m_A - m_{H^+}$	-87	-113 to 117

TABLE 10.1: (Type-II) Best fit points and 95% confidence intervals for the combined fit.
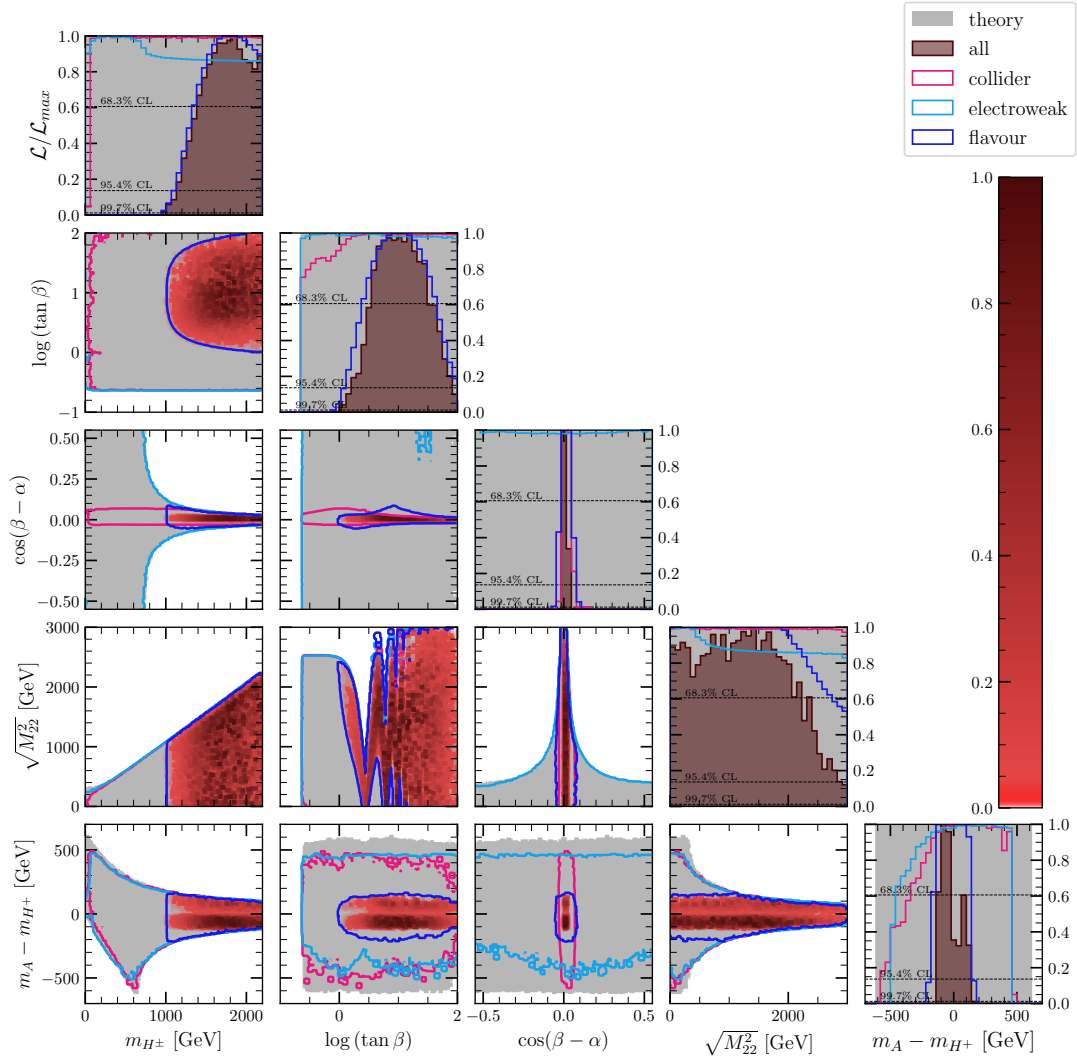
FIGURE 10.1: (Type-II) 1D and 2D profile likelihood ratio plots of the combined fit in planes of the benchmark parameters.

derived by starting with the mixing matrices in Equation 3.32. In this scenario we have the second doublet becoming SM-like with $h_1 \approx h$ and $v_2 \approx v$. Therefore, any constraint that sets a lower bound for $\tan\beta$ will also push λ_2 to the SM value of $\lambda = m_h^2/v^2 = 0.259$.

Note that if we had chosen a convention where the additional scalars appear in the second doublet rather than the first (as we do for the IDM), then we would instead have an upper bound for $\tan\beta$ due to the experimental constraints and λ_1 now corresponds to the SM quartic Higgs coupling in the limit $\tan\beta \to 0$. Also note that in the Higgs basis, we always have Λ_1 as the SM-like quartic coupling.

Figure 10.4 shows the physical basis parameters. We see lower bounds for m_H and m_A of 900 GeV. This is due to the lower bound on m_{H^+} discussed previously along with the restrictions on the mass splittings from the theoretical constraints. Finally, in Figure

Parameter	Best Fit	95% CI
λ_1	3.1	0.00019 to 5.6
λ_2	0.26	0.00015 to 0.88
λ_3	-0.61	-1.2 to 12
λ_4	5.2	-12 to 12
λ_5	-5.0	-6.26 to 5.48
m_h	125.06	124.66 to 125.57
m_H	220	150 to 2990
m_A	590	91 to 3000
$m_{H^\pm}$	210	94 to 3000
$\tan_\beta$	58	2.2 to 100
α	-0.038	-0.42 to 0.037
Λ_1	0.2582	0.2564 to 0.3928
Λ_2	3.14	0.00114 to 4.24
Λ_3	-0.61	-1.2 to 13.0
Λ_4	5.2	-12.0 to 12.0
Λ_5	-5.0	-6.26 to 5.39
Λ_6	0.01	-1.0 to 0.6
Λ_7	-0.061	-1.8 to 1.4
$\sin(\beta - \alpha)$	0.999779	0.98657 to 1.0
$\cos(\beta - \alpha)$	-0.02	-0.2 to 0.1
$\sqrt{M_{22}^2}$	250	1.9 to 2900
$m_H - m_A$	-372	-417 to 280
$m_H - m_{H^+}$	15	-290 to 290
$m_A - m_{H^+}$	390	-270 to 430

TABLE 10.2: (Type-I) Best fit points and 95% confidence intervals for the combined fit.

10.5 we show the bounds on the generic couplings. We can also see the effect of the SM-like Higgs collider constraints on the 1D h plot, where we notice that only a small region near 125.1 GeV is available. We can clearly see two distinct regions in the λ_3 and λ_4 planes. These correspond to the two solutions of the electroweak constraints.

Now we describe the Type-I 2HDM. Starting with Figure 10.6 there is no clear lower limit on m_{H^+}. But if we zoom in, it turns out that the collider constraints impose a lower bound of about 90 GeV. Meanwhile $\tan\beta$ has a lower bound of 2.2 due to flavour constraints (about the same as Type-II). We see that the flavour constraints still have
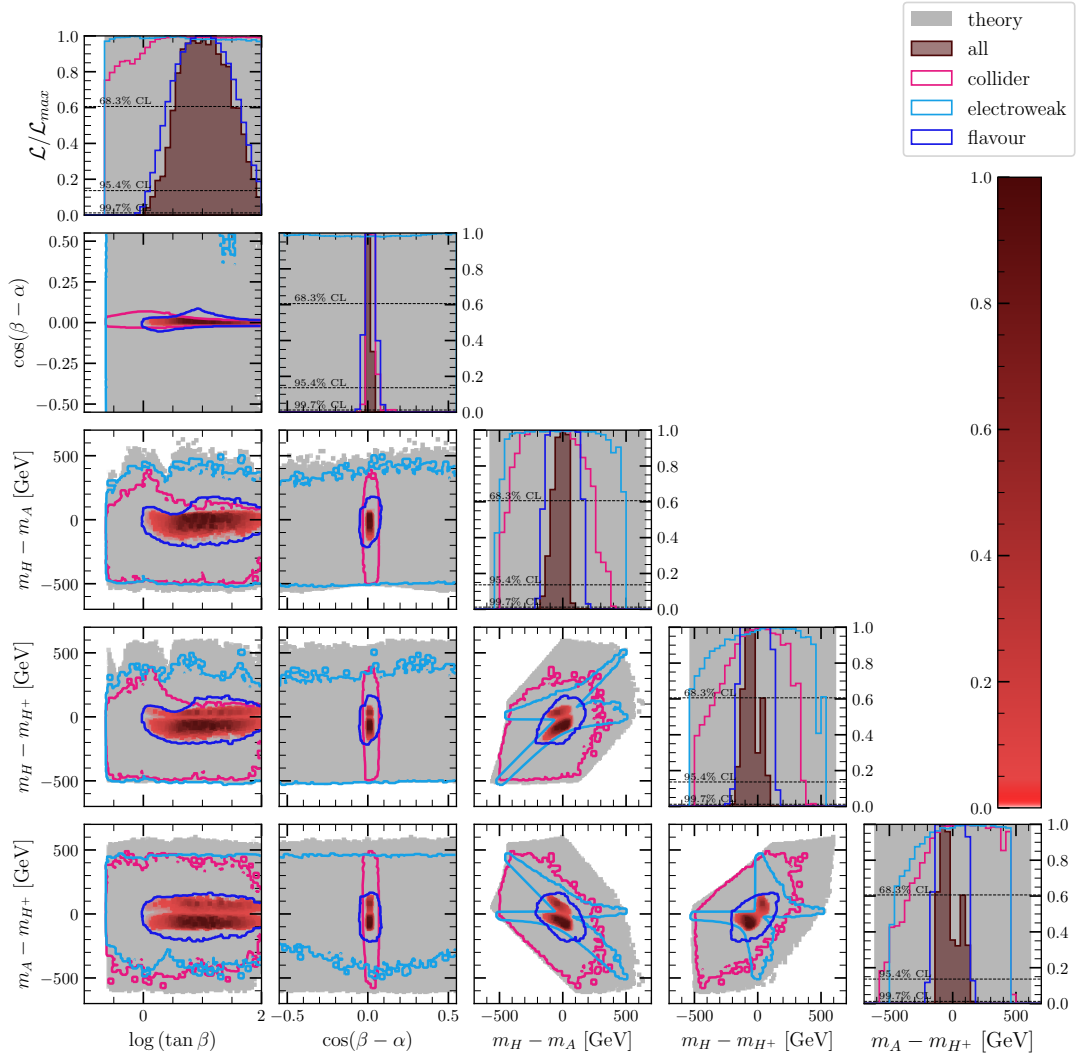
FIGURE 10.2: (Type-II) 1D and 2D profile likelihood ratio plots of the combined fit in planes of the angles and mass splittings.

an impact on the $\cos{(\beta - \alpha)}$ versus $\log \tan \beta$ plane up to $\tan \beta = 10$, after which only the collider observables have any impact. We see a much broader range for $\cos{(\beta - \alpha)}$, compared to Type-II.

In Figure 10.7, we see that there is no significant constraint of the mass-splitting planes in the Type-I 2HDM apart from the electroweak constraints. The lower bounds for the scalar masses are also quite low at 150, 91 and 94 for m_H, m_A, and m_{H^+} respectively. In fact, as shown on Figure 10.8, the peak likelihood happens at relatively low masses – around 220, 590, and 210 GeV respectively. Both the collider and electroweak observables have a slight preference for this low mass region while flavour constraints have no preference. Finally, in Figure 10.9, we see that the constraints on the generic couplings have a similar structure compared to Type-II, but the peaks of λ_3 and λ_4 are on the opposite side.
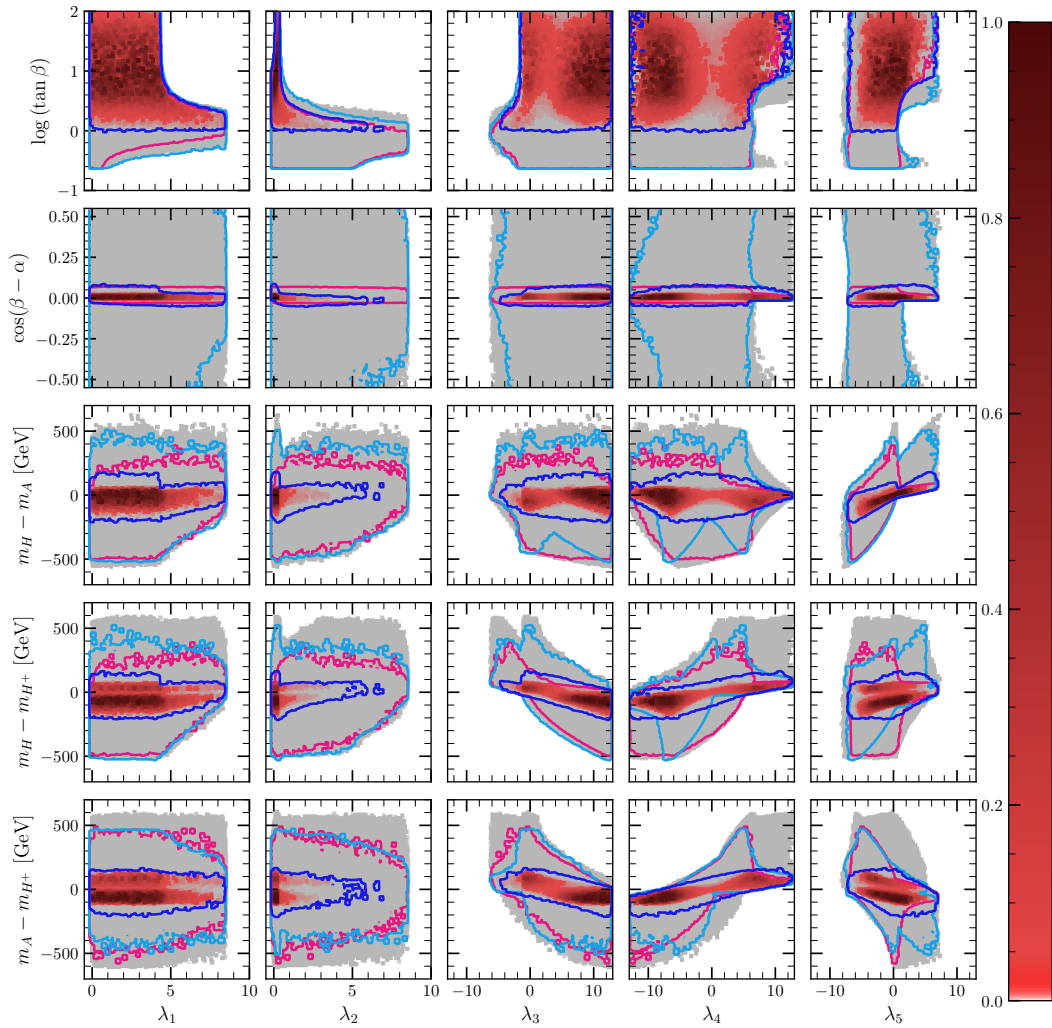
FIGURE 10.3: (Type-II) 1D and 2D profile likelihood ratio plots of the combined fit in planes of the angles/mass-splittings versus generic couplings. Colours have the same meaning as the previous plots.
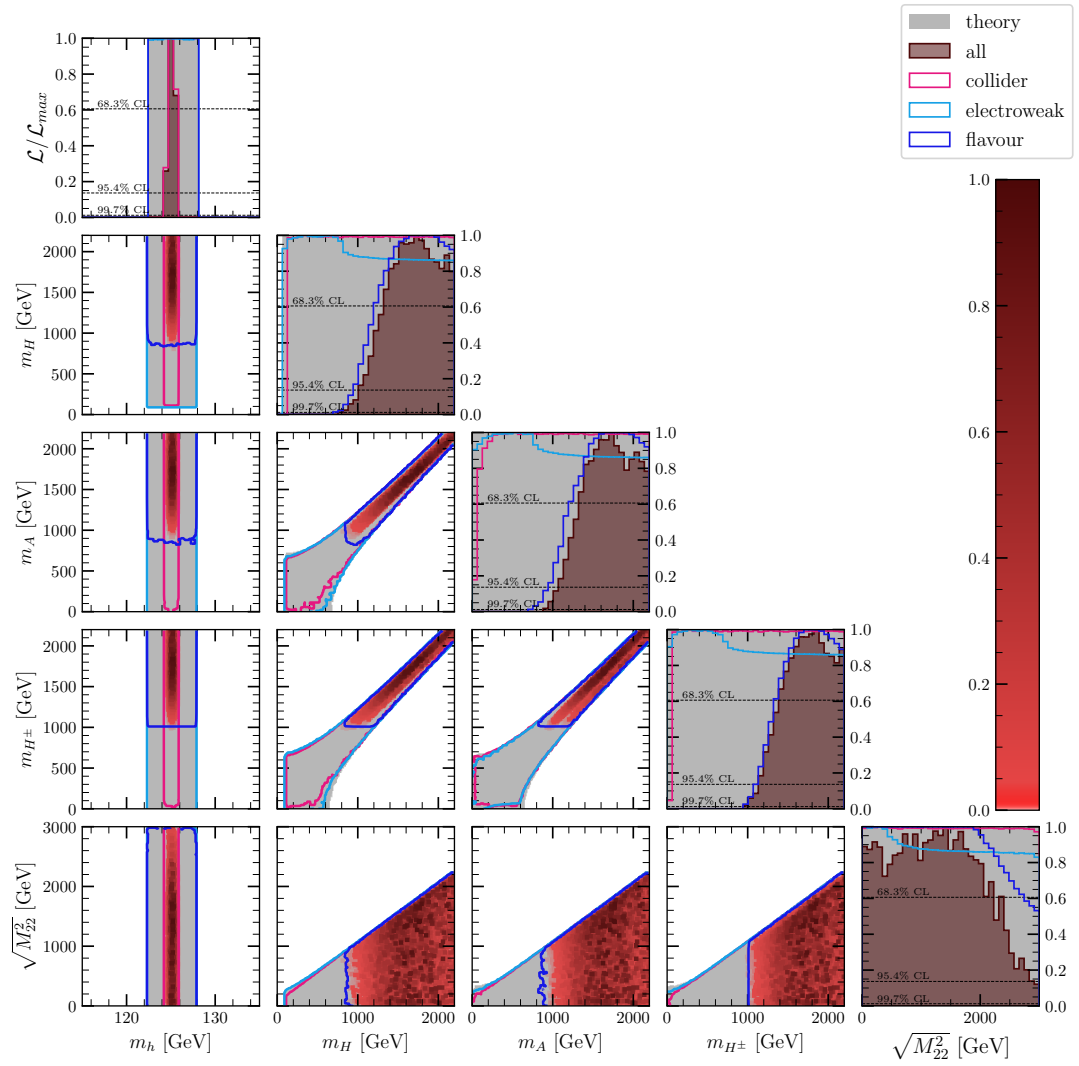
FIGURE 10.4: (Type-II) 1D and 2D profile likelihood ratio plots of the combined fit in planes of the mass parameters.
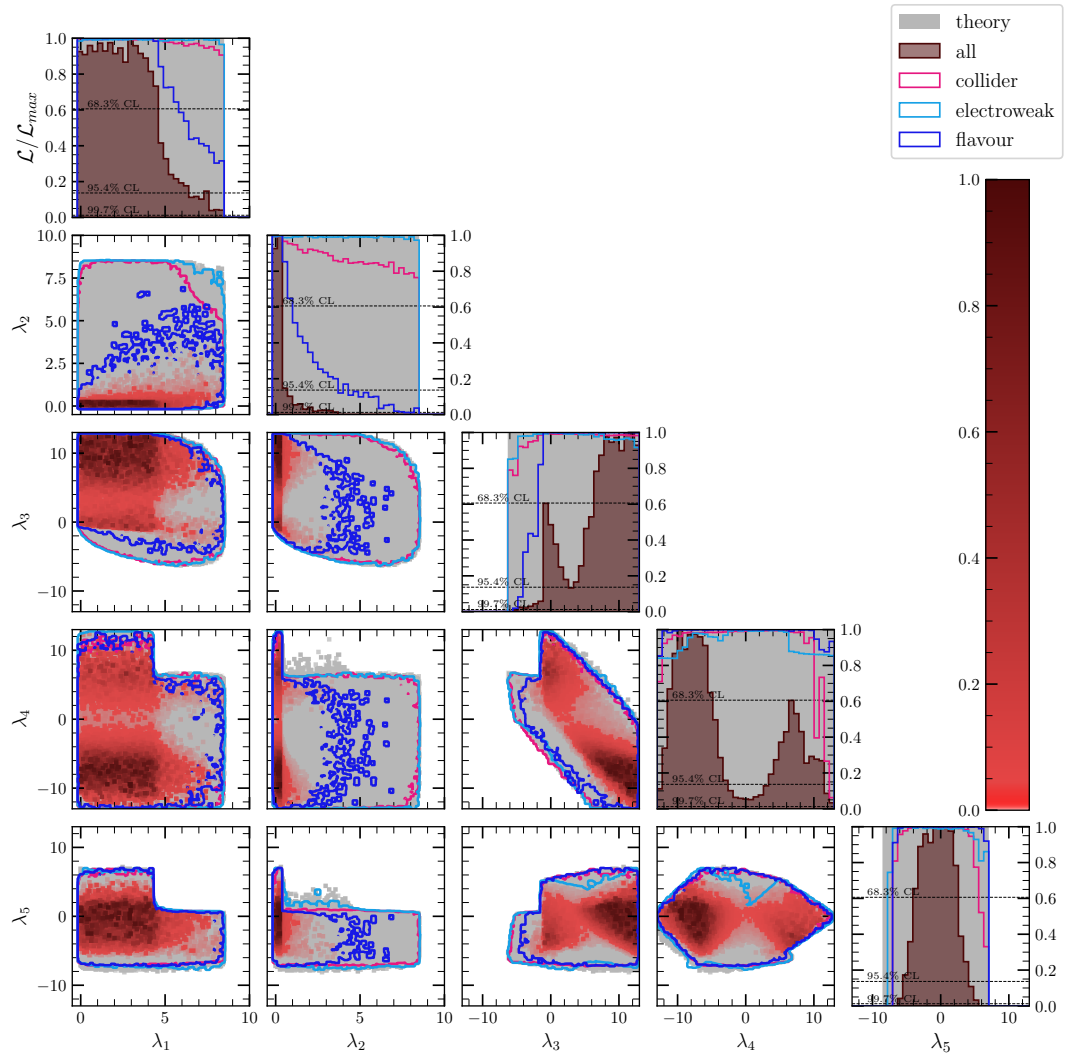
FIGURE 10.5: (Type-II) 1D and 2D profile likelihood ratio plots of the combined fit in planes of the generic couplings.
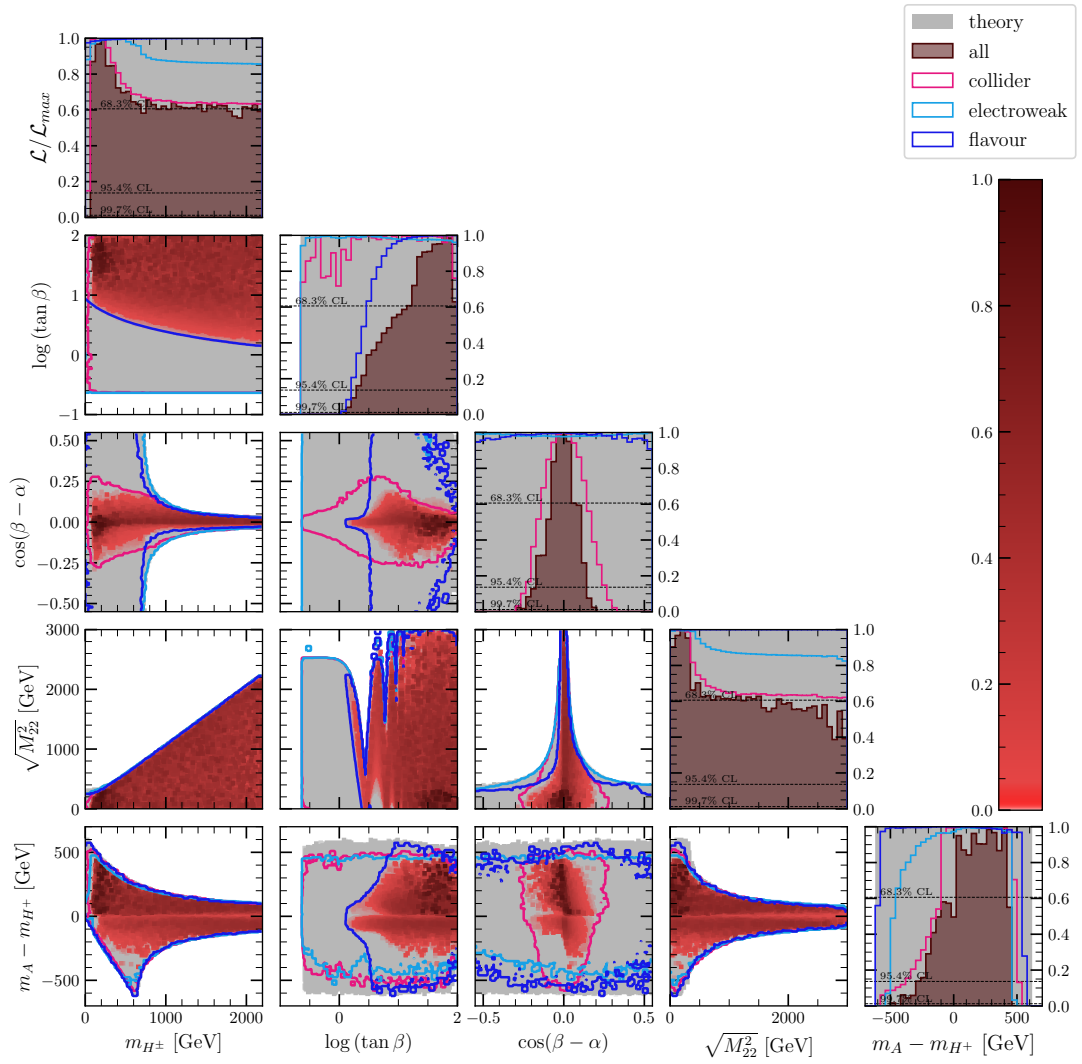
FIGURE 10.6: (Type-I) 1D and 2D profile likelihood ratio plots of the combined fit in planes of the benchmark parameters.
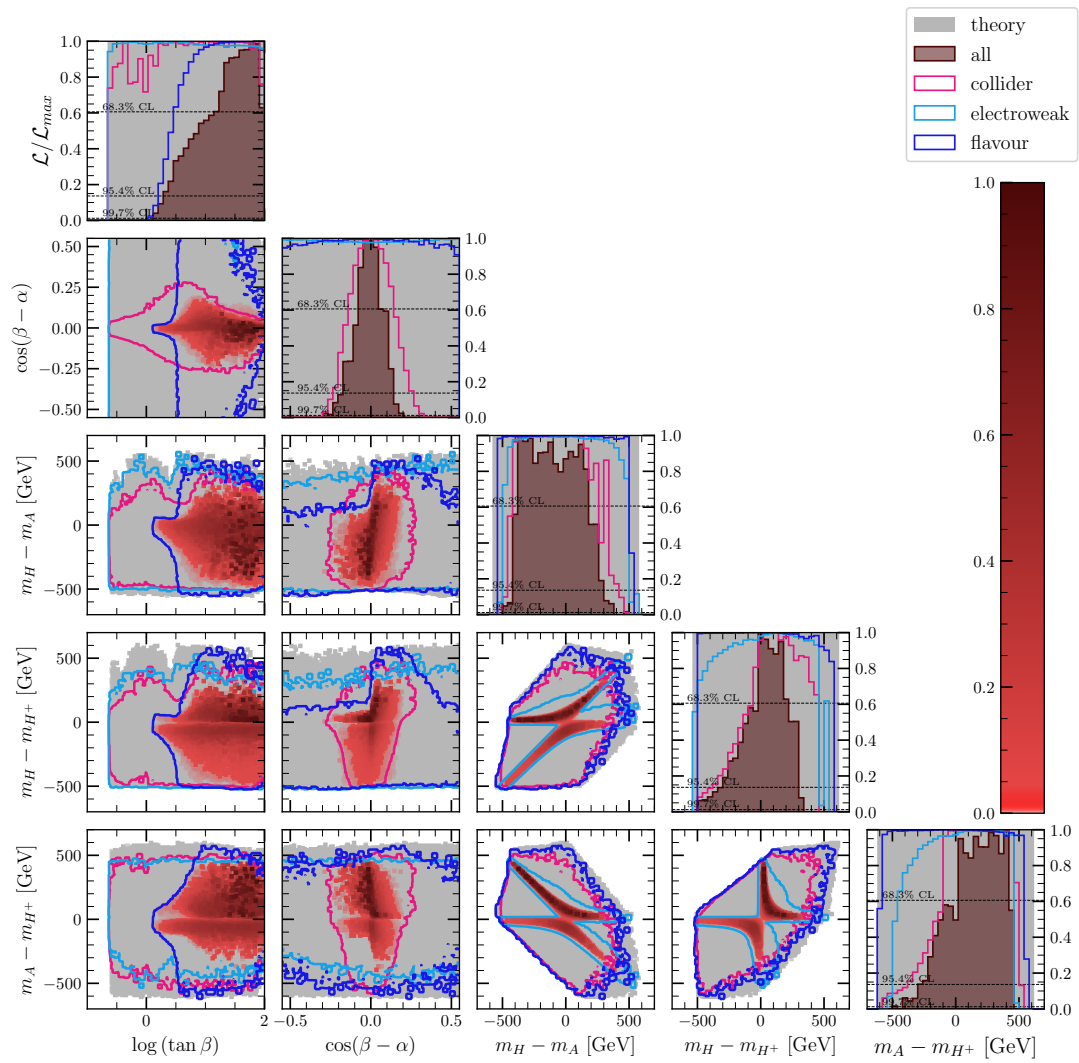
FIGURE 10.7: (Type-I) 1D and 2D profile likelihood ratio plots of the combined fit in planes of the angles and mass splittings.
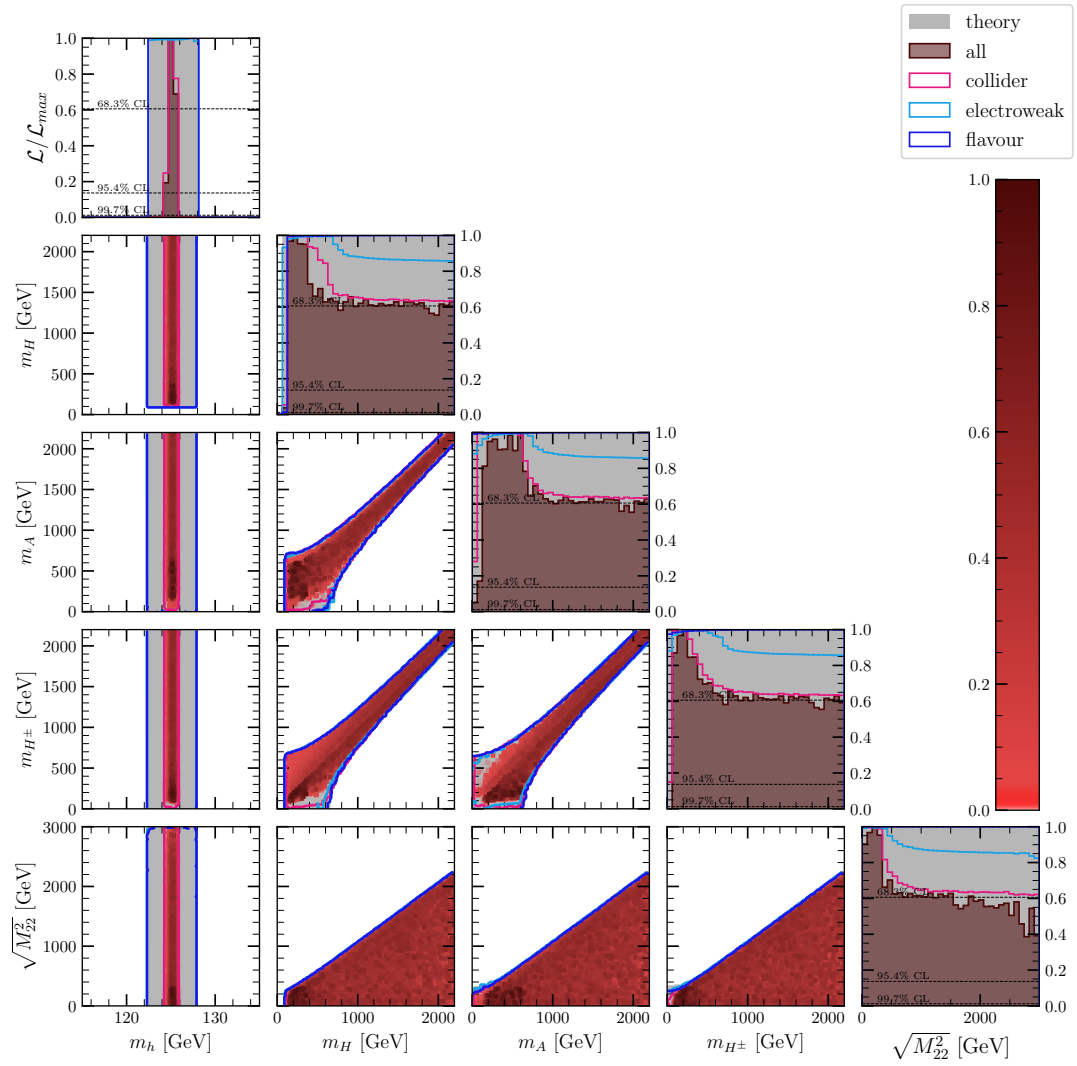
FIGURE 10.8: (Type-I) 1D and 2D profile likelihood ratio plots of the combined fit in planes of the mass parameters.
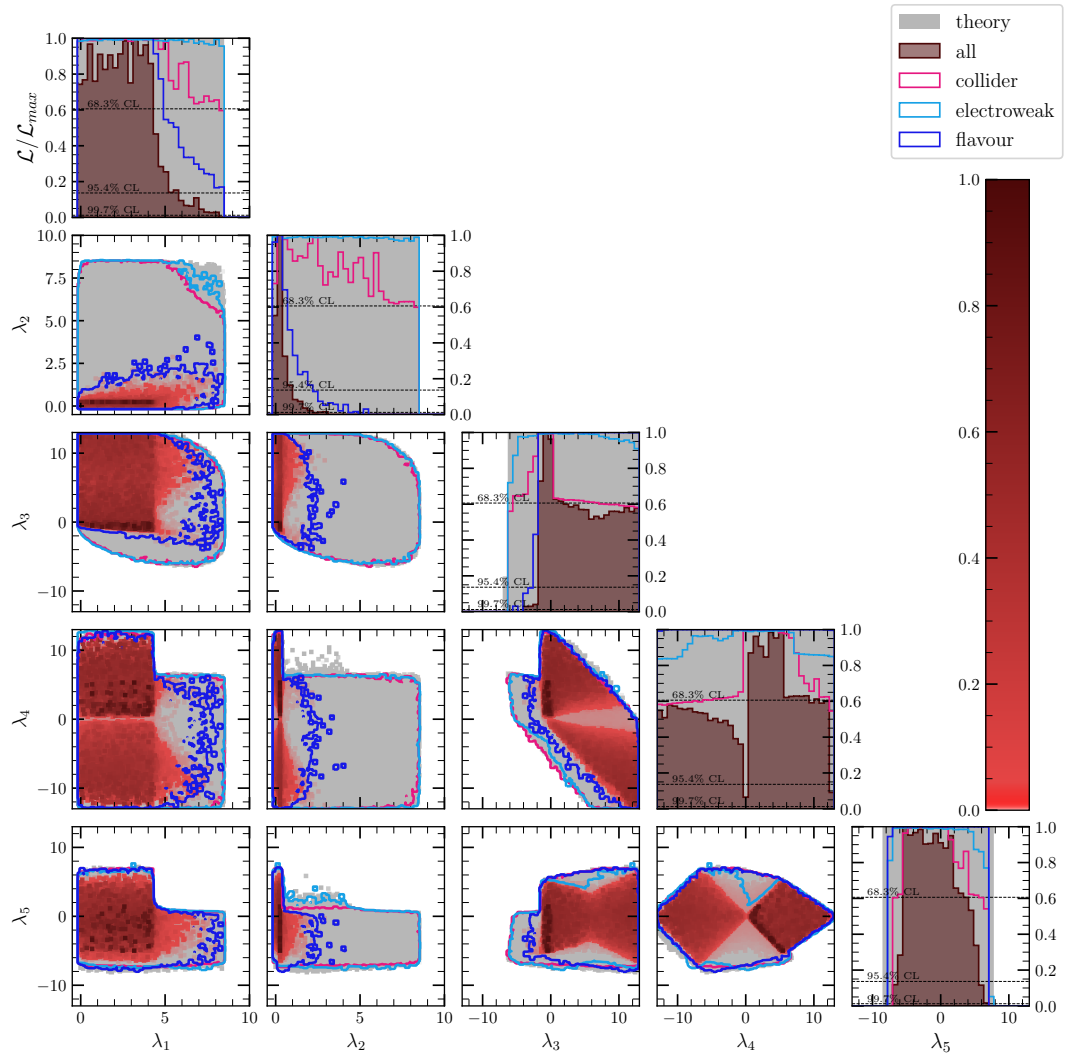
FIGURE 10.9: (Type-I) 1D and 2D profile likelihood ratio plots of the combined fit in planes of the generic couplings.

Chapter 11

Hidden-Higgs scenario in the Type-I/Type-II 2HDMs

We now present our results for the hidden-Higgs scenario in the Type-I and Type-II 2HDMs. Recall that in this scenario the heavier CP-even scalar, H, is assumed to be SM-like, by which we mean that it has a mass of 125 GeV. We then have an additional light scalar, $m_h < 125$ GeV, that so far has evaded detection. Collider experiments have confirmed that the 125 GeV scalar has couplings that are compatible with the SM Higgs boson. Hence, to satisfy collider constraints, we must have SM-like couplings for the 125 GeV scalar. As before, these results are provided at tree-level.

11.1 Theoretical Constraints

The theoretical constraints are shown in Figure 11.1. We see that the available regions are somewhat different compared to the regular Higgs scenario. In particular, the λ_1 versus λ_2 plane is far more restricted and λ_5 is has an upper bound of just 1. Figure 11.2 shows our usual benchmark planes. Here we see a crucial difference compared to the regular Higgs scenario – there is a strict upper limit of the charged Higgs mass m_{H^+} of just 700 GeV. Similarly, we also have the restriction $m_A < 700$ GeV. This is a result of the limits on the mass splittings from Equation 7.1. As before, $\log{(\tan{\beta})}$ and $\cos{(\beta - \alpha)}$ are completely open prior to experimental constraints (apart from the Yukawa perturbativity limit).
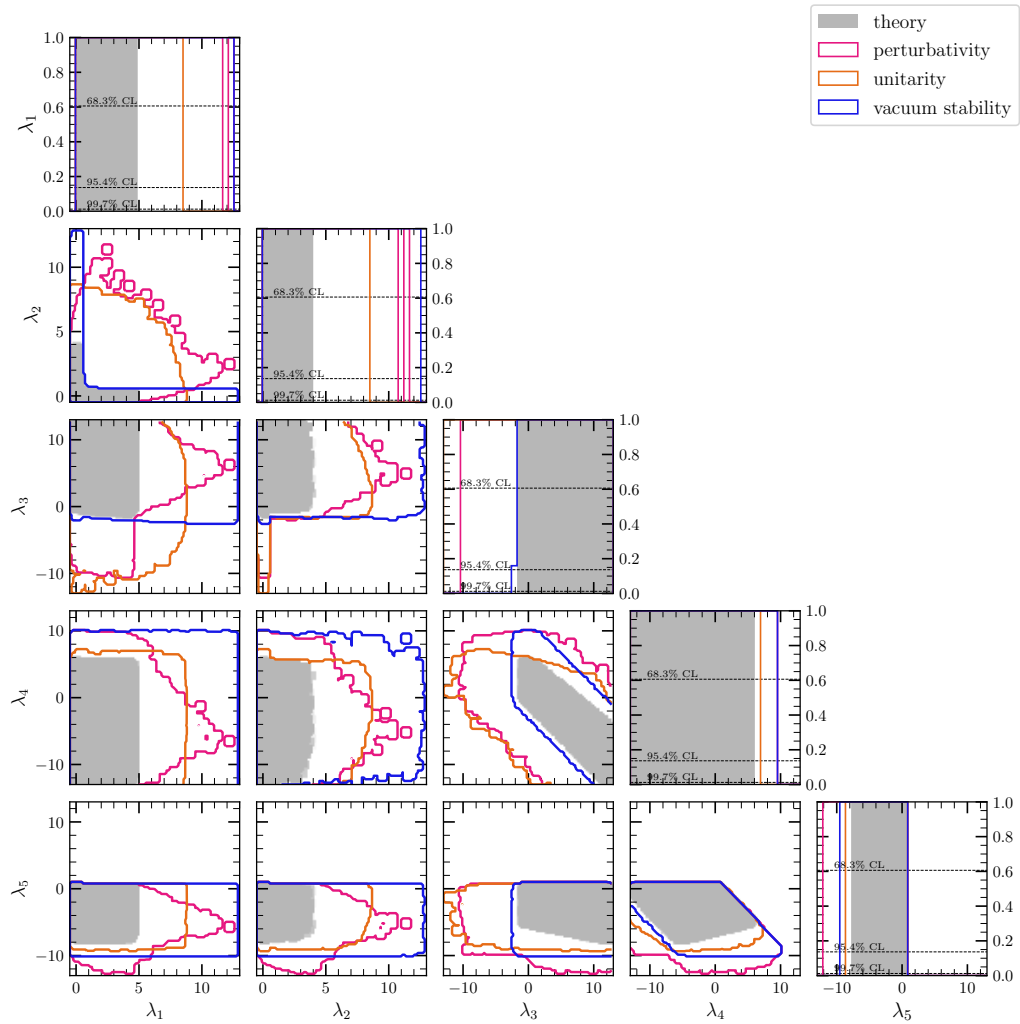
FIGURE 11.1: (HHS) 1D and 2D availability plots of the theoretical constraints in planes of the generic couplings.

11.2   Experimental Constraints

Results for the STU electroweak constraints are displayed in Figure 11.3. Since m_H is now fixed to the SM prediction, we consider mass splittings with m_h as a replacement, i.e. $m_h - m_A$ and $m_h - m_{H^+}$.

As before, there are two allowed regions. However, part of the plot appears to be cut off since it failed to satisfy theoretical constraints. This results in a stronger lower bound for $m_A - m_{H^+}$ while the bounds for $m_h - m_{H^+}$ and $m_h - m_A$ are weaker and actually no better than theoretical constraints alone. In Figure 11.4, we find that the hidden Higgs scenario has no trouble fitting the experimental values of the S, T, and U parameters from Equation 4.40.
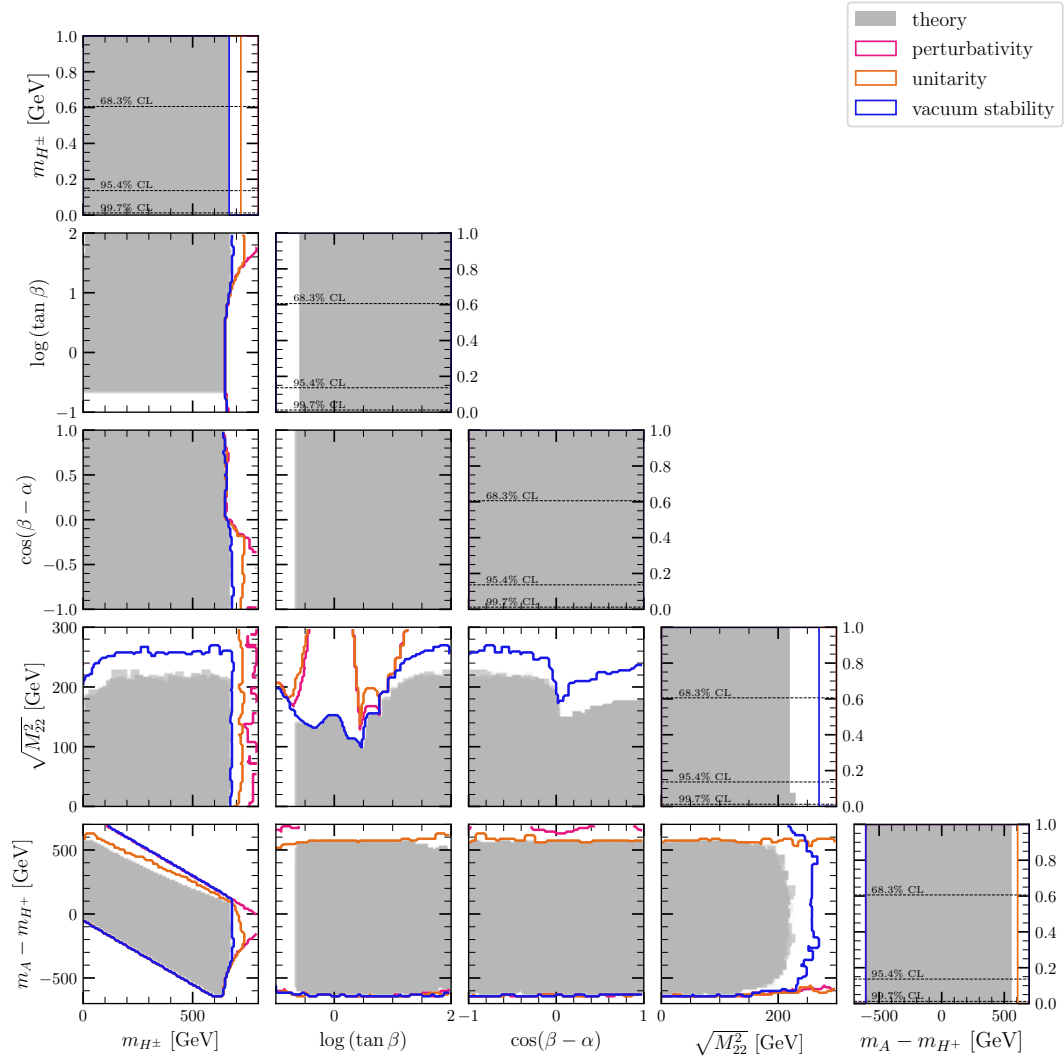
FIGURE 11.2: (HHS) 1D and 2D availability plots of the theoretical constraints in planes of the benchmark parameters.

The collider results are given in Figures 11.5 and 11.6 for Type-II and Type-I models respectively. Here we see a major difference compared to the regular Higgs scenario – $\cos(\beta - \alpha)$ must now be close to ± 1 rather than 0.

The reason is clear when we examine the HVV couplings which were given in Table 3.5. We find that the HVV coupling is proportional to $\sin(\beta - \alpha)$ rather than $\cos(\beta - \alpha)$. Therefore the SM-like scenario corresponds to $\cos(\beta - \alpha) = \pm 1$. The reduced Higgs-fermion couplings (c.f. Table 3.7) also differ for H and now take the form

$$\Delta k_1 = \frac{\sin\alpha}{\sin\beta} - 1 = \sqrt{1 - \sin^2(\beta - \alpha)} - \frac{\sin(\beta - \alpha)}{\tan\beta} - 1$$

$$\simeq -\frac{1}{2}\sin^2(\beta - \alpha) - \frac{\sin(\beta - \alpha)}{\tan\beta}, \tag{11.1}$$
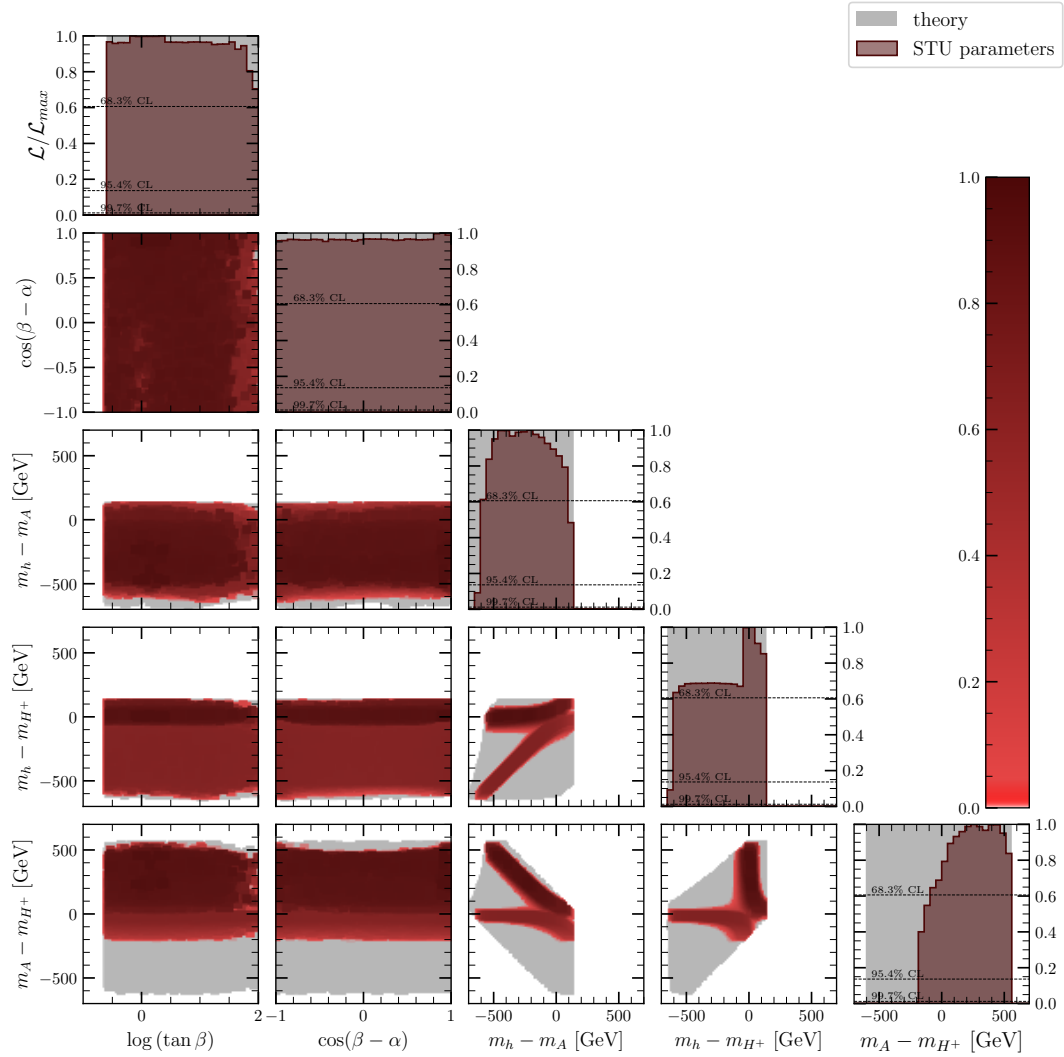
FIGURE 11.3: (HHS) 1D and 2D profile likelihood ratio plots of the STU oblique constraints in planes of the angles and mass-splittings.

$$\Delta k_2 = \frac{\cos\alpha}{\cos\beta} - 1 = \sqrt{1 - \sin^2(\beta - \alpha)} + \sin(\beta - \alpha)\tan\beta - 1$$

$$\simeq -\frac{1}{2}\sin^2(\beta - \alpha) + \sin(\beta - \alpha)\tan\beta. \tag{11.2}$$

Here, Δk_2 is the (deviation of the) reduced Hd_id_i and He_ie_i coupling in the Type-II 2HDM, while all other reduced Hff couplings are equal to Δk_1 (for both Type-I and Type-II). These are SM-like for $\sin(\beta - \alpha) = 0$ or, in the case of Type-I, when $\tan\beta \to \infty$. Additional solutions may arise when the terms approximately cancel, which can be seen in Figure 11.5, but these disappear in the combined collider fit.

In the Type-II 2HDM there is a single peak for $\tan\beta$ of 6.4, while there are two peaks in Type-I at 1 and 15. We can also see that Type-I collider results favour low m_{H^+} while Type-II results show no preference.
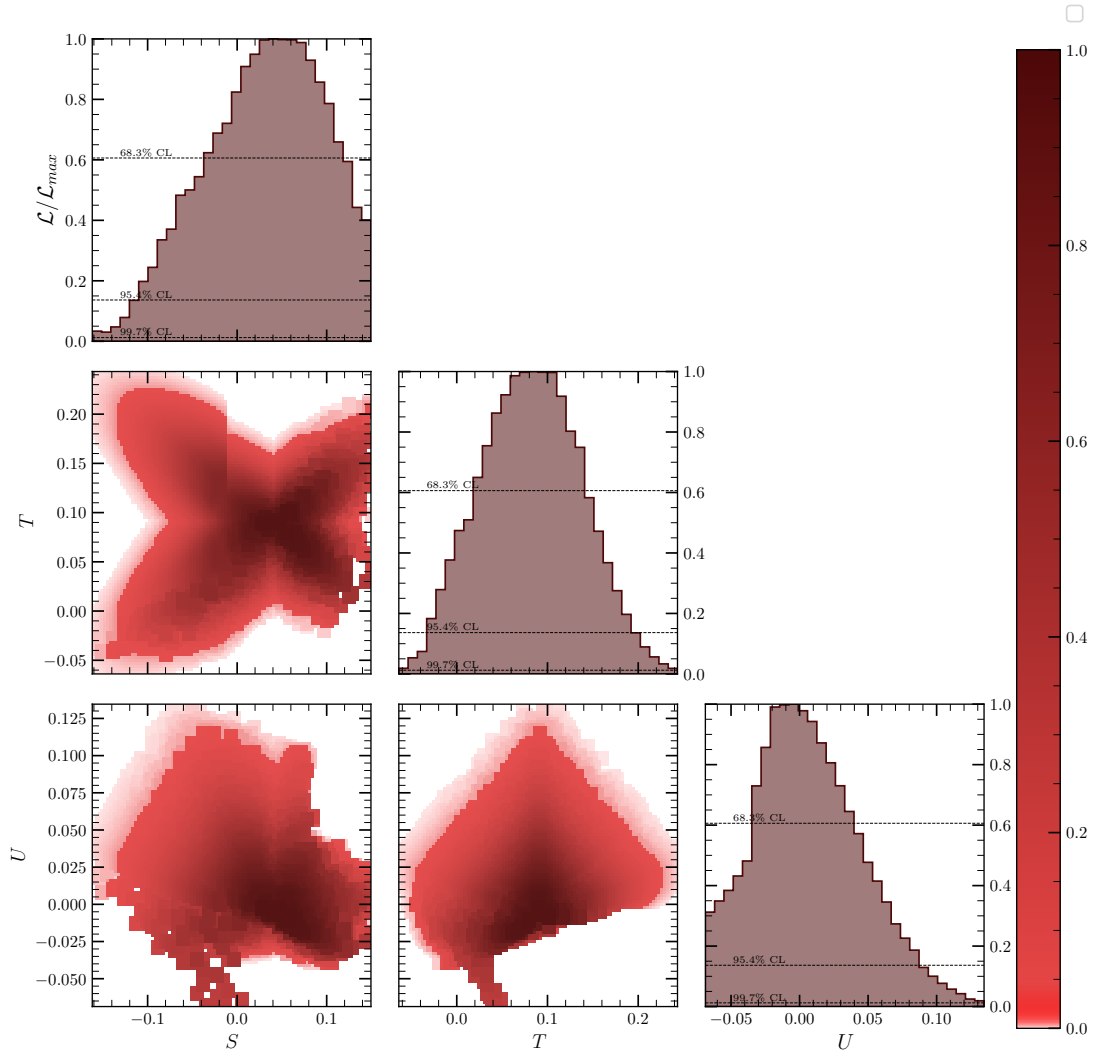
FIGURE 11.4: (HHS) 1D and 2D profile likelihood ratio plots of the STU oblique constraints in planes of the S, T, and U parameters.

The combined flavour fits are provided in Figures 11.7 (Type-II) and 11.8 (Type-I). We include the same flavour observables which were listed in Table 9.1. In general, the flavour constraints are very similar to the standard Higgs scenario. This is because the H^+-fermion couplings remain the same in the HHS (they depend on only $\tan\beta$ and $\cot\beta$). But, crucially, we now we have a strict upper bound for m_{H^+} due to theoretical constraints.

In the Type-II 2HDM regular Higgs scenario we had a lower bound for m_{H^+} of 1000 GeV. This conflicts with the upper bound set by theoretical constraints. In Figure 11.7, we can see that the flavour constraints just push m_{H^+} to the highest value allowed, which is 620 GeV. In the Type-I 2HDM, the m_{H^+} versus $\log(\tan\beta)$ plane is much more open and is similar to the regular Higgs scenario. There is no conflict with theoretical constraints here.
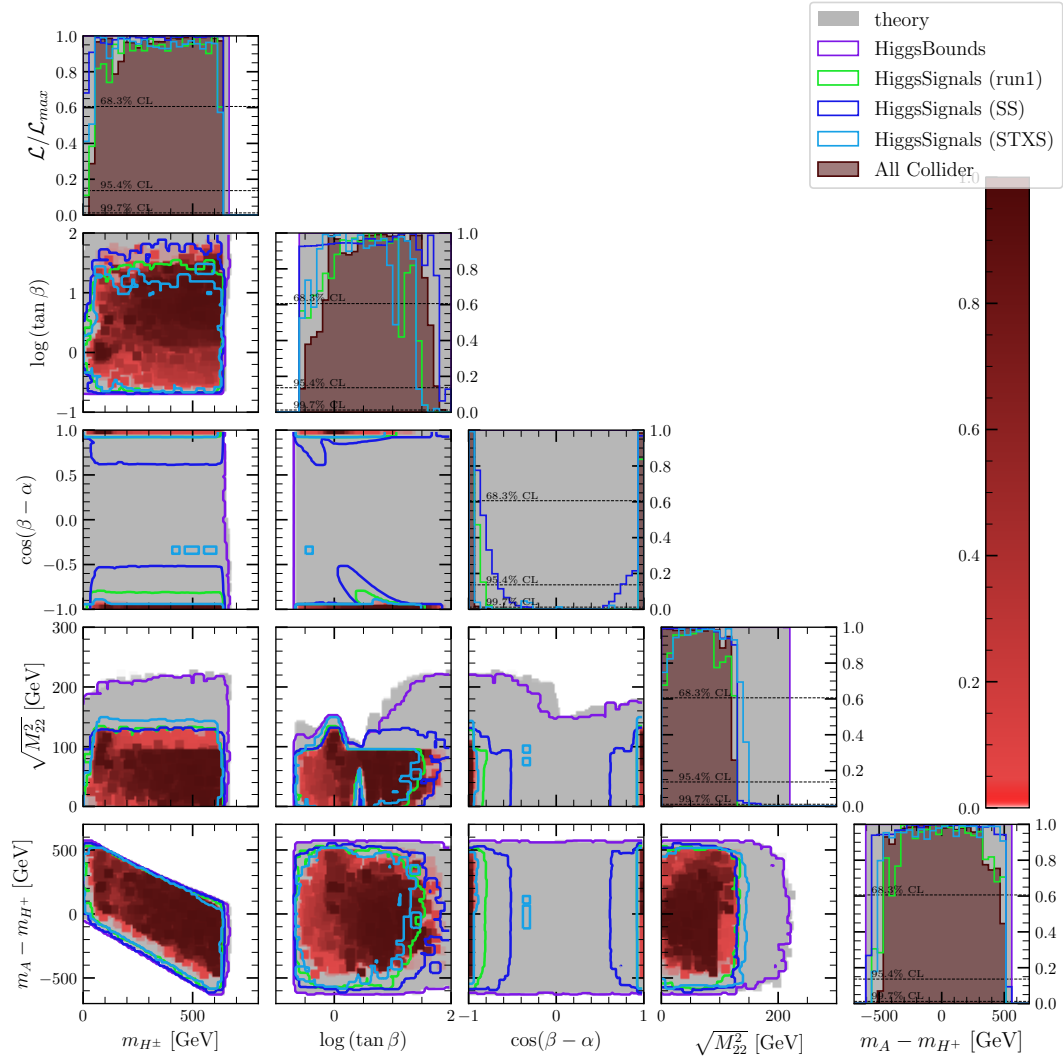
FIGURE 11.5: (Type-II HHS) 1D and 2D profile likelihood ratio plots of the collider constraints in planes of the benchmark parameters.

Unlike the regular Higgs scenario, there is no restriction on $\cos(\beta - \alpha)$ due to flavour constraints, but the value of $\tan\beta$ does get a lower bound of about 16 for both Type-I and Type-II.

11.3   Global Fits

Finally, we present the global fits for the Hidden Higgs scenario. The best-fits points and a 95% confidence interval for all parameters are provided in Tables 11.1 and 11.2.

Starting with Type-II and looking at the $m_A - m_{H^+}$ versus m_{H^+} plane in Figure 11.9, there is only a tiny region where collider, electroweak and flavour constraints are satisfied

Parameter	Best Fit	95% CI
λ_1	0.0519	0.0519 to 3.69
λ_2	0.2566	0.2562 to 0.2615
λ_3	12.3	10.4 to 12.5
λ_4	-6.34	-6.39 to -5.32
λ_5	-5.97	-6.05 to -4.81
m_h	90	66 to 98
m_H	124.75	124.49 to 125.52
m_A	609	547 to 612
$m_{H^\pm}$	618	561 to 620
$\tan_\beta$	6.4	4.21 to 11.5
α	-1.417	-1.776 to -1.417
Λ_1	0.2453	0.2453 to 0.2593
Λ_2	0.05034	0.05034 to 3.632
Λ_3	12.3	10.4 to 12.5
Λ_4	-6.33	-6.35 to -5.31
Λ_5	-5.96	-6.02 to -4.80
Λ_6	0.0357	0.000329 to 0.0357
Λ_7	-0.00445	-0.3200 to -0.00445
$\sin(\beta - \alpha)$	0.3039	0.0 to 0.3039
$\cos(\beta - \alpha)$	-0.953	-1.0 to -0.953
$\sqrt{M_{22}^2}$	83.3	16.9 to 85.0
$m_h - m_A$	-519	-527 to -455
$m_h - m_{H^+}$	-528	-531 to -469
$m_A - m_{H^+}$	-9.2	-23.0 to -1.2

TABLE 11.1: (Type-II HHS) Best fit points and 95% confidence intervals for the combined fit.

Parameter	Best Fit	95% CI
λ_1	3.69	0.00528 to 4.32
λ_2	0.259	0.2536 to 0.2606
λ_3	0.01	-0.4 to 10
λ_4	1.3	-6.5 to 5.1
λ_5	-1.2	-6.0 to -0.3
m_h	96.5	62.9 to 100.0
m_H	125.2	124.6 to 125.7
m_A	290	160 to 610
$m_{H^\pm}$	73	65 to 620
$\tan_\beta$	15.0	7.3 to 100
α	-1.55	-1.66 to 1.53
Λ_1	0.2576	0.2504 to 0.2598
Λ_2	3.66	0.00768 to 4.23
Λ_3	0.02	-0.4 to 10.0
Λ_4	1.4	-6.5 to 5.1
Λ_5	-1.2	-6.0 to -0.29
Λ_6	0.0094	-0.016 to 0.028
Λ_7	-0.24	-0.42 to 0.034
$\sin(\beta - \alpha)$	0.09	0.0 to 0.26
$\cos(\beta - \alpha)$	-0.9959	-1.0 to -0.96, 0.96 to 1.0
$\sqrt{M_{22}^2}$	43	4.5 to 170
$m_h - m_A$	-190	-540 to -66
$m_h - m_{H^+}$	23.1	-544 to 28.9
$m_A - m_{H^+}$	220	-62 to 480

TABLE 11.2: (Type-I HHS) Best fit points and 95% confidence intervals for the combined fit.
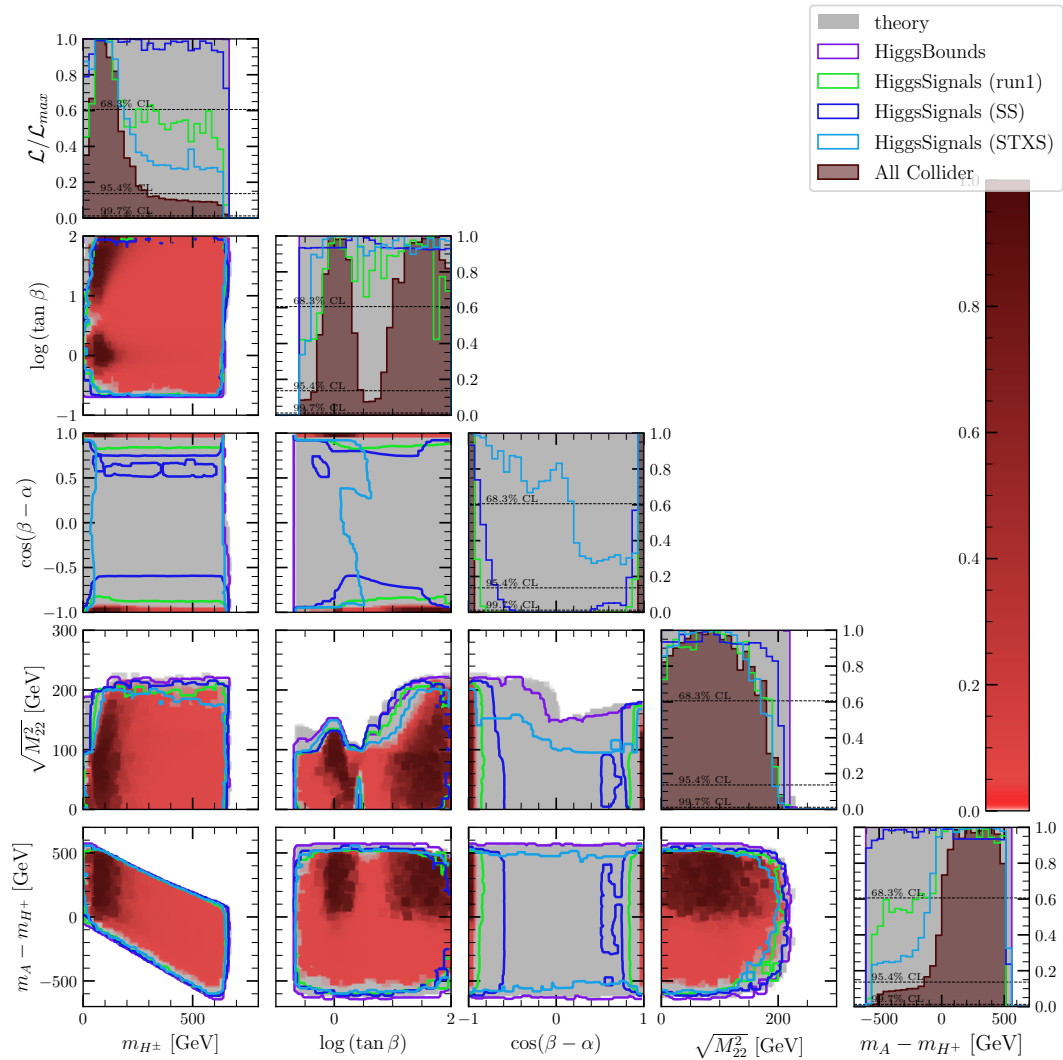
FIGURE 11.6: (Type-I HHS) 1D and 2D profile likelihood ratio plots of the collider constraints in planes of the benchmark parameters.

simultaneously. We get a prediction for m_{H^+} of 618 GeV, with a 95% confidence interval of 561 to 620 GeV.

There was a lot of difficulty in adequately sampling this scenario. The plots presented here contain over 4 million samples, yet the available region still appears patchy. Interestingly, the $\cos(\beta - \alpha) \approx 1$ region is eliminated when both collider and flavour constraints are combined, leaving $\cos(\beta - \alpha) \approx -1$. The preferred value of $\log(\tan\beta)$ was 6.4.

In Figure 11.11, we see that λ_3 is pushed above 10.4. Such a large coupling would likely be eliminated when we consider the NLO unitarity constraint. The preferred values of the remaining masses are: $m_h = 90$GeV and $m_A = 550$GeV which are also rather precisely determined.
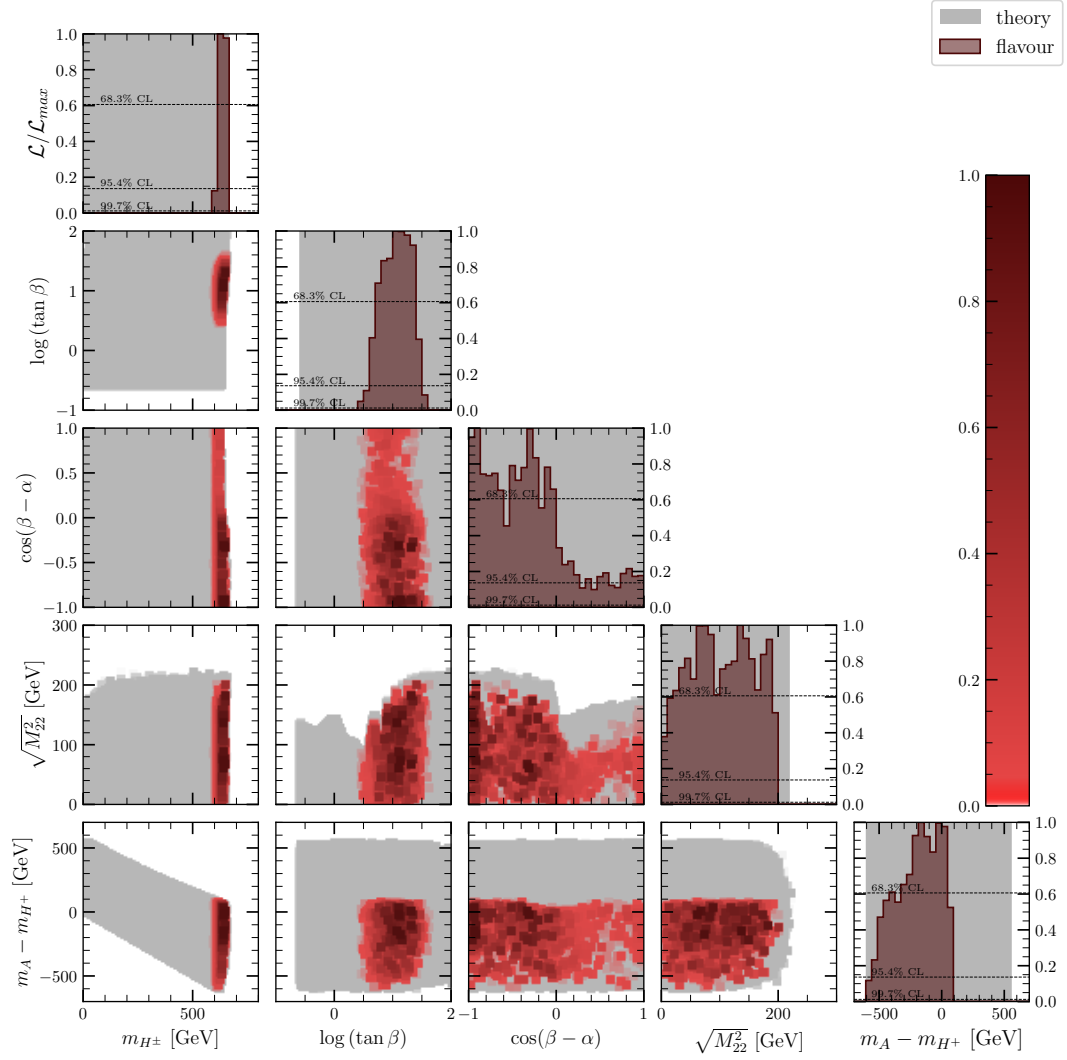
FIGURE 11.7: (Type-II HHS) 1D and 2D profile likelihood ratio plots of the combined flavour constraints in planes of the benchmark parameters.

In the Type I 2HDM, the parameter space is much more open due to the lack of a strict lower bound on m_{H^+} from any experimental constraints. There was a preference for $m_{H^+} = 73$ GeV, and both $+1$ and -1 are available for the parameter $\cos(\beta - \alpha)$.

The lower peak for $\log(\tan\beta)$ that was visible in the collider constraints has been eliminated by the flavour constraints, so we are left with a single peak at $\tan\beta = 15$. The remaining masses have the preferred values: $m_A = 290$ GeV and $m_h = 97$ GeV.
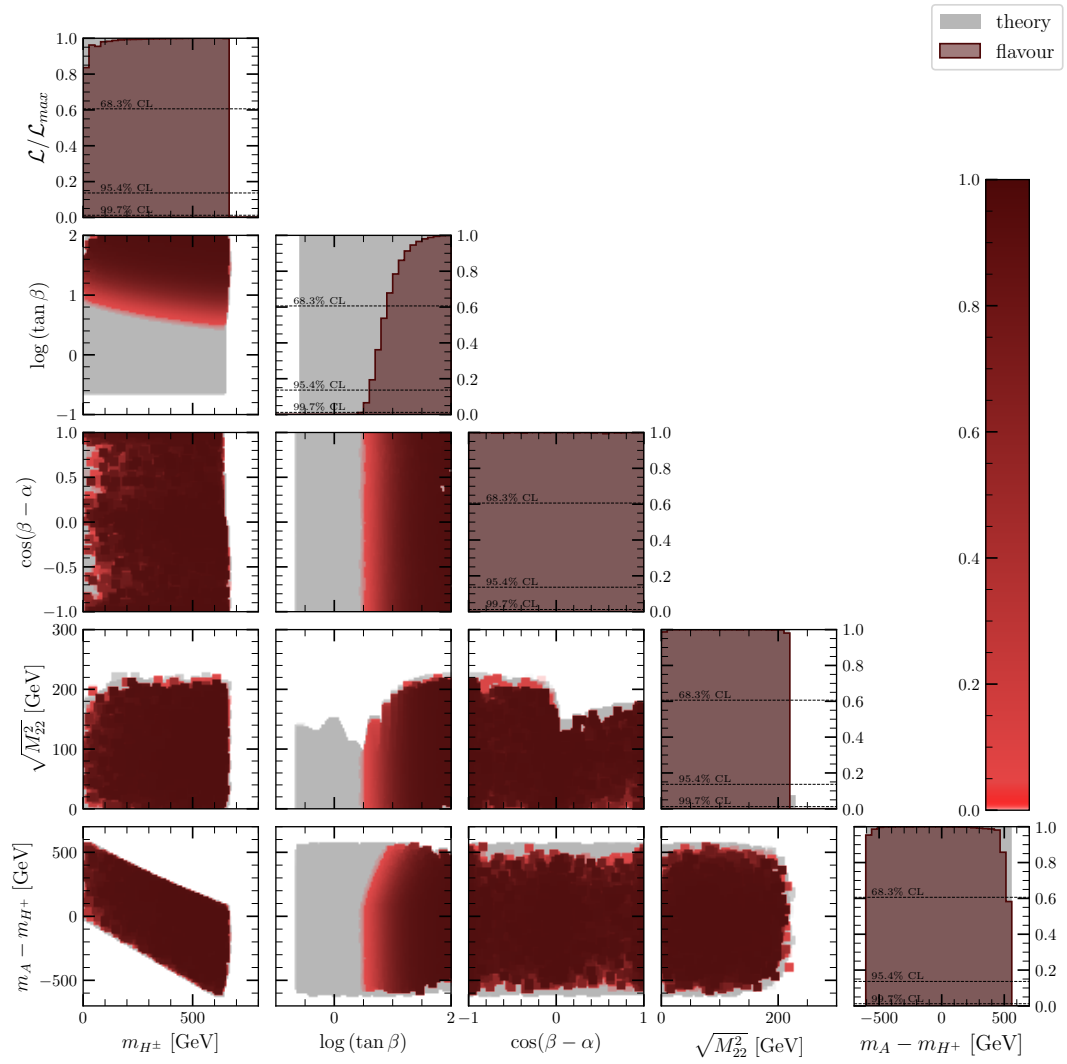
FIGURE 11.8: (Type-I HHS) 1D and 2D profile likelihood ratio plots of the combined flavour constraints in planes of the benchmark parameters.
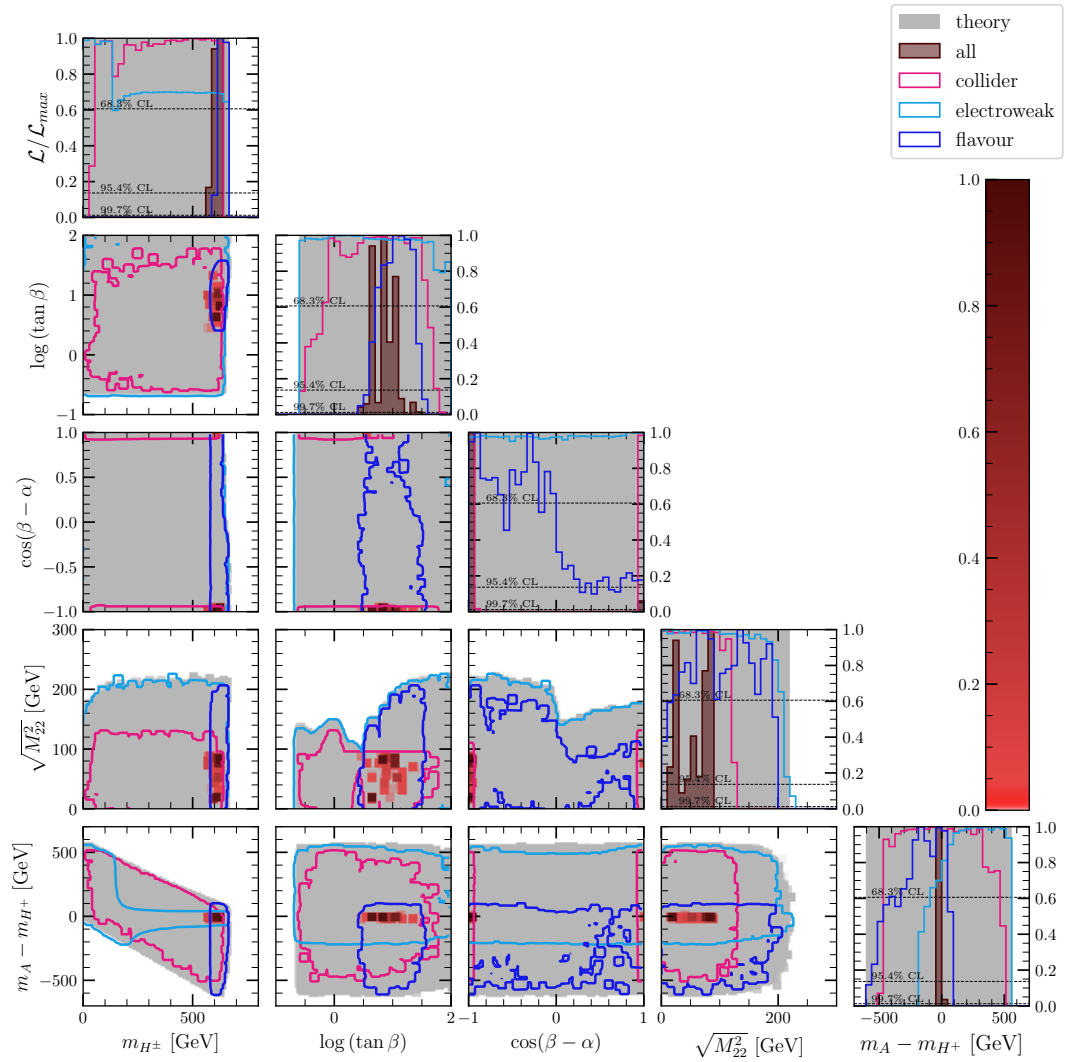
FIGURE 11.9: (Type-II HHS) 1D and 2D profile likelihood ratio plots of the combined fit in planes of the benchmark parameters.
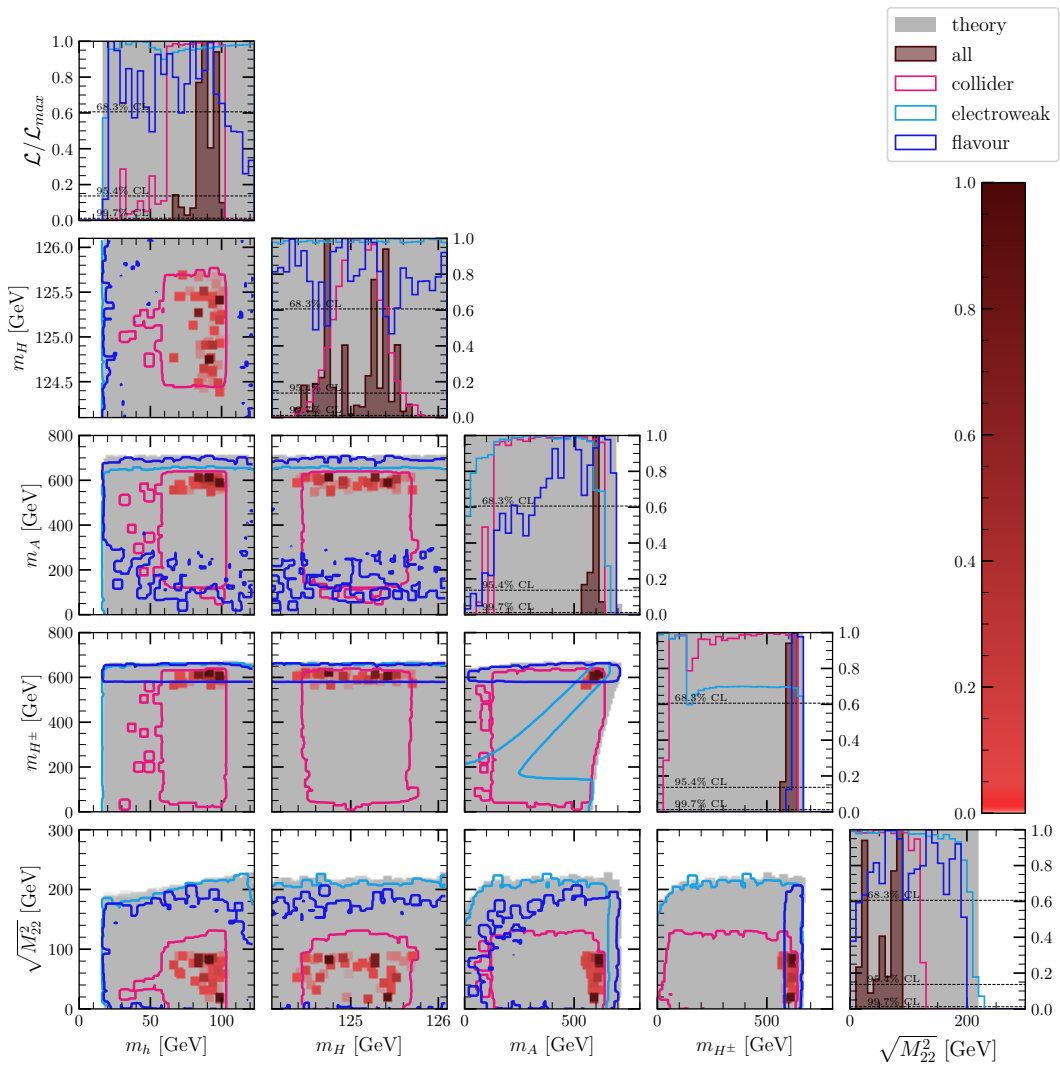
FIGURE 11.10: (Type-II HHS) 1D and 2D profile likelihood ratio plots of the combined fit in planes of the mass parameters.
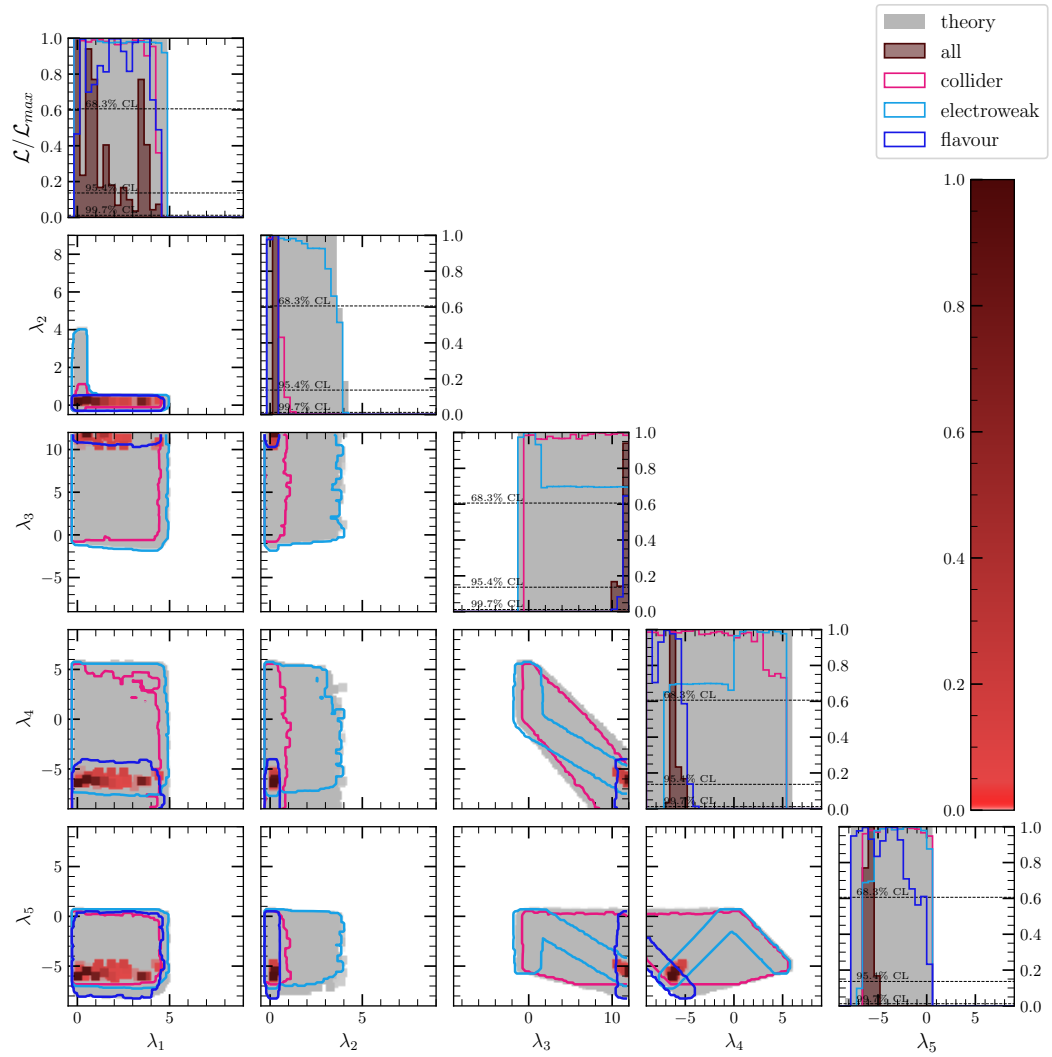
FIGURE 11.11: (Type-II HHS) 1D and 2D profile likelihood ratio plots of the combined fit in planes of the generic couplings.
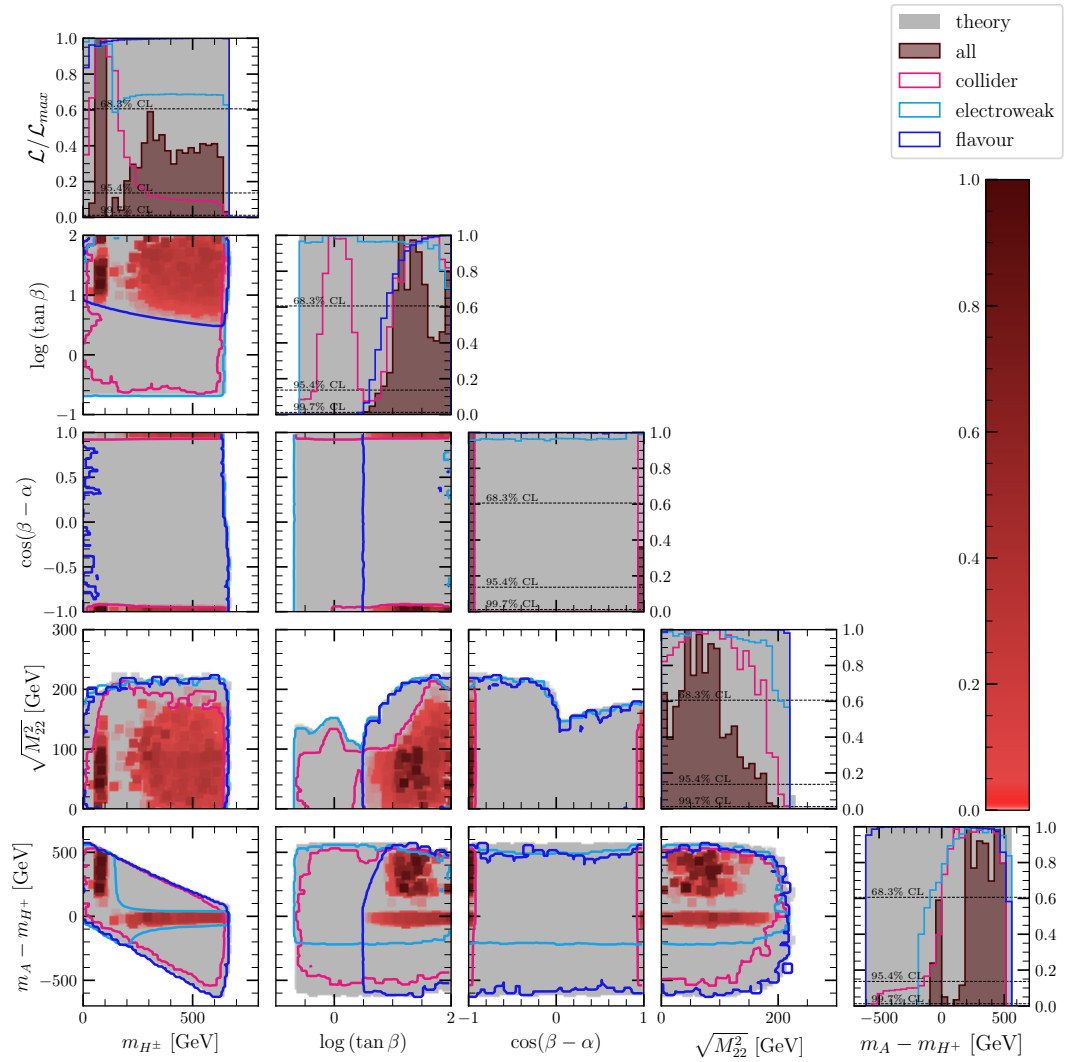
FIGURE 11.12: (Type-I HHS) 1D and 2D profile likelihood ratio plots of the combined fit in planes of the benchmark parameters.
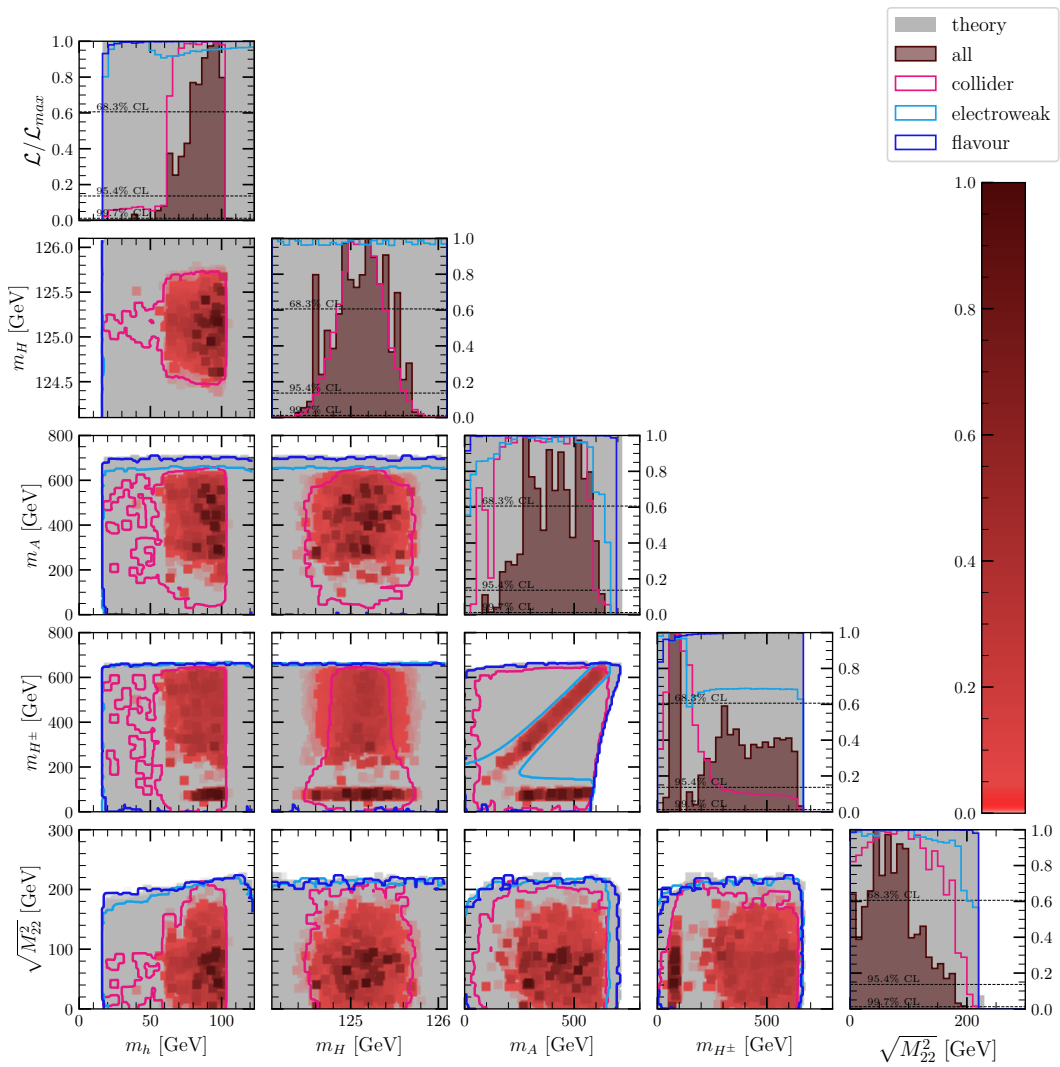
FIGURE 11.13: (Type-I HHS) 1D and 2D profile likelihood ratio plots of the combined fit in planes of the mass parameters.
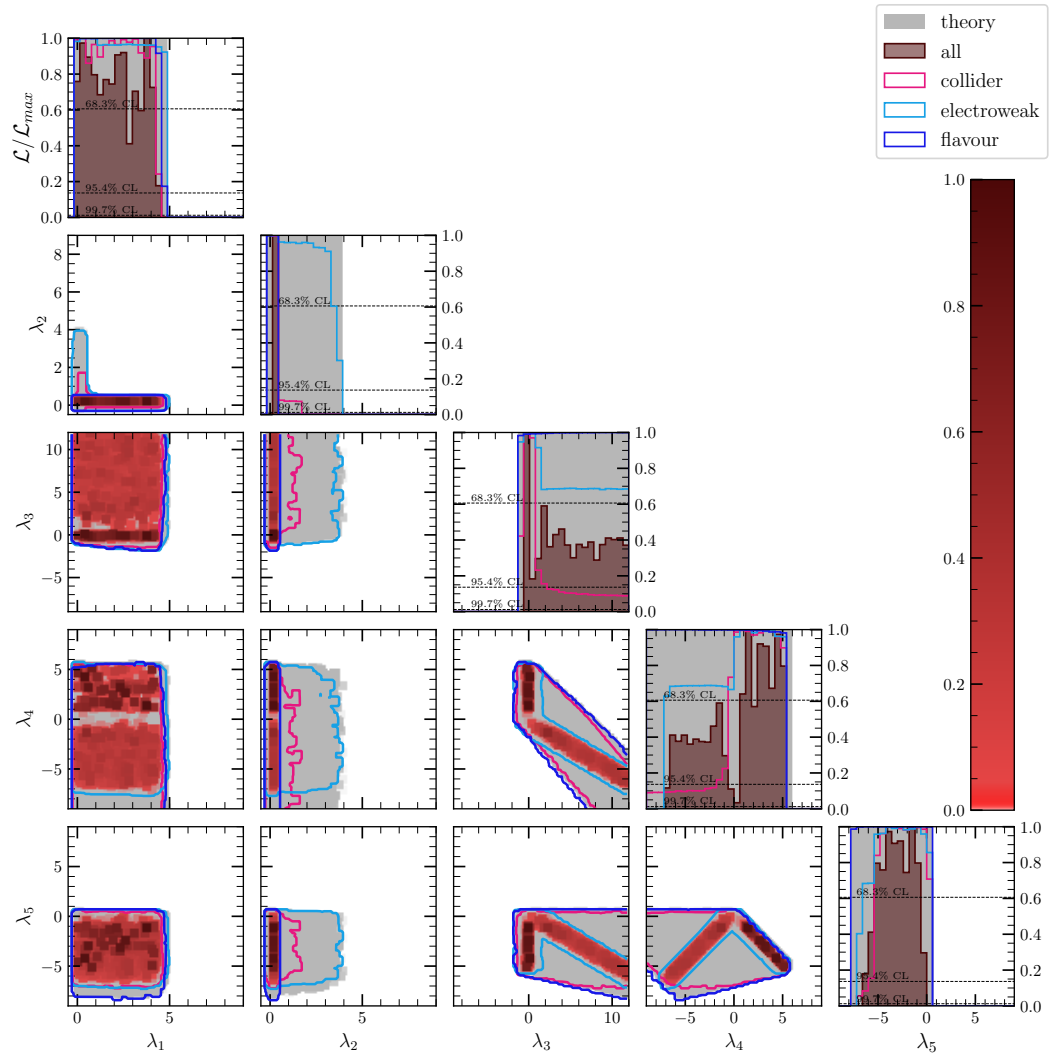
FIGURE 11.14: (Type-I HHS) 1D and 2D profile likelihood ratio plots of the combined fit in planes of the generic couplings.

Chapter 12

Preliminary results for Type-I/Type-II 2HDMs with FlexibleSUSY

We briefly discuss parameter scans with the FlexibleSUSY spectrum generator at 2 loop level. As inputs, FlexibleSUSY accepts the $\lambda_1, \ldots, \lambda_7$, $\tan \beta$, and m_{12}^2 parameters. Here $\tan \beta$ is provided at the scale of m_t while the remaining parameters are provided at the input scale, which is set to m_Z. All parameters are in the $\overline{MS}$-scheme. FlexibleSUSY then calculates the running masses at the input scale, along with the pole masses. The generic couplings presented in the results are provided at the input scale while the masses are provided at their pole.

12.1 Theoretical Constraints

The theoretical constraints are presented in Figures 12.1 and 12.2. The included constraints are similar to the ones used for tree-level scans; namely, vacuum stability (inclusive of vacuum meta-stability), S-matrix unitarity, and perturbativity. However, the unitarity constraint is done at NLO and includes wave-function, gauge coupling and Yukawa corrections. This is far more restrictive than the LO unitarity constraint that was used previously.

The theoretical constraints are model dependent due to the yukawa_corrections that are included in the NLO unitarity constraint, and also due to the running of the couplings, which differs between each model. However, this dependence is minor and therefore we only present the theoretical constraints for Type-II. These constraints are checked at two
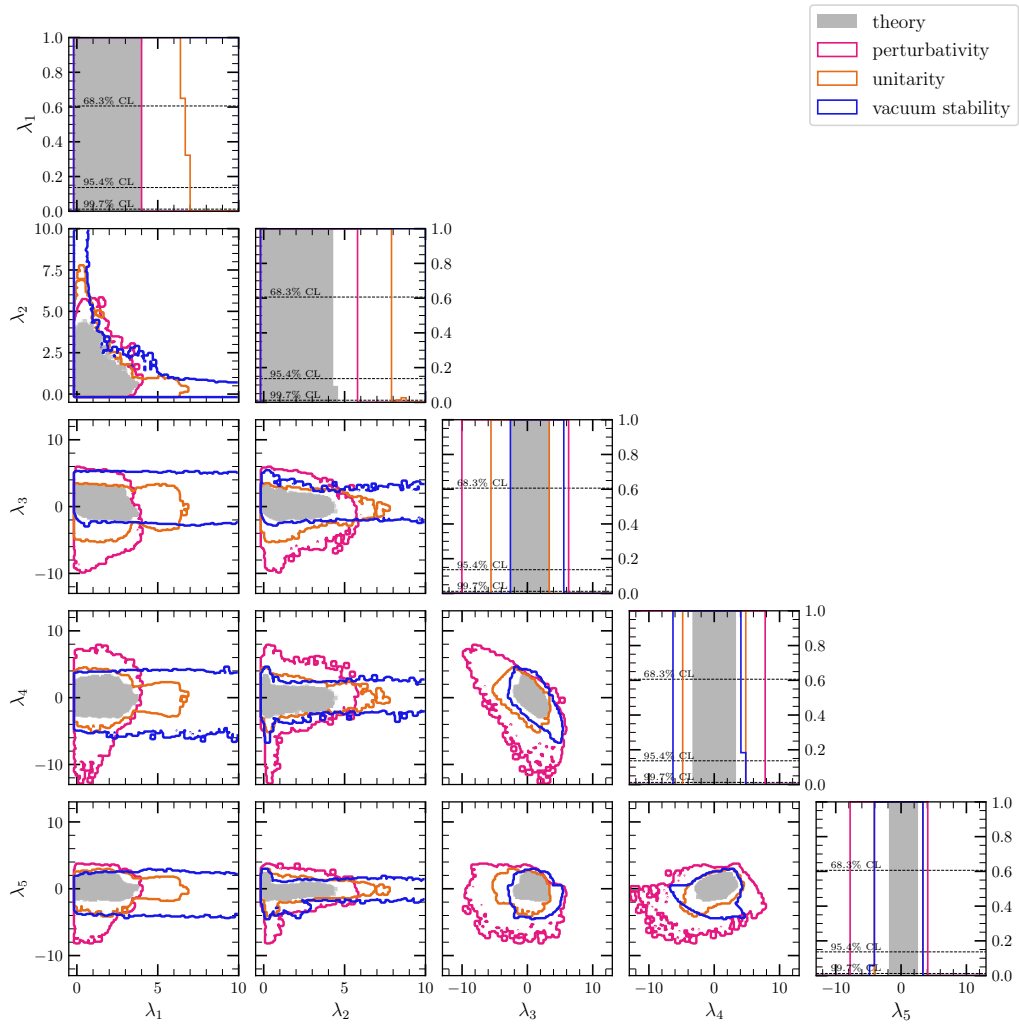
FIGURE 12.1: 1D and 2D availability plots of the theoretical constraints in planes of the generic couplings.

energy scales: m_Z and 1 TeV. It is assumed that if the constraint is satisfied at both scales then it is also met at all intermediate scales. For scanning purposes, the worst of the two likelihoods is used, i.e.

$$\ln \mathcal{L} = \min \Big(\ln \mathcal{L}(m_Z), \ln \mathcal{L}(1\,\text{TeV}) \Big). \tag{12.1}$$

Perturbativity checks on the loop corrections to the scalar masses are also applied, as explained in Section 4.1.4. This is not shown as a separate contour but instead included in the combined theoretical constraint.

In Figure 12.1, we first notice that the available parameter space for the couplings is smaller and closer to zero compared to the tree level results in Figure 8.1. In the combined theoretical constraint, all couplings are constrained to be less than 5. In the benchmark
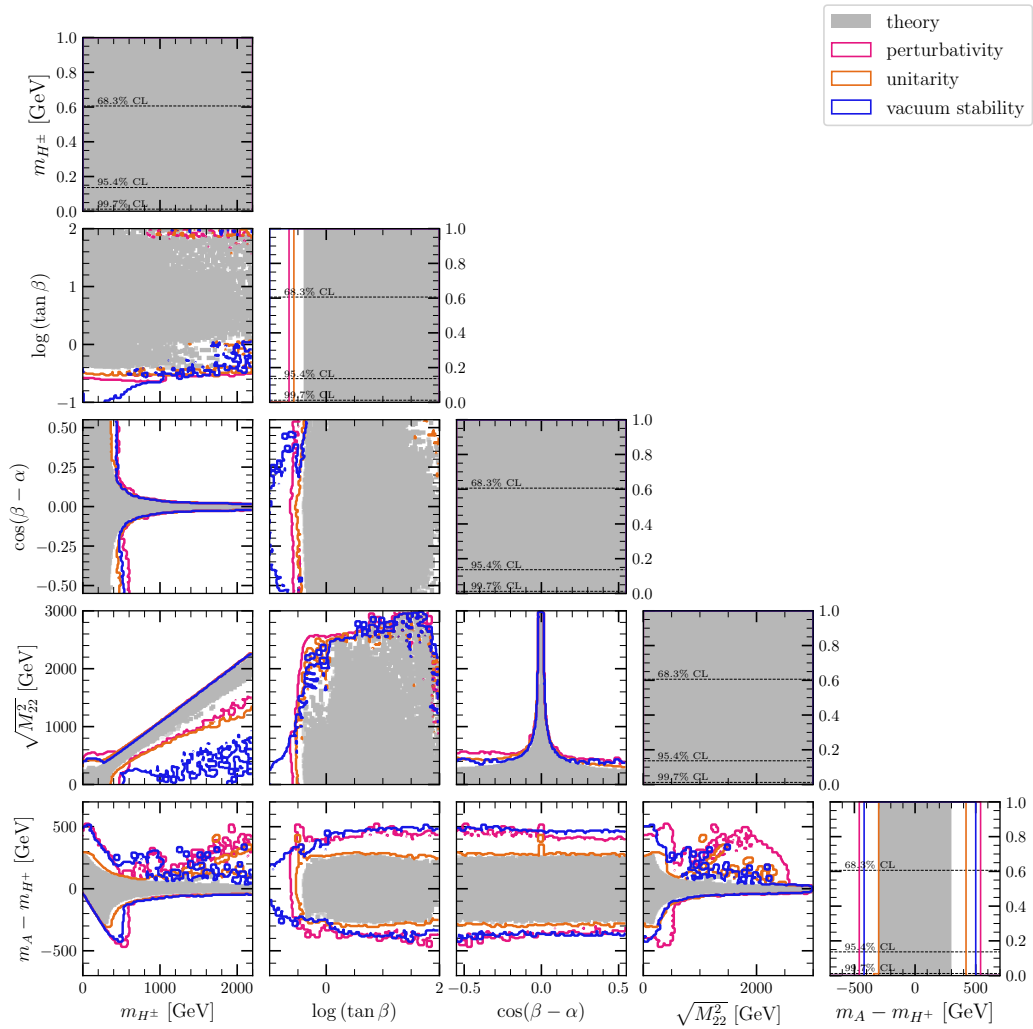
FIGURE 12.2: 1D and 2D availability plots of the theoretical constraints in planes of the benchmark parameters.

planes from Figure 12.2, we notice a few changes: (i) the restriction on $\cos(\beta - \alpha)$ is much stronger for masses above 500 GeV, (ii) the allowed range of the mass-splittings is much smaller, and (iii) the parameter space towards the bottom-right of the $\sqrt{M_{22}^2}$ vs. m_{H^+} plane has disappeared. Observation (ii) would imply that the flavour constraint would indirectly cause a strong limit on $\cos(\beta - \alpha)$ – possibly stronger than the collider constraints.

Furthermore, some of the planes are not well sampled. In particular, high $\log(\tan\beta)$ for the $\cos(\beta - \alpha)$ vs. $\log(\tan\beta)$ plane and also bottom-right/top-right corners of the $\log(\tan\beta)$ vs. m_{H^+} plane. These regions are highly fine-tuned, and despite multiple targeted scans, some parameter space is still missing (they were much worse before doing these targeted scans).

Some strange behaviour is seen on the $m_A - m_{H^+}$ vs. m_{H^+} plane. We notice a poorly
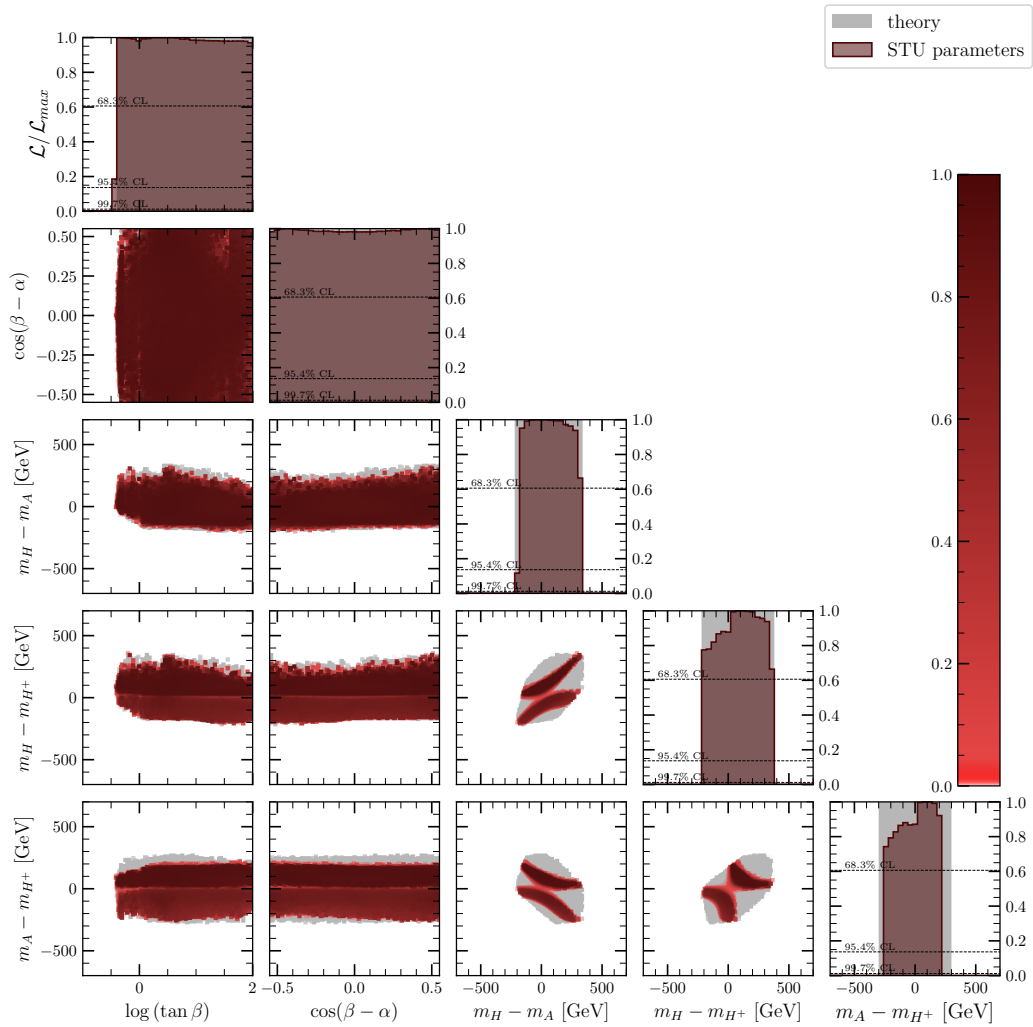
FIGURE 12.3: 1D and 2D profile likelihood ratio plots of the electroweak constraints in planes of the mass-splittings.

sampled region above the main region. This is a result of the way FlexibleSUSY is calculating the pole masses. It did not happen in the tree-level results from Figure 8.3, nor does it happen if we plot the running masses instead. The reason why FlexibleSUSY is doing this is still under investigation at the time of writing.

12.2 Experimental Constraints

The STU electroweak constraints are displayed on Figure 12.3. Again, these are almost model independent, so we just provide results for the Type-II 2HDM. The plotted ranges are the same as the tree-level results in Figure 9.1, but only a small circle of parameter space is available. This is because theoretical constraints now provide much stronger bounds on the mass-splitting planes. We can still see the two STU solutions. The
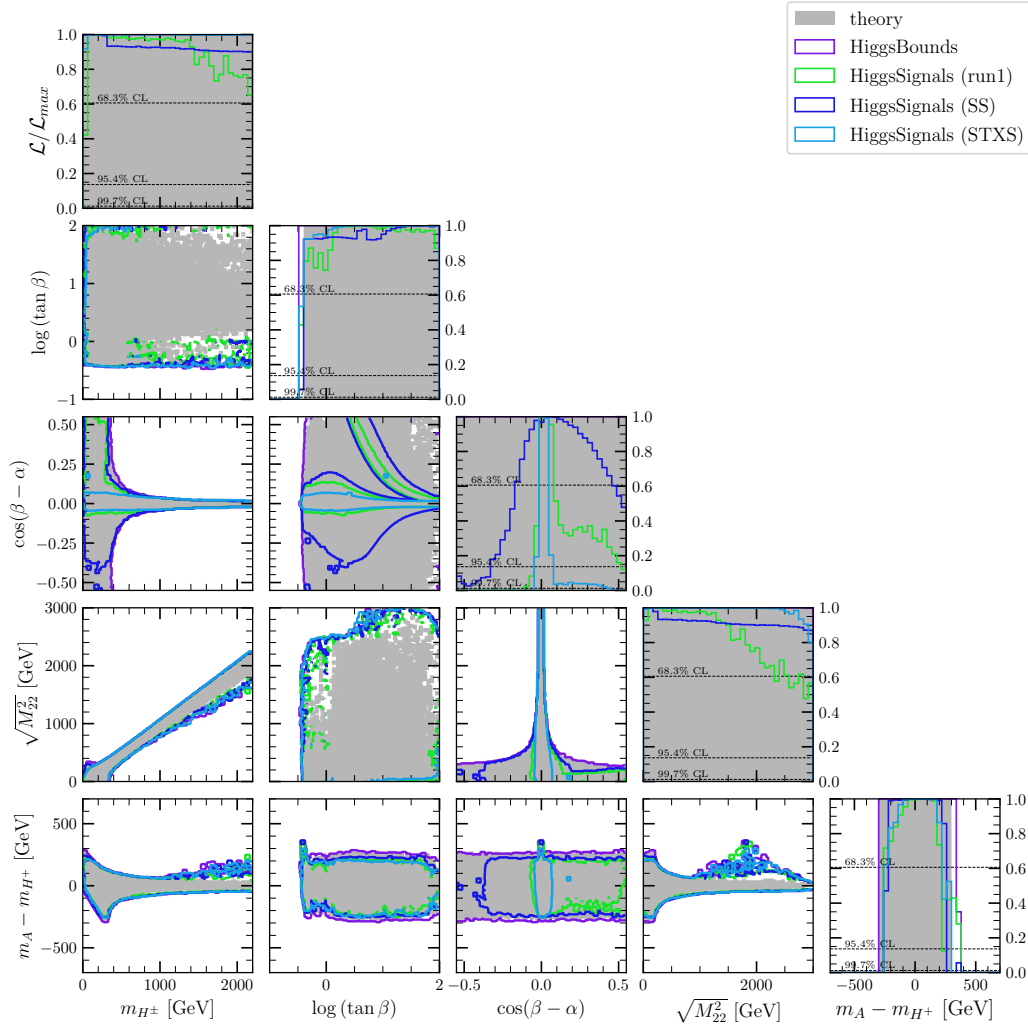
FIGURE 12.4: 1D and 2D profile likelihood ratio plots of the collider constraints in planes of the benchmark parameters.

STU constraints provide an upper bound for $m_A - m_{H^+}$ that is slightly stronger than theoretical constraints alone. But the bound on $m_H - m_{H^+}$ and $m_H - m_A$ is no better.

Collider results are given in Figures 12.4 and 12.5 for the Type-II and Type-I 2HDM respectively. These look very similar to the tree-level results. This is expected since there are no theoretical limits on the $\cos(\beta - \alpha)$ vs. $\tan\beta$ plane – which are the parameters relevant for collider observables. We also see some poor sampling density in Figure 12.5. This is expected since the collider constraints run much slower than theory/electroweak constraints and these planes are also much harder to sample compared with tree level.

We did not run flavour or combined fits for the FlexibleSUSY generated spectrum, but for the Type-II 2HDM, we expect the $\cos(\beta - \alpha)$ parameter to be forced closer to zero once the flavour constraints are included. The lower bounds for m_H and m_A should also be higher due to the tighter restrictions on the mass splittings.
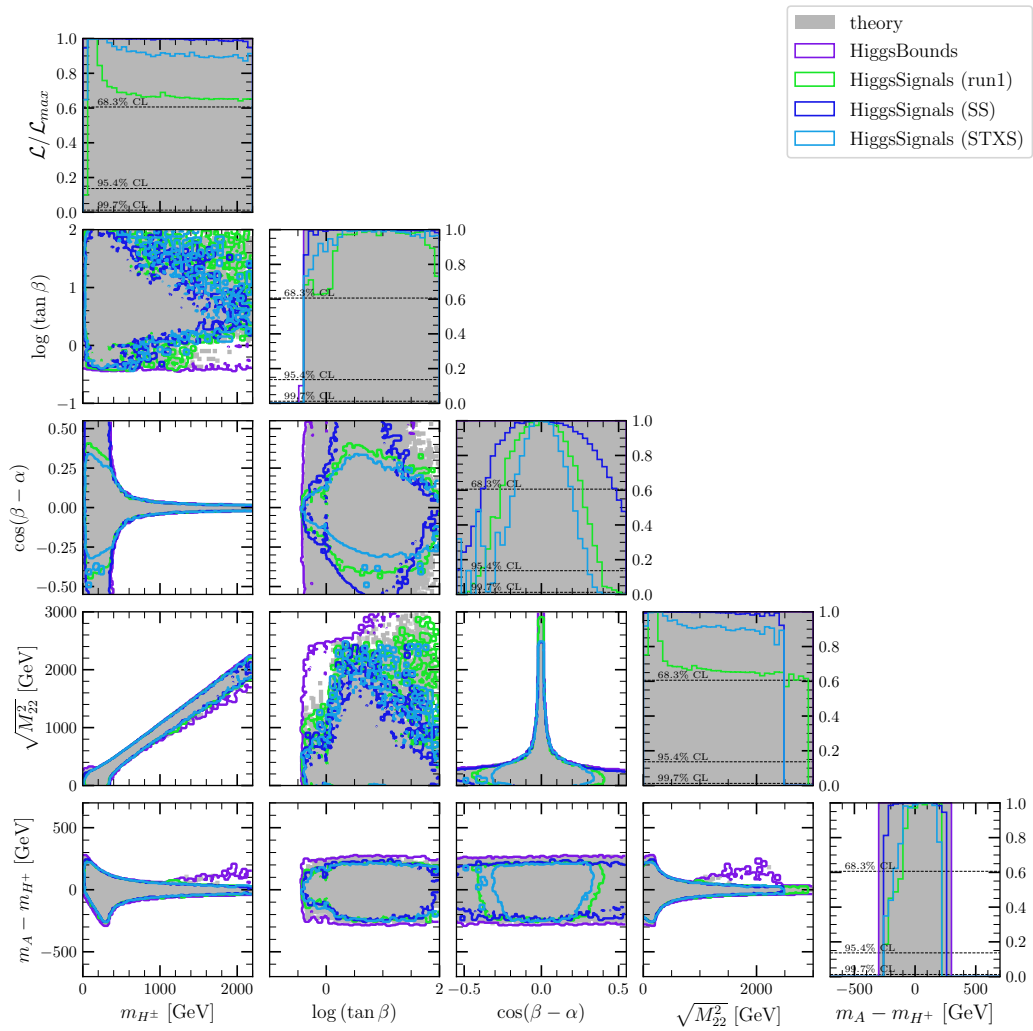
FIGURE 12.5: 1D and 2D profile likelihood ratio plots of the collider constraints in planes of the benchmark parameters.

Part III

GLOBAL FITS OF THE IDM

Chapter 13

Implementation of the IDM in GAMBIT

Initially, GUM was used to generate the code required to implement the IDM in GAMBIT. A new `.gum` input file was written with the appropriate options (see Appendix C for details). We chose to use SARAH, rather than Feynrules, since the former has the ability to generate a loop-level, SPheno-based spectrum generator and also expressions for the Wilson coefficients. We used the existing Lagrangian-level IDM model files from the SARAH package with some minor changes that are given in Appendix C. GUM is still relatively new software so various additions and bug fixes were necessary.

Firstly, modifications were made to extract the Wilson coefficients from SPheno. As explained in Section 6.2.3, SARAH already has the ability to generate code for calculating Wilson coefficients using FlavorKit. These are needed for calculation of flavour observables and the `DD_rel_WCs_flavscheme` capability which is used for the IceCube dark matter likelihoods. The SPheno subroutine, `CalculateLowEnergyConstraints` (in `Observables/LowEnergy_MODEL.f90`), is used to calculate all Wilson coefficients, flavour observables and electroweak observables. The latter is included in the default SPheno package, while the former two are added by SARAH. We added three new options to the `.gum` input files: `GetWilsonCoefficients`, `GetFlavorObservables`, and `GetElectroweakObservables`, which tell GUM to extract the Wilson coefficients, flavour observables and electroweak observables from SPheno respectively. A capability for each WC/observable is then added to GAMBIT and also the example .yaml input file that gets generated by GUM. This `.yaml` file can then be used to run a GAMBIT parameter scan with flavour and electroweak constraints.

The electroweak observables include the STU parameters, anomalous magnetic moments of charged leptons and electric dipole moments of charged leptons. These capabilities do

appear to be working correctly but are not yet used – we prefer 2HDMC's calculation of the STU parameters. Unfortunately, there is a bug in the WC calculations and therefore these capabilities are not yet used in our scans.

While modifying GUM, one problem we faced is that running SARAH is extremely slow, taking up to 30 minutes depending on the model and input options. This made debugging extremely difficult. Because we do not often need to change the SARAH model file, GUM was modified to automatically save all the SARAH outputs to a file. On the next run, the user can use the command line option `--usecache` to automatically use the saved SARAH outputs rather than calculating them from scratch. The rest of GUM only takes a few seconds to run, so this saves up to 30 minutes each time.

Some changes were also made to the CalcHEP outputs. There are actually two separate installations of CalcHEP used in GAMBIT. The first one is the usual CalcHEP backend while the second is part of the micrOMEGAs backend. Originally, GUM generated entirely separate code to set the input parameters for each CalcHEP version. This has now been changed so that the input code is the same, making it easier to maintain. Unfortunately, it is difficult to decouple CalcHEP from micrOMEGAs so two installations of CalcHEP will remain for now. An extra check has been added to ensure all CalcHEP model parameters are accounted for – if not an error is thrown.

Unfortunately, there were also problems with the CalcHEP model files generated by SARAH. Hence, we took a different approach where GAMBIT will generate its own CalcHEP model files automatically. A new capability was added called `calchep_model_GAMBIT`. This generates a set of model files which accept couplings as inputs rather than the model parameters. It depends on another new capability called `coupling_table`, which is used to get all the couplings of a GAMBIT model. For the 2HDM, most couplings are calculated using the 2HDMC backend. The Goldstone and SM couplings were coded manually. On the first run the `coupling_table` along with the particles for the model determine how the CalcHEP model files are generated. After this `calchep_model_GAMBIT` only assigns the parameters. These capabilities may be easily extended to work with other models.

One challenge we faced was finding the appropriate Lorentz factor for each vertex. Our solution involved, firstly, using a default Lorentz factor based on the spin of each particle in the vertex. These are listed in Table 13.1. This will not work for effective couplings such as hZZ and $h\gamma\gamma$ (which are needed because CalcHEP only considers tree-level diagrams, while these important couplings only occur at loop-level). To solve this problem, there is a model-dependent override for the Lorentz factor when it differs from the default value.

The CalcHEP frontend has been overhauled. Firstly, the CalcHEP model file is specified using a capability so that multiple model files can be used for the same GAMBIT model. In

Coupling type	CalcHEP Lorentz factor
$hhh, hhhh$	1
ffh	1
VVh	(m1.m2)
Vhh	(-m1.p2+m1.p3)
$ff\slashed{V}$	G(m3)
VVV	(p1.m3*m1.m2-p2.m3*m1.m2-p1.m2*m1.m3+p3.m2*m1.m3+p2.m1*m2.m3-p3.m1*m2.m3)
$VVVV$	(2*m1.m2*m3.m4-1*m1.m3*m2.m4-1*m1.m4*m2.m3)

TABLE 13.1: Default Lorentz factors used for the generated CalcHEP model files. Here h, f and V represent generic spin-0, spin-1/2 and spin-1 particles respectively. The terms in the Lorentz factor have the following meaning: p1,p2,... represent particle momenta, m1,m2,... represent Lorentz indices (i.e. $\eta_{\mu_1}, \eta_{\mu_2}, \ldots$) and G(m1), G(m2), ... represent gamma matrices (e.g. γ^{μ_1}.)

particular the user may select either `calchep_model_GAMBIT` or `calchep_model_IDM` for the IDM. One problem in the previous implementation is that it required the use of particle names from the CalcHEP model files rather than the GAMBIT names. Therefore a translation was done within DecayBit and DarkBit when the CalcHEP backend convenience functions were being called. In the new version, only the GAMBIT names are required for these convenience functions, thus hiding the implementation details of the CalcHEP models. The translation is done automatically in the CalcHEP frontend based on the current model files.

The IDM implementation in GAMBIT was initially generated by GUM with an interface to a SPheno spectrum generator. However, we found that the pole masses were not consistent with expectations.[1] Hence, we also implemented a tree-level spectrum generator – which is used for our scans of the IDM. The existing 2HDMC interface has been updated to support the IDM – which is used for calculation of the couplings and decay rates.

The theoretical constraints for the IDM were also implemented. Note that the 2HDM theoretical constraints will not work (other than the LO unitarity constraint), so we need separate constraints for the IDM.

Because the IDM uses a different convention from the typical Type-I 2HDM (as explained in Section 3.9), a new function was added to switch between the two conventions, based on the expressions in Equation 3.73. Initially this was done due to the code not being

---

[1]They differed from the tree-level expressions by hundreds of GeV and the mass hierarchy also differed. Increasing the tree-level m_{H^+} did not usually result in an increase for the SPheno pole mass.

compatible with the IDM conventions. This was eventually fixed, but we still used this function to check that results in both conventions are consistent.

Finally, a new physical basis for the IDM was added consisting of the following parameters: m_h, m_H, m_A, m_{H^+}, λ_2, and λ_{345}.

Chapter 14

Theoretical Constraints in the IDM

We now turn to the IDM, starting with just the theoretical constraints. We use a physical basis to perform our parameter scans, which includes the following parameters: m_h, m_H, m_A, m_{H^+}, λ_2, and λ_{345}. The parameter ranges are given in Table 14.1. Unlike the 2HDM, there is no true decoupling limit since the theory becomes non-perturbative as $m_H, m_A, m_{H^+} \to \infty$. However, masses as high as 10^4 are still permitted. To save computer hours we do not scan the entire mass range here (the high mass region is not touched by experimental constraints anyway). We did not use any hybrid bases here. The IDM is somewhat easier to sample in the physical basis since it has only 5 free parameters – two of which are couplings. We did, however, include 11 parameter range combinations to ensure that all planes of interest are sufficiently well sampled.

We only present tree level results here. An interface to SPheno with a loop-level spectrum generator has been setup, but the pole masses are not consistent with expectations and still need further investigation.

Parameter	Range
m_h	124.1 to 126.1
m_H	10 to 3000
m_A	10 to 3000
m_{H^+}	10 to 3000
λ_2	0 to 12.57
λ_{345}	-12.57 to 12.57

TABLE 14.1: Parameter ranges used for the IDM.
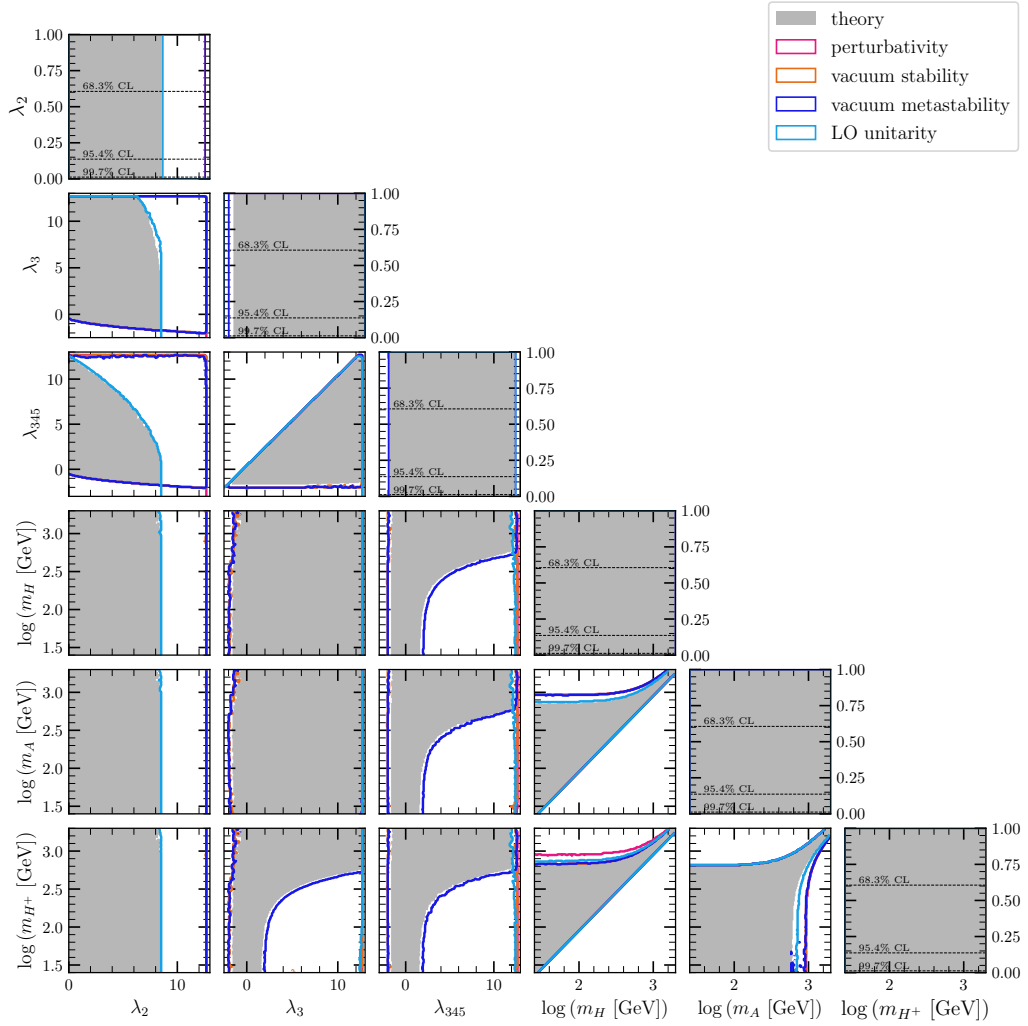
FIGURE 14.1: (IDM) 1D and 2D availability plots of the theoretical constraints in planes of parameters taken from set A.

We use the standard IDM notation where H is a $\mathbb{Z}_2$-odd scalar, while h is $\mathbb{Z}_2$-even and corresponds to the SM Higgs boson. This differs from the standard 2HDM notation where H is assumed to be the heavier CP-even scalar while h is a lighter CP-even scalar. As mentioned in Section 3.9, all h couplings with fermions and gauge bosons are exactly SM-like, and thus we have $h = h_{SM}$ with $\lambda_{SM} = \lambda_1$. We consider two sets of parameters for our plots given by

(A) λ_2, λ_3, λ_{345}, $\log(m_H)$, $\log(m_A)$, $\log(m_{H^+})$,

(B) $\log\sqrt{m_{22}^2}$, $m_H - m_A$, $m_H - m_{H^+}$, $m_A - m_{H^+}$

The couplings λ_2, λ_3, λ_{345} are chosen since they represent the DM-h_{SM}, H^+-h_{SM} and DM-DM couplings respectively (see Table 3.8). The mass splittings provide a good benchmark for the STU electroweak observables. We plot the logarithm of the masses to
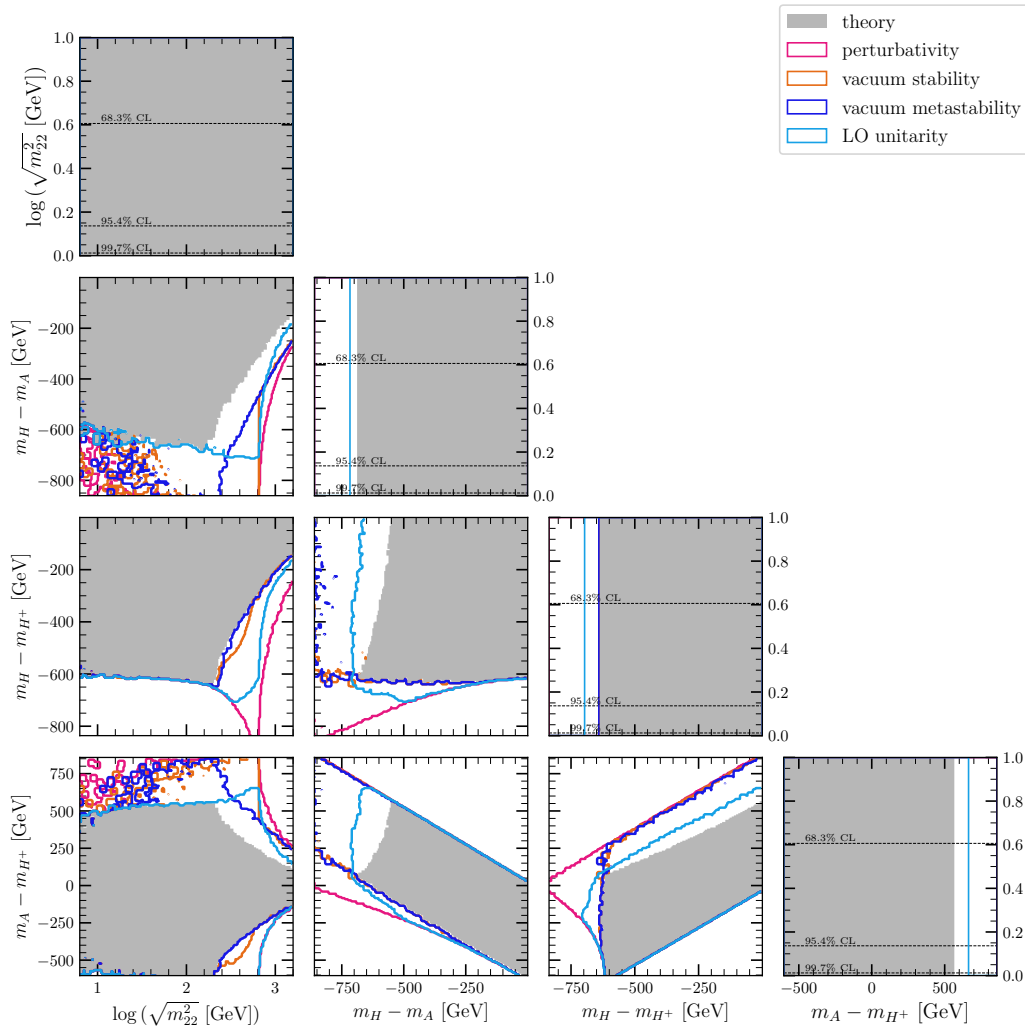
FIGURE 14.2: (IDM) 1D and 2D availability plots of the theoretical constraints in planes of parameters taken from set B.

highlight the low-mass region, which is constrained by both collider and direct detection constraints as we show later.

Recall that H and A are relatively CP-odd but their actual CP-state is arbitrary since there are no SM-DM interactions that could determine it. We may take either H or A as the DM candidate, however the choice is arbitrary since the two particles switch roles under $\lambda_5 \to -\lambda_5$. To avoid this redundancy, we take H to be the DM candidate and fix $\lambda_5 < 0$. Therefore we require that $m_H < m_A$ and $m_H < m_{H^+}$[1].

The theoretical constraints we consider are: vacuum stability, vacuum meta-stability, leading-order unitarity, and perturbativity and are given in Figures 14.1 and 14.2. We

---

[1]This is not enforced in the parameter ranges since GAMBIT does not have the ability to set one parameter range relative to another. Instead, it is enforced when we fix the sign of λ_5. Therefore, the input parameters m_H and m_A may be swapped when the spectrum is generated. This is not a problem since the input parameters are not used anywhere after this.

also eliminate any points with a charged vacuum or charged DM candidate (in all cases). This latter requirement [48] is enforced by

$$\lambda_4 - |\lambda_5| < 0. \tag{14.1}$$

We observe that large values of λ_{345} at small masses violate vacuum meta-stability, and that the mass-splittings are small when the masses are large. The DM-DM coupling, λ_2, has an upper bound of 9 due to unitarity. When comparing with the 2HDM results we need to take into account the swapped conventions. For example we can see a resemblance between λ_2 vs λ_3 (IDM) and λ_1 vs. λ_3 (2HDM Figure 8.1).

Chapter 15

Experimental Constraints in the IDM

In this section we highlight the individual effects of the experimental constraints. We begin with the STU electroweak constraints in Figure 15.1. As usual, the mass-splitting planes provide the ideal benchmark. Previously in the 2HDM, we found two separate regions for the STU constraints in the mass-splitting planes (c.f. Figure 9.1). But in the IDM, we find that part of the original plot is cut off; partly due to theoretical constraints and also because we require $m_H < m_A$. Fits of the S, T, and U parameters are shown in Figure 15.2. We see that the IDM cannot quite produce the experimental value for the S parameter (of 0.4) simultaneously with the T and U parameters. This is because a region in the middle of the S versus T plot has been eliminated by the theoretical constraints.

The collider results are provided in Figure 15.3. Since the fermion and gauge boson couplings with h are SM-like at tree-level, they automatically satisfy collider constraints within the experimental uncertainty. But there are still two processes that are relevant for IDM Higgs searches at the LHC: $h \to HH$ and $h \to \gamma\gamma$ (via H^+). The former is kinematically open when $m_h > 2m_H$ and leads to an invisible branching ratio. This results in a lower bound m_H of 63 GeV. The exception is when λ_{345} and λ_3 are close to zero (less than 0.02), since these determine the hHH/hAA and hH^+H^- couplings. In this scenario, the DM sector is decoupled from the SM.

The precision measurements of the $W^\pm$ and Z decay rates require that: $m_H + m_{H^+} > m_W$, $m_A + m_{H^+} > m_W$, $m_H + m_h > m_Z$, and $2m_{H^+} > m_Z$. This limits the charged scalar mass $m_{H^+} > 70$ GeV. For $m_A < 100$ and $m_H < 80$ GeV, there is only a narrow surviving region of $m_A - m_H < 8$ GeV. Outside this region is excluded by the LEP data since it would lead to a visible di-jet or di-lepton signal. We find that the collider constraints give a small preference for $\lambda_{345} < 0$, $\lambda_2 < 0$ and masses near 160 GeV.
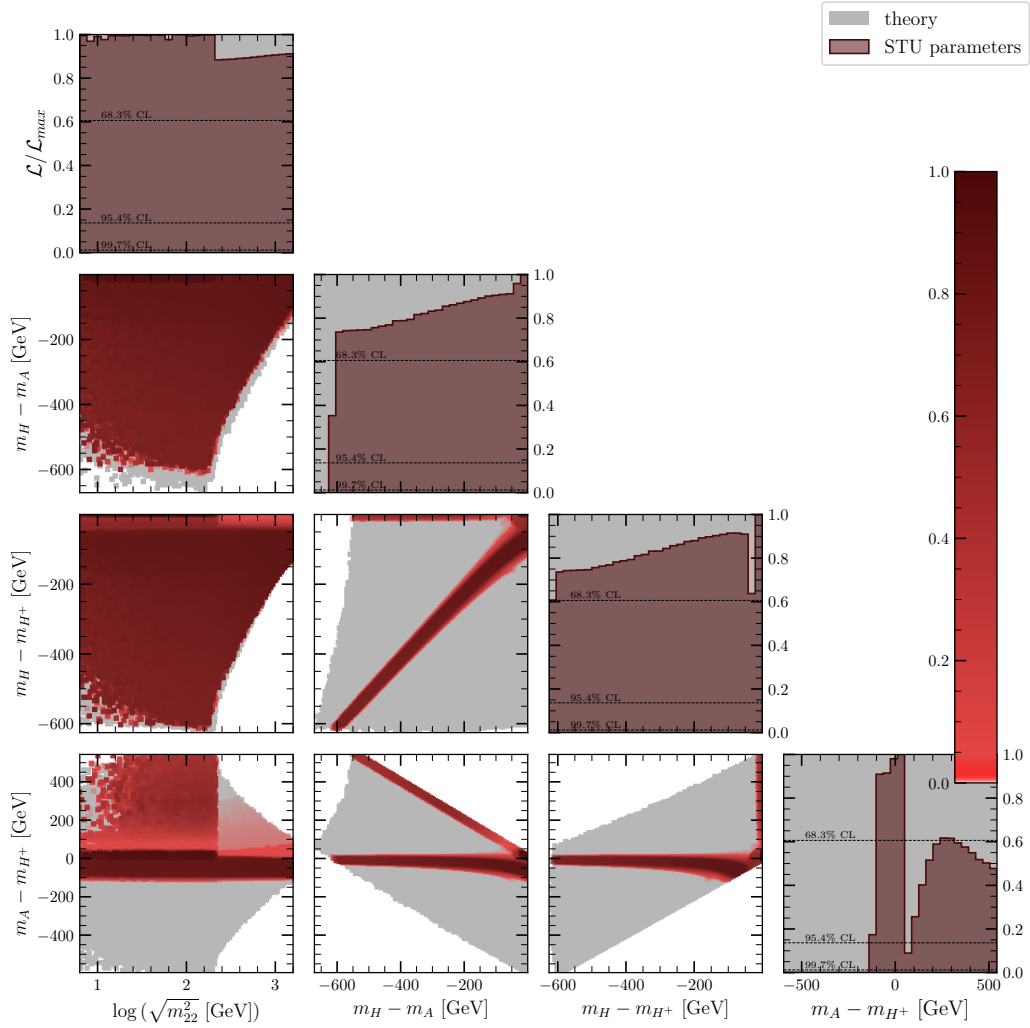
FIGURE 15.1: (IDM) 1D and 2D profile likelihood ratio plots of the STU electroweak constraint in planes of parameters taken from set B.

The relic density of our DM candidate, H, depends on the parameters m_H, m_A, m_{H^+}, and λ_{345}. Figures 15.4 and 15.5 give us an idea of how it varies as a function of m_H and λ_{345}. Here we consider partially degenerate masses $m_A = m_{H^+} = m_h + \Delta$ where $\Delta = 1$ and 100 respectively for each figure. As discussed in Section 4.5, a larger DM annihilation rate leads to a lower relic density. The features of these plots are explained as follows:

- There are two dips near $m_H = 45$ GeV corresponding to the resonances for $HA \to Z$ and $HH^+ \to W^+$. These processes are independent of λ_{345}. It disappears in the $\Delta = 100$ GeV plot since in this case $m_H + m_A \gg m_Z$ and $m_H + m_{H^+} \gg m_W$.

- The sharpest dip occurs at $m_H = 65$ GeV and corresponds to DM annihilation into the Higgs boson: $HH \to h$. This is the same in both figures with the relic density reaching below 10^{-6}.
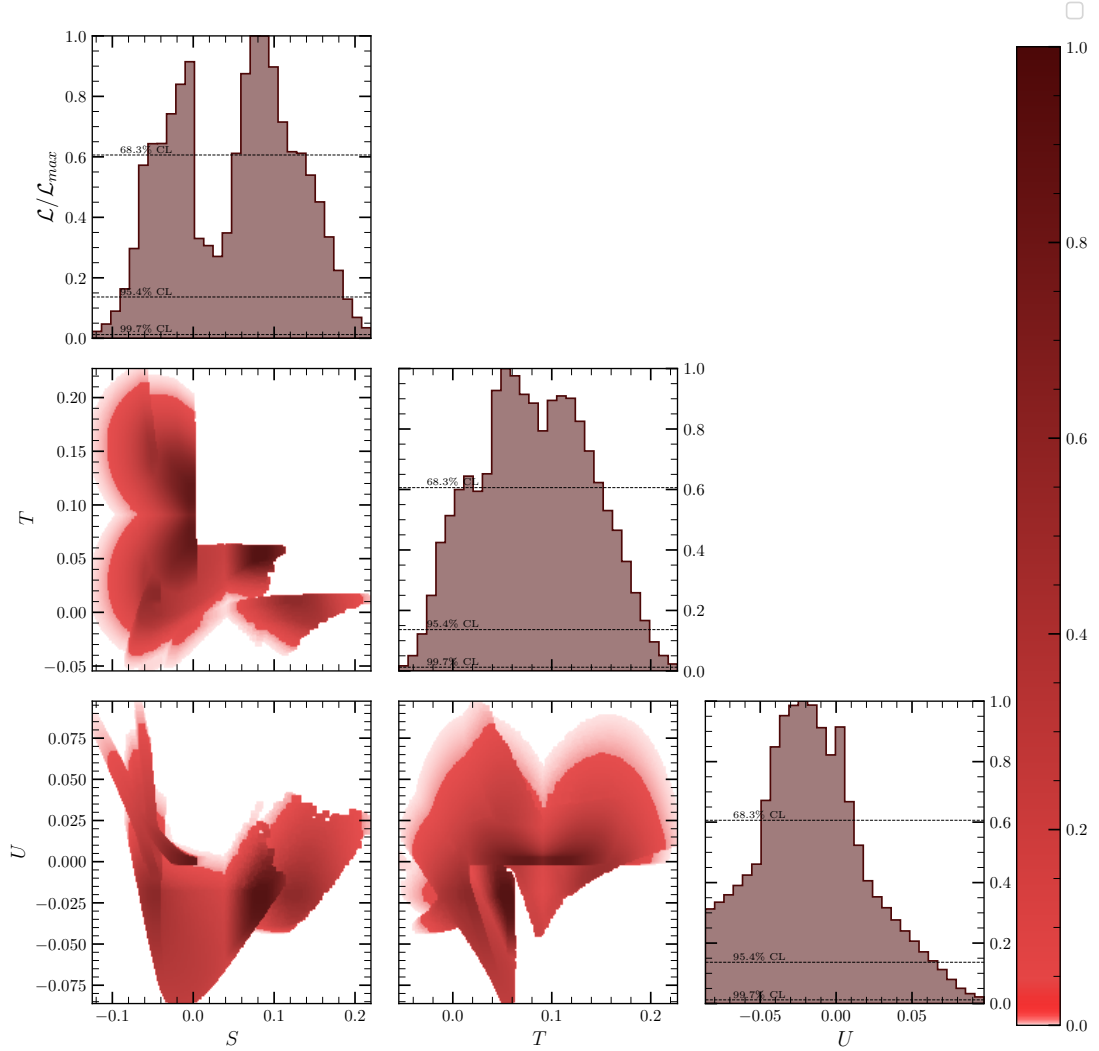
FIGURE 15.2: (IDM) 1D and 2D profile likelihood ratio plots of the STU electroweak constraint in planes of the S, T, and U parameters.

- We have a wider shallow dip at 80-90 GeV which corresponds to the $HH \rightarrow W^+W^-$ and $HH \rightarrow ZZ$ annihilation channels.

- We have a small dip at 125 GeV due to the $HH \rightarrow hh$ annihilation channel. This only happens for large λ_{345} since this also happens to be the $hhHH$ coupling.

- For $\Delta = 1$ GeV, the effective co-annihilation of scalars keeps the DM density below the Planck limit for $m_H < 65$ GeV. For $\Delta = 100$ GeV, the co-annihilation is suppressed and the relic density is below the Planck limit only for large values of λ_{345}.

- For large m_H co-annihilation becomes less important than $HH \rightarrow VV$. In particular, the couplings with the longitudinal components are important. This coupling is equal to $\bar{\lambda}_{345}$ or λ_3 for $HHWW$ or $HHZZ$ respectively.
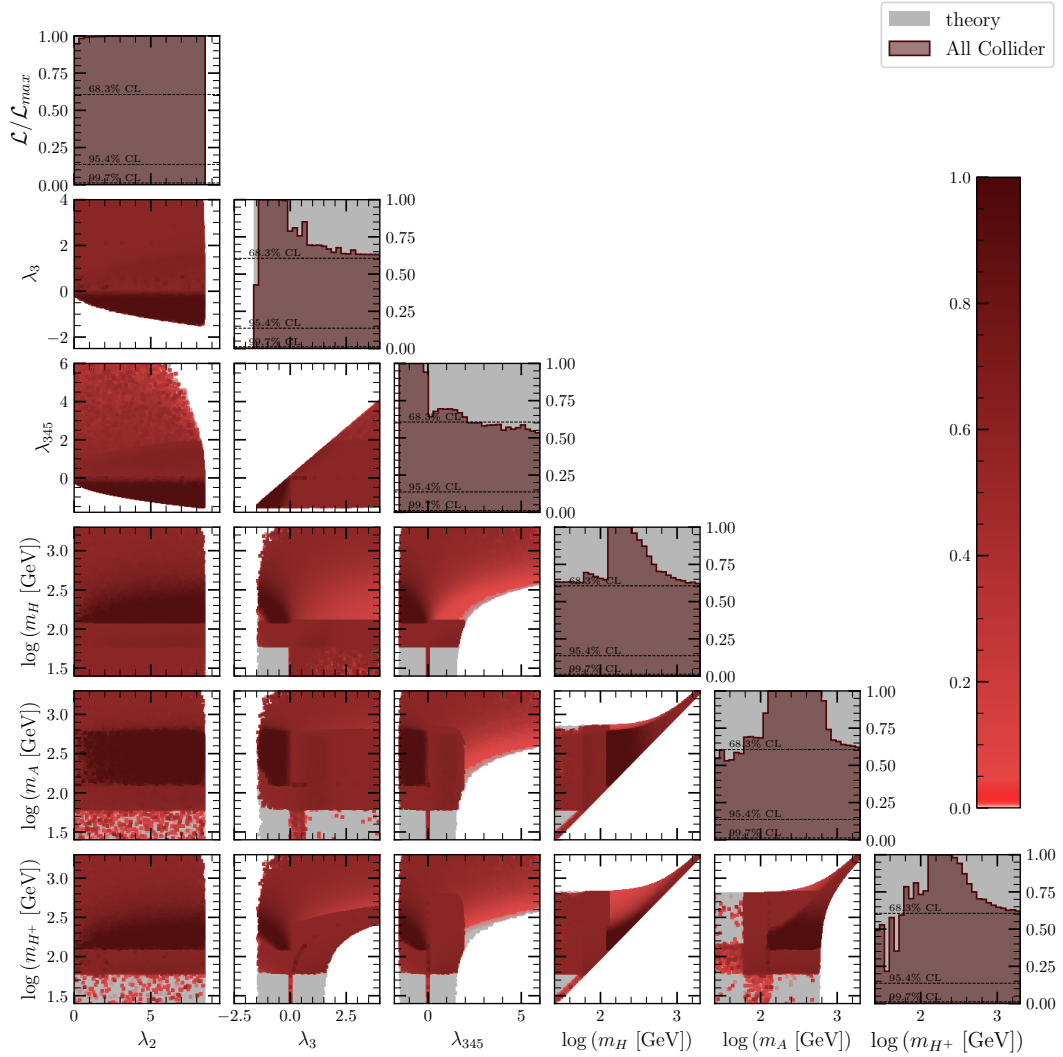
FIGURE 15.3: (IDM) 1D and 2D profile likelihood ratio plots of the collider constraints in planes of parameters taken from set A.

- For small mass splittings, $\bar{\lambda}_{345} \equiv \lambda_3 + \lambda_4 - |\lambda_5|$ and λ_3 are small. This leads to a small annihilation cross-section $\langle \sigma v \rangle$ which decreases with growing m_H. Eventually this causes a relic density above the Planck limit.

- For large mass splittings, the annihilation cross-section remains larger and therefore the relic density remains below the Planck limit for large m_H.

Measurements of the CMB taken by the Planck experiment have determined that the DM relic density has a value of 0.120 ± 0.001. We apply this constraint as an upper bound so that other DM candidates may provide the remaining relic density. In isolation, the relic density constraint is not significant, but it has more impact in the global fits we consider later.
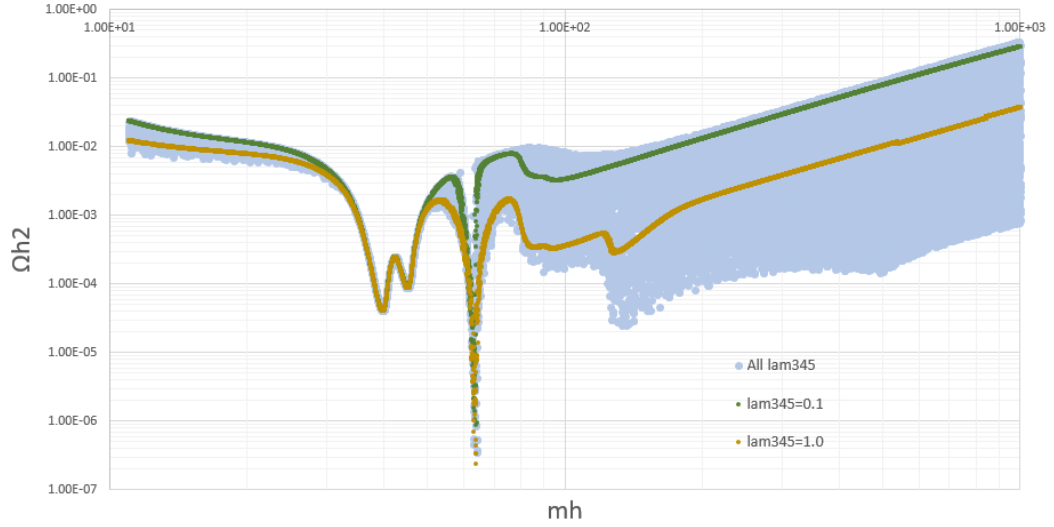
FIGURE 15.4: (IDM) The relic density, $\Omega_{DM}h^2$, as a function of the DM mass, m_H, for various λ_{345} values with $\Delta = 1$.
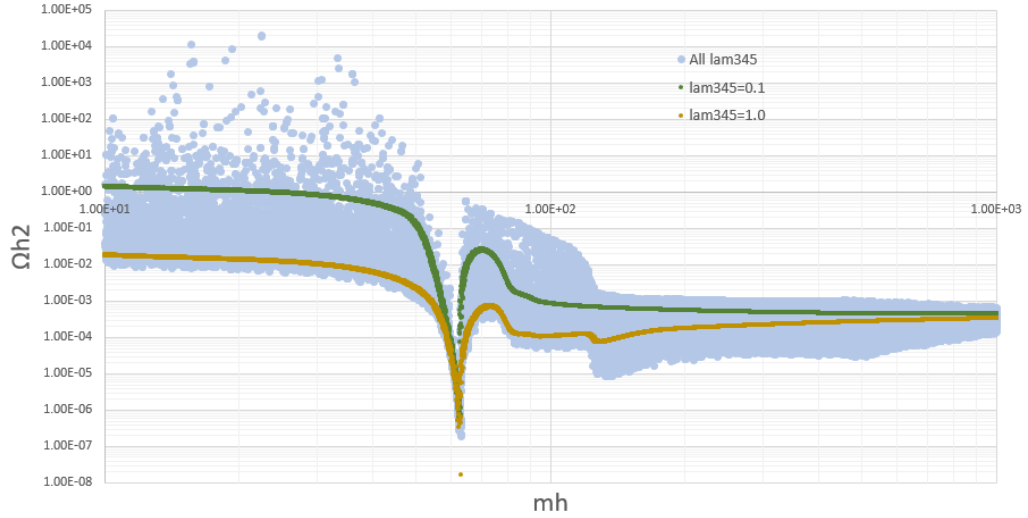
FIGURE 15.5: (IDM) The relic density, $\Omega_{DM}h^2$, as a function of the DM mass, m_H, for various λ_{345} values with $\Delta = 100$.

The DD experiments place lower bounds on the spin-independent DM-nucleon couplings. These are calculated by microOMEGAs and given to DDCalc to calculate Direct Detection likelihoods. The couplings are re-scaled by $R_\Omega \equiv \Omega_{DM}/\Omega_{DM}^{Panck}$ to take into account H representing only part of the total DM density. The experiments included are: XENON 1T (2018), LUX (2016), LUZ-ZEPLIN (2022), PandaX 4T (2021), PandaX (2017/2016), DarkSide 50 (2017), CRESST II (2015), CRESST III (2018), CDMS (2014), SIMPLE (2014), and PICO (2017). Direct detection experiments tend to constrain the low-m_H region where $R_\Omega \, \sigma_{SI}$ is high. Separate contours for each experiment are displayed in Figure 15.6 along with the combined DM fit.

There are currently 3 GAMBIT indirect detection likelihoods that are compatible with
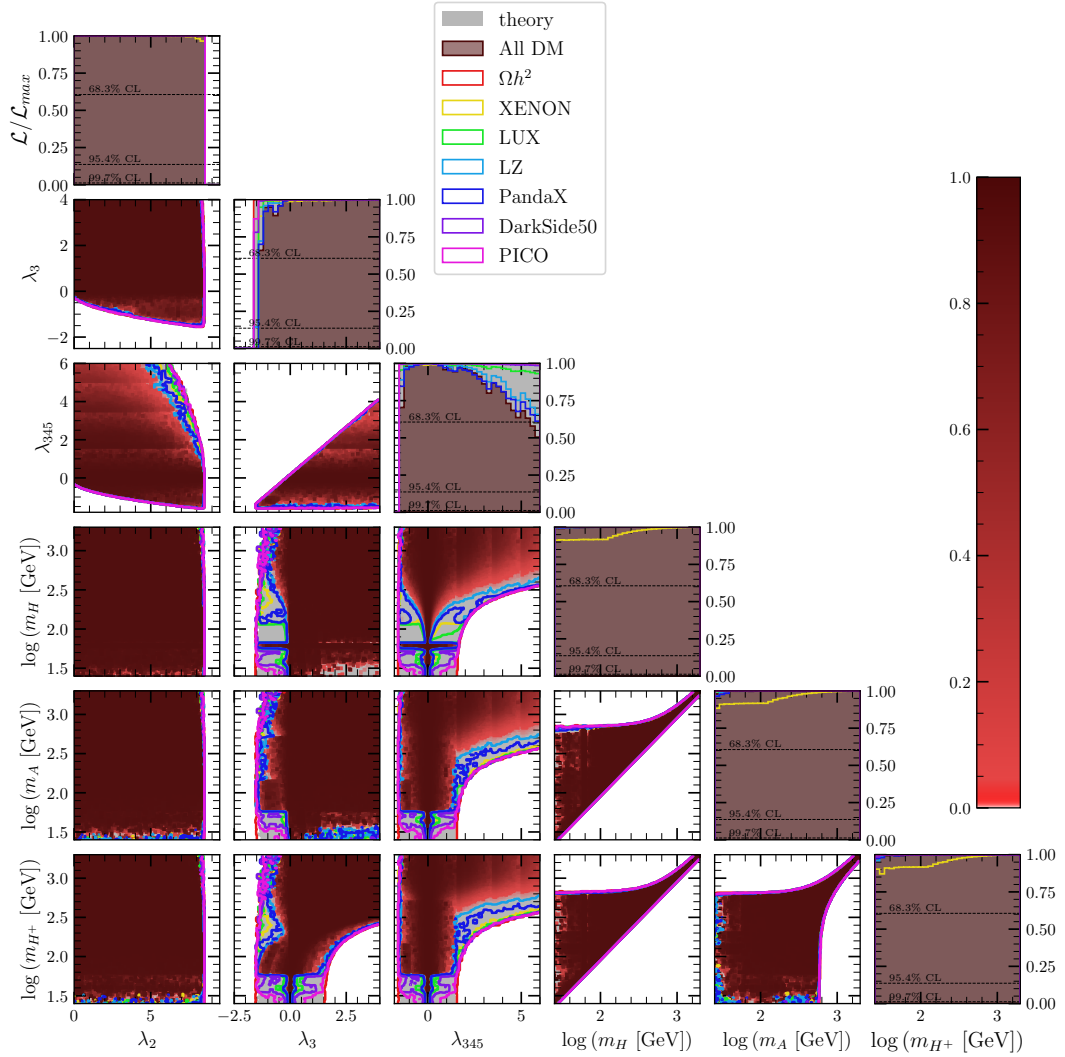
FIGURE 15.6: (IDM) 1D and 2D profile likelihood ratio plots of the dark matter constraints in planes of parameters taken from set A. Here Ωh^2 is the Planck upper bound on the relic density and LZ is short for LUX-ZEPLIN. Note that the banding along the λ_{345} axis is not a real feature. It is caused by having several targeted scans along this axis. The parameter becomes increasingly finely tuned towards 12 so this setup is necessary.

the IDM. These are `lnL_FermiGC`, `lnL_HESSGC`, and `lnL_FermiLATdwarfs`. The first two fit the gamma ray measurements from the galactic centre while the last fits the gamma ray measurements from dwarf galaxies.

The galactic centre measurements have shown a gamma ray excess that may be explained by DM. However, it has been shown that pulsars are just as likely to be the cause. To be conservative, we choose to exclude these likelihoods. We found that the constraints from the FermiLAT measurements of dwarf galaxies have a very minor effect and are not competitive with DD experiments. Therefore, we do not show a separate contour for this constraint, but it is included in the combined DM fit. We also do not display

separate contours for the CRESST, CDMS and SIMPLE experiments since their effect is very minor but they are included in the combined fit. We can see that the recent LUX-ZEPLIN (LZ) and PandaX results provide the strongest constraints.

Looking at the λ_{345} vs $\log(m_H)$ plane we see that much of the low mass region is eliminated except when λ_{345} is close to zero (where the h-DM couplings are small). This is due to the larger DM-nucleon cross-section. There is an exception when $m_H = 63$ GeV, where the relic density is low (due to $HH \to h$ annihilations). There is also a small bump at the $HA \to Z \; / \; HH^+ \to W^+$ resonance near 45 GeV. The effect on the other planes is minor, but we can see that $\lambda_3 > 0$ for most of the low m_H region and other masses also have a lower bound of 63 GeV except when λ_{345} and λ_3 are close to 0. For larger DM masses, the direct annihilation into WW, ZZ, and HH pairs opens, and the relic density drops further, making direct detection experiments insensitive to this region.

Chapter 16

Global fits of the IDM

Finally, we present the global fits for the IDM. The best-fit values for all parameters are provided in Table 16.1.

Starting with parameter set A in Figure 16.1, we see that the available regions are dictated mainly by the dark matter direct search constraints and look similar to the DM fits from Figure 15.6. In the case of $\log{(m_{H+})}$ vs. $\log{(m_A)}$, the STU electroweak

Parameter	Best Fit	95% CI
λ_1	0.2583	0.2564 to 0.2602
λ_2	3.34	0 to 8.38
λ_3	7.95	-1.0 to 12.5
λ_4	-8.56	-12.4 to 0.752
λ_5	-0.0468	-6.35 to 0
λ_{345}	-0.66	-1.40 to 5.82
m_h	125.1	124.7 to 125.6
m_H	2022	12 to 2162
m_A	2023	64 to 2185
$m_{H^\pm}$	2086	13 to 2200
m_{22}^2	4109000	-40780 to 4670000
m_{11}^2	-7830	-7886 to -7772
$m_H - m_A$	-0.7	-533 to 0
$m_H - m_{H+}$	-64	-541 to -0.2
$m_A - m_{H+}$	-63	-103 to 201

TABLE 16.1: (IDM) Best fit points and 95% confidence intervals for the combined fit.
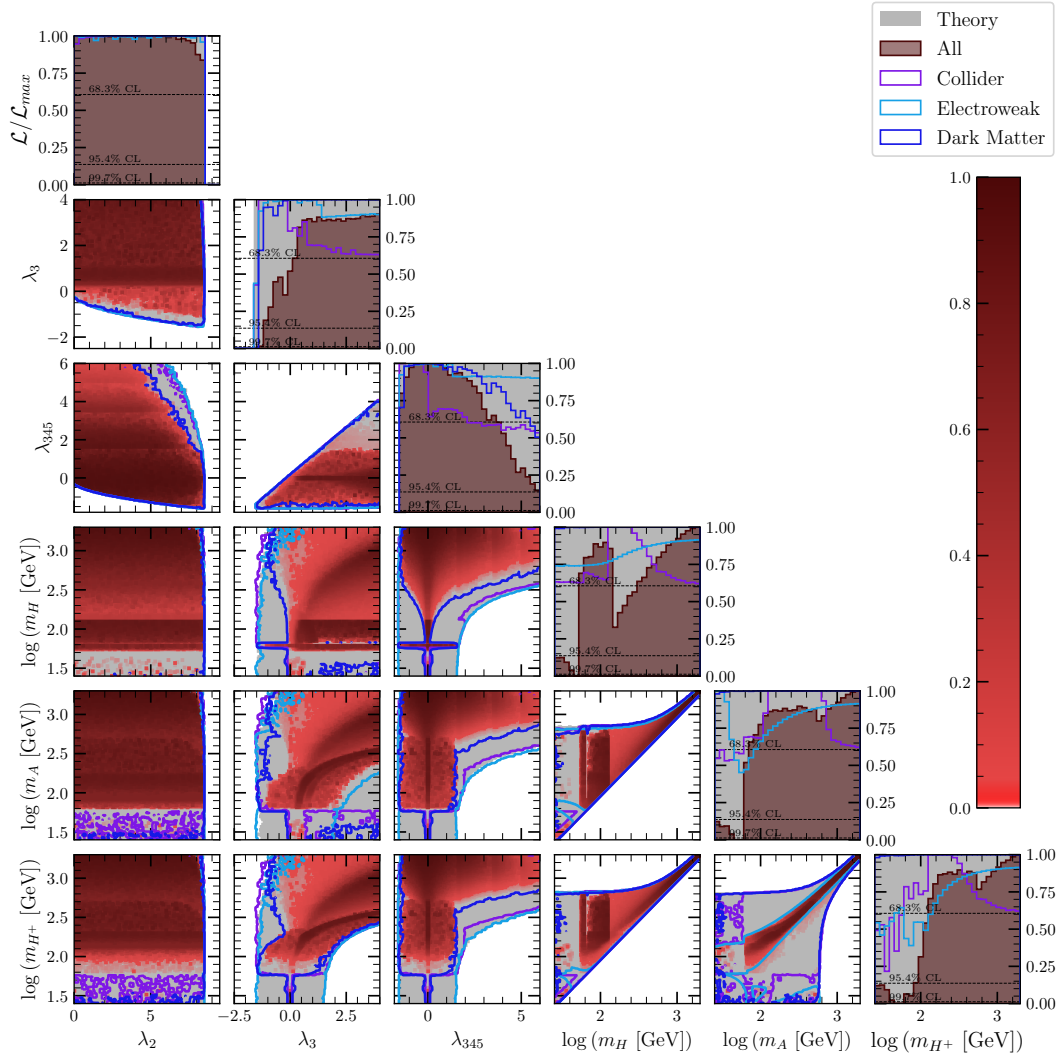
FIGURE 16.1: (IDM) 1D and 2D profile likelihood ratio plots of all constraints in planes of parameters taken from set A.

constraint is more important. To see why, we refer to the $m_H - m_{H^+}$ vs. $m_A - m_{H^+}$ plane in Figure 15.1. Here the STU constraint forces $m_A - m_{H^+}$ to be near zero for most of the parameter space, hence why m_A and m_{H^+} appear to be roughly proportional.

The low mass region is poorly sampled and in particular there is a lower bound for m_H of 58 at the 68% CL with only a few points below this at the 95% CL. This restriction is due to the combination of the relic density and collider constraints. The other masses have similar behaviour – m_{H^+} and m_A have lower bounds of 107 and 64 GeV, respectively when just above the 95% CL line with a few points below this that are available at the 95% CL. The tiny low mass region that is still available requires $\lambda_{345} \approx \lambda_3 \approx 0$ and either $m_H \approx m_A$ or $m_H \approx m_{H^+}$.

Now moving to parameter set B, in Figure 16.2 we find that collider and dark matter
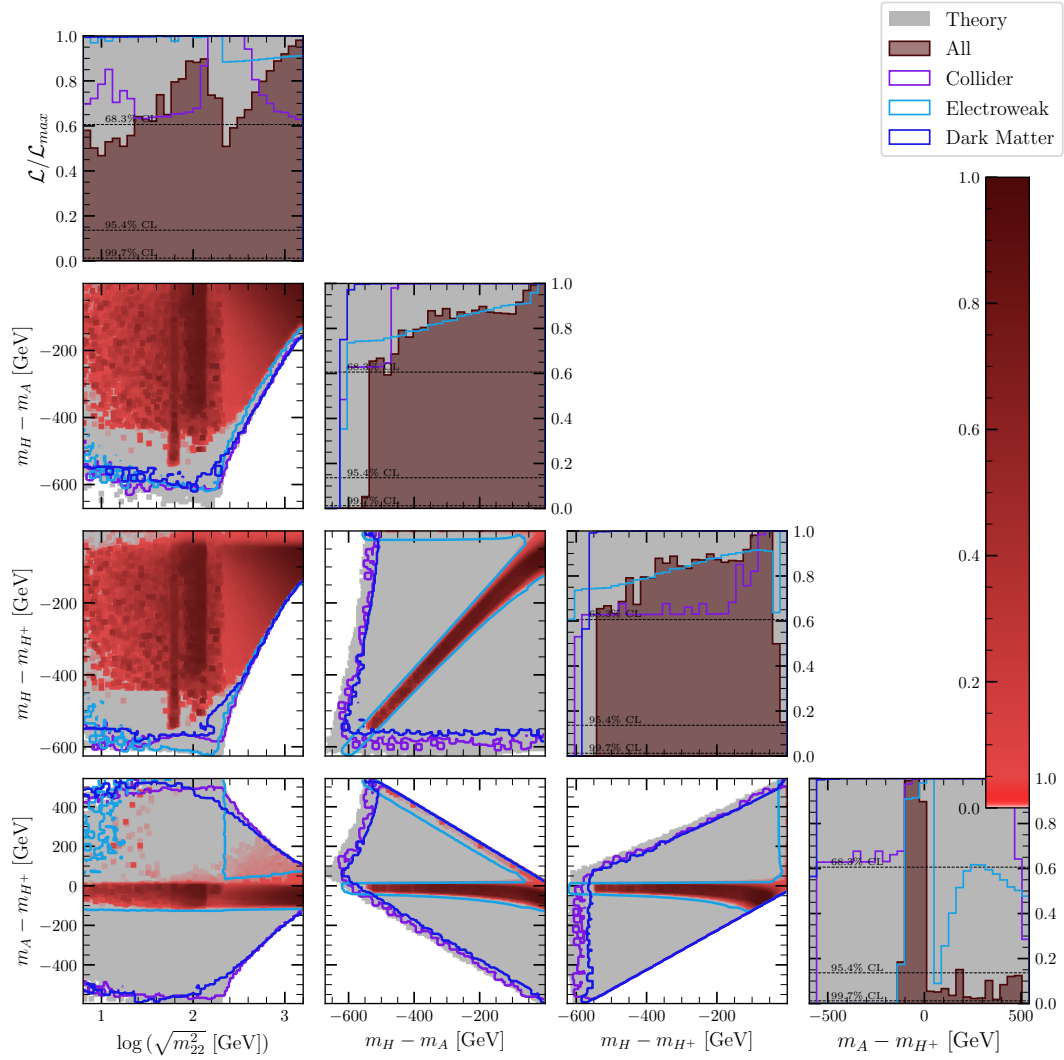
FIGURE 16.2: (IDM) 1D and 2D profile likelihood ratio plots of all constraints in planes of parameters taken from set B.

constraints have little effect on the mass-splittings, while the STU constraints remain as the most important. We see that one of the 'arms' set by the STU constraints is not well sampled. This is because much of this arm corresponds to the low mass region, which is almost entirely eliminated. However, it can likely still be improved using additional targeted scans of this region. We also give a plots for parameter set A versus parameter set B in Figure 16.3.

It is also interesting to examine how the relic density varies over the parameter space. We show $\log\left(\Omega_{DM}h^2\right)$ on the Z-axis in Figure 16.4, where we choose to display the value at the maximum likelihood point in each bin. We can clearly see that the Planck limit of $\log\left(\Omega_{DM}h^2\right) < 0.92$ has been applied. The blue regions correspond to $m_H = 63$ GeV, otherwise the relic density is mostly above 10^{-3}.
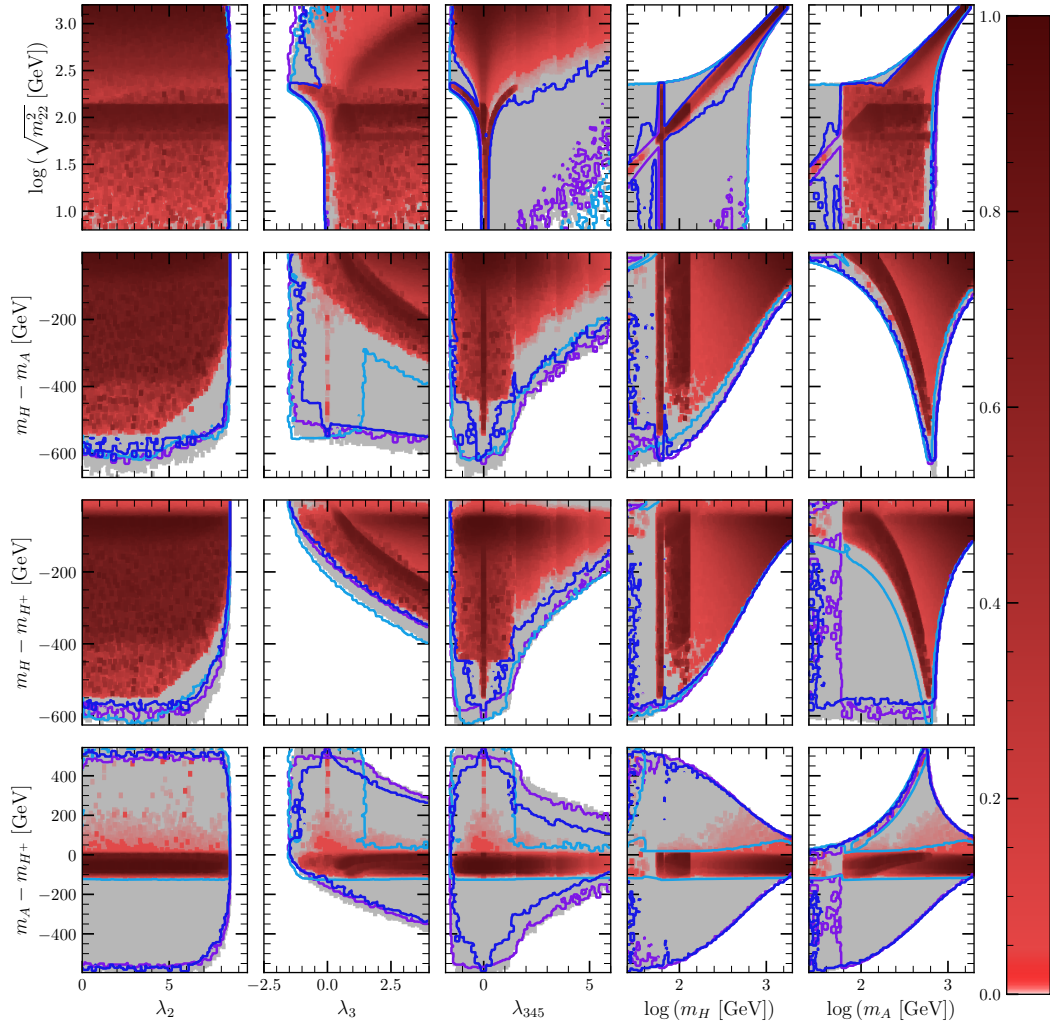
FIGURE 16.3: (IDM) 1D and 2D profile likelihood ratio plots of all constraints for parameter set A against B.

Although we did not focus on this scenario, one would find that there is a low mass region where $m_H \in (50, 80)$ GeV and a high-mass region where $m_H > 400$ GeV. In the high-mass region the masses, m_H, m_A, and m_{H^+}, are near degenerate. This results in suppressed decay rates for A and H^+. An interesting phenomenon occurs when $m_{H^+} - m_H \lesssim 0.2$ GeV. The charged scalar would decay slowly enough to leave tracks in the detectors of collider experiments – but they would disappear part-way.
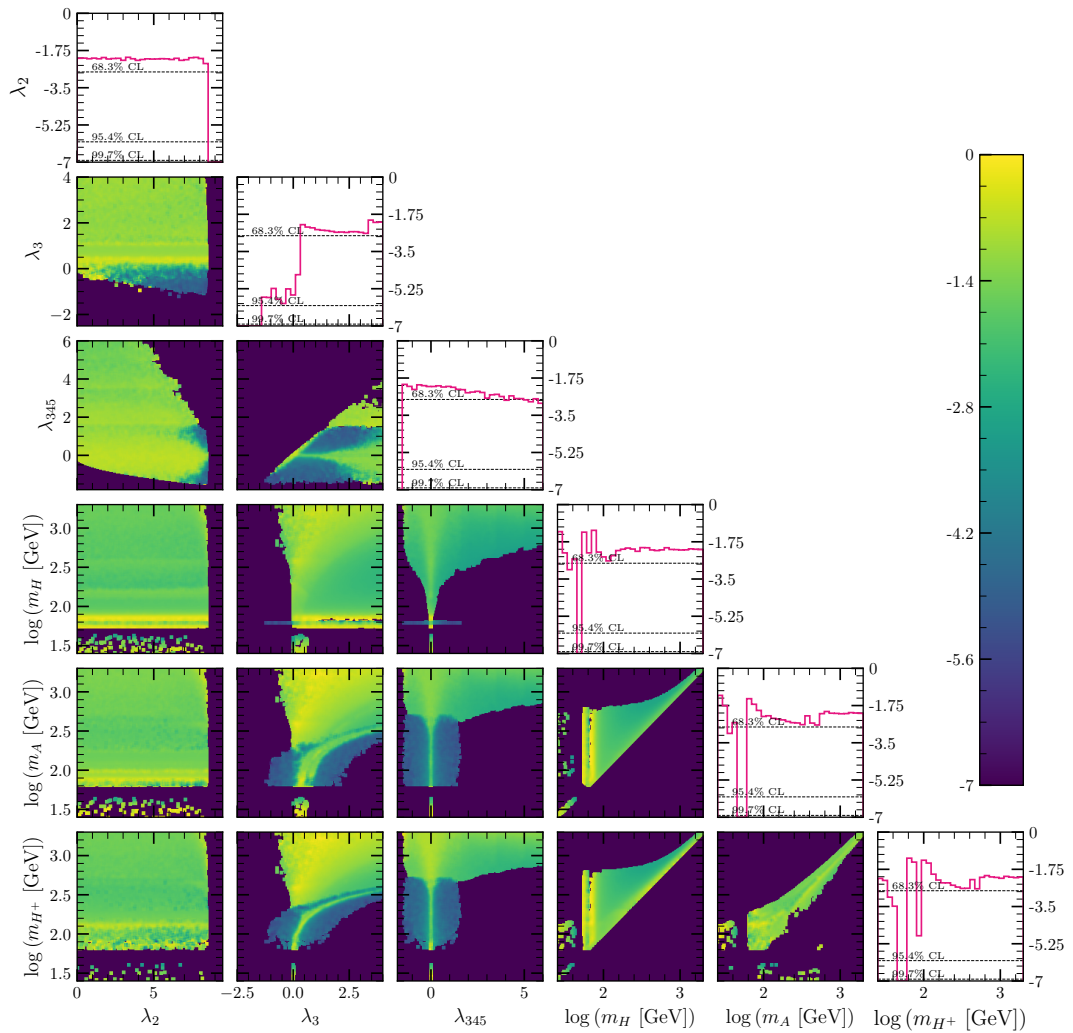
FIGURE 16.4: (IDM) The logarithm of the relic density at the maximum likelihood point in planes of parameters taken from set A. This is shown on the Z-axis for 2D plots and the y-axis for 1D plots.

Chapter 17

Conclusions

We explored the $\mathbb{Z}_2$-symmetric IDM and two softly-broken $\mathbb{Z}_2$-symmetric 2HDMs, namely the Type-I and Type-II 2HDMs. The latter two have interesting new flavour phenomenology while the former provides a DM candidate.

The 2HDM was previously implemented in GAMBIT, but was further improved with new features, bug fixes, and performance improvements. In particular, a variety of new bases were implemented to improve sampling density in various planes of interest. The `hybrid_Higgs2` basis typically performed the best while the `physical` basis performed the worst.

Global fits were done using GAMBIT, and separate plots were presented for each theoretical and experimental constraint. In the 2HDMs, the theoretical constraints did not place any restrictions on couplings or the charged-Higgs mass in the planes relevant for collider and flavour observables. Further, there were no theoretical limits on the scalar masses. There was, however, a restriction on the mass-splittings and the $\cos(\beta - \alpha)$ parameter at large masses.

The electroweak STU constraints restricted the mass-splitting versus mass-splitting planes. There were two allowed regions of roughly the same shape but rotated 180 degrees about the centre. The overall restriction on the mass-splitting parameters was slightly stronger than theoretical constraints alone, but only at low masses.

Only the collider and flavour constraints are model dependent. Firstly, the collider constraints restricted the $\cos(\beta - \alpha)$ versus $\tan\beta$ plane to be close to the SM-like limit. In particular $\cos(\beta - \alpha)$ was pushed close to zero. This restriction was stronger for Type-II due to the lack of a true SM-like limit for the $\tan\beta$ parameter. In Type-I, the lower limits for the additional scalars were set purely by the collider constraints; these were $m_H > 150$ GeV, $m_A > 91$ GeV, and $m_{H^+} > 94$ GeV.

Extra FCCCs provided by the charged scalar, H^+, resulted in contributions to the Wilson coefficients which were used to calculate the flavour observables. A lower bound for $\tan\beta$ of about 2 was found for both models; also a lower bound for m_{H+} of 1100 GeV was found in the Type-II 2HDM. We commented that this was unusually high compared to the current literature. For Type-II, we also observed a strong limit on $\cos(\beta-\alpha)$ when flavour and theoretical constraints were combined.

The combined fits showed similar behaviour to the separate experimental constraints. However, for the Type-II 2HDM, both collider and flavour constraints give a restriction on $\cos(\beta-\alpha)$, and both were important when plotted against $\tan\beta$. Furthermore, the flavour constraints combined with theoretical constraints to give a much stronger restriction on the mass splittings. In Type-II, limits on the mass-splittings combined with the mentioned limit on m_{H+} resulted in lower bounds for the other scalar masses of $m_A > 1100$ GeV and $m_H > 1000$ GeV.

Results for the hidden-Higgs scenario, where $m_H = 125$ GeV and $m_h < 125$ GeV, were presented separately. The main difference was that the masses m_A and m_{H+} have a strict upper limit of 600 GeV set by the theoretical constraints. In the Type-II 2HDM, we found that this conflicts with the lower bound for m_{H+} set by the flavour constraints, resulting in m_{H+} pushed up to the maximum allowed value of 600 GeV. The other key difference was that collider constraints pushed $\cos(\beta-\alpha)$ towards ± 1 rather than 0, as this is the SM-like limit for the hidden-Higgs scenario. We found Type-II extremely difficult to sample due to the highly restricted parameter space; meanwhile, the Type-I parameter space was more open since the flavour constraints do not give a lower bound for m_{H+}.

Preliminary results using the FlexibleSUSY spectrum generator at 2 loop level were presented; the main difference being the much stricter restriction on the couplings due to *i*) the NLO unitarity constraint, and *ii*) the fact that all theoretical constraints were checked at both m_Z and 1 TeV. The experimental constraints gave similar behaviour to the tree-level results, except where the parameter space was limited by theoretical constraints. We noticed that $\cos(\beta-\alpha)$ was much more restricted at large masses. We commented that when combined with flavour constraints, there is likely to be a tight restriction on this parameter in the Type-II 2HDM.

The IDM implementation in gambit was initially generated by gum. Due to problems with the generated CalcHEP model files, a new capability was added to GAMBIT to generate them automatically. A tree-level spectrum generator was also added due to problems with SPheno. The theoretical constraints were added, along with a new physical basis to assist with parameter scans.

For the IDM scans, we used the convention $m_H < m_A$ – enforce by setting $\lambda_5 < 0$, and also eliminated points with a charged DM candidate. Theoretical constraints gave a restriction on the DM-SM couplings, λ_{354}, $\bar{\lambda}_{354}$ and λ_2, at low m_H, though the couplings were opened up at higher masses. The STU electroweak constraints behave similarly to the 2HDM with two solutions on the mass splitting planes. However, part of the plot was cut by i) the theoretical constraints, and ii) the fact that $m_H < m_A$. There was a strong lower bound for $m_A - m_{H+}$ set by these constraints. The collider constraints mainly eliminated the low m_H, m_A, and m_{H+} regions, except when the SM-DM couplings were close to 0. We found that the relic density of the DM candidate had a strong dip at $m_H = 63$ GeV with $\Omega_{DM}h^2 < 10^{-6}$ corresponding to the $HH \to h$ annihilation channel, with smaller dips for the $HA \to Z$, $HH^+ \to W^+$, $HH \to ZZ$, and $HH \to W^+W^-$ resonances. The DM direct detection constraints also restrict the low m_H region, except when either i) the SM-DM couplings were close to zero, or when ii) m_H was close to the Higgs resonance at 63 GeV. The recent LZ and PandaX experiments provide the strongest constraints. The global fits were similar to the combined DD fit; the main difference was from the combination of the relic density and collider constraints – which eliminated much of the low-mass region even when the couplings were small.

To summarise, we ran global scans of three 2HDMs and translated the results into 2D confidence regions and 1D confidence intervals at the 95% CL – which are expected to contain the true parameter values 95% of the time. We may also like to know which model is preferred and if they are good extensions of the SM in the first place. To answer such questions, we would need to perform hypothesis tests and determine the p-values. Although we did not perform such tests, we expect the Type-II HHS 2HDM to perform poorly due to the conflict between flavour and theoretical likelihoods. Meanwhile, all other models/scenarios have plenty of parameter space where all constraints are satisfied simultaneously (with some of this corresponding to an SM-like limit). This is with the exception of a few flavour constraints in the Type-II 2HDM which preferred a small charged scalar mass – although these constraints exhibit an excess over the SM. At this stage, it is unclear if any additional scalars exist, or what their masses would be. To find out, we would either need a positive discovery of an additional scalar, or stronger experimental constraints to eliminate more parameter space, leaving just a single region for a given mass.

Outlook: Further testing of FlexibleSUSY and SPheno is in progress and the results will be published when we are satisfied that they are working properly. Issues with the SPheno Wilson coefficients and observables will be investigated, and once working will be used as a cross-check. The remaining DM constraints will be tested, and we will also consider scenarios where the IDM provides 100% of the relic abundance.

Further Work: There are plenty more 2HDM scenarios to be considered. We did not consider the other $\mathbb{Z}_2$-symmetric Type-X and Type-Y models. The fermiophobic limit in the Type-I 2HDM, which is similar to the IDM, is yet to be investigated. The aligned 2HDM is another example where FCNCs are eliminated. The Type-III 2HDM, which includes FCNCs, may offer a better explanation of anomalies in flavour observables, although requires some fine-tuning. The most general 2HDM with CP-violation offers further new phenomenology and may help explain the observed baryon asymmetry. Another thing to consider is the possibility of a strong first order electroweak phase transition, which may occur in the 2HDM.

Appendix A

Modified Pippi plotting package

The Pippi plotting package is frequently used to plot GAMBIT results, however the original version, developed by Pat Scott,[1] was found to be inadequate. The software has now largely been re-written with new features and improved performance. Some of the key changes include:

- The ability to specify grid plots within the input file to be generated. All the plots presented in this thesis made use of this feature.

- The ability to load an arbitrary number of datasets so that we can plot contours from each on the same axes. This is used, for example, when we want separate contours for flavour, electroweak and collider observables on the same plot.

- The ability to specify a folder rather than a single `.hdf5` data file. All datasets contained inside this folder are loaded and merged together before plotting the results.

- The ability to automatically save the merged dataset and delete the original files. This makes it unnecessary to merge the data beforehand and means we only have to load the data once prior to plotting it.

- The ability to define new data columns which are then processed by a custom python function to calculate them from existing columns.

- Names of data columns can now be any string. Previously, one had to number the data columns, making it difficult to know what was actually being plotted.

The modified version of pippi can be found at https://github.com/Alex0125698/pippi. An example input file is provided below. The new options are explained in the comments.

---

[1] See https://github.com/patscott/pippi.

```
; Example pip file by A.S. Woodcock


-----------------------------
---load stage-----------------


; the datasets to extract datasteams from;
; (*) if multiple datasets are given then each will be binned and overlayed on the
 ↪same plots
;     in this case both share the same stream names (see below)
; Supports: .txt, .csv, .hdf5, .mat, a folder, or any archives of these (.zip .tar
 ↪.tar.gz)
; in the case of a folder, all datasets contained within will be loaded and
 ↪appended together


dataset_0 = 'data/THDMItree_theory/samples:/data'
dataset_1 = 'data/THDMItree_perturbativity/samples:/data'
dataset_2 = 'data/THDMItree_NLO/samples:/data'
dataset_3 = 'data/THDMItree_stability/samples:/data'
dataset_labels = {'theory' 'perturbativity' 'unitarity' 'vacuum stability'}


; essentially just renames everything. Syntax: "custom name":"name within hdf5"
assign_to_pippi_datastream =
{
  LogLike:'LogLike'
  lam1:'#THDM_spectrum @SpecBit::get_THDM_spectrum_as_map::lambda1 dimensionless'
  lam2:'#THDM_spectrum @SpecBit::get_THDM_spectrum_as_map::lambda2 dimensionless'
  lam3:'#THDM_spectrum @SpecBit::get_THDM_spectrum_as_map::lambda3 dimensionless'
  lam4:'#THDM_spectrum @SpecBit::get_THDM_spectrum_as_map::lambda4 dimensionless'
  lam5:'#THDM_spectrum @SpecBit::get_THDM_spectrum_as_map::lambda5 dimensionless'
  mh_pole:'#THDM_spectrum @SpecBit::get_THDM_spectrum_as_map::h0_1 Pole_Mass'
  mH_pole:'#THDM_spectrum @SpecBit::get_THDM_spectrum_as_map::h0_2 Pole_Mass'
  mA_pole:'#THDM_spectrum @SpecBit::get_THDM_spectrum_as_map::A0 Pole_Mass'
  mHp_pole:'#THDM_spectrum @SpecBit::get_THDM_spectrum_as_map::H+ Pole_Mass'
  tanb:'#THDM_spectrum @SpecBit::get_THDM_spectrum_as_map::tanb dimensionless'
  alpha:'#THDM_spectrum @SpecBit::get_THDM_spectrum_as_map::alpha dimensionless'
  M222:'#THDM_spectrum @SpecBit::get_THDM_spectrum_as_map::M22_2 mass1'
  cba:'process'
  mH_mA:'process'
  mH_mHp:'process'
  mA_mHp:'process'
}


; remove all points outside these ranges
data_ranges = {
  lam1:{0,12.5} lam2:{0,12.5} lam3:{-12.5,12.5} lam4:{-12.5,12.5} lam5:{-12.5,12.5}
  mh_pole:{20, 140} mA_pole:{20, 5000} mHp_pole:{20, 5000} mH_pole:{20, 5000}
```

```
}

; delete all points which have an invalid likelihood
cut_invalid_likelihood = T

; as above but checks all loaded columns, not just the likelihood
cut_invlid_points = F

; write the loaded data back to a file (supports: .txt .hdf5 .mat)
output_load_stage = 'alldata.hdf5'
delete_old_files = T

; limit the number of points for improved performance
limit_point_count_to = ;3000000


-----------------------------
---processing stage-----------

; enable the processing stage, can be skipped if we just want to count the number
 ↪of points
enable_processing_stage = T

; provide the name of the function within pippi_processing perform the processing
 ↪(see example)
processing_function_name = 'processA'

; write the processed data to a file
output_processing_stage = None


-----------------------------
---bin stage------------------

; Note: binning will be done for all plots provided in the plot stage below

; enable the binning stage
enable_bin_stage = T

; likelihood_type = ... maybe easier to deal with it in processing section
log_likelihood_datastream = LogLike
multiplicity_datastream = None
prior_datastream = None

; set the default number of bins for 1D or 2D plots
default_bins_1D = 35
default_bins_2D = 100

; override the defaults for specific observables
number_of_bins_1D =
```

```
number_of_bins_2D =

; interpolate the binned data for smoother/more accurate plots
; Options: step, linear-spline, cubic-spline
interpolation_method_1D = 'step'
interpolation_method_2D =

; how many times bigger the interpolated bin count should be
interpolation_scaling_1D = 1
interpolation_scaling_2D = 1

; write the binned data to a file
output_bin_stage = None



-----------------------------
---plot stage-----------------

dataset_colorScheme_1D = {'grey_fill' 'maroon_outline' 'orange_outline'
 ↪'blue_outline' 'light_blue_outline'}
dataset_colorScheme_2D = {'grey_fill' 'maroon_outline' 'orange_outline'
 ↪'blue_outline' 'light_blue_outline'}

; enable the plotting stage
enable_plot_stage = T

; set countours for 1D plots
oneD_contour_levels = { 68.3 95.4 99.7 }

; set countours for 2D plots
twoD_contour_levels = { 95.4 }

; use loagarithmic axes for specific datastreams
use_log_scale =

; set the axis range for specific datastreams
axis_ranges = {
  lam1:{-0.5,6} lam2:{-0.5,6} lam3:{-6,6} lam4:{-6,6} lam5:{-6,6}
  Lam1:{-0.5,2} Lam2:{-0.5,4} Lam3:{-6,6} Lam4:{-6,6} Lam5:{-6,6} Lam6:{-4,4}
 ↪Lam7:{-4,4}
}

; which datastreams to make 1D (histogram) plots out of
oneD_plots =

; which pairs of datastreams to make 2D (histogram) plots out of
twoD_plots =
```

```
; create figures with multiple plots arranges into a grid

grid_plot_0 =
{
  { mHp_pole, None, None, None, None },
  { {mHp_pole,log_tanb}, log_tanb, None, None, None },
  { {mHp_pole,cba}, {log_tanb,cba}, cba, None, None },
  { {mHp_pole,sqrt_M222}, {log_tanb,sqrt_M222}, {cba,sqrt_M222}, sqrt_M222, None },
  { {mHp_pole,mA_mHp}, {log_tanb,mA_mHp}, {cba,mA_mHp}, {sqrt_M222,mA_mHp}, mA_mHp
↪},
}


grid_plot_1 =
{
  { log_tanb, None, None, None, None },
  { {log_tanb,cba}, cba, None, None, None },
  { {log_tanb,mH_mA}, {cba,mH_mA}, mH_mA, None, None },
  { {log_tanb,mH_mHp}, {cba,mH_mHp}, {mH_mA,mH_mHp}, mH_mHp, None },
  { {log_tanb,mA_mHp}, {cba,mA_mHp}, {mH_mA,mA_mHp}, {mH_mHp,mA_mHp}, mA_mHp },
}


grid_plot_labels = { 'benchmarks' 'anglesVmass' 'anglesVangles' 'lamVlam'
↪'anglesVlam' 'lamVmass' 'massVmass' 'LambVLamb' 'LambVangles' 'LambVmass'}

; names of each datastream in LaTeX format that are shown on plots
quantity_labels =
{
  LogLike:'-lnlike'
  lam1:'$\lambda_1$'
  lam2:'$\lambda_2$'
  lam3:'$\lambda_3$'
  lam4:'$\lambda_4$'
  lam5:'$\lambda_5$'
  mh_pole:'$m_{h}$ [GeV]'
  mH_pole:'$m_{H}$ [GeV]'
  mA_pole:'$m_{A}$ [GeV]'
  mHp_pole:'$m_{H^\pm}$ [GeV]'
  tanb:'$\tan_{\beta}$'
  cba:'$\cos(\beta-\alpha)$'
  mH_mA:'$m_H-m_A$ [GeV]'
  mH_mHp:'$m_H-m_{H^+}$ [GeV]'
  mA_mHp:'$m_A-m_{H^+}$ [GeV]'
}


; draw the colorbas on 2D plots (adds just 1 to the side for grid polts)
draw_colorBars = T


; draw the best fit marker (or posterior mean marker)
```

```
draw_best_fit_marker = T

; add a best fit legend entry
draw_best_fit_legend_entry = T

; reference point loation for 1D plots
reference_point_location_1D = None

; reference point loation for 2D plots
reference_point_location_2D = None

; reference point legend entries
reference_point_legend_entry_1D = None

; reference point legend entries
reference_point_legend_entry_2D = None

; extra legend entries
extra_legend_entries_1D = None
extra_legend_entries_2D = None

; credits line to be displayed above all plots
blame = None

; logo file to be added to all plots
logo_file = None

; locations of the legends and logo
legend_location_1D = 'default'
legend_location_2D = 'default'
legend_location_grid = 'default'
logo_location = 'default'

; the output file for plots where '\$\$\$' is substituted for the plot name. If
 ↪None then plots are drawn to screen. Format .png or .pdf
; @@@ is substituted for the current date

output_plot_stage = 'plots_@@@/THDMItree/theory_\$\$\$.pdf'
```

Appendix B

Example **YAML** input file

Here we provide a complete example of a YAML file for the 2HDM. This file can be used for running a GAMBIT parameter scan and includes theoretical, flavour, collider, and precision likelihoods.

```
##########################################################################
## GAMBIT configuration for the following                              ##
##                                                                     ##
## Models: THDM, THDMI, THDMII, THDMLS, THDMflipped                    ##
##                                                                     ##
## Includes all compatible likelihoods:                               ##
## theoretical, collider, electroweak, flavour                        ##
##                                                                     ##
## Requires backends:                                                  ##
## thdmc, SuperISO, HiggsBounds, HiggsSignals, HEPLike                 ##
##                                                                     ##
## Author: A.S. Woodcock                                               ##
## Date: 22/JUL/2022                                                   ##
##                                                                     ##
##########################################################################


Parameters:

    StandardModel_SLHA2: !import include/StandardModel_SLHA2_defaults.yaml

    THDMII_hybrid_Higgs2atQ:

      mh:
          range: [123, 127]
          prior_Type: flat
      mHp:
```

```yaml
        range: [140, 2500]
        prior_Type: flat
      cba:
        range: [-0.55, +0.55]
        prior_Type: flat
      tanb:
        range: [0.001, 70]
        prior_Type: flat
      Lambda4:
        range: [-4, +5]
        prior_Type: flat
      Lambda5:
        range: [-3, +4]
        prior_Type: flat
      Lambda7:
        range: [-2, +2.5]
        prior_Type: flat
      lambda6:
        fixed_value: 0.0
      lambda7:
        fixed_value: 0.0
      Qin:
        fixed_value: 91.1876 # = mZ


################################
##     PRINTER SELECTION      ##
################################


Printer:
  printer: cout



################################
##     SCANNER SELECTION      ##
################################


Scanner:

  use_scanner: random

  scanners:
    random:
      plugin: random
      point_number: 5000000
      like:  LogLike
```

```
################################
##  OBSERVABLES / LIKELIHOODS  ##
################################


ObsLikes:

--#-#
  #       THEORETICAL LIKELIHOODS        #
--#-#

  # Checks that the LO or NLO scattering-matrix is unitary
  - purpose:    LogLike
    capability: unitarity_LogLikelihood_THDM
    function: NLO_unitarity_LogLikelihood_THDM

  # Stability of the 2HDM Potential
  - purpose:    LogLike
    capability: stability_LogLikelihood_THDM

  # Perturbativity check on h0 mass loop-corrections
  - purpose:    LogLike
    capability: light_scalar_mass_corrections_LogLikelihood_THDM

  # Perturbativity check on heavy scalar mass loop-corrections
  - purpose:    LogLike
    capability: heavy_scalar_mass_corrections_LogLikelihood_THDM

  # enforces a mass range for all scalars
  - purpose:    LogLike
    capability: scalar_mass_range_LogLikelihood_THDM

  # Perturbativity check on lambdas and scalar couplings
  - purpose:    LogLike
    capability: perturbativity_LogLikelihood_THDM
    function: perturbativity_LogLikelihood_THDM

  # perturbativity constraint on yukawas
  - purpose:    LogLike
    capability: perturbativity_yukawas_LogLikelihood_THDM

--#-#
  #       COLLIDER LIKELIHOODS            #
--#-#

  # HiggsSignals 2.5.0 likelihood
```

```yaml
 - purpose: LogLike
   capability: LHC_Higgs_LogLike
   function: calc_HS_2_LHC_LogLike


 # HiggsBounds 5.8.0 likelihood
 - purpose: LogLike
   capability: LEP_Higgs_LogLike
   function: calc_HB_5_LEP_LogLike


--#-#
 #      PRECISION LIKELIHOODS         #
--#-#


 # Constraint on the S, T, U parameters
 - purpose:   Observable
   capability: oblique_parameters_LogLikelihood
   function: get_oblique_parameters_LogLikelihood


--#-#
 #      FLAVOR LIKELIHOODS            #
--#-#


 # Bs2llp (Bs2mutau, Bs2tautau)
 - purpose:   LogLike
   capability: Bs2ll_LogLikelihood


 # B2Kllp (B2Kmue, B2Ktaumu, B2Ktautau)
 - purpose:   LogLike
   capability: B2Kll_LogLikelihood


 # B -> mu mu
 - purpose:   LogLike
   capability: B2mumu_LogLikelihood_Atlas
   sub_capabilities: [BRuntag_Bsmumu, BR_Bdmumu]
 - purpose:   LogLike
   capability: B2mumu_LogLikelihood_LHCb
   sub_capabilities: [BRuntag_Bsmumu, BR_Bdmumu]
 - purpose:   LogLike
   capability: B2mumu_LogLikelihood_CMS
   sub_capabilities: [BRuntag_Bsmumu, BR_Bdmumu]


 # Bc lifetime
 - purpose:   LogLike
   capability: Bc_lifetime_LogLikelihood


 # RK and RKstarnunu
 - purpose:   LogLike
   capability: B2Xsnunu_LogLikelihood
```

```yaml
  # Tree-level leptonic and semi-leptonic B & D decay measurements
  # (RD, RDstar, BDmunu, BDstarmunu, Btaunu, Rmu, Dstaunu, Dsmunu, Dmunu, Dtaunu, RDemu)
  - purpose:    LogLike
    capability: SL_LogLikelihood


  # b -> s gamma
  - purpose:    LogLike
    capability: b2sgamma_LogLikelihood


  # B -> K* gamma
  - purpose:    LogLike
    capability: B2Kstargamma_LogLikelihood


  # RK
  - purpose:    LogLike
    capability: RK_LogLikelihood_LHCb


  # RKstar
  - purpose:    LogLike
    capability: RKstar_LogLikelihood_LHCb


  # B -> K* mu mu Angular
  - purpose:    LogLike
    capability: B2KstarmumuAng_LogLikelihood_Atlas
    sub_capabilities: [FL, S3, S4, S5, S7, S8]
  - purpose:    LogLike
    capability: B2KstarmumuAng_LogLikelihood_CMS
    sub_capabilities: [P1, P5prime]
  - purpose:    LogLike
    capability: B2KstarmumuAng_LogLikelihood_LHCb_2020
    sub_capabilities: [FL, AFB, S3, S4, S5, S7, S8, S9]
  - purpose:    LogLike
    capability: B2KstarmumuAng_LogLikelihood_Belle
    sub_capabilities: [P4prime, P5prime]


  # B -> K* l l Angular
  - purpose:    LogLike
    capability: B2KstarellellAng_LogLikelihood_Belle
    sub_capabilities: [P4prime, P5prime]


  # B_u -> K* mu mu Angular
  - purpose:    LogLike
    capability: Bu2KstarmumuAng_LogLikelihood_LHCb_2020
    sub_capabilities: [FL, AFB, S3, S4, S5, S7, S8, S9]


  # B -> K* e e angular low q2
  - purpose:    LogLike
```

```
      capability: B2KstareeAng_Lowq2_LogLikelihood_LHCb_2020
      sub_capabilities: [FLee, AT_Re, AT_2, AT_Im]


  # B -> K* mu mu BR
  - purpose:    LogLike
    capability: B2KstarmumuBr_LogLikelihood_LHCb


  # B -> K mu mu BR
  - purpose:    LogLike
    capability: B2KmumuBr_LogLikelihood_LHCb


  # Bs -> Phi mu mu BR
  - purpose:    LogLike
    capability: Bs2phimumuBr_LogLikelihood



################################
##         OBSERVABLES       ##
################################

  # entire 2HDM spectrum
  - capability: THDM_spectrum
    type: map_str_dbl
    purpose: Observable


  # 2HDM decay rates and branching ratios
  - capability: all_BFs
    purpose: Observable


##################################
##  Likelihood/Observable Rules  ##
##################################


Rules:

  - capability: RK_LogLikelihood_LHCb
    function: RK_LogLikelihood_LHCb


  - capability: RKstar_LogLikelihood_LHCb
    function: RKstar_LogLikelihood_LHCb


  - capability: THDM_spectrum
    type: map_str_dbl
    options:
      print_minimal_yukawas: true

  - capability: decay_rates
```

```yaml
    function: all_decays

  - capability: all_BFs
    function: get_decaytable_as_map
    options:
      skip_particles: [
↪'H-','W+','W-','Z0','e+_2','e+_3','e-_2','e-_3','mu+','mu-','pi+','pi-','pi0','tau+','tau-','tbar','u_
      print_BF_error: False
      print_as_widths: True

  - capability: perturbativity_LogLikelihood_THDM
    options:
      check_other_scale: 1000

  - capability: stability_LogLikelihood_THDM
    options:
      check_other_scale: 1000
      check_metastability: true

  - capability: unitarity_LogLikelihood_THDM
    options:
      check_other_scale: 1000
      # options below only for NLO unitarity
      check_correction_ratio: true
      wave_function_corrections: true
      gauge_corrections: true
      yukawa_corrections: true

  - capability: scalar_mass_range_LogLikelihood_THDM
    options:
      check_other_scale: -1
      minimum_scalar_mass: 0
      maximum_scalar_mass: 5000

  - capability: Higgs_Couplings
    function: THDM_higgs_couplings_2HDMC

  - capability: prediction_b2sgamma
    function: SuperIso_prediction_b2sgamma

  - capability: prediction_B2mumu
    function: SuperIso_prediction_B2mumu

  - capability: B2KstarmumuAng_LogLikelihood_Atlas
    function: HEPLike_B2KstarmumuAng_LogLikelihood_Atlas
    options:
      ignore_lowq2_bin: true
```

```yaml
  - capability: B2KstarmumuAng_LogLikelihood_Belle
    function: HEPLike_B2KstarmumuAng_LogLikelihood_Belle
    options:
      ignore_lowq2_bin: true


  - capability: B2KstarmumuAng_LogLikelihood_LHCb_2020
    function: HEPLike_B2KstarmumuAng_LogLikelihood_LHCb_2020
    options:
      ignore_lowq2_bin: true


  - capability: B2KstarmumuBr_LogLikelihood_LHCb
    function: HEPLike_B2KstarmumuBr_LogLikelihood_LHCb
    options:
      ignore_lowq2_bin: true


  - capability: LHC_Higgs_LogLike
    options:
      # -1:all, 0:RUN1_SS, 1:LATEST_SS, 2:LATEST_STXS
      HS_analysis: -1



##########################
# Logging setup
##########################



Logger:

  redirection:
    [Debug]       :   "debug.log"
    [Default]     :   "default.log"
    [DecayBit]    :   "DecayBit.log"
    [PrecisionBit] :  "PrecisionBit.log"
    [ColliderBit] :   "ColliderBit.log"
    [SpecBit]     :   "SpecBit.log"



##########################
# Name/Value Section
##########################



KeyValues:

  likelihood:
    print_invalid_points: false
    debug: false
```

```yaml
dependency_resolution:
  prefer_model_specific_functions: true
  use_old_routines: false

exceptions:
  dependency_resolver_error: fatal
  dependency_resolver_warning: non-fatal
  core_warning: fatal

default_output_path: "runs/THDMI_HH"
debug: false
```

Appendix C

GUM and SARAH model files for the IDM

The GUM and SARAH model files are best explained using an example. We provide the files for the IDM below including additional comments within.

```
## .gum (YAML) file for the Inert Doublet Model (IDM) in GUM

# -- the Mathematica package used, model name, plus package-specific info
math:
  # Name of Mathematica package, either 'feynrules' or 'sarah'
  package: sarah
  # Name of Model within that package. This will also be the name of the GAMBIT model.
  model: Inert
  # Lagrangian within the sarah file
  lagrangian: LTotal

# -- PDG code for the annihilating DM candidate in the model
wimp_candidate: 35

# -- Outputs for GUM to hook up to GAMBIT
output:
  # spectrum generator capable of computing one-loop masses and tree-level
  # decay branching fractions in a variety of BSM models. The model-specific
  # code is generated by SARAH
  spheno: true
  calchep: true
  pythia: false
  # computes the stability of the scalar potential for generic extended scalar sectors
  vevacious: false
  # for computing various DM observables for BSM models with WIMP candidates, such as
  # the relic abundance, direct detection
```

```
  micromegas: true


# Options for outputs
output_options:
  spheno:
    IncludeLoopDecays: false
    IncludeWilsonCoefficients: true
    IncludeFlavorObservables: true
    IncludeElectroweakObservables: true
```

The the main SARAH model file is given below. The remainder will be available on the GAMBIT repository.

```
(* SARAH: a "spectrum generator" generator *)


Off[General::spell]


Model`Name = "Inert_gum";
Model`NameLaTeX = "Inert doublet Model";
Model`Authors = "A.Woodcock, B.Herrmann, F.Staub";
Model`Date = "2022-SEP";




(*-----------------------------------------*)
(*   Particle Content*)
(*-----------------------------------------*)


(* Global Symmetries *)


(* format is 1: symmetry, 2: name *)


Global[[1]] = {Z[2], Z2};


(* Gauge symmetries & Gauge Fields *)


(* 1: Gauge field name *)
(* 2: Gauge group *)
(* 3: name of group *)
(* 4: corresponding coupling name *)
(* 5: is the group brken later *)
(* 6: Z2 rep *)


Gauge[[1]]={B,   U[1], hypercharge, g1, False, 1};
Gauge[[2]]={WB, SU[2], left,        g2, True,  1};
Gauge[[3]]={G,  SU[3], color,       g3, False, 1};

(* Matter Fields *)
```

```
(* 1: name of matter field *)
(* 2: number of generations *)
(* 3: names of SU[2] doublet components *)
(* 4: the weak hypercharge *)
(* 5: the SU[2] rep *)
(* 6: the SU[3] rep *)
(* 7: the Z2 rep *)

(* NOTE: for SUSY models we have SuperFields instead of FermionFiolds and
 ScalarFields *)

FermionFields[[1]] = {q, 3, {uL, dL},      1/6, 2,  3, 1};
FermionFields[[2]] = {l, 3, {vL, eL},     -1/2, 2,  1, 1};
FermionFields[[3]] = {d, 3, conj[dR],      1/3, 1, -3, 1};
FermionFields[[4]] = {u, 3, conj[uR],     -2/3, 1, -3, 1};
FermionFields[[5]] = {e, 3, conj[eR],        1, 1,  1, 1};


ScalarFields[[1]] =  {Hd, 1, {Hd0, Hdm},    -1/2, 2,  1,  1};
ScalarFields[[2]] =  {Hu, 1, {Hup, Hu0},     1/2, 2,  1, -1};



(*---------------------------------------------*)
(*   DEFINITION                               *)
(*---------------------------------------------*)



(* GaugeES -> Lagrangian with Gauge-symmetric eigenstates *)
(* EWSB -> Lagrangian with eigenstates after Gauge-symmetry breaking*)
(*         these can be considered the mass eigenstates *)
NameOfStates={GaugeES, EWSB};

(* ----- Before EWSB ----- *)

(* Define the gauge-symmetric lagrangian *)

(* we only need to define the scalar potential and Yukawa sector *)
(* the fermion-gauge and gauge-gauge interactions derived via Gauge principle *)

DEFINITION[GaugeES][Additional]= {
  {LagHC,  { AddHC->True}},
  {LagNoHC,{ AddHC->False}}
};



LagNoHC = -(MHD conj[Hd].Hd + MHU conj[Hu].Hu + Lambda1 conj[Hd].Hd.conj[Hd].Hd +
```

```
            Lambda2 conj[Hu].Hu.conj[Hu].Hu + Lambda3 conj[Hu].Hu.conj[Hd].Hd  +
 Lambda4 conj[Hu].Hd.Hu.conj[Hd]);



LagHC = -(Lambda5/2 Hu.Hd.Hu.Hd + Yd Hd.q.d + Ye Hd.l.e - Yu conj[Hd].q.u);



(* For the EWSB lagrangian, we redefine the gauge and fermion sectors *)
(* and define the VEVs *)

(* 1: the gauge eigenstates to be mixed *)
(* 2: the resulting EWSB state *)
(* 3: denotes matrix which diagonalises the mass matrix *)

DEFINITION[EWSB][GaugeSector] =
{
  {{VB,VWB[3]}, {VP,VZ}, ZZ},
  {{VWB[1],VWB[2]}, {VWp,conj[VWp]}, ZW}
};



(* ----- VEVs ---- *)

(* above here we have already defined all aspects of the model *)
(* but in practise we are interested in mass states after gauge symmetry breaking
 *)
(* so we define the rotations to these mass states *)



(* we only list the neutral Higgs doublet components *)
(* since we don't want a VEV for the charged components *)



DEFINITION[EWSB][VEVs]=
{    {Hd0, {v, 1/Sqrt[2]}, {G0, [ImaginaryI]/Sqrt[2]}, {hh, 1/Sqrt[2]}},
     {Hu0, {0, 0},         {A0, [ImaginaryI]/Sqrt[2]}, {H0, 1/Sqrt[2]}} };



(* ---- Mixings ---- *)

(* what vector bosons, scalars and fermions mix among each other *)

(* 1: the gauge eigenstates to be mixed *)
(* 2: the resulting EWSB state *)
(* 3: denotes matrix which diagonalises the mass matrix *)

DEFINITION[EWSB][MatterSector]=
{    {{Hup, conj[Hdm]}, {Hp, ZP}},
```

```
        {{{dL}, {conj[dR]}}, {{DL,ZDL}, {DR,ZDR}}},
        {{{uL}, {conj[uR]}}, {{UL,ZUL}, {UR,ZUR}}},
        {{{eL}, {conj[eR]}}, {{EL,ZEL}, {ER,ZER}}}};

(* While SARAH works internally often with Weyl spinors, Dirac spinors are commonly
used by Monte-Carlo tools and also by SPheno. Therefore, we have to define the
 relation between the two- and four-component fermions *)

DEFINITION[EWSB][DiracSpinors]={
 Fd ->{  DL, conj[DR]},
 Fe ->{  EL, conj[ER]},
 Fu ->{  UL, conj[UR]},
 Fv ->{  vL, 0}};
```

Appendix D

Parameterisations of the 2HDM scalar sector

This appendix lists the parameterisations of the 2HDM scalar potential commonly used throughout the literature. We do so for the most general 2HDM that is consistent with basic QFT principles and the SM gauge symmetry. Parameterisations are mathematically equivalent, i.e., related through a set of definitions. However, symmetries are realised differently in different notations (i.e. using different representations of the parameters).

Notation 1

This notation (based on [104]) is useful for studying symmetries and basis transformations.

$$\mathcal{V}_{2HDM} = \mu_{ij}\Phi_i^\dagger\Phi_j + \frac{1}{2}\Lambda_{ijkl}\Phi_i^\dagger\Phi_j\Phi_k^\dagger\Phi_l, \quad i,j,k,l \in \{1,2\} \tag{D.1}$$

Notation 2

This notation (based on [105]) shows all interactions amongst Higgs doublets explicitly.

$$\begin{aligned}
\mathcal{V}_{2HDM} = {} & m_{11}^2\Phi_1^\dagger\Phi_1 + m_{22}^2\Phi_2^\dagger\Phi_2 - (m_{12}^2\Phi_1^\dagger\Phi_2 + \text{H.c.}) \\
& + \frac{1}{2}\lambda_1(\Phi_1^\dagger\Phi_1)^2 + \frac{1}{2}\lambda_2(\Phi_2^\dagger\Phi_2)^2 + \lambda_3(\Phi_1^\dagger\Phi_1)(\Phi_2^\dagger\Phi_2) \\
& + \lambda_4(\Phi_1^\dagger\Phi_2)(\Phi_2^\dagger\Phi_1) + \left[\frac{1}{2}\lambda_5(\Phi_1^\dagger\Phi_2)^2\right.
\end{aligned}$$

$$+ \lambda_6(\Phi_1^\dagger \Phi_1)(\Phi_1^\dagger \Phi_2) + \lambda_7(\Phi_2^\dagger \Phi_2)(\Phi_1^\dagger \Phi_2) + \text{H.c} \Big] \tag{D.2}$$

It is related to Notation 1 via

$$m_{11}^2 \equiv \mu_{11}, \quad m_{12}^2 \equiv -\mu_{12}, \quad m_{22}^2 \equiv \mu_{22}, \quad \lambda_1 \equiv \Lambda_{1111}, \lambda_2 \equiv \Lambda_{2222}, \quad \lambda_3 \equiv \Lambda_{1221},$$

$$\lambda_4 \equiv \Lambda_{1122}, \lambda_5 \equiv \Lambda_{1212}, \quad \lambda_6 \equiv \Lambda_{1112}, \quad \lambda_7 \equiv \Lambda_{1222}. \tag{D.3}$$

Notation 3

This notation is useful for analysing the vacuum structure.

$$V = A_i x^i + \frac{1}{2} B_{ij} x^i x^j \tag{D.4}$$

$$x_i \equiv \begin{bmatrix} \Phi_1^\dagger \Phi_1 \\ \Phi_2^\dagger \Phi_2 \\ Re\left(\Phi_1^\dagger \Phi_2\right) \\ Im\left(\Phi_1^\dagger \Phi_2\right) \end{bmatrix}, \quad A_i \equiv \begin{bmatrix} m_{11}^2 \\ m_{22}^2 \\ Re\left(m_{12}^2\right) \\ Im\left(m_{12}^2\right) \end{bmatrix}, \quad B_{ij} \equiv \begin{bmatrix} \lambda_1 & \lambda_3 & 2\lambda_6 & 0 \\ \lambda_3 & \lambda_2 & 2\lambda_7 & 0 \\ 2\lambda_6 & 2\lambda_7 & 2\left(\lambda_4 + \lambda_5\right) & 0 \\ 0 & 0 & 0 & 2\left(\lambda_4 - \lambda_5\right) \end{bmatrix} \tag{D.5}$$

Notation 4

This notation, called the Minkowski spacetime parameterisation, (based on [35]) is useful for studying the existence and number of minima of the scalar potential.

$$\mathcal{V} = -M_\mu r^\mu + \frac{1}{2} \Lambda_{\mu v} r^\mu r^v \tag{D.6}$$

$$\Lambda_{\mu v} \equiv \frac{1}{2} \begin{bmatrix} (\lambda_1 + \lambda_2)/2 + \lambda_3 & Re(\lambda_6 + \lambda_7) & -Im(\lambda_6 + \lambda_7) & (\lambda_1 + \lambda_2)/2 \\ Re(\lambda_6 + \lambda_7) & \lambda_4 + Re(\lambda_5) & -Im(\lambda_5) & Re(\lambda_6 - \lambda_7) \\ -Im(\lambda_6 + \lambda_7) & -Im(\lambda_5) & \lambda_4 - Re(\lambda_5) & -Im(\lambda_6 - \lambda_7) \\ (\lambda_1 + \lambda_2)/2 & Re(\lambda_6 - \lambda_7) & -Im(\lambda_6 - \lambda_7) & (\lambda_1 + \lambda_2)/2 - \lambda_3 \end{bmatrix} \tag{D.7}$$

$$M_\mu \equiv (M_0, M_i) \equiv \left(-\frac{1}{2} \left(m_{11}^2 + m_{22}^2 \right), \ Re \left(m_{12}^2 \right), Im \left(m_{12}^2 \right), \frac{1}{2} \left(m_{22}^2 - m_{11}^2 \right) \right) \quad \text{(D.8)}$$

$$r_\mu \equiv \begin{bmatrix} \Phi_1^\dagger \Phi_2 + \Phi_2^\dagger \Phi_2 \\ -2Re \left(\Phi_1^\dagger \Phi_2 \right) \\ -2Im \left(\Phi_1^\dagger \Phi_2 \right) \\ -\Phi_1^\dagger \Phi_2 + \Phi_2^\dagger \Phi_2 \end{bmatrix} \quad \text{(D.9)}$$

Note that contravariant and covariant components here are related via a Minkowski matrix. The reason why it is called the Minkowski spacetime parameterisation is apparent once we consider basis transformations. Following our discussion from Section 3.4, we need to first generalise the basis transformation to the full $GL(2, C)$ group [1,2] via the modification of the scalar KED given by [34]

$$\mathcal{T}_{Scalar} = K_\mu \rho^\mu, \ \text{ where: } \rho^\mu \equiv (\partial_\alpha \Phi_a)^\dagger \sigma^\mu (\partial^\alpha \Phi_a), \ \sigma^0 \equiv 1, \text{ and } K_\mu \text{ is arbitrary.} \quad \text{(D.10)}$$

Our usual scalar KED from Equation 3.5 corresponds to $K_\mu = (1, 0, 0, 0)$. The $GL(2, C)$ basis transformation,

$$\Phi_a' = N_{ab} \Phi_b, \ \text{ where } N \in GL(2, C), \quad \text{(D.11)}$$

induces a corresponding $O(1, 3)$ transformation on r^μ and M^μ, and an $O(1, 3) \otimes O(1, 3)$ transformation on $\Lambda_{\mu v}$ – hence justifying why we had named it the Minkowski spacetime parameterisation. Note that the possible values of r^μ do not map out the full Minkowski space since it can also be proven that $r^\mu r_\mu > 0$. This property is useful when deriving the vacuum stability conditions. The transformations can be written as

$$r_\mu' = R_{\mu v} r_v, \ \ M_\mu' = R_{\mu v} M_v, \ \ \Lambda_{\mu v}' = R_{\mu \alpha} R_{v \beta} \Lambda_{\alpha \beta}, \quad \text{(D.12)}$$

---

[1]This is the most general group of 2×2 matrix transformations.

[2]Note that only the $SL(2, C)$ subset of $GL(2, C)$ contains non-trivial transformations since multiplication of all the fields by the same real nonzero constant can be compensated for by a re-scaling of all observables.

where:

$$R_{ij} \equiv \frac{1}{2}\,\mathrm{Tr}\Big\{(N^\dagger \sigma_i N \sigma_j)\Big\} \in SO(3),$$
$$R_{0\mu} \equiv R_{\mu 0} \equiv \delta_{\mu 0}. \tag{D.13}$$

Appendix E

Basis conversions

Unless stated otherwise, all equations are derived for the general 2HDM with $\lambda_6, \lambda_7 \neq 0$ but assume a normal / CP-violating minimum (i.e. not for the C-violating minimum).

E.1 Generic to Higgs

$$\Lambda_1 = \lambda_1 \cos^4 \beta + \lambda_2 \sin^4 \beta + \frac{1}{2}\lambda_{345} \sin^2 (2\beta) + 2\sin (2\beta) \left[\cos^2 \beta \lambda_6 + \sin^2 \beta \lambda_7 \right],$$

$$\Lambda_2 = \lambda_1 \sin^4 \beta + \lambda_2 \cos^4 \beta + \frac{1}{2}\lambda_{345} \sin^2 (2\beta) - 2\sin (2\beta) \left[\sin^2 \beta \lambda_6 + \cos^2 \beta \lambda_7 \right],$$

$$\Lambda_3 = \frac{1}{4}\sin^2 (2\beta) (\lambda_1 + \lambda_2 - 2\lambda_{345}) + \lambda_3 - \sin (2\beta) \cos (2\beta) (\lambda_6 - \lambda_7),$$

$$\Lambda_4 = \frac{1}{4}\sin^2 (2\beta) (\lambda_1 + \lambda_2 - 2\lambda_{345}) + \lambda_4 - \sin (2\beta) \cos (2\beta) (\lambda_6 - \lambda_7),$$

$$\Lambda_5 e^{-2i\chi} = \frac{1}{4}\sin^2 (2\beta) (\lambda_1 + \lambda_2 - 2\lambda_{345}) + \lambda_5 - \sin (2\beta) \cos (2\beta) (\lambda_6 - \lambda_7),$$

$$\Lambda_6 e^{-2i\chi} = -\frac{1}{2}\sin (2\beta) \left(\lambda_1 \cos^2 \beta - \lambda_2 \sin^2 \beta - \lambda_{345} \cos (2\beta) \right) + \cos \beta \cos (3\beta)\lambda_6 + \sin \beta \sin (3\beta)\lambda_7$$

$$\Lambda_7 e^{-2i\chi} = -\frac{1}{2}\sin (2\beta) \left(\lambda_1 \sin^2 \beta - \lambda_2 \cos^2 \beta + \lambda_{345} \cos (2\beta) \right) + \cos \beta \cos (3\beta)\lambda_7 + \sin \beta \sin (3\beta)\lambda_6$$

$$(\text{E.1})$$

E.2 Higgs to Generic

The Higgs basis to Generic basis translations were obtained using MATLAB's symbolic toolbox. The code is located here: https://github.com/Alex0125698/THDM_basis_translations.

$$\lambda_1 = -\Big(2\Lambda_2 - 2\Lambda_1 + \cos 2\beta(\Lambda_{345} - 6\Lambda_2 - 3\Lambda_1) - 4(\Lambda_1 - \Lambda_2)\cos 4\beta - 3\Lambda_1 \cos 6\beta - \Lambda_3 \cos 6\beta$$
$$- \Lambda_4 \cos 6\beta - \Lambda_5 \cos 6\beta + 5\Lambda_6 \sin 2\beta + \Lambda_7 \sin 2\beta + 3(\Lambda_6 + \Lambda_7)\sin 6\beta\Big)/(4(2\cos 2\beta + \cos 6\beta))$$

$$\lambda_2 = -\Big(2\Lambda_1 - 2\Lambda_2 + \cos 2\beta(\Lambda_{345} - 6\Lambda_2 - 3\Lambda_1) + 4(\Lambda_1 - \Lambda_2)\cos 4\beta - 3\Lambda_1 \cos 6\beta - \Lambda_3 \cos 6\beta$$
$$- \Lambda_4 \cos 6\beta - \Lambda_5 \cos 6\beta + 5\Lambda_6 \sin 2\beta + \Lambda_7 \sin 2\beta + 3(\Lambda_6 + \Lambda_7)\sin 6\beta\Big)/(4(2\cos 2\beta + \cos 6\beta))$$

$$\lambda_3 = \Big(\Lambda_6 - 3\Lambda_7 + 6(\Lambda_6 - \Lambda_7)\cos 4\beta + (\Lambda_6 + \Lambda_7)\cos 8\beta + 2\Lambda_2 \sin 4\beta + 2\Lambda_3 \sin 4\beta$$
$$- 2\Lambda_4 \sin 4\beta + \Lambda_1 \sin 8\beta - 2\Lambda_5 \sin 4\beta + 3\Lambda_3 \sin 8\beta - \Lambda_4 \sin 8\beta - \Lambda_5 \sin 8\beta\Big)/(4(\sin 4\beta + \sin 8\beta))$$

$$\lambda_4 = \Big(\Lambda_6 - 3\Lambda_7 + 6(\Lambda_6 - \Lambda_7)\cos 4\beta + (\Lambda_6 + \Lambda_7)\cos 8\beta + 2\Lambda_2 \sin 4\beta - 2\Lambda_3 \sin 4\beta$$
$$+ 2\Lambda_4 \sin 4\beta + \Lambda_1 \sin 8\beta - 2\Lambda_5 \sin 4\beta - \Lambda_3 \sin 8\beta + 3\Lambda_4 \sin 8\beta - \Lambda_5 \sin 8\beta\Big)/(4(\sin 4\beta + \sin 8\beta))$$

$$\lambda_5 = \Big(\Lambda_6 - 3\Lambda_7 + 6(\Lambda_6 - \Lambda_7)\cos 4\beta + (\Lambda_6 + \Lambda_7)\cos 8\beta + 2\Lambda_2 \sin 4\beta - 2\Lambda_3 \sin 4\beta$$
$$- 2\Lambda_4 \sin 4\beta + \Lambda_1 \sin 8\beta + 2\Lambda_5 \sin 4\beta - \Lambda_3 \sin 8\beta - \Lambda_4 \sin 8\beta + 3\Lambda_5 \sin 8\beta\Big)/(4(\sin 4\beta + \sin 8\beta))$$

$$\lambda_6 = \Big(\Lambda_6/4 + \Lambda_7/4 + \cos 2\beta(\Lambda_6/2 + \Lambda_7/2) - ((\Lambda_6 - 3\Lambda_7)\cos 4\beta)/4 + (\Lambda_1 \sin 2\beta)/4 - (\Lambda_2 \sin 2\beta)/4$$
$$- (\Lambda_2 \sin 4\beta)/4 + (\Lambda_3 \sin 4\beta)/4 + (\Lambda_4 \sin 4\beta)/4 + (\Lambda_5 \sin 4\beta)/4\Big)/(\cos 2\beta^2 + \cos 2\beta(2\cos 2\beta^2 - 1))$$

$$\lambda_7 = -\Big(\Lambda_6/4 + \Lambda_7/4 - \cos 2\beta(\Lambda_6/2 + \Lambda_7/2) - ((\Lambda_6 - 3\Lambda_7)\cos 4\beta)/4 - (\Lambda_1 \sin 2\beta)/4 + (\Lambda_2 \sin 2\beta)/4$$
$$- (\Lambda_2 \sin 4\beta)/4 + (\Lambda_3 \sin 4\beta)/4 + (\Lambda_4 \sin 4\beta)/4 + (\Lambda_5 \sin 4\beta)/4\Big)/(\cos 2\beta^2 - \cos 2\beta(2\cos 2\beta^2 - 1))$$

$$(\text{E.2})$$

For the $Z2$-symmetric models with $\lambda_6, \lambda_7 = 0$ we can use the much simpler expressions provided below.

$$\lambda_1 = (3\Lambda_1)/4 + \Lambda_2/4 - \Big(\Lambda_1/4 - \Lambda_2/4 - \cos 2\beta(\Lambda_1/2 - \Lambda_2/2) + (\Lambda_6 \sin 4\beta)/2\Big)/\cos 2\beta^2$$

$$\lambda_2 = (3\Lambda_1)/4 + \Lambda_2/4 - \Big(\Lambda_1/4 - \Lambda_2/4 + \cos 2\beta(\Lambda_1/2 - \Lambda_2/2) + (\Lambda_6 \sin 4\beta)/2\Big)/\cos 2\beta^2$$

$$\lambda_3 = \Lambda_2/2 + \Lambda_3/2 - \Lambda_4/2 - \Lambda_5/2 - \Lambda_7 \cot 2\beta$$

$$\lambda_4 = \Lambda_2/2 - \Lambda_3/2 + \Lambda_4/2 - \Lambda_5/2 - \Lambda_7 \cot 2\beta$$

$$\lambda_5 = \Lambda_2/2 - \Lambda_3/2 - \Lambda_4/2 + \Lambda_5/2 - \Lambda_7 \cot 2\beta \qquad (\text{E.3})$$

E.3 Generic to Physical

Conversion from the generic basis to physical basis (see Ref [39]).

$$m_A^2 = \bar{m}^2 - \frac{v^2}{2}\left(2\lambda_5 + \lambda_6 \cot\beta + \lambda_7 \tan\beta\right)$$

$$m_{H^+}^2 = m_A^2 + \frac{v^2}{2}\left(\lambda_5 - \lambda_4\right)$$

$$m_h^2 = m_A^2 \cos^2(\beta - \alpha) + v^2(\lambda_1 \cos^2\beta \sin^2\alpha + \lambda_2 \sin^2\beta \cos^2\alpha - 2\lambda_{345}\cos\alpha\cos\beta\sin\alpha\sin\beta$$
$$+ \lambda_5 \cos^2(\beta - \alpha) - 2\lambda_6 \cos\beta\sin\alpha\cos(\beta + \alpha) + 2\lambda_7 \sin\beta\cos\alpha\cos(\beta + \alpha))$$

$$m_H^2 = m_A^2 \sin^2(\beta - \alpha) + v^2(\lambda_1 \cos^2\beta \cos^2\alpha + \lambda_2 \sin^2\beta \sin^2\alpha + 2\lambda_{345}\cos\alpha\cos\beta\sin\alpha\sin\beta$$
$$+ \lambda_5 \sin^2(\beta - \alpha) + 2\lambda_6 \cos\beta\cos\alpha\sin(\beta + \alpha) + 2\lambda_7 \sin\beta\sin\alpha\sin(\beta + \alpha))$$

$$\tan(2\alpha) = \frac{2m_{12}^2/v^2 - \lambda_{345}\sin(2\beta)}{2m_{12}^2/v^2 \cot(2\beta) - \lambda_1 \cos^2\beta - \lambda_2 \sin^2\beta} \tag{E.4}$$

E.4 Physical to Generic

Conversion from the physical basis to generic basis (see Ref [39]).

$$\lambda_1 = \frac{m_H^2 \cos^2\alpha + m_h^2 \sin^2\alpha - m_{12}^2 \tan\beta}{v^2 \cos^2\beta} - \frac{3}{2}\lambda_6 \tan\beta + \frac{1}{2}\lambda_7 \tan^3\beta$$

$$\lambda_2 = \frac{m_H^2 \sin^2\alpha + m_h^2 \cos^2\alpha - m_{12}^2 \cot\beta}{v^2 \sin^2\beta} + \frac{1}{2}\lambda_6 \cot^3\beta - \frac{3}{2}\lambda_7 \cot\beta$$

$$\lambda_3 = \frac{(m_H^2 - m_h^2)\cos\alpha\sin\alpha + 2m_{H^+}^2 \sin\beta\cos\beta - m_{12}^2}{v^2 \sin\beta\cos\beta} - \frac{1}{2}\lambda_6 \cot\beta - \frac{1}{2}\lambda_7 \tan\beta$$

$$\lambda_4 = \frac{(m_A^2 - 2m_{H^+}^2)\cos\beta\sin\beta + m_{12}^2}{v^2 \sin\beta\cos\beta} - \frac{1}{2}\lambda_6 \cot\beta - \frac{1}{2}\lambda_7 \tan\beta$$

$$\lambda_5 = \frac{m_{12}^2 - m_A^2 \sin\beta\cos\beta}{v^2 \sin\beta\cos\beta} - \frac{1}{2}\lambda_6 \cot\beta - \frac{1}{2}\lambda_7 \tan\beta$$

$$m_{11}^2 = -\frac{1}{2\cos\beta}\left(m_H^2 \cos\alpha\cos(\beta - \alpha) - m_h^2 \sin\alpha\sin(\beta - \alpha)\right) + m_{12}^2 \tan\beta$$

$$m_{11}^2 = -\frac{1}{2\sin\beta}\left(m_h^2 \cos\alpha\sin(\beta - \alpha) + m_H^2 \sin\alpha\cos(\beta - \alpha)\right) + m_{12}^2 \cot\beta \tag{E.5}$$

E.5 Higgs to Physical

Conversion from the Higgs basis to physical basis (see Ref [47]).

$$m_{H^+}^2 = Y_2 + \frac{1}{2}\Lambda_3 v^2$$

$$m_A = Y_2 + \frac{v^2}{2}\left(\Lambda_3 + \Lambda_4 - \Lambda_5\right)$$

$$m_{H,h}^2 = \frac{1}{2}\left(m_A^2 + (\Lambda_1 + \Lambda_5)\,v^2 \pm \sqrt{\left(m_A^2 + v^2\left(\Lambda_5 - \Lambda_1\right)\right)^2 + 4v^4\Lambda_6^2}\right)$$

$$\cos\left(\beta - \alpha\right) = -\frac{\Lambda_6 v^2}{\sqrt{\left(m_H^2 - m_h^2\right)\left(m_H^2 - \Lambda_1 v^2\right)}}$$

$$\sin\left(\beta - \alpha\right) = \frac{|\Lambda_6|\,v^2}{\sqrt{\left(m_H^2 - m_h^2\right)\left(\Lambda_1 v^2 - m_h^2\right)}} \tag{E.6}$$

E.6 Physical to Higgs

Conversion from the physical basis to Higgs basis (see Ref [47]). For the general 2HDM the expressions are,

$$\Lambda_1 = \frac{1}{v^2}\left(\sin^2\left(\beta - \alpha\right)m_h^2 + \cos^2\left(\beta - \alpha\right)m_H^2\right),$$

$$\Lambda_4 = \Lambda_5 + \frac{2}{v^2}\left(m_A^2 - m_{H^+}^2\right),$$

$$\Lambda_5 = \frac{1}{v^2}\left(\sin^2\left(\beta - \alpha\right)m_H^2 + \cos^2\left(\beta - \alpha\right)m_h^2 - m_A^2\right),$$

$$\Lambda_6 = \frac{1}{v^2}\left(\left(m_h^2 - m_H^2\right)\sin\left(\beta - \alpha\right)\cos\left(\beta - \alpha\right)\right). \tag{E.7}$$

The remaining Higgs basis parameters are obtained easily for a $\mathbb{Z}_2$-symmetric 2HDM. These are

$$\bar{m}^2 \equiv 2m_{12}^2/\sin\left(2\beta\right),$$

$$\Lambda_7 = \Lambda_6 + 2\cot\left(2\beta\right)\left(\Lambda_5 + \frac{1}{v^2}\left(m_A^2 - \bar{m}^2\right)\right),$$

$$\Lambda_2 = \Lambda_1 + 2\left(\Lambda_6 + \Lambda_7\right)\cot\left(2\beta\right),$$

$$\Lambda_3 = \Lambda_1 + 2\Lambda_6\cot\left(2\beta\right) - \left(\Lambda_6 - \Lambda_7\right)\tan\left(2\beta\right) - \Lambda_4 - \Lambda_5. \tag{E.8}$$

Appendix F

Vacuum stability using the Minkowski parameterisation

We can also write the potential using the Minkowski space-time parameterisation. Here the positivity condition implies that $\Lambda_{\mu v}$ is positive-definite inside and on the future light-cone (i.e. that $\Lambda_{\mu v} r^\mu r^v > 0$ inside LC^+ for all r^μ, r^v). It turns out that this is equivalent to the following conditions (see Appendix A of ref [34] for proof):

   i $\Lambda_{\mu v}$ can be diagonalised by an $SO(3,1)$ transformation (with the diagonalised matrix having real eigenvalues).

   ii $\Lambda_0 > \Lambda_1, \Lambda_2, \Lambda_3,$ where $\Lambda \equiv \Lambda^{\mu\rho} g_{\rho v}$ in the basis where $\Lambda_{\mu v}$ is diagonal.

  iii $\Lambda_0 > 0$

For the general 2HDM, the restrictions that arise on the parameters are very complicated. However they become very simple when $\lambda_{6,7} = 0$. In this case, the parameter matrix takes the form

$$\Lambda^{\mu v} = \frac{1}{2} \begin{bmatrix} \frac{1}{2}(\lambda_1 + \lambda_2) + \lambda_3 & 0 & 0 & -\frac{1}{2}(\lambda_1 + \lambda_2) \\ 0 & \lambda_4 + Re\ \lambda_5 & -Im\ \lambda_5 & 0 \\ 0 & -Im\ \lambda_5 & \lambda_4 - Re\ \lambda_5 & 0 \\ -\frac{1}{2}(\lambda_1 + \lambda_2) & 0 & 0 & \frac{1}{2}(\lambda_1 + \lambda_2) - \lambda_3 \end{bmatrix}. \tag{F.1}$$

One can show that a $SO(3,1)$ transformation diagonalises this matrix if and only if: $\lambda_1 + \lambda_2 > |\lambda_1 + \lambda_2|$, leading to

$$\lambda_1 > 0, \ \lambda_2 > 0. \tag{F.2}$$

The diagonalised matrix then takes the form

$$\Lambda^{\mu v} = \frac{1}{2} \begin{bmatrix} \sqrt{\lambda_1 \lambda_2} + \lambda_3 & & & \\ & \lambda_4 + \lambda_5 & & \\ & & \lambda_4 - \lambda_5 & \\ & & & \sqrt{\lambda_1 \lambda_2} - \lambda_3 \end{bmatrix}, \tag{F.3}$$

and the remaining conditions on the eigenvalues lead to

$$\lambda_3 + \sqrt{\lambda_1 \lambda_2} > 0, \quad \lambda_3 + \lambda_4 - |\lambda_5| + \sqrt{\lambda_1 \lambda_2} > 0. \tag{F.4}$$

Notice that these are the same inequalities that we derived using the radial parameterisation, although this time we have proven that they are sufficient. Note that these only apply for $\lambda_{6,7} = 0$. For the most general stability conditions, see ref [32].

Appendix G

Spontaneous CP-violation

So far we have just been assuming a normal VEV from Equation 3.27, which led to the minimisation conditions in Equation 3.30. Note that the normal VEV was just a special case of the more general CP-breaking VEV. In this section we will derive a more general set of conditions that ensure that our vacuum does not spontaneously break CP. The general (CP-breaking) VEVs are denoted

$$\left\langle 0 \left| \varphi_i^0 \right| 0 \right\rangle = \frac{v_i}{\sqrt{2}} e^{i\xi_i}, \quad i = 1, 2. \tag{G.1}$$

Since $\xi_i \neq 0$ corresponds to VEVs with an imaginary component, it may seem like it would lead to spontaneous CP-violation. However, it may still be possible to render both VEVs real via an appropriate basis transformation – leading to a CP-conserving vacuum. The minimisation conditions for our general VEVs are

$$
\begin{aligned}
m_{11}^2 &= m_{12}^2 \tan\beta \cos\xi - \frac{1}{2}v^2(\lambda_1 \cos^2\beta + (\lambda_3 + \lambda_4 + \lambda_5 \cos{(2\xi)})\sin^2\beta \\
&\quad + 3\lambda_6 \sin\beta \cos\beta \cos\xi + \lambda_7 \sin^2\beta \tan\beta \cos\xi), \\
m_{22}^2 &= m_{12}^2 \cot\beta \cos\xi - \frac{1}{2}v^2(\lambda_2 \sin^2\beta + (\lambda_3 + \lambda_4 + \lambda_5 \cos{(2\xi)})\cos^2\beta \\
&\quad + 3\lambda_7 \sin\beta \cos\beta \cos\xi + \lambda_6 \cos^2\beta \cot\beta \cos\xi), \\
m_{12}^2 \sin\xi &= \frac{1}{2}v^2 \left(2\lambda_5 \sin\beta \cos\beta \cos\xi + \lambda_6 \cos^2\beta + \lambda_7 \sin^2\beta \right),
\end{aligned}
\tag{G.2}
$$

where $\xi \equiv \xi_2 - \xi_1$. The last equation becomes trivial when $\sin \xi = 0$ and we just recover the usual minimisation conditions for a normal VEV – which is CP-conserving. For $\sin \xi \neq 0$, the latter equation leads to

$$\cos \xi = \frac{m_{12}^2 - \frac{1}{2}\lambda_6 v_1^2 - \frac{1}{2}\lambda_7 v_2^2}{\lambda_5 v_1 v_2}. \tag{G.3}$$

Clearly if the following condition is met, we don't get a solution for $\cos \xi$

$$\left| m_{12}^2 - \frac{1}{2}\lambda_6 v_1^2 - \frac{1}{2}\lambda_7 v_2^2 \right| \geq \lambda_5 v_1 v_2. \tag{G.4}$$

Assuming our potential does indeed have a minimum then under this condition it must correspond to $\sin \xi = 0$ (and hence $\xi = n\pi$). We are left with no/π relative phase difference, and if any complex phase remains, it can be eliminated via a hypercharge transformation $\Phi_i \rightarrow e^{i\xi_1}\Phi_i$, followed by a field transformation: $\Phi_2 \rightarrow (-1)^n \Phi_2$. This yields real and non-negative VEVs.

For $\sin \xi \neq 0$ where we are left with a complex phase, it may be possible to do a basis transformation that renders the VEVs real. This can be accomplished without explicitly considering all possible basis choices for the scalar fields by making use of the Higgs basis.

It can be shown that if all Higgs basis parameters are real for some χ (c.f. Equation 3.61) then the corresponding VEVs are also real and CP-conserving [106]. Hence, based on Equation 3.47, we arrive at a condition that ensures real VEVs exist given by

$$Im\left(\Lambda_5^* \Lambda_6^2\right) = Im\left(\Lambda_5^* \Lambda_7^2\right) = Im\left(\Lambda_6^* \Lambda_7\right) = 0. \tag{G.5}$$

It is also possible to translate these back to the generic basis, although the resulting conditions are much more complex so we do not list them here.

Bibliography

[1] Wikipedia, "Standard model of elementary particles."
https://en.wikipedia.org/wiki/File:
Standard_Model_of_Elementary_Particles.svg, 2021. [Online; accessed 06-August-2021].

[2] ATLAS and C. Collaborations, *Measurements of the higgs boson production and decay rates and constraints on its couplings from a combined atlas and cms analysis of the lhc pp collision data at $\sqrt{s} =$ 7 and 8 tev, JHEP* **08** (2016) 045, [arXiv:1606.02266].

[3] LHC Higgs Cross Section Working Group: J. R. Andersen *et. al.*, *Handbook of LHC Higgs Cross Sections: 3. Higgs Properties*, arXiv:1307.1347.

[4] A. Beniwal, *Investigation of Higgs Portal Dark Matter Models.* PhD thesis, University of Adelaide, 2018.

[5] L. collaboration, R. Aaij, *et. al.*, *Precise determination of the b0s-b0sbar oscillation frequency*, arXiv:2104.04421.

[6] L. collaboration, R. Aaij, *et. al.*, *Measurement of the $b_s^0 \to \mu^+\mu^-$ decay properties and search for the $b^0 \to \mu^+\mu^-$ and $b_s^0 \to \mu^+\mu^-\gamma$ decays, Phys. Rev. D* **105** (2022) 012010, [arXiv:2108.09283].

[7] J. A. Vazquez, L. E. Padilla, and T. Matos, *Inflationary cosmology: From theory to observations, Rev. Mex. Fis. E* **17** (2020) 1, [arXiv:1810.09934].

[8] D. Hooper, *Tasi 2008 lectures on dark matter*, 2009.

[9] M. A. Deliyergiyev, *Recent progress in search for dark sector signatures, Open Physics* **14** (2016) 281–303, [arXiv:1510.06927].

[10] J. Billard, M. Boulay, *et. al.*, *Direct detection of dark matter – appec committee report*, arXiv:2104.07634.

[11] T. Saab, *An introduction to dark matter direct detection searches & techniques*, arXiv:1203.2566.

[12] GAMBIT Collaboration: P. Athron, C. Balázs, *et. al.*, *GAMBIT: The Global and Modular Beyond-the-Standard-Model Inference Tool*, *Eur. Phys. J. C* **77** (2017) 784, [`arXiv:1705.07908`]. Addendum in [107].

[13] W. Porod, F. Staub, and A. Vicente, *A Flavor Kit for BSM models*, *Eur. Phys. J. C74* (2014) 2992, [`arXiv:1405.1434`].

[14] R. Santos and A. Barroso, *Renormalization of two-higgs-doublet models*, *Phys. Rev. D* **56** (1997) 5366–5385, [`hep-ph/9701257`].

[15] I. J. R. Aitchison and A. J. G. Hey, *Gauge theories in particle physics: A practical introduction, fourth edition - 2 volume set.* Graduate student series in physics. CRC Press, Boca Raton, FL, 4 ed., 2012.

[16] D. Griffiths, *Introduction to elementary particles.* Wiley-VCH Verlag, Weinheim, Germany, 2 ed., 2008.

[17] J. J. Thomson, *XL. cathode rays*, *Lond. Edinb. Dublin Philos. Mag. J. Sci.* **44** (1897) 293–316.

[18] G. Aad, T. Abajyan, *et. al.*, *Observation of a new particle in the search for the standard model higgs boson with the ATLAS detector at the LHC*, *Phys. Lett. B* **716** (2012) 1–29, [`arXiv:1207.7214`].

[19] G. Bertone and D. Hooper, *A history of dark matter*, *Rev. Mod. Phys.* **90** (2018) 45002, [`arXiv:1605.04909`].

[20] CDF Collaboration, T. Aaltonen, *et. al.*, *High-precision measurement of the W boson mass with the CDF II detector*, *Science* **376** (2022) 170–176.

[21] B. Abi, T. Albahri, *et. al.*, *Measurement of the positive muon anomalous magnetic moment to 0.46 ppm*, *Phys. Rev. Lett.* **126** (2021) 141801, [`arXiv:2104.03281`].

[22] H. Nilles, *Supersymmetry, supergravity and particle physics*, *Physics Reports* **110** (1984) 1–162.

[23] M. D. Schwartz, *Quantum field theory and the standard model.* Cambridge University Press, Cambridge, England, 2013.

[24] T. Lancaster and S. J. Blundell, *Quantum field theory for the gifted amateur.* Oxford University Press, London, England, 2014.

[25] G. 't Hooft and M. Veltman, *Regularization and renormalization of gauge fields*, *Nuclear Physics B* **44** (1972) 189–213.

[26] G. t. Hooft, *Gauge theory and renormalization (erice, august 1994)*, 1994.

[27] A. Zee, *Group theory in a nutshell for physicists.* In a Nutshell. Princeton University Press, Princeton, NJ, 2016.

[28] N. Jeevanjee, *An introduction to tensors and group theory for physicists.* Birkhauser, Basel, Switzerland, 2 ed., 2015.

[29] M. Bona, M. Ciuchini, *et. al.*, *Model-independent constraints on δf = 2 operators and the scale of new physics*, *Journal of High Energy Physics* **2008** (2008) 049–049, [arXiv:0707.0636].

[30] G. Blankenburg, J. Ellis, and G. Isidori, *Flavour-changing decays of a 125 GeV higgs-like particle*, *Physics Letters B* **712** (2012) 386–390, [arXiv:1202.5704].

[31] G. Branco, P. Ferreira, *et. al.*, *Theory and phenomenology of two-Higgs-doublet models*, *Phys. Rept.* **516** (2012) 1–102, [arXiv:1106.0034].

[32] M. Maniatis, A. von Manteuffel, O. Nachtmann, and F. Nagel, *Stability and symmetry breaking in the general two-Higgs-doublet model*, *Eur. Phys. J. C* **48** (2006) 805–823, [hep-ph/0605184].

[33] J. F. Gunion and H. E. Haber, *Conditions for CP-violation in the general two-Higgs-doublet model*, *Phys. Rev. D* **72** (2005) 095002, [hep-ph/0506227].

[34] I. P. Ivanov, *Minkowski space structure of the Higgs potential in 2HDM. II. Minima, symmetries, and topology*, *Phys. Rev. D* **77** (2008) 015017, [arXiv:0710.3490].

[35] C. C. Nishi, *cp violation conditions in n-higgs-doublet potentials*, *Phys. Rev. D* **74** (2006) 036003, [hep-ph/0605153].

[36] G. Ecker, W. Grimus, and W. Konetschny, *Quark mass matrices in left-right symmetric gauge theories*, *Nuclear Physics B* **191** (1981) 465–492.

[37] I. P. Ivanov, *General two-order-parameter ginzburg-landau model with quadratic and quartic interactions*, *Phys. Rev. E* **79** (2009) 021116, [arXiv:0802.2107].

[38] P. M. Ferreira, H. E. Haber, and J. P. Silva, *Generalized cp symmetries and special regions of parameter space in the two-higgs-doublet model*, *Phys. Rev. D* **79** (2009) [arXiv:0902.1537].

[39] J. F. Gunion and H. E. Haber, *Cp-conserving two-higgs-doublet model: The approach to the decoupling limit*, *Phys. Rev. D* **67** (2003) [hep-ph/0207010].

[40] A. Barroso, P. M. Ferreira, R. Santos, and J. P. Silva, *Stability of the normal vacuum in multi-higgs-doublet models*, *Physical Review D* **74** (2006) [hep-ph/0608282].

[41] H. E. Haber and D. O'Neil, *Basis-independent methods for the two-higgs-doublet model ii. the significance of tan β*, *Physical Review D* **74** (2006) [`hep-ph/0602242`].

[42] M. Dubinin and A. Semenov, *Triple and quartic interactions of higgs bosons in the general two-higgs-doublet model*, 1998.

[43] S. Davidson and H. E. Haber, *Basis-independent methods for the two-higgs-doublet model*, *Phys. Rev. D* **72** (2005) 035004, [`hep-ph/0504050`].

[44] H. Serôdio, *Yukawa alignment in a multi higgs doublet model: An effective approach*, *Physics Letters B* **700** (2011) 133–138, [`arXiv:0908.1554`].

[45] S. L. Glashow and S. Weinberg, *Natural conservation laws for neutral currents*, *Phys. Rev. D* **15** (1977) 1958–1965.

[46] E. A. Paschos, *Diagonal neutral currents*, *Phys. Rev. D* **15** (1977) 1966–1972.

[47] H. E. Haber and O. Stål, *New LHC benchmarks for the $$\mathcal{CP}$$ CP-conserving two-higgs-doublet model*, *The European Physical Journal C* **75** (2015) [`arXiv:1507.04281`].

[48] A. Belyaev, G. Cacciapaglia, I. P. Ivanov, F. Rojas, and M. Thomas, *Anatomy of the inert two higgs doublet model in the light of the lhc and non-lhc dark matter searches*, *Phys. Rev. D* **97** (2018) 035011, [`arXiv:1612.00511`].

[49] M. Gustafsson, *The inert doublet model and its phenomenology*, *PoS* **Charged030** (2010) [`arXiv:1106.1719`].

[50] A. Arhrib, Y.-L. S. Tsai, Q. Yuan, and T.-C. Yuan, *An Updated Analysis of Inert Higgs Doublet Model in light of the Recent Results from LUX, PLANCK, AMS-02 and LHC*, *JCAP* **1406** (2014) 030, [`arXiv:1310.0358`].

[51] A. W. El Kaffas, W. Khater, O. M. Ogreid, and P. Osland, *Consistency of the two Higgs doublet model and CP violation in top production at the LHC*, *Nucl. Phys. B* **775** (2007) 45–77, [`hep-ph/0605142`].

[52] D. Eriksson, J. Rathsman, and O. Stal, *2HDMC: Two-Higgs-Doublet Model Calculator Physics and Manual*, *Comput. Phys. Commun.* **181** (2010) 189–205, [`arXiv:0902.0851`].

[53] M. D. Goodsell and F. Staub, *Unitarity constraints on general scalar couplings with SARAH*, *The European Physical Journal C* **78** (2018) [`arXiv:1805.07306`].

[54] B. Bellazzini, L. Martucci, and R. Torre, *Symmetries, sum rules and constraints on effective field theories*, *Journal of High Energy Physics* **2014** (2014) [`arXiv:1405.2960`].

[55] A. Arhrib, *Unitarity constraints on scalar parameters of the standard and two higgs doublets model*, 2000.

[56] S. Kanemura, T. Kubota, and E. Takasugi, *Lee-quigg-thacker bounds for higgs boson masses in a two-doublet model*, *Physics Letters B* **313** (1993) 155–160, [hep-ph/9303263].

[57] I. F. Ginzburg and I. P. Ivanov, *Tree-level unitarity constraints in the most general two higgs doublet model*, *Physical Review D* **72** (2005) [hep-ph/0508020].

[58] V. Cacchio, D. Chowdhury, O. Eberhardt, and C. W. Murphy, *Next-to-leading order unitarity fits in two-higgs-doublet models with soft z2 breaking*, *Journal of High Energy Physics* **2016** (2016) [arXiv:1609.01290].

[59] B. Grinstein, C. W. Murphy, and P. Uttayarat, *One-loop corrections to the perturbative unitarity bounds in the cp-conserving two-higgs doublet model with a softly broken z2 symmetry*, *Journal of High Energy Physics* **2016** (2016) [arXiv:1512.04567].

[60] D. Chowdhury and O. Eberhardt, *Global fits of the two-loop renormalized two-higgs-doublet model with soft z2 breaking*, *Journal of High Energy Physics* **2015** (2015) [arXiv:1503.08216].

[61] C. T. Hill, C. N. Leung, and S. Rao, *Renormalization group fixed points and the higgs boson spectrum*, *Nuclear Physics B* **262** (1985) 517 – 537.

[62] L. Reina, *Tasi 2011: lectures on higgs-boson physics*, 2012.

[63] P. Bechtle, O. Brein, S. Heinemeyer, G. Weiglein, and K. E. Williams, *HiggsBounds: Confronting Arbitrary Higgs Sectors with Exclusion Bounds from LEP and the Tevatron*, *Comp. Phys. Comm.* **181** (2010) 138–167, [arXiv:0811.4169].

[64] P. Bechtle, S. Heinemeyer, O. Stål, T. Stefaniak, and G. Weiglein, *HiggsSignals: Confronting arbitrary Higgs sectors with measurements at the Tevatron and the LHC*, *Eur. Phys. J. C* **74** (2014) 2711, [arXiv:1305.1933].

[65] S. Iguro, Y. Omura, and M. Takeuchi, *Testing the 2hdm explanation of the muon g-2 anomaly at the lhc*, *JHEP* **11** (2019) 130, [arXiv:1907.09845].

[66] Y. H. Ahn, S. K. Kang, and R. Ramos, *Implications of the new cdf-ii w-boson mass on two-higgs-doublet models*, *Phys. Rev. D* **106** (2022) 055038, [arXiv:2204.06485].

[67] I. Maksymyk, C. P. Burgess, and D. London, *Beyond s, t and u*, *Phys. Rev. D* **50** (1994) 529, [hep-ph/9306267].

[68] O. Atkinson, M. Black, A. Lenz, A. Rusov, and J. Wynne, *Cornering the two higgs doublet model type ii*, *JHEP* **04** (2022) 172, [arXiv:2107.05650].

[69] R. Barbieri, L. J. Hall, and V. S. Rychkov, *Improved naturalness with a heavy higgs: An alternative road to lhc physics*, *Phys. Rev. D* **74** (2006) 015007, [hep-ph/0603188].

[70] J. Haller, A. Hoecker, *et. al.*, *Update of the global electroweak fit and constraints on two-Higgs-doublet models*, *Eur. Phys. J.* **C78** (2018) 675, [arXiv:1803.01853].

[71] Gfitter Group: M. Baak, J. Cúth, *et. al.*, *The global electroweak fit at NNLO and prospects for the LHC and ILC*, *Eur. Phys. J. C* **74** (2014) 3046, [arXiv:1407.3792].

[72] Y. Grossman, *Introduction to flavor physics*, *CERN Yellow Report* **CERN-2010-002** (2010) 111–144, [arXiv:1006.3534].

[73] A. Arbey, F. Mahmoudi, O. Stal, and T. Stefaniak, *Status of the charged higgs boson in two higgs doublet models*, *Eur. Phys. J. C* **78** (2018) 182, [arXiv:1706.07414].

[74] A. V. Manohar, *Introduction to effective field theories*, 2018.

[75] G. Rajasekaran, *Fermi and the theory of weak interactions*, *Resonance* **19** (2014) 18–44, [arXiv:1403.3309].

[76] GAMBIT Flavour Workgroup: F. U. Bernlochner, M. Chrząszcz, *et. al.*, *FlavBit: A GAMBIT module for computing flavour observables and likelihoods*, *Eur. Phys. J. C* **77** (2017) 786, [arXiv:1705.07933].

[77] P. Athron, C. Balazs, *et. al.*, *Likelihood analysis of the flavour anomalies and $g − 2$ in the general two higgs doublet model*, *JHEP* **37** (2022) 2022, [arXiv:2111.10464].

[78] W. Altmannshofer, P. Ball, *et. al.*, *Symmetries and Asymmetries of $B \to K^* \mu^+ \mu^-$ Decays in the Standard Model and Beyond*, *JHEP* **01** (2009) 019, [arXiv:0811.1214].

[79] F. Mahmoudi, *SuperIso v2.3: A Program for calculating flavor physics observables in Supersymmetry*, *Comp. Phys. Comm.* **180** (2009) 1579, [arXiv:0808.3144].

[80] J. Bhom and M. Chrzaszcz, *HEPLike: an open source framework for experimental likelihood evaluation, Comput. Phys. Commun.* **254** (2020) 107235, [`arXiv:2003.03956`].

[81] A. Arbey and F. Mahmoudi, *Dark matter and the early universe: a review, Prog. Part. Nuc. Phys.* (2021) 103865, [`arXiv:2104.11488`].

[82] F. S. Queiroz, *Dark matter overview: Collider, direct and indirect detection searches*, 2016.

[83] F. Kahlhoefer, *Review of lhc dark matter searches, Int. J. Mod. Phys. A* **32** (2017) 1730006, [`arXiv:1702.02430`].

[84] J. M. Gaskins, *A review of indirect searches for particle dark matter*, `arXiv:1604.00014`.

[85] R. Durrer, *The cosmic microwave background: The history of its experimental investigation and its significance for cosmology, Class. Quantum Grav.* **32** (2015) 124007, [`arXiv:1506.01907`].

[86] Planck Collaboration, P. A. R. Ade, *et. al., Planck 2015 results. XIII. Cosmological parameters, A&A* **594** (2016) A13, [`arXiv:1502.01589`].

[87] F. James, *Statistical methods in experimental physics (2nd edition)*. World Scientific Publishing, Singapore, Singapore, 2 ed., 2006.

[88] G. Cowan, *Statistical Data Analysis*. Oxford science publications. Clarendon Press, Oxford, England, 1998.

[89] GAMBIT Scanner Workgroup: G. D. Martinez, J. McKay, *et. al., Comparison of statistical sampling methods with ScannerBit, the GAMBIT scanning module, Eur. Phys. J. C* **77** (2017) 761, [`arXiv:1705.07959`].

[90] A. Kvellestad, P. Scott, and M. White, *GAMBIT and its Application in the Search for Physics Beyond the Standard Model, Prog. Part. Nuc. Phys.* **113** (2020) 103769, [`arXiv:1912.04079`].

[91] F. Mahmoudi, *SuperIso v3.0, flavor physics observables calculations: Extension to NMSSM, Comp. Phys. Comm.* **180** (2009) 1718.

[92] W. Porod, *SPheno, a program for calculating supersymmetric spectra, SUSY particle decays and SUSY particle production at e^+e^- colliders, Comp. Phys. Comm.* **153** (2003) 275–315, [`hep-ph/0301101`].

[93] G. Bélanger, F. Boudjema, A. Pukhov, and A. Semenov, *microMEGAs4.1: Two dark matter candidates*, *Comp. Phys. Comm.* **192** (2015) 322–329, [`arXiv:1407.6129`].

[94] T. Bringmann, J. Edsjö, P. Gondolo, P. Ullio, and L. Bergström, *DarkSUSY 6 : An Advanced Tool to Compute Dark Matter Properties Numerically*, *JCAP* **1807** (2018) 033, [`arXiv:1802.03399`].

[95] GAMBIT Models Workgroup: P. Athron, C. Balázs, *et. al.*, *SpecBit, DecayBit and PrecisionBit: GAMBIT modules for computing mass spectra, particle decay rates and precision observables*, *Eur. Phys. J. C* **78** (2018) 22, [`arXiv:1705.07936`].

[96] B. C. Allanach *et. al.*, *SUSY Les Houches Accord 2*, *Comp. Phys. Comm.* **180** (2009) 8–25, [`arXiv:0801.0045`].

[97] B. C. Allanach, *SOFTSUSY: a program for calculating supersymmetric spectra*, *Comp. Phys. Comm.* **143** (2002) 305–331, [`hep-ph/0104145`].

[98] P. Athron, J.-h. Park, D. Stöckinger, and A. Voigt, *FlexibleSUSY - A spectrum generator generator for supersymmetric models*, *Comp. Phys. Comm.* **190** (2015) 139–172, [`arXiv:1406.2319`].

[99] GAMBIT Dark Matter Workgroup: T. Bringmann, J. Conrad, *et. al.*, *DarkBit: A GAMBIT module for computing dark matter observables and likelihoods*, *Eur. Phys. J. C* **77** (2017) 831, [`arXiv:1705.07920`].

[100] S. Bloor, T. E. Gonzalo, P. Scott, *et. al.*, *The GAMBIT Universal Model Machine: from Lagrangians to Likelihoods*, 2021. in preparation.

[101] F. Staub, *SARAH*, [`arXiv:0806.0538`].

[102] F. Staub, *Exploring new models in all detail with SARAH*, *Adv. High Energy Phys.* **2015** (2015) 840780, [`arXiv:1503.04200`].

[103] F. Rajec, *Two-Higgs-Doublet Models - A Global Study*. PhD thesis, University of Adelaide, 2020.

[104] Y.-L. Wu and L. Wolfenstein, *Sources of cp violation in the two-higgs-doublet model*, *Physical Review Letters* **73** (1994) 1762–1764, [`hep-ph/9409421`].

[105] F. J. Botella and J. P. Silva, *Jarlskog-like invariants for theories with scalars and fermions*, *Phys. Rev. D* **51** (1995) 3870–3875, [`hep-ph/9411288`].

[106] J. F. Gunion and H. E. Haber, *Conditions for cp-violation in the general two-higgs-doublet model*, *Phys. Rev. D* **72** (2005) [`hep-ph/0506227`].

[107] GAMBIT Collaboration: P. Athron, C. Balázs, *et. al.*, *GAMBIT: The Global and Modular Beyond-the-Standard-Model Inference Tool. Addendum for GAMBIT 1.1: Mathematica backends, SUSYHD interface and updated likelihoods*, *Eur. Phys. J. C* **78** (2018) 98, [arXiv:1705.07908]. Addendum to [12].